



HAL
open science

Homogénéisation et optimisation topologique de panneaux architecturés

Laurent Laszczyk

► **To cite this version:**

Laurent Laszczyk. Homogénéisation et optimisation topologique de panneaux architecturés. Autre. Université de Grenoble, 2011. Français. NNT : 2011GRENI088 . tel-00721807

HAL Id: tel-00721807

<https://theses.hal.science/tel-00721807>

Submitted on 30 Jul 2012

HAL is a multi-disciplinary open access archive for the deposit and dissemination of scientific research documents, whether they are published or not. The documents may come from teaching and research institutions in France or abroad, or from public or private research centers.

L'archive ouverte pluridisciplinaire **HAL**, est destinée au dépôt et à la diffusion de documents scientifiques de niveau recherche, publiés ou non, émanant des établissements d'enseignement et de recherche français ou étrangers, des laboratoires publics ou privés.

THÈSE

Pour obtenir le grade de

DOCTEUR DE L'UNIVERSITÉ DE GRENOBLE

Spécialité : **Matériaux, Mécanique, Génie Civil et Electrochimie**

Arrêté ministériel : 7 Août 2006

Présentée par

Laurent LASZCZYK

Thèse dirigée par **Y. BRÉCHET**

et codirigée par **O. BOUAZIZ, R. DENDIEVEL**

préparée au sein du laboratoire **Science et Ingénierie des Matériaux et Procédés**

et de l'école doctorale **Ingénierie - Matériaux, Mécanique, Energétique, Environnement, Procédés et Production**

Homogénéisation et optimisation topologique de panneaux architecturés

Homogenization and topological optimization of architected panels

Thèse soutenue publiquement le **24 novembre 2011**,
devant le jury composé de :

John W. HUTCHINSON

Professeur, Harvard University, USA, Président

Patrice CARTRAUD

Professeur, École Centrale de Nantes, Rapporteur

Samuel FOREST

Directeur de Recherche, École des Mines ParisTech, Rapporteur

Yves BRÉCHET

Professeur, Grenoble-INP, Directeur de thèse

Rémy DENDIEVEL

Professeur, Grenoble-INP, Directeur de thèse

Olivier BOUAZIZ

Ingénieur de Recherche, ArcelorMittal, Co-Directeur de thèse



Remerciements

Aussi riche soit elle, la thèse est une longue expérience semée d'obstacles et d'embûches. Ce n'est que grâce à tout ceux qui m'ont entouré que je m'en sors (presque) indemne.

Je souhaite remercier en premier lieu les membres du jury qui m'ont fait l'honneur d'examiner en détail mon travail et le plaisir de venir à Grenoble assister à ma soutenance. Thank you John Hutchinson for the interest you give to my work and the relevance of your comments. À Patrice Cartraud pour la lecture très détaillée et la fine analyse de mon manuscrit. À Samuel Forest que j'ai eu la chance de côtoyer à de nombreuses reprises tout au long de ma thèse et que je remercie pour son entrain inconditionnel.

Je m'empresse ensuite de remercier la *dream team* qui m'a encadré pendant tout ce temps. Rémy Dendievel pour sa présence au quotidien, sa confiance quelque soit la situation surtout juste avant les échéances. C'était aussi un plaisir de participer à ses enseignements pendant lesquels j'ai beaucoup appris en pédagogie. Yves Bréchet pour son soutien et la richesse des échanges sur ma thèse et des discussions scientifiques en générales. Il restera pour moi un modèle d'efficacité lorsqu'il s'agit d'initier un projet qui fait sens, que ce soit un mini-projet étudiant ou un labex. Olivier Bouaziz que je ne me lasserai jamais d'écouter exposer ses nouvelles idées toujours plus surprenantes. J'aurai juste un petit regret de ne pas avoir réussi à valoriser autant qu'espéré mon travail en collaboration avec ArcelorMittal. Guillaume Parry qui ne fait pas parti du jury de soutenance faute de place mais qui a été présent à mes côtés notamment sur les modèles mécaniques.

Je remercie tous les membres du GPM2 qui m'ont entouré pendant ces 3 années. Les très bonnes relations que j'ai eu la chance d'entretenir ont fait que c'était un plaisir de venir au labo tous les matins. Et j'espère pouvoir revenir régulièrement pour déguster un délicieux café accompagné de blagues en tout genre. J'apporterai des croissants pour être sûr de voir Didier.

Je dois beaucoup aussi aux thésards, jeunes et anciens, encore en rédaction ou déjà ingénieur ou chercheur CNRS. Merci à Jean-Philippe et Pierre qui on été très impliqué dans mon sujet de thèse du début à la fin. À Guillaume, Nico, Throsten (les anciens de PM) pour les séances fartage au labo, les sorties skating entre 12h et 14h, mais aussi les discussions interminables sur la métallurgie. Julien, Julliette, Alex, Rémy Boiss', les anciens GPM2 respectivement pour les sorties en montagne et les blagues. Greg pour les ragots. Thibault, Mathilde, Bastien, David, Sergey, les plus "jeunes" du GPM2. Jenn pour les séances de Matlab-sauna et bien d'autres moments. Tonio avec qui j'ai presque été en couple, c'est pas peu dire ...

Merci à tous les potes qui m'ont supporté et changé les idées pendant les soirées et les week-end. Merci la Bobine pour le soutien logistique de ces moments de détente. Un merci tout particulier à Jo avec qui j'ai partagé la période de rédaction à base de tartes maison et de chute de slack.

À mes parents qui m'ont remonté le moral plus d'une fois. Mon frère et ma sœur avec notamment une course à l'accouchement pleine de suspense entre Anatole et ce présent manuscrit (j'ai perdu!). Et surtout un grand merci à Malika qui a été extrêmement impliquée pour que tout se passe dans les meilleures conditions. Ces années de thèse ont été incroyables.

Merci.

Foreword

This PhD thesis is part of the *CPR (Contrat de Programmes de Recherche)* dedicated to “Multi-functional Architected Materials”. This research program was funded by the CNRS and the industries involved, aiming at developing upstream methods for modeling, selecting and designing architected materials in connection with industrial specifications. The two industries that were part of the project were ArcelorMittal and EDF. They interacted with three academic laboratories : SIMAP Grenoble (*Science et ingénierie des matériaux et des procédés*), CdM Paris (*Centre des Matériaux*) and CETHIL Lyon (*Centre de thermique de Lyon*). Two other PhD studies were performed in parallel : “Generalized effective properties of architected materials” by Duy Trinh at the CdM, and “New materials with high thermal inertia and high conductivity applied to hosting structures for phase change materials” by Juan-Pablo Arzamendia at the CETHIL.

CONTENTS

Contents	8
Résumé étendu	9
0.1 La structure sandwich :	
Exemple emblématique de panneau architecturé	13
0.2 Homogénéisation périodique de panneaux architecturés	19
0.3 Optimisation de forme	22
0.4 Conception optimale d'un panneau sandwich isolant	27
General introduction	33
1 An emblematic architected material : the sandwich structure	43
1.1 Applications and specifications	46
1.2 Materials and architectures	49
1.2.1 Composites	49
1.2.2 Porous and cellular materials	50
1.3 Mechanical properties of sandwich materials	53
1.4 Mechanical shell and plate models	58
1.4.1 Bi-dimensional plane-strain specific case	58
1.4.2 General plate models	62
1.5 Experimental identification	67
2 Homogenization of periodic architected panels	73
2.1 Periodic homogenization of elastic properties	76
2.1.1 Bulk media	76
2.1.2 Panels	78
2.1.3 Conclusion	83
2.2 Level-set method and ersatz phase	84
2.3 Validation of the homogenization approach	90
2.3.1 Four-point bending tests	90
2.3.2 Full-field FEM simulations of tests	91
2.3.3 Effective approach	93
2.3.4 Conclusion	96
2.4 Homogenization of embossed steel sheets	98
2.4.1 Embossed patterns	98
2.4.2 Adaptive mesh	100

2.4.3	Membrane and flexural compliances	101
2.4.4	Transverse-shear compliance	109
2.4.5	Global stiffness	110
3	Shape optimization	115
3.1	Shape derivative and optimization algorithm	121
3.1.1	Shape Derivative	121
3.1.2	Optimization algorithm	122
3.1.3	Numerical results	125
3.2	Optimization of 2D architected panel	128
3.2.1	A multi-functional optimization	129
3.2.2	Influence of the prescribed area fraction	138
3.2.3	Influence of unit cell shape factor	139
3.2.4	Influence of the initial geometry	140
3.3	Prototype samples produced by selective laser sintering	141
4	Optimal design of an insulation sandwich panel	147
4.1	From specifications to optimization problem	151
4.1.1	Panel description	151
4.1.2	Specifications	153
4.1.3	Optimization problem	156
4.2	Shape optimization	162
4.2.1	Influence of the relative importance between thermal and mechanical objectives	165
4.2.2	Influence of the prescribed area fraction	166
4.2.3	Influence of the initial geometry	167
4.2.4	Influence of the unit cell shape factor	170
4.2.5	Summary	172
4.3	From optimization results to prototype panels	173
4.3.1	Selection of promising designs	173
4.3.2	Adjusting to process requirements	174
4.4	Prototype panels performances	176
4.4.1	Thermal transient analysis	176
4.4.2	Prototypes testing	178
	Conclusions & perspectives	195

Appendix A: Tensors notations	203
A.1 General notations	205
A.2 Kelvin's notation	205
A.3 Rotations and anisotropy	206
References	209

RÉSUMÉ ÉTENDU

en français

Introduction

Dans un contexte de développement de semi-produit pour les industries du transport et du bâtiment, les matériaux multi-fonctionnels permettent de répondre à plusieurs fonctions “primaires” et évitent ainsi le recours à des composants distincts pour chacune de ces fonctions. Il est alors envisageable de gagner en performance à condition de trouver un matériau techniquement réalisable et économiquement viable. Le nombre de matériaux monolithiques étant fini, les matériaux architecturés permettent d’élargir les possibilités par combinaison de plusieurs matériaux constitutifs. En particulier pour des propriétés contradictoires (rigidité, isolation thermique, acoustique, etc.), les matériaux architecturés sont en mesure de proposer de très bons compromis.

L’arrangement des phases et le choix des matériaux constitutifs sont autant de paramètres qui permettent de concevoir sur mesure une solution architecturée. Cependant, cette extraordinaire diversité de configuration complexifie la sélection du meilleur compromis. Une méthode traditionnelle par essais-erreurs n’est pas appropriée et les méthodes d’optimisation semblent fournir des outils pertinents pour résoudre en partie ce problème.

Le cas de l’industrie automobile est représentative des problématiques liées au transport en général. Alors que les directives européennes ne cessent de réduire les limites d’émission de gaz et particules (“Commercial vehicles fact sheet”, n° 1, ACEA), la masse des véhicules ne fait qu’augmenter depuis les années 80. La figure 1 présente l’évolution de la masse des véhicules personnels par catégorie. Cette augmentation est engendrée par les

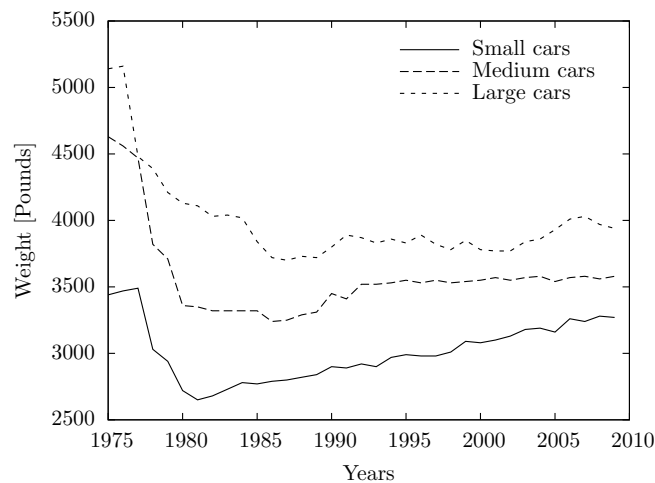


Figure 1: *Évolution de la masse (moyenne par catégorie de taille) des véhicules personnels aux États-Unis d’Amérique entre 1975 et 2009 (Davis et al., 2010).*

normes de sécurité et la demande croissante de confort. Le gain énergétique et écologique potentiellement obtenu par l’allègement est tel aujourd’hui que le développement de solutions plus performantes, mais plus onéreuses, deviennent rentables. C’est le cas des

matériaux architecturés.

Sans parler d'allègement, les cahiers des charges issus du bâtiment peuvent être rempli avec de hautes performances lorsqu'il s'agit de propriétés contradictoires. C'est souvent le cas pour combiner des propriétés structurales (rigidité, résistance mécanique) et des propriétés fonctionnelles (isolation thermique ou acoustique par exemple). Les considérations économiques restent cependant un frein important au développement de tels produits.

La conception sur mesure de matériaux architecturés est proposée dans le cadre de cette thèse comme une extension des méthodes de sélection des matériaux (Ashby, 2005). Celles-ci consistent à traduire un cahier des charges en indice de performance. Cet indice permet de sélectionner les matériaux les plus performants sur une carte des propriétés (e.g. module de flexion en fonction de la conductivité thermique sur la figure 2). La conception de matériaux architecturés vise à combiner plusieurs matériaux (ou un matériau et du vide) pour obtenir une solution qui se rapproche le plus possible des "trous intéressants" sur les cartes des propriétés.

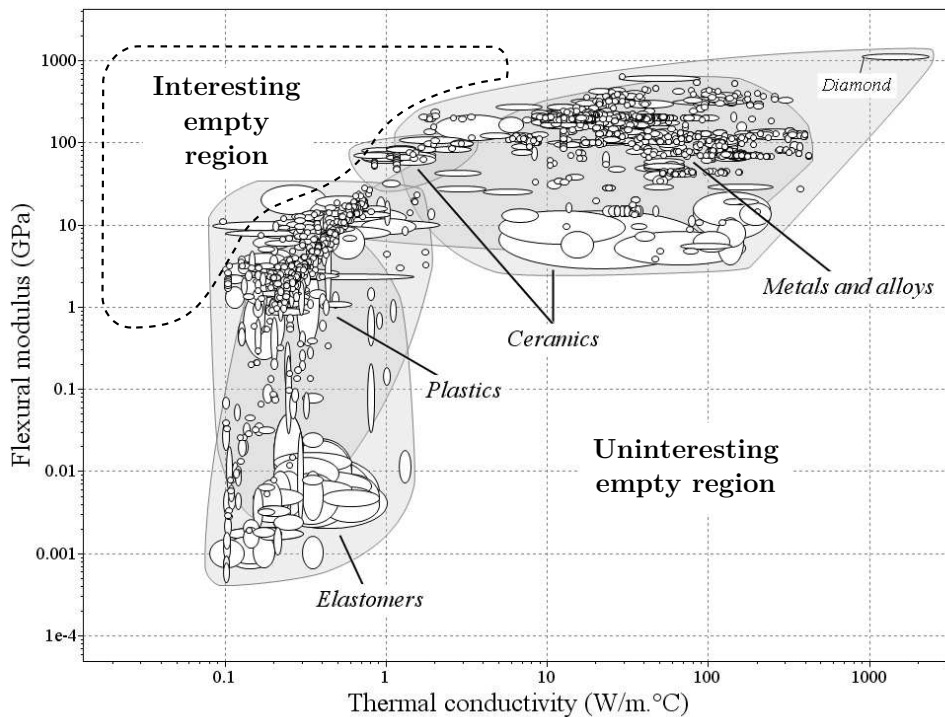


Figure 2: Principales classes de matériaux représentées sur une carte module de flexion versus densité. Une partie de la carte est accessible par des matériaux existants. Le reste est vide et justifie le développement de matériaux architecturés pour combler ces "trous intéressants" (coin supérieur gauche de la carte).

La particularité des matériaux architecturés est la coexistence des échelles. Le terme "architecturé" suggère qu'il existe une ou plusieurs phases supposées homogènes, qui sont

distribuées dans l'espace. Le terme "matériaux", au contraire, affirme que la distribution des phases est suffisamment fine pour être considérée comme homogène à échelle d'une pièce (au moins vis à vis des propriétés concernées). On s'attend naturellement à ce que les méthodes d'homogénéisation fournissent des outils appropriés pour évaluer la performance des solutions proposées. Les applications qui motivent ces travaux concernent des produits sous forme de panneau. cette catégorie de matériaux architecturés, avec comme exemple emblématique le panneau sandwich, illustre particulièrement bien cette coexistence des échelles.

Dans ce contexte, ce travail de thèse traite de la conception optimale de panneaux architecturés à travers trois points principaux : la description des méthodes d'homogénéisation d'un panneau ; l'optimisation de panneaux architecturés modèles pour la rigidité en flexion et le cisaillement ; et l'optimisation multi-fonctionnelle de raidisseur de panneaux sandwich isolants. Une introduction préliminaire sur les notions de matériaux architecturés, de sélection des matériaux et les modèles mécaniques (plaques et coques) dédiés aux panneaux est proposée en s'appuyant sur l'exemple emblématique du panneau sandwich.

0.1 La structure sandwich : Exemple emblématique de panneau architecturé

Une structure dite "sandwich" est un panneau constitué de trois couches, deux couches (appelées parements ou peaux) disposés symétriquement de chaque côté d'une couche centrale (appelé cœur ou âme). Deux matériaux différents sont choisis pour les parements et le cœur. Le premier est choisi pour sa rigidité en traction-compression, le deuxième pour sa légèreté et sa rigidité en cisaillement. Cette répartition spatiale des deux matériaux assure une grande rigidité en flexion pour une masse réduite.

Cette structure illustre particulièrement bien le concept de "matériaux architecturés" qui est de trouver un bon compromis entre propriétés contradictoires grâce à la combinaison de plusieurs matériaux et leur distribution dans l'espace.

La structure sandwich permet d'introduire aussi la notion de "matériau hiérarchique" puisque cette architecture simple de premier niveau (peaux-âme) est souvent complétée par l'utilisation de matériaux eux-même architecturés. Par exemple, des composites stratifiés fibres-matrice sont utilisés pour les parements. Mais on rencontre surtout une grande variété de matériaux architecturés pour le cœur du sandwich : des matériaux poreux, des mousses, ou plus généralement des matériaux cellulaires comme ceux présentés sur la figure 3. Alors que les peaux sont fortement contraint par la fonctionnalité de rigidité du panneau en flexion, le cœur a plus de liberté et peut judicieusement contribuer à une propriété supplémentaire telle que l'isolation thermique ou l'absorption d'énergie aux chocs.

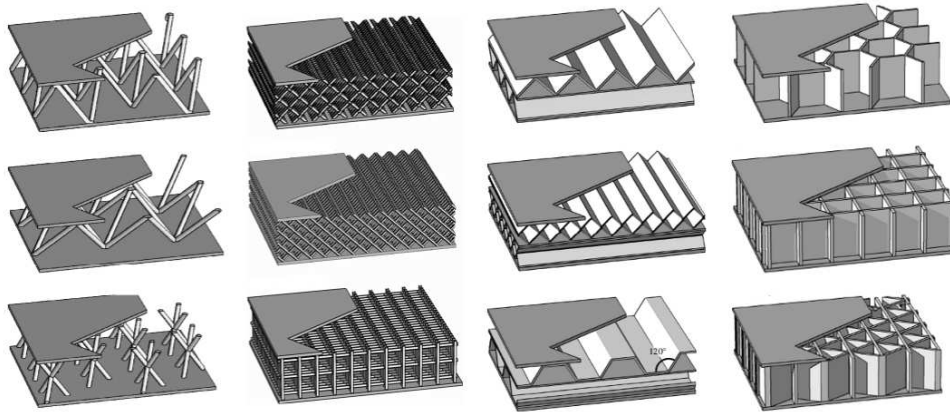


Figure 3: Exemples de matériaux architecturés utilisés pour l'âme de structure sandwich. Ces géométries de treillis, de gaufrages et de nids d'abeille sont sélectionnés pour leur forte capacité d'absorption d'énergie aux chocs. (Wadley, 2006)

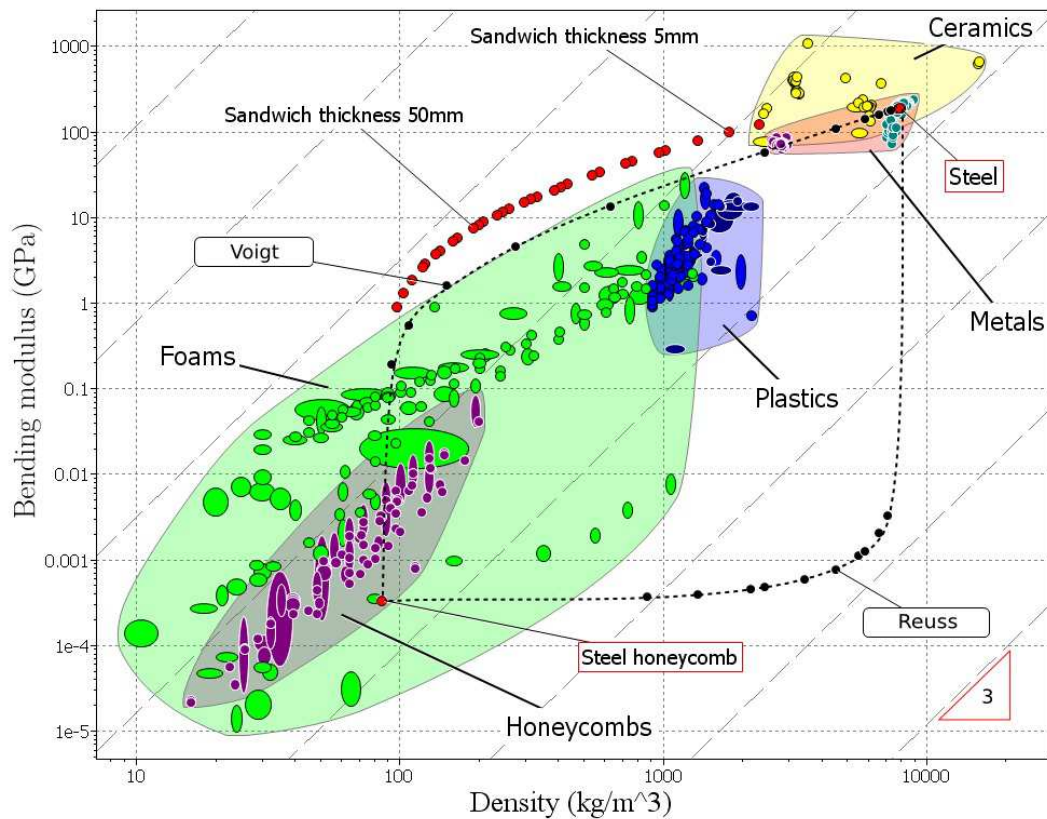


Figure 4: Carte des propriétés module de flexion – masse volumique qui compare des structures sandwich constituées de parements acier et d'une âme en nids d'abeille acier (rond rouge), avec les bornes de Voigt et Reuss sur le module Young (rond noir). Les droites pointillées correspondent à l'indice de performance $E^{1/3}/\rho$ (rigidité en flexion d'une plaque à masse minimum) et montre que la structure sandwich est meilleur que tous les matériaux monolithiques.

Sélection des matériaux et propriétés équivalentes Le succès d'un matériaux architecturés réside dans le choix des matériaux à combiner et leur répartition afin d'obtenir un bon compromis. On cherche en effet à conserver au maximum les avantages de chacun des matériaux et non les inconvénients de chacun. Alors que la problématique de l'arrangement spatial des phases est abordée par des méthodes d'optimisation de forme dans la suite de la thèse, celle du choix des matériaux constitutifs peut être traitée par des méthodes de sélection des matériaux. Dans les deux cas, il est nécessaire de définir des indices de performance (ou fonctions objectif) qui traduisent le cahier des charges et évalue la pertinence de chaque solution (couple matériaux-géométrie). La figure 4 est une illustration de l'utilisation de carte des propriétés pour comparer la performance de plusieurs solutions, monolithiques ou architecturés.

Les indices de performance pour les matériaux architecturés font naturellement intervenir des modules équivalents ou macroscopiques qui résultent d'une étape d'homogénéisation. Il convient d'être particulièrement précautionneux dans le choix de ces propriétés équivalentes, notamment lors de comparaison de matériaux architecturés avec des matériaux monolithique. La figure 4 illustre les surprises que l'on peut rencontrer. Les matériaux sandwich représenté sur cette carte dépassent les expressions de Voigt et Reuss, qui ne sont pas des bornes pour le module de flexion.

Lorsque l'on s'intéresse à la rigidité globale en flexion, l'épaisseur relative du panneau et le rapport des modules de peaux et d'âme peuvent rendre la contribution du cisaillement transverse non-négligeable. Ce point est illustré dans le manuscrit et sert de justification à la prise en compte du module de cisaillement transverse dans les problèmes d'optimisation traités par la suite.

Nous nous intéressons plus particulièrement aux performances en rigidité mécanique de panneaux architecturés. Les modèles de poutre et de plaque sont alors des cadres appropriés à l'étape d'homogénéisation qui permet de calculer les modules équivalents de rigidité.

Modèles mécaniques de poutre et de plaque L'élancement des poutres et plaques motive à définir des modèles macroscopiques qui s'affranchissent d'une ou deux coordonnées spatiales. L'approche suivie dans cette thèse est celle de Reissner et consiste à définir des efforts macroscopiques. Dans le cas du modèle poutre de Timoshenko, ces

efforts sont :

$$\begin{cases} N(x_1) = \int_{-h/2}^{h/2} \sigma_{11} dx_3 \\ M(x_1) = \int_{-h/2}^{h/2} \sigma_{11} x_3 dx_3 \\ Q(x_1) = \int_{-h/2}^{h/2} \sigma_{13} dx_3 \end{cases} \quad (1)$$

où σ_{ij} sont les composantes du tenseur des contraintes et h l'épaisseur du panneau (figure 5). Ces efforts macroscopiques sont dénommés *force tangentielle* N , *moment fléchissant* M et *force normale* Q .

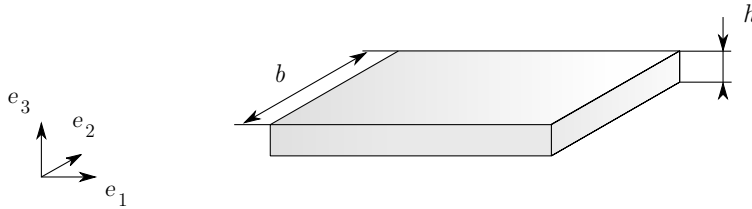


Figure 5: Plaque homogène d'épaisseur h et largeur b .

Les cinématiques associées sont respectivement la *déformation tangentielle* e , la *courbure* χ et le *taux de cisaillement* γ (figure 6). La loi de comportement élastique reliant ces déformations aux efforts macroscopiques peut s'écrire sous la forme suivante pour faire apparaître les coefficients de souplesse :

$$\begin{bmatrix} e \\ \chi \\ \gamma \end{bmatrix} = \begin{bmatrix} a & b & k \\ b & d & l \\ k & l & f \end{bmatrix} \begin{bmatrix} N \\ M \\ Q \end{bmatrix} \quad (2)$$

où les composantes sur la diagonale renseignent sur la réponse élastique du panneau aux sollicitations élémentaires : la souplesse en traction a , la souplesse en flexion d et la souplesse en cisaillement transverse f .

Dans le manuscrit, la généralisation au modèle plaque de Reissner-Mindlin est présenté en détail.

Identification des modules de flexion et cisaillement transverse par essais de flexion quatre points Les essais de flexion (trois ou quatre points) sont très fréquemment utilisés pour caractériser les panneaux. L'essai de flexion quatre points présente l'avantage de solliciter la poutre avec un moment fléchissant homogène entre les deux appuis centraux (figure 7).

La souplesse de flexion est déduite de la pente de la courbe force-déplacement (figure 8)

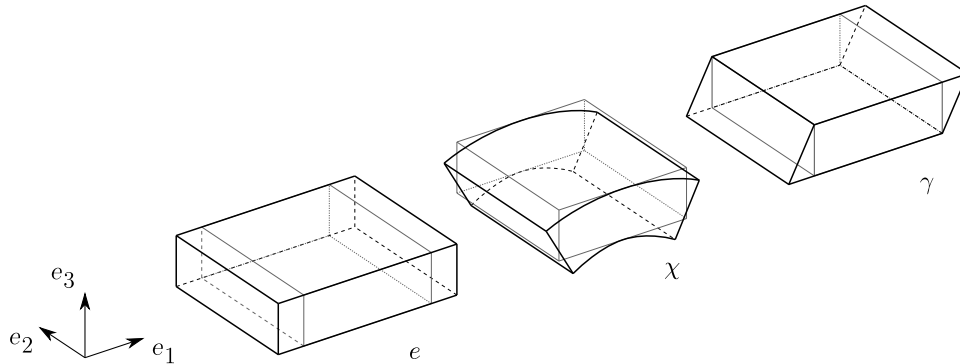


Figure 6: Parallélépipèdes soumis aux trois déformations macroscopiques du modèle poutre de Timoshenko.

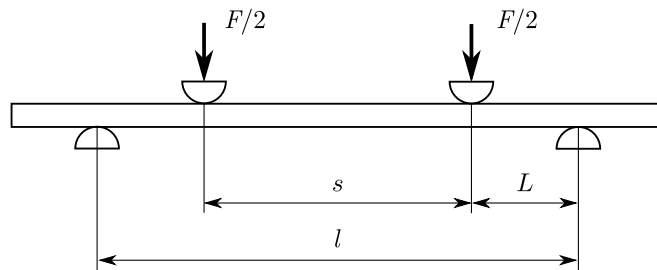


Figure 7: Schéma d'un essai de flexion quatre points. Le chargement est réparti sur les deux point d'appuis supérieurs. Les distances entre appuis supérieurs est dénommée s , la portée l , et la longueur en cisaillement L .

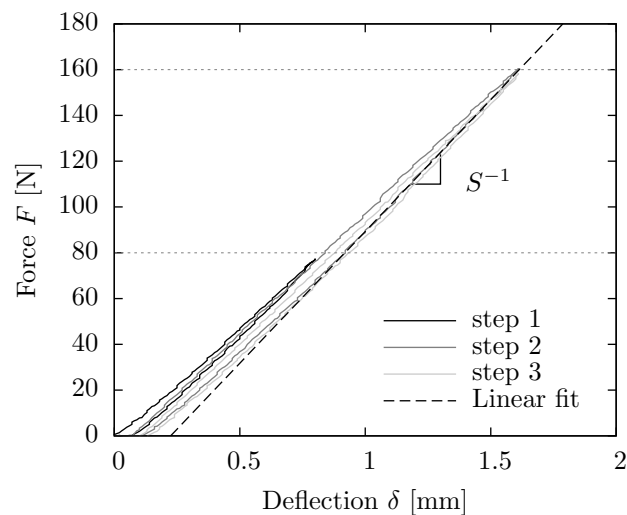


Figure 8: Courbes force-déplacement de trois séquences de charge-décharge en flexion quatre points. La souplesse S est mesurée sur la pente des deuxième et troisième décharges entre 80 et 160 N.

telle que :

$$S = \frac{\partial \delta}{\partial F} \quad (3)$$

où F est la force totale appliquée sur les deux appuis supérieurs, et δ est leur déplacement vertical. Plusieurs séquences de charge-décharge sont effectuées et la pente est mesurée sur le début des deuxième et troisième décharges.

L'évolution des efforts macroscopique le long de la poutre sont tracés sur la figure 9. Par intégration de l'énergie élastique sur la poutre, on obtient l'expression suivante pour la souplesse en flexion quatre points S_{4p} :

$$S_{4p} = \frac{(3l - 4L)L^2}{12} d + \frac{L}{2} f \quad (4)$$

où la portée l et la longueur en cisaillement L sont illustrées sur la figure 7. La souplesse en flexion trois points S_{3p} est déduite de l'expression précédente en choisissant $L = l/2$:

$$S_{3p} = \frac{l^3}{48} d + \frac{l}{4} f \quad (5)$$

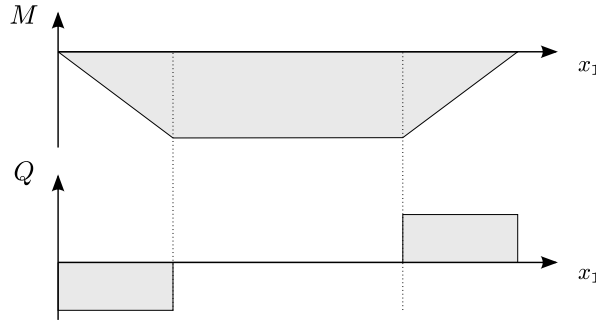


Figure 9: Variations of the bending moment M and the transverse force Q along the beam for a four-point bending test.

En négligeant la contribution du cisaillement, on peut obtenir une sur-estimation de la souplesse de flexion d . Si celle-ci n'est pas négligeable, les normes internationales ASTM (C393, D7250) propose une procédure expérimentale pour déterminer à la fois la souplesse en flexion et en cisaillement transverse. Cette procédure consiste à effectuer plusieurs essais de flexion avec une longueur de cisaillement L fixe et différentes portées l . Les souplesses mesurées sont tracées en fonction de l et doivent s'aligner sur une droite. L'équation d'Allen (4) permet de relier les coefficients de souplesse à la pente S' et à l'ordonnée à l'origine S_0 de cette droite :

$$\begin{cases} d = \frac{4}{L^2} S' \\ f = \frac{8}{3} S' + \frac{2}{L} S_0 \end{cases} \quad (6)$$

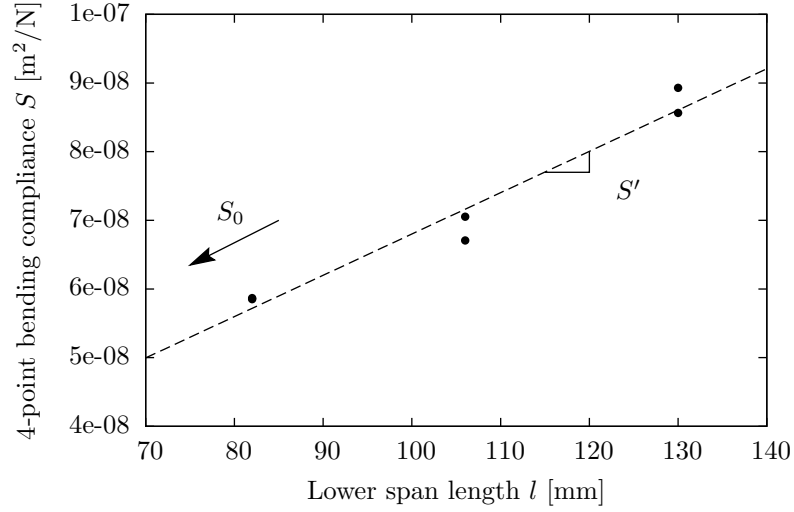


Figure 10: Mesures de souplesse en flexion quatre points S pour plusieurs valeur de portée l . Les coefficients de souplesse en flexion et cisaillement sont calculés à partir de la pente s' et l'ordonnée à l'origine S_0 de la tendance linéaire.

La position des appuis doit être choisie de sorte que le rapport de longueur l/L doit être compris entre 3 et 5. En outre, la longueur en cisaillement L dépend aussi de l'épaisseur du panneau, de la largeur des appuis et de la longueur interne de l'architecture du panneau. Le rapport L/h doit être supérieur à 2. La géométrie des appuis peut être cylindrique ou rectangulaire. Il faut juste vérifier que les surfaces de contact soit simultanément suffisamment grandes pour limiter l'indentation et suffisamment petite en comparaison de la longueur de cisaillement L . L'indentation provoquera une non-linéarité sur les courbes de force-déplacement due à la plastification sous l'appuis. Des appuis trop larges impliqueront une estimation trop rigide du coefficient de cisaillement.

Même si le cisaillement transverse est pris en compte, l'éclatement de la poutre doit être suffisant pour vérifier les hypothèses d'un modèle poutre (ou plaque). Ainsi, on choisit typiquement une épaisseur relative h/l inférieur à 0.3. Le choix de la largeur doit prendre en compte la longueur interne de l'architecture (comme pour la longueur de cisaillement). Cependant, il convient de la choisir de sorte que le rapport b/h soit compris entre 2 et 5 selon l'épaisseur (respectivement du plus épais au plus fin).

0.2 Homogénéisation périodique de panneaux architecturés

Cette partie détaille uniquement l'étape d'homogénéisation qui est un pré-requis pour la sélection ou l'optimisation de motifs de panneaux ou tôles architecturés. Nous nous intéressons dans le cadre de cette thèse uniquement à des architectures périodiques dont les propriétés équivalentes peuvent être calculées exactement sur la cellule périodique.

Procédure d'homogénéisation Cette étape d'homogénéisation, illustrée sur la figure 11, consiste à substituer au panneau architecturé tridimensionnel une coque ou une plaque bidimensionnelle dont les propriétés homogènes permettent d'estimer le comportement moyen du panneau. Ces propriétés homogènes équivalentes sont identifiées sur une cellule périodique soumise à des chargements élémentaires (traction, flexion pure, cisaillement transverse, etc.).

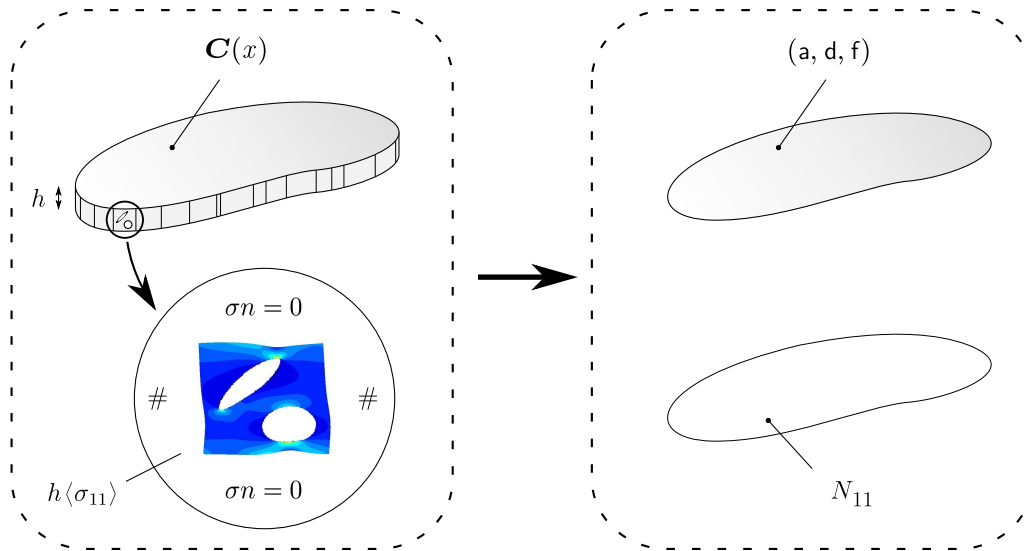


Figure 11: Homogénéisation périodique de panneau : le panneau hétérogène tridimensionnel est remplacé par une coque ou plaque bidimensionnelle avec des propriétés homogènes équivalentes.

En ce qui concerne le modèle coque, les sollicitations élémentaires de traction et flexion sont appliquées par l'intermédiaire d'une pré-déformation. Les frontières de la cellule périodique sont alors soumises à des conditions de périodicité ou libre de contrainte pour les faces supérieures et inférieures du panneau. Il est possible d'imposer les efforts macroscopiques en ajoutant des équations globales sur ces efforts dont les inconnues sont les composantes de pré-déformation. L'identification des coefficients de souplesse est possible soit par ces valeurs de pré-déformations, soit par l'énergie de déformation totale.

Dans le cas du cisaillement transverse, il n'est pas possible de soumettre la cellule périodique à une telle sollicitation en conservant les conditions aux limites de bord libre sur les faces supérieures et inférieures. Ce chargement n'est pas équilibré par lui-même. Deux stratégies sont alors envisagées : relaxer le problème en imposant une contrainte de cisaillement pur sur l'ensemble des frontières de la cellule (SUBC : *static uniform boundary conditions*) ; ou imposer une force volumique proportionnelle à la contrainte de flexion pure afin d'équilibrer le chargement de cisaillement transverse (BG : *bending gradient*).

Contribution du cisaillement transverse Ce paragraphe illustre l'influence du cisaillement transverse dans un cas de chargement classique de panneau, et compare les deux stratégies d'homogénéisation pour le cisaillement. Pour cela une géométrie modèle de panneau architecturé est choisit. Un échantillon de cette géométrie a été réalisée par fabrication additive (frittage laser de poudre polyamide) et testée en flexion (figure 12).

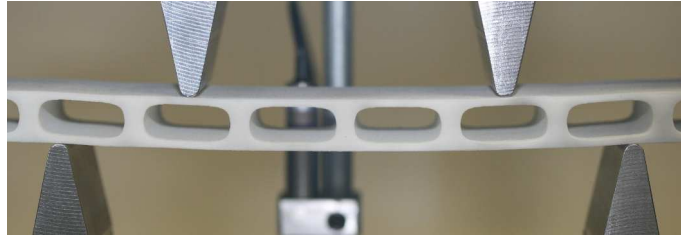


Figure 12: Échantillon modèle en configuration d'essai de flexion quatre-points. Il a été réalisé par frittage laser de poudre polyamide.

La figure 13 présente des mesures et estimations de souplesse en flexion quatre points en fonction de la portée l et pour trois valeurs de longueur en cisaillement L . Des données expérimentales sont comparées à des simulations par éléments finis et à l'expression analytique d'Allen (4) qui utilise des coefficients de souplesse identifiés numériquement avec les chargements SUBC ou BG. Il est mise en évidence une très bonne prédiction du comportement moyen lorsque les conditions aux limites sont respectées, i.e. avec le chargement issu du gradient de flexion (BG).

Tôles gaufrées en acier Une autre application de cette procédure d'homogénéisation de panneau est présentée dans ce chapitre. Il s'agit de tôles gaufrées en acier et du choix de paramètres géométriques afin d'obtenir les propriétés souhaitées. Plusieurs motifs de gaufrage sont étudiés, en particulier un motif hexagonal dont les propriétés équivalentes calculées sont représentées sur la figure 14 en fonction de l'amplitude de gaufrage H .

À partir de ces résultats de calcul sur la cellule périodique, on peut déduire en utilisant des règles de proportionnalité les propriétés pour d'autres jeux de paramètres géométriques. Il est alors envisageable de construire un abaque représenté sur la figure 15. On peut alors sélectionner directement sur cet abaque une tôle gaufrée ayant le même module de flexion qu'une tôle plate de référence, mais pour une épaisseur moindre. En contrepartie, on génère une diminution du module de traction, que l'on peut mesurer sur la même figure.

Cette étude démontre alors comment les méthodes d'homogénéisation et celle de sélection des matériaux permettent de construire des outils graphiques efficaces pour la conception sur mesure de panneaux architecturés.

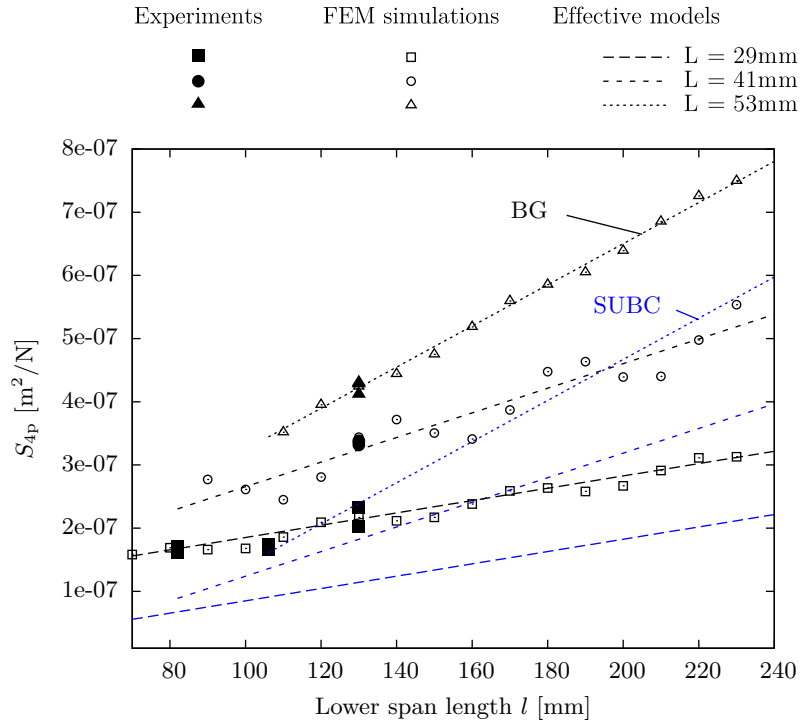


Figure 13: Comparaison de l'équation analytique (4) avec les simulations éléments finis et les données expérimentales. La souplesse en cisaillement f est calculée avec : des conditions aux limites en contrainte uniformes (lignes bleues) ; une force surface issue du gradient de flexion (lignes noires).

0.3 Optimisation de forme

Les propriétés équivalentes caractérisent précisément les performances en rigidité des panneaux architecturés. La procédure d'homogénéisation décrite précédemment permet de identifier ces modules à partir des énergies de déformation résultant de calculs d'élasticité sur la cellule périodique. Tous les outils sont alors disponibles pour résoudre le problème d'optimisation cherchant à maximiser un compromis entre les différentes propriétés mécaniques (flexion et cisaillement transverse par exemple).

Optimisation topologique par ligne de niveau Il existe d'innombrables méthodes d'optimisation, plus ou moins approprié au problème que l'on se pose ici. Nous nous sommes intéressés aux techniques d'optimisation de forme. Plus particulièrement, les techniques d'optimisation topologique autorise une très grande liberté quant à la topologie (i.e. plus ou moins le nombre de trous) et ne nécessite pas de paramétrisation de la géométrie. La méthode par ligne de niveau consiste à définir la géométrie implicitement par l'intermédiaire d'une fonction dit *level-set*. Son iso-valeur égale à zéro définit la frontière de la géométrie et donc la modification itérative de cette fonction permet de transformer

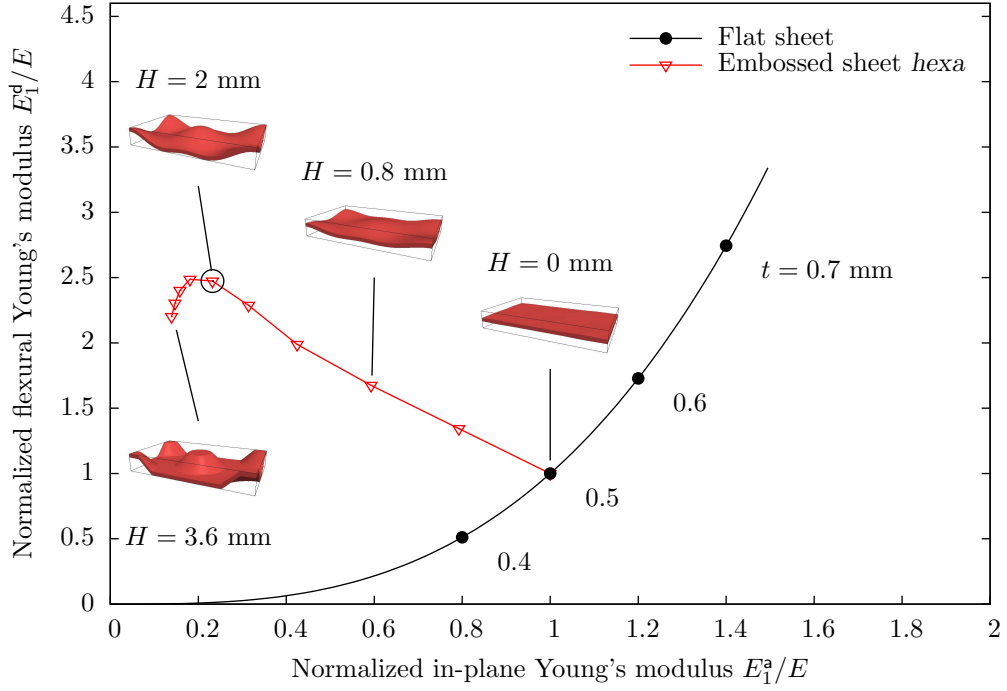


Figure 14: Variations des modules de traction et de flexion en fonction de l'amplitude du gaufrage H . Deux types de motifs sont étudiés : les motifs non-seuillés, puis les motifs seuillés à 2 mm pour $H > 2$ mm.

progressivement la géométrie. C'est cette méthode qui a été choisie et implémentée pour optimiser la géométrie d'une cellule périodique bidimensionnelle de panneau architecturé.

L'évolution de la fonction level-set est gérée par une équation de transport. Dans le cas d'un problème d'optimisation de la compliance d'une structure (ou du coefficient de souplesse équivalent d'une cellule périodique), le champ de vitesse est déduit de la densité locale d'énergie élastique. Chaque itération consiste donc à résoudre un ou plusieurs calculs par éléments finis pour chaque sollicitation, puis à résoudre quelques itérations de l'équation de transport en utilisant les résultats des calculs précédents.

Formulation du problème d'optimisation Nous avons noté l'importance de la contribution du cisaillement transverse à la rigidité globale en flexion d'un panneau dans certaines configurations. Il est évident qu'une optimisation mono-objectif de la rigidité en flexion pure aboutirait à la géométrie non satisfaisante de deux plaques uniformes disjointes. Il est alors nécessaire de prendre en compte la rigidité en cisaillement transverse dans une fonction multi-objectif comme par exemple une rigidité de flexion trois points ou un produit de puissance. En choisissant ce dernier, le problème d'optimisation s'écrit :

$$\min_{\{\Omega \subset V \text{ s.t. } F(\Omega)=0\}} J_\alpha(\Omega) = \mathbf{d}^\alpha f^{(1-\alpha)} \quad (7)$$

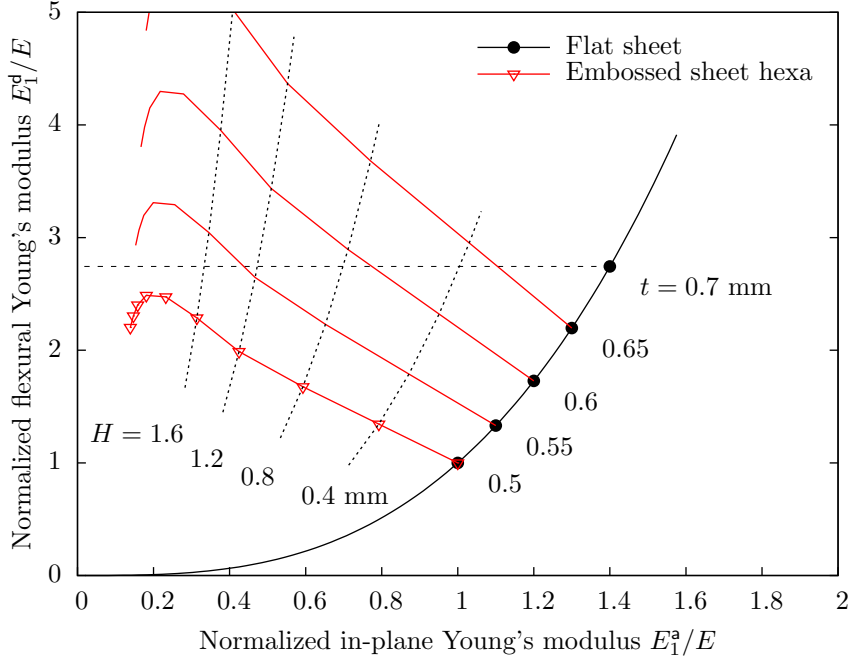


Figure 15: *Abaque permettant de choisir les valeurs appropriées des paramètres géométriques (l'épaisseur de tôle t et l'amplitude de gaufrage H) en fonction des modules de rigidité souhaités. La masse économisée par rapport à une tôle plate est donnée par la réduction d'épaisseur.*

où la contrainte $F(\Omega) = 0$ force la fraction de surface à la valeur \bar{A}_f , en exprimant :

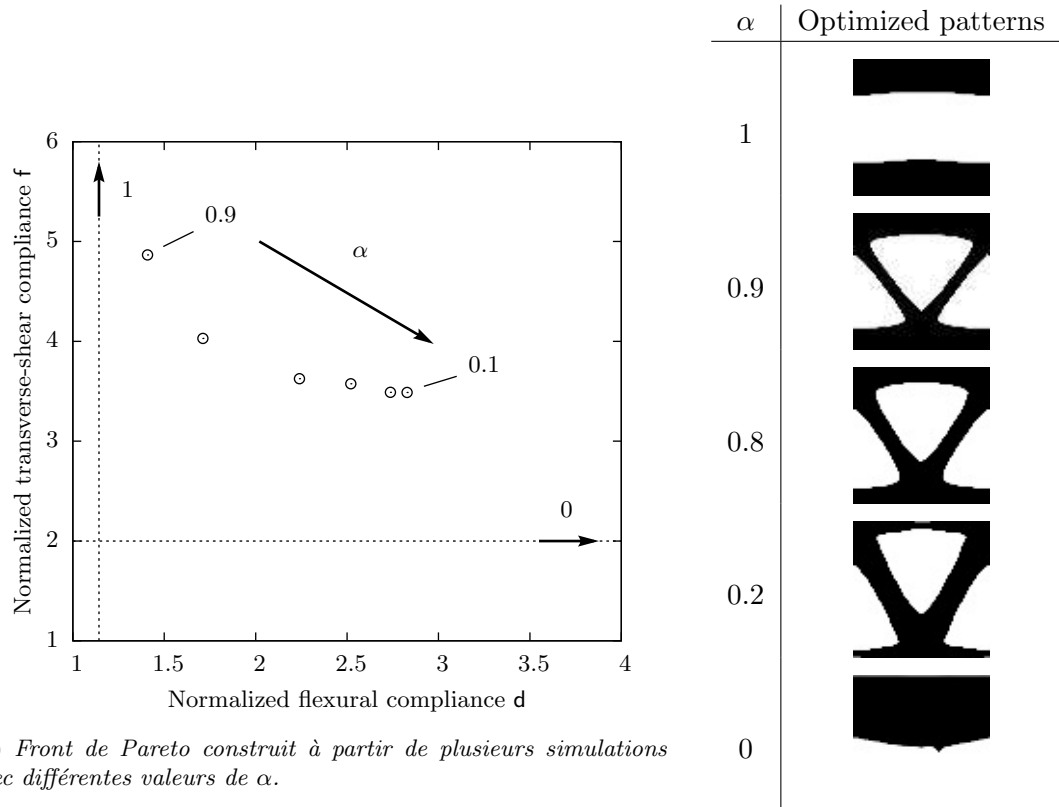
$$F(\Omega) = \frac{\mathcal{A}(\Omega)}{\mathcal{A}(V)} - \bar{A}_f \quad (8)$$

L'application \mathcal{A} désigne l'aire du domaine auquel elle s'applique. La fonction objectif $J_\alpha(\Omega)$ introduit le coefficient α qui quantifie l'importance relative entre flexion et cisaillement. Choisir $\alpha = 1$ revient à optimiser uniquement la souplesse en flexion, et $\alpha = 0$ uniquement la souplesse en cisaillement.

Les détails techniques de l'implémentation de la méthode d'optimisation, ainsi que l'influence de chacun des paramètres sont décrits dans le manuscrit. Seul l'influence du coefficient α et celle de la géométrie initiale sont mentionnées dans ce résumé étendu.

Constructions de fronts de Pareto Le coefficient α introduit dans la fonction objectif du problème (7) contrôle l'importance relative de la flexion par rapport au cisaillement transverse. En effectuant plusieurs simulations avec des valeurs de α allant de 0 à 1, il est possible de construire une estimation du front de Pareto. Le front de Pareto d'un problème d'optimisation multi-fonctionnel est l'ensemble des solutions optimales, i.e. des solutions pour lesquelles il n'en existe aucune autre qui soit meilleur sur tous les indices de performance.

Sur la figure 16a le meilleur compromis recherché entre flexion et cisaillement se situe en bas à gauche. Les lignes droites pointillées représentent les valeurs extrêmes inatteignables et les points correspondent aux motifs de cellule périodique optimisés pour les différentes valeurs de α . La même géométrie initiale et la même contrainte de surface sont utilisées pour toutes les simulations. Les points semblent s'aligner sur une courbe convexe qui s'apparente à un front de Pareto pour ce problème.



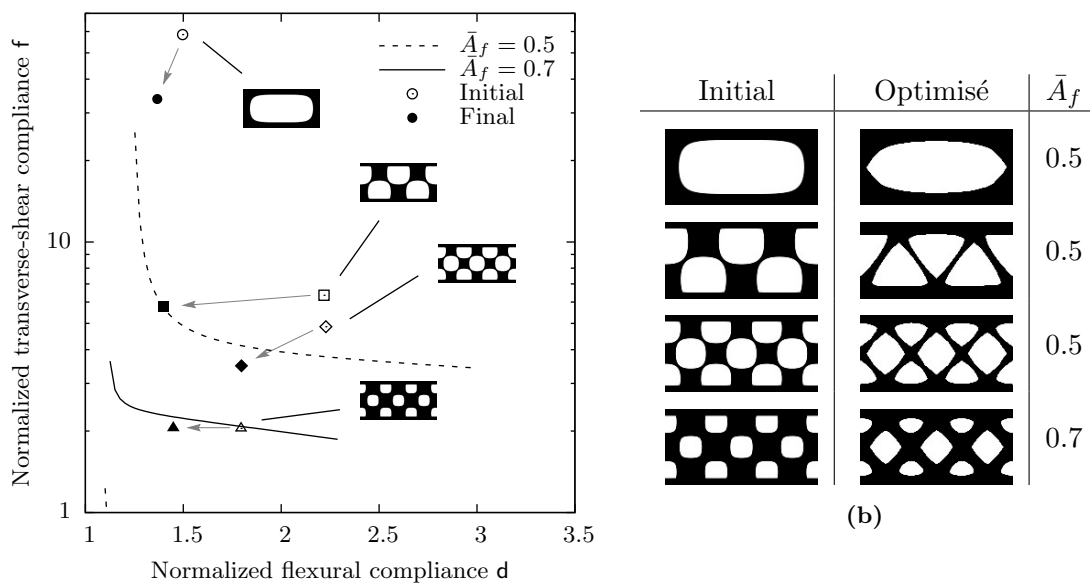
(a) Front de Pareto construit à partir de plusieurs simulations avec différentes valeurs de α .

(b) Motifs optimisés après 50 itérations avec $\bar{A}_f = 0.5$.

Figure 16: Construction d'un front de Pareto en optimisant la fonction objectif (7) à partir de la même géométrie initiale mais différentes valeurs du coefficient α . La fraction de surface est imposée à $\bar{A}_f = 0.5$.

Sensibilité à la géométrie initiale Malgré la méthode d'optimisation choisie qui autorise des changements topologiques par coalescence des trous, les résultats montrent une forte sensibilité à la géométrie initiale. La figure 17 présente en particulier trois géométries initiales ayant un nombre de trous différent et les géométries optimisées correspondantes pour une même contrainte de surface $\bar{A}_f = 0.5$. On observe que la topologie est conservée lors de l'optimisation et que le compromis trouvé en terme de souplesses mécaniques est très différent pour chaque cas.

Parmi les nombreuses simulations d'optimisation effectuées à partir de différentes géométries initiales montrent que la topologie peut être modifiée dans certain cas, mais la forte influence de la géométrie de départ sur le résultat est toujours observée. Cette sensibilité provient de la nature du problème d'optimisation. L'expression d'une fonction objectif qui dépend des propriétés équivalentes impliquent une non-unicité de la solution du problème d'optimisation du fait de l'homogénéité des sollicitations pour les déterminer. Cependant cet inconvénient peut aussi devenir un avantage car il rend possible l'amélioration d'une solution existante tout en restant dans un domaine restreint qui assure la faisabilité de la solution optimisée.



(a) Représentation des souplesses en flexion et en cisaillement pour quatre géométries initiales et les géométries optimisées correspondantes.

Figure 17: Comparaison des rigidités des motifs initiaux et finaux pour trois différentes topologies initiales et deux valeurs de fraction surfacique $\bar{A}_f = 0.5$ et 0.7 . Le coefficient d'échange est $\alpha = 0.5$.

Les motifs périodiques initiaux et finaux de la figure 17 ont été réalisés par frittage laser sélectif de poudre polyamide. Ces échantillons sont présentés sur la figure 18. Ils ont

été testés en flexion quatre points avec différentes longueurs de cisaillement afin d'identifier les modules de souplesse en flexion et en cisaillement. Ces résultats sont présentés dans le manuscrit et comparés aux prédictions numériques par homogénéisation.

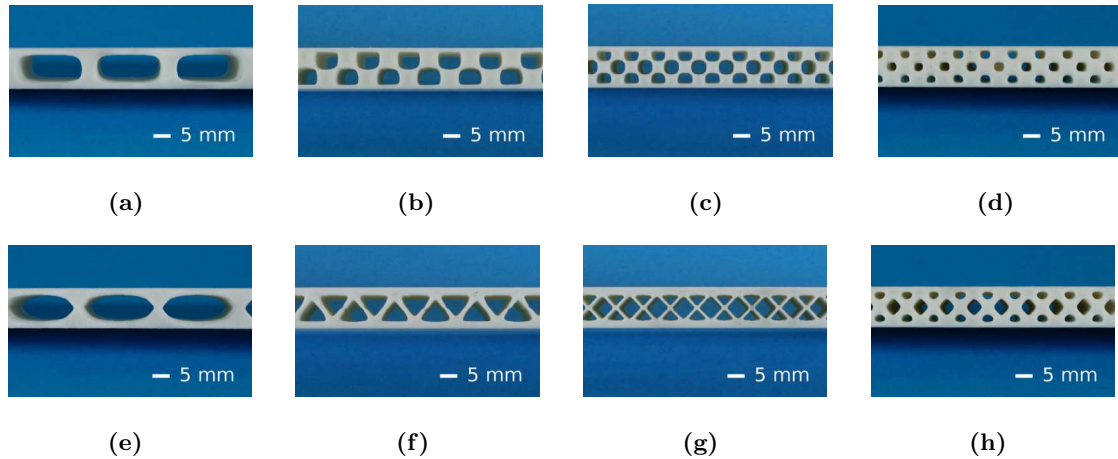


Figure 18: Échantillons produits par frittage laser sélectif en polyamide : géométries initiales (a-d), et géométries optimisées associées (e-h).

0.4 Conception optimale d'un panneau sandwich isolant

Nous arrivons à la partie de synthèse de ce travail qui consiste à mettre en œuvre les outils développés dans le cadre d'une amélioration d'un produit industriel existant. Il s'agit d'un panneau sandwich isolant conçu et fabriqué par la société *Sainte-Marie Constructions Isothermes*. Le panneau est constitué de deux parements en acier inoxydable espacés par des raidisseurs en acier. L'espace entre les parements et les raidisseurs est comblé avec de la laine minérale isolante. Un schéma du panneau est présenté sur la figure 19. Le problème que l'on se propose de traiter est l'optimisation des motifs des raidisseurs avec une contrainte de non-évidement dans les zones de pliage (*folding distances*).

Formulation du problème d'optimisation issu du cahier des charges L'étude détaillée des fonctions à remplir par le panneau a mis en évidence deux propriétés à prendre en compte dans le problème d'optimisation. Il s'agit de la rigidité mécanique globale en flexion (qui fait intervenir les modules équivalent de flexion pur et de cisaillement), et la diffusivité thermique (qui fait intervenir principalement la conductivité équivalente). La diffusivité caractérise l'augmentation transitoire de la température sur une face du panneau lorsque l'on chauffe l'autre face. Cette propriété d'isolation thermique est certifiée par la norme A754(18) de l'Organisation Internationale de la Marine.

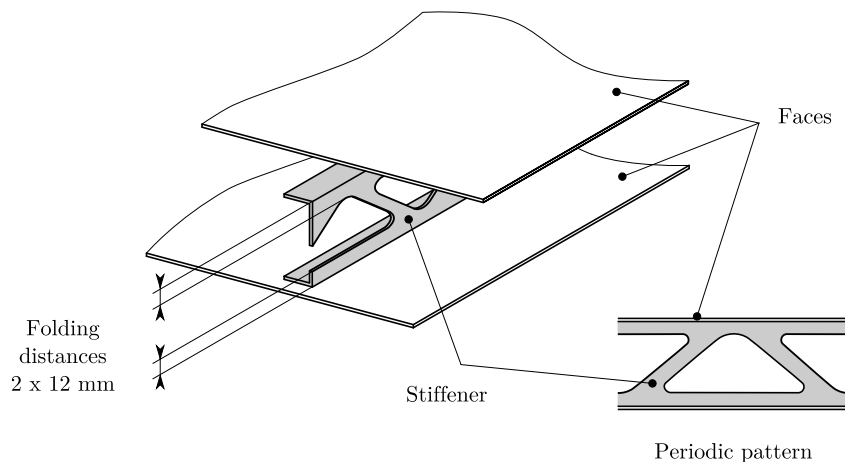


Figure 19: Schéma du squelette du panneau sandwich, constitué de deux parements (faces) et de raidisseurs (stiffeners) régulièrement espacés. La zone de pliage (folding distance) doit restée exempte de trou.

Finalement, le problème d'optimisation choisit fait intervenir un produit de puissance d'une fonction objectif mécanique proportionnelle au coefficient de souplesse en cisaillement, et d'une fonction objectif thermique proportionnelle à la conductivité thermique :

$$J(\Omega) = J_m^{(1-\alpha)} J_{th}^\alpha \quad (9)$$

où le coefficient α quantifie l'importance relative de la fonction thermique sur la fonction mécanique. Comme précédemment, une contrainte de surface est ajoutée pour stabiliser le problème.

Front de Pareto et influence des différents paramètres Plusieurs simulations d'optimisation avec des valeurs du coefficient α permettent de construire un front de Pareto comme celui tracé sur la figure 20a. Les motifs optimisés correspondants sont représentés à côté, figure 20b. Ces géométries constituent une famille de motifs optimisés à partir du même motif initial, et donc avec des caractéristiques semblables. L'opération a été répétée en modifiant chacun des paramètres un à un, tels que la géométrie initiale, la fraction de surface, le rapport de forme de cellule périodique. Cela a permis de résumer l'effet de chacun de ces paramètres sur les deux fonctions objectif mécanique et thermique, ainsi que sur l'optimalité des géométries obtenues (tableau 1).

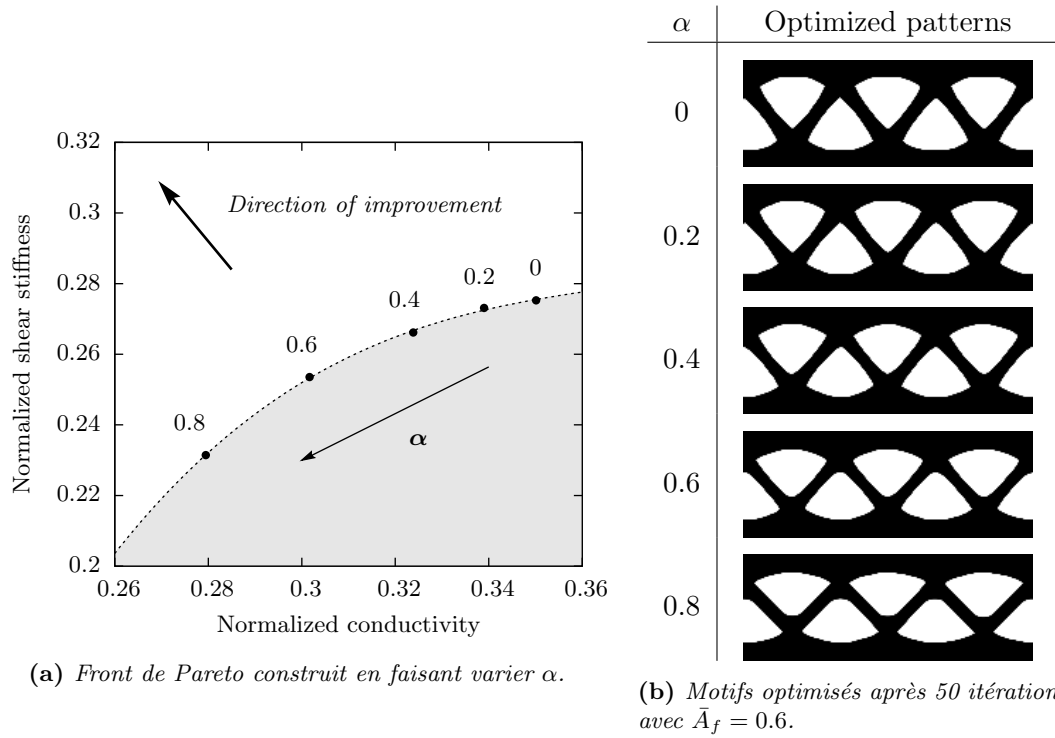


Figure 20: Influence du coefficient α sur les motifs optimisés et leurs propriétés. Ces résultats sont obtenus à partir de la même géométrie initiale et pour une fraction de surface imposée à $\bar{A}_f = 0.6$.

	Rigidité en cisaillement	Isolation thermique	Optimalité
Augmentation du coefficient α	--	++	0
Augmentation de la fraction de surface $\bar{\rho}$	+++	---	0
Augmentation du nombre de trous dans le motif initial	+	+	+ pour les motifs initiaux réguliers
Augmentation de la largeur de cellule l_c	--	+++	+

Table 1: Résumé de l'effet de chaque paramètre sur les performances et l'optimalité des motifs périodiques obtenus.

Sélection de quelques géométries de raidisseur Parmi l'ensemble des motifs périodiques optimisés, quatre ont été choisis comme prototype pour poursuivre l'étude. Ils ont été choisis de sorte que leur propriété thermique soit similaire à celle du raidisseur de référence mais pourvus d'une rigidité en cisaillement plus importante. Plusieurs valeurs de fraction de surface et de nombre de trou sont représentées parmi ces motifs sélectionnés.

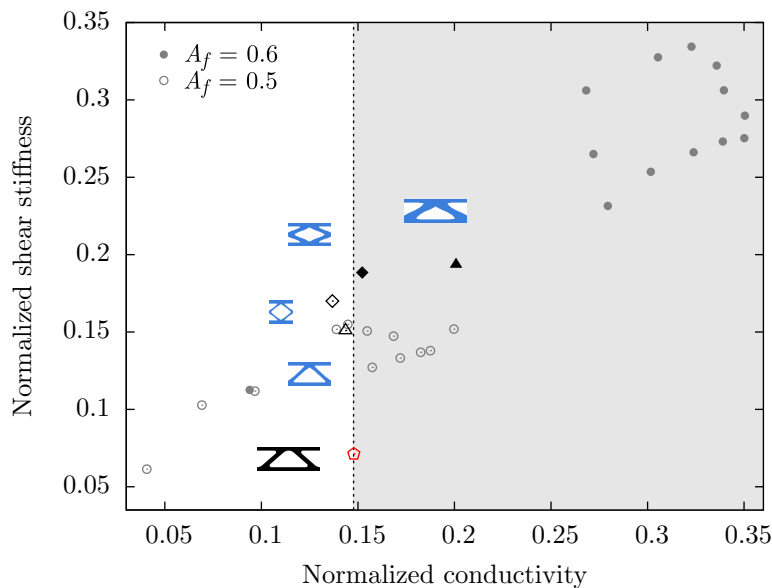


Figure 21: Sélection de quatre motifs intéressants au sein des familles de géométrie obtenues par optimisation.

Des modifications géométriques de régularisation ont été apportées à ces motifs en perspective d'une production en série. Elles sont présentées en détail dans le manuscrit, ainsi que leur impact sur les performances de chaque motif.

Sur ces motifs régularisés, une étude plus approfondie a été menée sur leurs propriétés thermiques et mécaniques. Des simulations thermiques en régime transitoire ont été effectuées sur ces géométries de raidisseur en trois dimensions en prenant en compte les parements et la laine minérale. Des résultats graphiques sont présentés sur la figure 22. Les performances mécaniques globales en flexion ont été mesurées expérimentalement sur des essais de flexion quatre points avec plusieurs distances de cisaillement. Deux échantillons prototypes ont été fabriqués par la société *Sainte-Marie Constructions Isothermes* aux dimensions de $2980 \times 340 \times 80$ mm. La comparaison des courbes force-déplacement pour une dimension d'essai est présentée sur la figure 23. La rigidité globale caractérise la pente de la première partie élastique. Elle est mesurée précisément sur la pente à la décharge de cycle de charge-décharge dans ce régime élastique. Les coefficients de souplesse en flexion et en cisaillement sont déterminés par plusieurs essais avec les longueurs de cisaillement différentes.

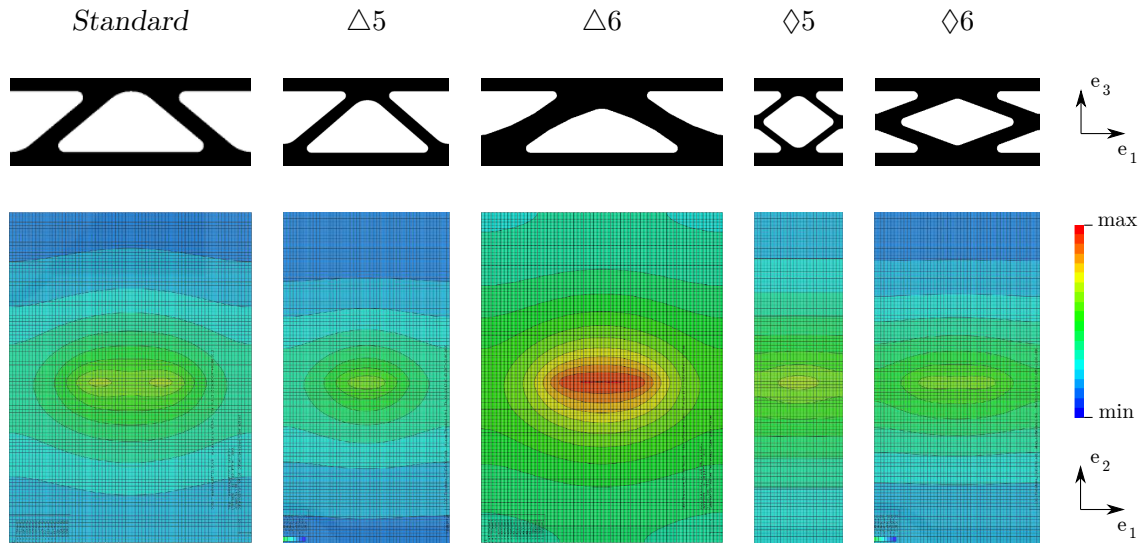


Figure 22: Analyse thermique transitoire tridimensionnelle du raidisseur de référence (standard) et des prototypes. Le champ de température (après 60 min) de la face non-exposée est tracé en correspondance avec le motif du raidisseur qui est situé horizontalement au centre de la face représentée.

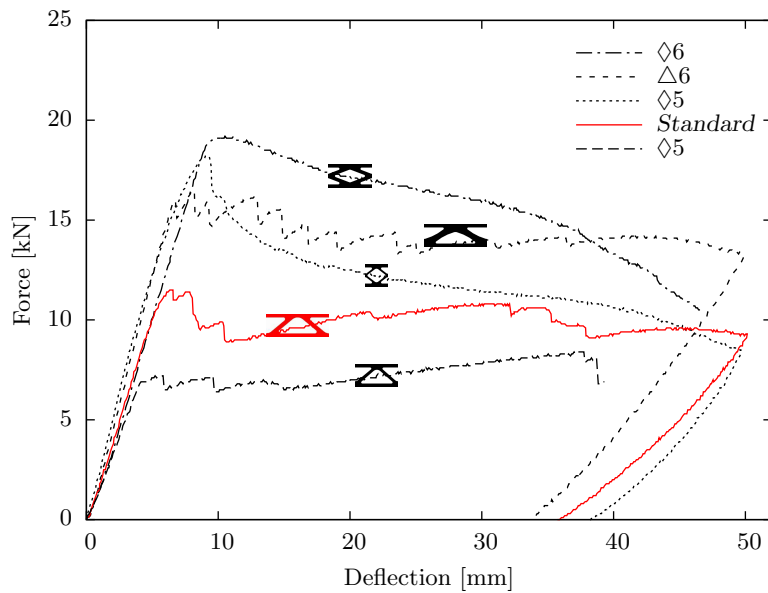


Figure 23: Courbes de force-déplacement pour un essai de flexion quatre points pour les quatre prototypes et le panneau de référence. Le modèle ◇6 apparaît être le plus performant en terme de force maximum.

Finalement, que ce soit pour ses performances thermiques ou mécaniques (rigidité et force maximum), le modèle prototype ◇6 s'est révélé être le meilleur. Il a donc été retenu par la société *Sainte-Marie Constructions Isothermes* pour devenir le prochain design des

raidisseurs de ce panneau sandwich isolant.

Conclusions et perspectives

Afin de proposer des solutions matériau performantes pour des cahiers des charges multi-fonctionnels, la tendance aujourd'hui est de développer des matériaux architecturés dont l'arrangement spatial des différentes phases permet d'ajuster les propriétés sur mesure. Les structures sandwich fournissent un cas d'étude privilégié pour ce type d'approche. Le choix d'un matériau architecturé pour le cœur contribue à obtenir un produit très performant en terme de masse, d'encombrement, de rigidité et résistance mécanique, et aussi d'isolation thermique par exemple. Le bon compromis entre ces propriétés résultera du choix optimal de l'architecture et du dimensionnement.

Dans ce manuscrit de thèse, des outils numériques de conception optimale de matériaux architecturés périodiques ont été développés et validés. Pour cela, trois points essentiels ont été abordés :

- l'**homogénéisation** du motif périodique de panneaux architecturés afin d'identifier les modules de traction, flexion et cisaillement transverse ;
- la **sélection**, le **dimensionnement** et l'**optimisation** du motif permettant de fournir le meilleur compromis entre les multiples propriétés et une masse minimum. Les propriétés considérées sont respectivement le module de flexion et le module de cisaillement, ou la conductivité thermique et le module de cisaillement ;
- la **validation expérimentale** par des essais de flexion sur des échantillons modèles et des prototypes de structures sandwich à grandes échelles.

Ce travail est une contribution au développement de méthodes systématiques de conception optimale de matériaux architecturés et plus particulièrement de structures sandwich multi-fonctionnelles. Le résultat le plus probant est sûrement la proposition finale d'une géométrie optimisée de raidisseur dans le cadre de l'étude sur les panneaux isolants. Après les tests de qualification à la résistance au feu, cette géométrie sera probablement intégrée par la société *Sainte-Marie Constructions Isothermes* dans la prochaine version de ce produit. Concernant les tôles gaufrées en acier, ce type de matériau architecturé fait partie des innovations potentielles d'ArcelorMittal pour répondre aux défis futurs d'allègement des véhicules. Les méthodes d'optimisation topologique s'ajoutent aux outils existants pour la conception sur mesure des matériaux architecturés.

GENERAL INTRODUCTION

Multi-functional materials, capable of performing multiple “primary” functions are a promising route for implementing new applications if they satisfy both technical and economical criteria. Such multi-functionality however is more and more difficult to fulfill with traditional materials. In situations where structural functions as well as functional ones (thermal, electromagnetic, acoustic . . .) are simultaneously required, single materials are very often unable to fulfill complex and even contradictory requirements. The standard strategy of materials science, micro-structure optimization, can improve materials properties, but give only a limited degree of freedom. With multi-functional materials, we have to play with the co-existence of the different constituents (phase, material, etc.), their spatial arrangement, their connections.

The price to pay for this extra richness is the extraordinary wide variety of potential solutions which have to be investigated. This results in a strong difficulty to follow a conventional trial and error strategy and consequently a new strategy is requested for such innovative materials where modeling plays a crucial role. Materials of interest for multi-criteria design have to be identified via modeling before being produced and tested.

Multi-functional specifications for materials and products Automotive industry is one of the main European actors in research and development of innovative designs and materials (4% of the turnover of the sector is invested each year in research and development). Environmental requirements and safety — largely competitive with cost saving — are among the major driving forces. For example, from the 1990’s the EU standards (Euro 1 in 1992 to Euro 6 today) define more and more restrictive limits on gas and particulate emissions (figure 24). The respect of these standards was made possible in the last decades thanks to large improvement of engine efficiency.

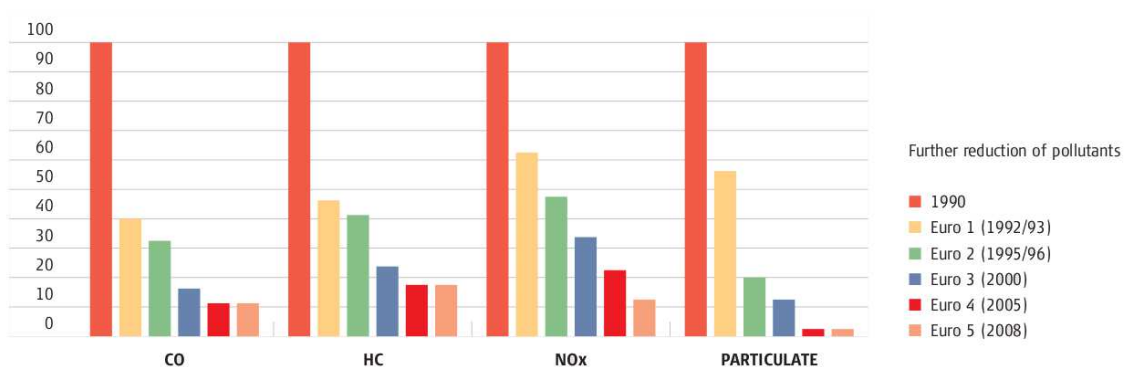


Figure 24: Emission limits for the evolving EU standards in terms of carbon monoxide (CO), total hydrocarbon (HC), nitrogen oxydes (NOx) and particulate matter (Source : “Commercial vehicles fact sheet”, n° 1, ACEA).

In parallel, after a substantial decrease before the 1980’s, the weight of cars (figure 25)

tends to slightly and regularly increase. This is the consequence of increasing the average cubic capacity of new cars and increasing the number of additional features to improve the safety and the conveniences of the passengers (such as airbags, electronics for the engine monitoring and the driver assistance systems ...). Weight saving becomes an issue for car-makers. One of the results has been the introduction of more expensive but lighter materials such as aluminum alloys and polymer-based composites. From 1990 to 2000, an average increase of +50 to +100 kg of aluminum alloys and +110 to +140 kg of polymer-based composites can be noticed into cars of size class M2 (family's cars).

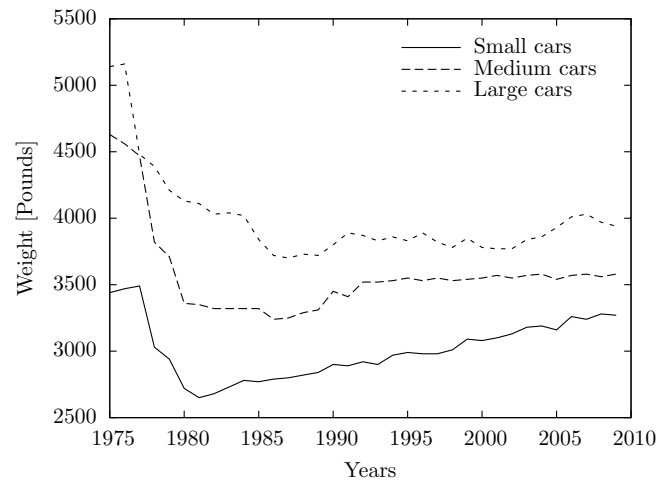


Figure 25: Sales-weighted curb weight of new domestic and import cars in the US by size class (model years 1975–2009) (Davis et al., 2010).

Weight has to be saved on constitutive materials by obviously keeping satisfied the specifications : structural (stiffness, strength, etc.) as well as functional (thermal insulation, acoustic absorption, etc.). For instance, the car roofs have to ensure a prescribed stiffness at minimal weight. Same function is required for car bonnet with an additional prescribed crash energy absorption to ensure the requirements for the pedestrian crash (part of the “European new car assessment program”, Euro NCAP). Another typical example is the thermal screen that protects the silencer. It has to fulfill both requirements on stiffness and thermal insulation at minimum weight.

This trend to fulfill more and often conflicting requirements is common to numerous fields of industrial interest. For example in the building industry, energy saving and comfort are ones of the main objectives of the environmental high quality standards (HQE). The improvement of thermal insulation and acoustic absorption of the constitutive materials while keeping good structural properties is crucial. The specific case of insulation panels dedicated to safety rooms on offshore platforms will be emphasized later as an illustration of the multi-criteria optimization procedure.

Architected materials The trend to combine multiple functions required for material products drive to search for attributes that are not offered by any single material. Material selection based on performance metrics and charts (Ashby, 2005) is an efficient approach to detect promising materials. The chart on figure 26 locates the main material classes with respect to flexural stiffness and thermal conductivity. It reveals some “holes” unfilled with any single material. Some parts of these holes are inaccessible because of the limitation of the size of the atoms and the nature of the forces that bind them. But others remain empty and could be, in principle, filled. For a structural application, only the upper-left corner is interesting and defines a vector for material development. More generally, to investigate these empty regions, the traditional strategy is based on the development of new alloys, new polymers chemistry and new composition of ceramics. It results in an incremental improvement of the properties from the old existing materials. In comparison, the alternative strategy of mixing and organizing materials reveal a more step-like evolution of the gain. The success of the fiber reinforced plastics, foams and sandwich structures is an encouragement to explore the way of architected materials (Fleck et al., 2010).

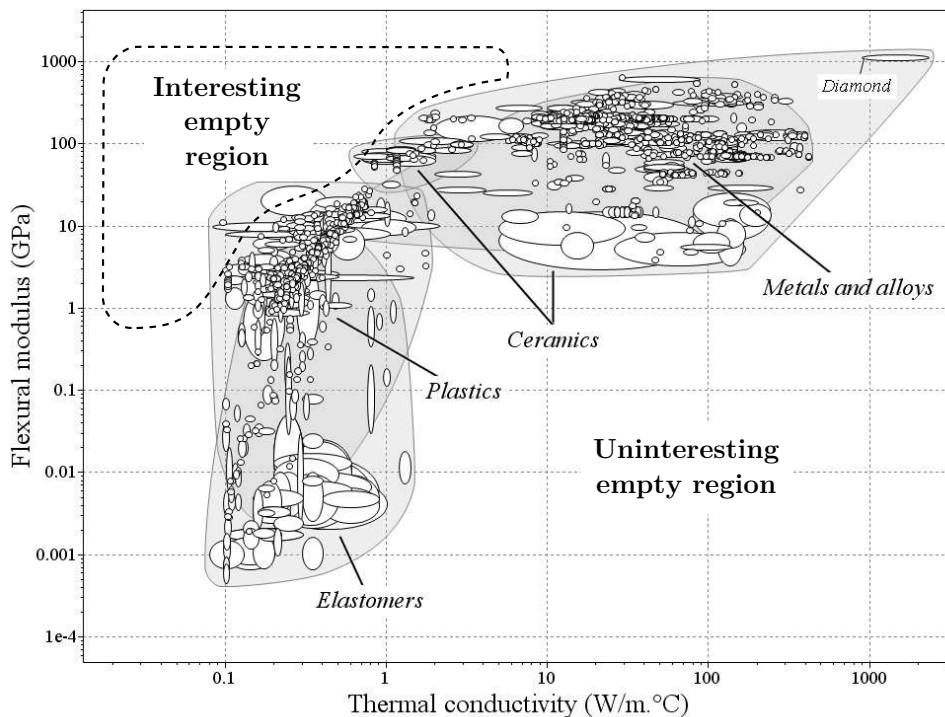


Figure 26: Flexural-modulus–density chart on which lie the main classes of materials. Part of the space is occupied by materials, part is empty (the “holes”). Developing new materials in the direction of the upper-left corner allows components with greater stiffness to conductivity ratio.

What is an *architected material*? It is a combination of two or more existing mate-

rials, or one material and space. The denomination of *architected material* is preferred to *hybrid materials* which refers more specifically to the mix of organic and inorganic materials at the atomistic scale (Portier et al., 2001, Walcarius, 2001). The architected materials that combine one single material and empty space are part of the *porous materials* at large volume fraction of matter and of the *cellular materials* at low volume fraction.

Two ideas underly the concept of architected materials. The first is the duality of the scales. Sometimes, architected materials are thought and discussed as an association of materials with details on the spatial distribution of matter. Sometimes, it is convenient — for designing and comparing with monolithic materials — to view them as “materials” with their own density, mechanical and thermal properties. The second concept is the ability of tailoring the architected materials through geometrical degree of freedom in order to tune the effective properties. For instance, the stiffness, strength and permeability of metallic foam can be modified by the type of porosity (open or close cells), the connectivity, the volume fraction, the cell size, etc.

Materials from nature often reveal architectures and moreover an imbrication of different levels of architecture denoted *hierarchical structures*. For instance, the glass sponge *Euplectella*, which lives in deep waters, reveals a skeleton with a shape of complex cellular structure made of glass spicules. The spicules themselves are made of concentric layers of silica separated by thin protein layers in order to improve the fracture toughness. Usually, architectures observed in nature are extremely sophisticated and can be interpreted as the result of a slow evolution (optimization?) process — millions of years of natural selection.

The central idea of this PhD is not to mimic the natural architected materials but to follow the approach of tailoring the material distribution driven by a relevant performance metric or objective function. This can be seen as a first step in a “material by design” strategy. The next one, not treated here, will be multiplying the levels of architectures. It could be to assemble different architected materials within a component or to develop specific microstructures for the constitutive material of a foam or a truss. The tailored blanks (figure 28) are an example of how joint steel sheets (made of different alloys with different thicknesses) can be used to design a component with a tunable behavior to crash.

The emblematic case of sandwich panel : material or structure? Both! As an emblematic case of architected materials, the sandwich panel maintains a certain duality about these two scales. Sometimes it is viewed as two sheets bounded on a core material and sometimes as a “material” in the general sense with effective properties. Whereas a structure typically gives a response only for one or few loadings, an effective behavior implies a response for any loadings. This enables the comparison with monolithic materials and the use of classical rules of design.

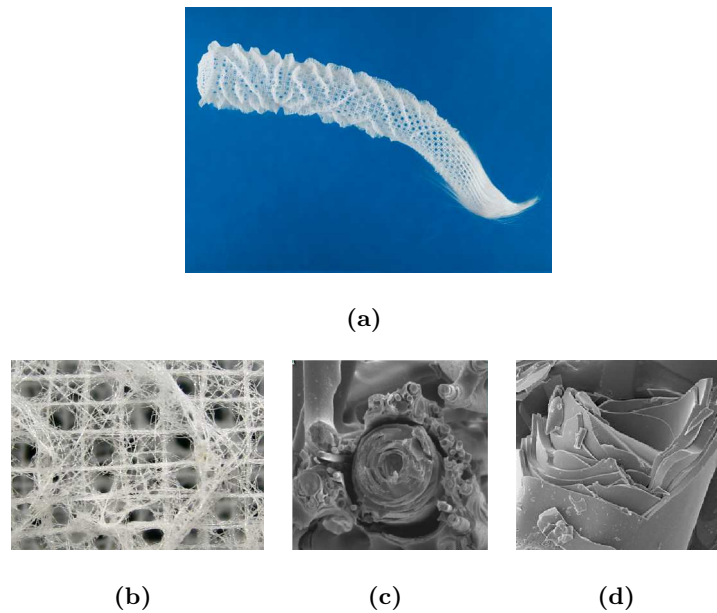


Figure 27: *The glass sponge Euplectella : an example from nature of hierarchical system. Its skeleton (a) is a complex cellular structure (b) made of glass spicules (c) that are concentric layers of silica and protein (Dunlop et al., 2011).*

The distinction between structure and material is clear when speaking about the effective shear modulus of a metallic foam in comparison with the deflection of a bridge under its weight. But, when the separation between scales is not clear, the relevant effective properties are no more intrinsic and may include parameters from the structure level. This is the case for sandwich panels when the bending modulus depends on the slenderness and the type of loading.

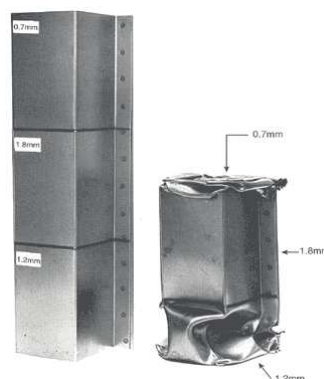


Figure 28: *Example of tailored blank. The inner view of a front door made by butt welding of two sheets of different steel alloys. [Source: ArcelorMittal]*

How can we distribute matter efficiently ? While convinced by the benefits of architected materials, the key issue is how to design them. For example, an hybrid material made with two different constitutive materials : phase A (with good property P_1 but poor property P_2) and phase B (with good property P_2 but poor property P_1). How to choose the distribution of the phases A and B such that the result will combine the strength and not the weakness of both ?

This optimization problem is usually solved intuitively thanks to engineering knowledges. Electric cables is a famous example where architecture enables to combine a high tensile strength, a low flexural stiffness and a low resistivity. But in many multi-functional problems, finding the architecture that gives the best combination of conflicting properties is not as straightforward. Numerical optimization methods can help. The distribution of constitutive phases — seen as an optimization variable — have to be searched for in a so large admissible space that exploring by trial and error is not an appropriate strategy. The topological optimization techniques might be relevant tools in this case.

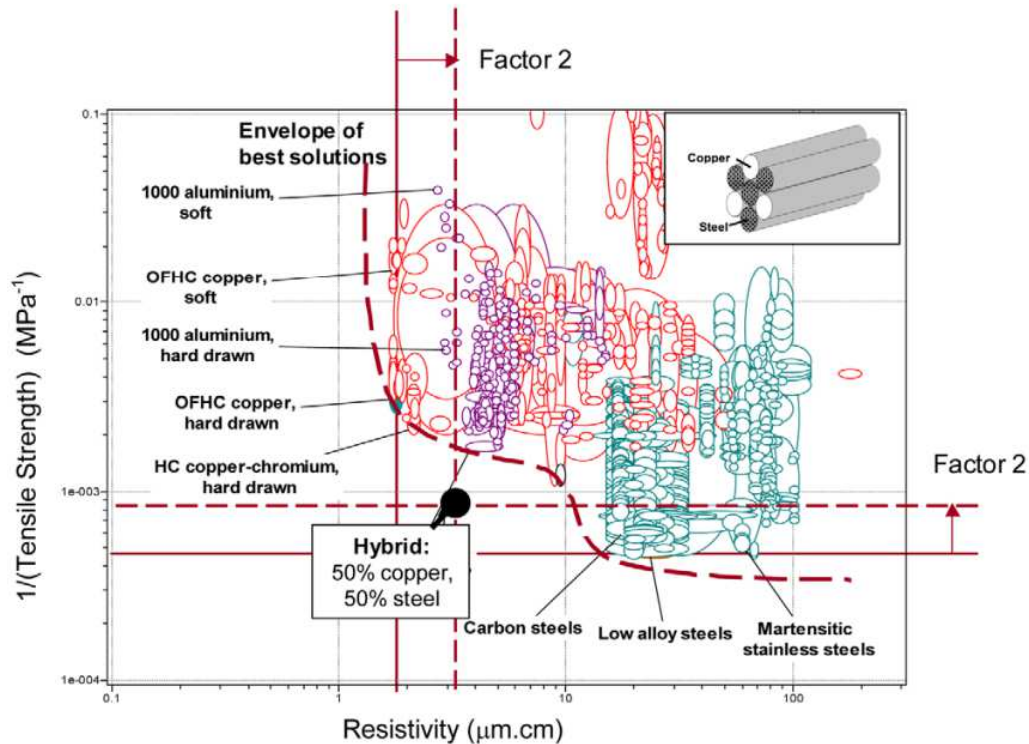


Figure 29: Designing a hybrid — here, one with high strength and high electrical conductivity. The figure shows the resistivity and reciprocal of tensile strength for 1700 metals and alloys. We seek materials with the lowest values of both. The construction is for a hybrid of hard-drawn OFHC copper and drawn low alloy steel, but the figure itself allows many hybrids to be investigated. (Ashby and Bréchet, 2003)

In this context, the present work deals with the design of architected panels following the three main steps : description of homogenization methods required to estimate panels properties, optimization of model architected panel that combine flexural and shear stiffness, and optimal design of a multi-functional sandwich panel.

With a special interest on the case of sandwich panel, chapter 1 describes some features of architected panels. It focuses on the description of the mechanical characteristics of such panels with a special interest on how can be used material selection methods. Shell and plate models are described in order to introduced the membrane, flexural and transverse-shear moduli. A particular interest is given to the transverse-shear contribution within the global bending response of a panel. The experimental identification of the relevant moduli are described (three and four-point bending tests).

The issue of evaluating the performances of any unit cell architecture lies in the estimation of effective properties. Chapter 2 is dedicated to the description and the use of periodic homogenization methods in order to identify the effective plate properties. Based on the described homogenization procedure, selection and parametric study is presented on an example of architected steel sheet in the context of innovative steel solutions development for automotive applications.

A parametric approach reveals to be reducing and justifies the application of topological optimization techniques to the specific problem of periodic architected material. After a short introduction to shape optimization (on literature and theoretical bases), chapter 3 presents the application of the level-set method to the mechanical but multi-functional optimization problem that consists in searching the best compromise between flexural and transverse-shear compliances at a given weight. Some experiments on prototypes produced by additive manufacturing validates the numerical results.

Finally, a complete procedure is proposed in chapter 4 for the optimal design of sandwich stiffeners. Insulation sandwich panels, developed and produced by the company *Sainte-Marie Construction Isothermes*, provide interesting conflicting specifications. These specifications leads to a multi-functional optimization problem on the stiffeners, which is treated with the tools developed in chapter 2 and 3. Prototypes were produced and tested to validation the optimization approach and select a promising design.

CHAPTER 1

**An emblematic architected
material : the sandwich structure**

Introduction

As mentioned in the general introduction, sandwich structure is an emblematic example of the architected material and an ideal case to apply the strategy of “materials by design”.

The sandwich structure consists in the association of two materials : a core light material in-between two faces (or skins) of a stiff material. The main interest is to combine a high flexural stiffness with lightness. The flexural stiffness, through the moment of inertia, strongly depends on the thickness. The insertion of a light material in the middle increases the thickness while keeping reasonable the global weight. The introduction of such a concept into the human-made structures is quite recent (first discussed by Duleau in 1820 and really developed during the two World Wars for aircraft construction (Zenkert, 1997)), but again some examples from nature show similar architected structures (figure 1.1).

In different contexts of applications, it enables to perform multi-functional specifications thanks to a wide choice of material combinations and architectures. Section 1.1 presents some applications and typical specifications the sandwich structure is dedicated for. In the section 1.2, different architected materials often included in sandwich structures are described, while the section 1.3 lists and describes the elastic mechanical properties of the sandwich material itself. In order to examine in more details the kinematic and the stress distributions into the sandwich panels — but more generally into any kind of stiffened panels — the macroscopic shell and plate models are presented in the section 1.4. The question of identification of the macroscopic compliance components is treated in the last section 1.5.



Figure 1.1: *Sandwich-like structure of a bird bone.*

1.1 Applications and specifications

Among applications that require flexural stiffness at a minimum weight, the aerospace and aeronautic industries were the first to afford the development of sandwich structures. The driving force being the high cost — in fuel or payload — of the weight saved on a satellite or an airplane. An example is the use of aluminum honeycomb sandwich in an satellite container on figure 1.2a. These ten last past years, the trend was to increase the percentage of carbon fibers reinforced plastic (CFRP) in aircraft production. The next-generation of the Airbus aircraft A350 will be made of more than 50% of composites. The use of composite laminates provides a high stiffness–lightness ratio and extends the service intervals between maintenance and corrosion inspections. In combination with polymer honeycombs, it results in high performance panels that competes with aluminum structures (figure 1.2b).



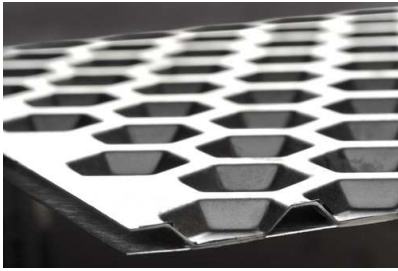
(a) *Satellite container made of aluminum honeycomb sandwich panels.*



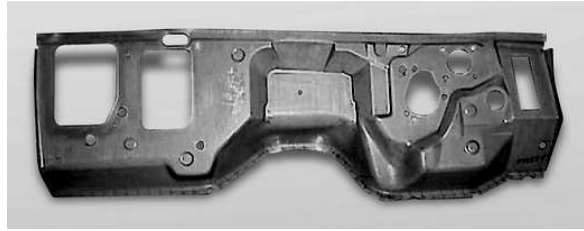
(b) *Nasa development of sandwich with glass fibers reinforced polymer faces and a honeycomb polymer core.*

Figure 1.2: *Examples of sandwich materials used in the aerospace industry.*

More generally, all the transportation applications (train, shipbuilding and automotive industries) are concerned. The choice of the materials and the architectures evolves according to the value-added to each product and the rate of production. The available fundings for the development of the BMW/Oracle America’s cup trimaran enable the use of high performance sandwich material specifically designed and hand manufactured, such as curved panels with honeycomb core and non-uniform ply sequences of CFRP faces. At the opposite, the automotive applications are submitted to a market with a larger volume of sold pieces and a relatively low profit margin. The result is the development of new materials strongly constrained by high-rate and low-cost processes. Only few exceptions exist for small market of specific vehicles such as refrigerating vehicles. For instance, corrugated panels (figure 1.3a) made of hydroformed steel sheets brazed together are developed in such context.



(a) A corrugated panel obtained by brazing of two hydroformed steel sheets produced by Borit NV. It reveals high performance for flexural stiffness, fire and electromagnetic shielding.



(b) A car component obtained by deep-drawing of a QuietSteel sheet (steel-polymer sandwich) produced by ArcelorMittal. It performs high acoustic absorption.

Figure 1.3: Architected materials developed for automotive applications.

But even more than specific stiffness, sandwich structures enable to perform multiple other requirements mostly thanks to specific core materials :

- *Energy absorption.* Sandwich panels are widely used for their ballistic properties. The core material, in this case, is not only chosen for its lightness but also its high level of energy dissipation. When subjected to an impact test, the sandwich panel is expected to behave such that the kinetic energy of the projectile is absorbed by both perforating the upper face and damaging the core material, while keeping the back face unperforated (Hanssen et al., 2006, Zeng et al., 2010).
- *Acoustic absorption.* The QuietSteel, a steel-polymer sandwich developed by ArcelorMittal (figure 1.3b), make use of the viscoelastic behavior of the polymer to shift the resonance frequency and to produce a high acoustic absorption of the sheet for the given in-use range of frequency (see Grootenhuis (1970) for details on vibrations with viscoelastic materials). Sometimes, the tunable architecture of the core is a way to control the absorption behavior of the structure (Gasser et al., 2004).
- *Thermal insulation and Fire shielding.* The choice of an aerated core material is particularly adapted to the combination of lightness and thermal insulation since air have an extremely low thermal conductivity (Ashby, 2005). The problematic is then to combine insulation and stiffness, while just local stiffeners or joints will fall down the insulation. In the case of fire shielding, the heat capacity and fusion temperature are additional properties to take into account for the materials selection.
- *Thermal transfer.* Contrary to the previous passive properties, it is also possible to confer on the sandwich structure active properties about thermal exchange. Some cellular cores allow one or two fluids to flow inside the panel and exchange heat with the outside or in-between the fluids. The heat can be also stored by filling the honeycomb cells with a phase change material (Hasse et al., 2010). This is a

promising way, in houses and buildings, to store the heat from daylight and release it later.

- *Dielectric constant.* In the field of telecommunication, some structures need to be as much as possible transparent to microwaves, like radomes that shield microwave antennas (Ashby, 2005). Again, the use of an aerated core material leads to a low dielectric constant while stiffness is ensured by the skins (Huynen et al., 2011).

The last but not least applicative field is the construction industry. While for the previous high performance applications the sandwich structure is usually more expensive (because of both process and material costs), its high structural stiffness allows sometime the use of cheaper constitutive material. This is the case for most of the interior doors that are flush doors. It consists in a wood frame filled with a cardboard honeycomb core and covered by two faces of plywood or vinyl. Concerning the multi-functional aspect, steel-polymer-foam sandwich panels — such as Ondatherm panels by ArcelorMittal - (figure 1.4a) — are commonly found in walls of sport facilities or commercial building, due to their thermal insulating ability as well as their high acoustic absorption and fire resistance. At the opposite of large series productions, the building construction is made of unique projects and small markets that enable the development of innovative and unusual association of materials. Figure 1.4b shows a sandwich plate with a honeycomb polymer core and glass or steel fibers reinforced concrete. It results in a light, stiff and strong panel that shows the same surface aspect than a monolithic concrete wall.



(a) *Insulation panel Ondatherm T proposed by ArcelorMittal to build walls with high acoustic and thermal properties as much as fire protection.*



(b) *Association of polymer honeycomb Nidaplast with a fiber reinforced concrete Ductal.*

Figure 1.4: *Examples of sandwich structures in the construction industry.*

1.2 Materials and architectures

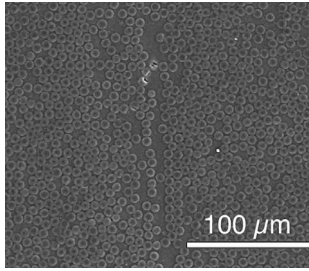
Through the detail of the applications listed above as examples, an overview of the variety of materials and architected has been proposed. This section will describe a non-exhaustive list of architected material that are themselves used as constitutive materials in sandwich structures.

1.2.1 Composites

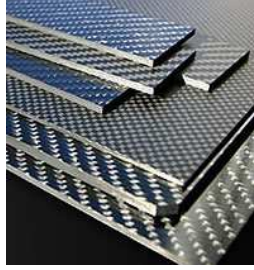
The term *composites* is widely recognized to name inclusion or fiber reinforced materials. As mentioned previously, glass or carbon fiber reinforced plastic (resp. GFRP or CFRP) are typically used for high technology products (sports articles, aircraft, military products), and become common in numerous other fields such as public transportation or machine engineering (Wielage and Thielemann, 2004). The concept of composites is to combine the interesting properties of two materials by mixing them. In the case of reinforced plastics, it consists in combining the lightness and/or cheapness of a polymer matrix with the stiffness and strength of inclusions or fibers. Different topologies of reinforcement exist :

- *Inclusions*. Polymer matrices are usually charged by inclusions for cost saving almost without losing any mechanical properties. Several cases also concern multi-functional objectives such as electromagnetic properties, conductivity or fire resistance. Metallic matrices stiffened by ceramic inclusions were widely studied but have been confronted to a limited resulting toughness.
- *Short fibers*. Introducing short fibers into polymer matrices leads to a larger increase of the mechanical properties than introducing inclusions, still keeping the ability to process with injection molding techniques.
- *Unidimensional fibers*. This is the most frequently encountered type of reinforcement (figure 1.5a) due to the terrific increase of the mechanical properties. Anisotropic properties may appear but can be removed by imposing a symmetric sequence of plies. While the inescapable hand-crafted manufacture has curbed the use of such materials, the emerging of mechanization to assemble pre-impregnated plies participates to the democratization of laminates.
- *Textiles*. The 2D or 3D woven fabrics (figure 1.5b and c) are being studied as a solutions to avoid the sensibility of unidimensional composites to defects and buckling. The development of predictive models for properties and processing — such as resin transfer molding (RTM) — remains a key issue.

The most common polymers for matrix material are polyester and epoxy resin. Their low viscosity enables to relatively easily transfer into fabrics. The thermoplastic polymers often give better impact strength. The three most encountered fiber materials are glass,



(a) Microstructure of an unidirectional CFRP (Gonzalez and Llorca, 2007).



(b) Plates of 2D-woven CFRP.



(c) Interlock fabric preform made of carbon fibres destined to be filled with a polymer matrix by RTM process (De Luycker et al., 2009).

Figure 1.5: Three types of arrangement of reinforcing fibers : (a) unidirectional, (b) 2d-woven and (c) interlocked or 3D-woven.

carbon and aramid. The essential criteria of choice is the Young's modulus over price ratio. The ratio between high performance carbon and glass fibre is around 5 for the Young's modulus and higher than 10 for the price (Carlsson et al., 2004).

Laminated or woven composite plates are frequently joined on honeycomb or other cellular core materials to produce a sandwich structure. It results in a two-level hierarchical material.

1.2.2 Porous and cellular materials

Porous and cellular materials are architected materials made of one single constitutive material and space. The term *porous* usually names the high relative density materials, while *cellular* refers to low relative densities. Both may concern random or organized architectures. As mentioned for specific applications (section 1.1), these materials are particularly efficient as core materials in order to provide lightness, impact energy absorption, thermal insulation, dielectric constant, etc.

Three main architectures must be mentioned :

- *Porous materials.* That means bulk materials with distributed pores. These architectures have relatively few degrees of freedom (volume fraction and pore size) which are often statistical due to the randomness of the distribution. With some specific processes, it becomes possible to control the spatial organization of the pores (Jauffrès et al., 2011) and give more deterministic degrees of freedom.
- *Foams.* The wide concept of foam — what ever ceramic, metallic or organic — is originally related to a process based on bubbles. However, the classification in terms of random cellular material predominates and includes similar architectures made with

other processes such as salt-replication (Despois et al., 2007). The possibilities in terms of design are large. One can change the volume fraction, size and morphology of the pores (close-cells), connectivity of the struts (open-cells), etc. Their low relative density is well appreciated as core material and the diversity in constitutive materials facilitates the joining with the skins. The remaining disadvantage is the quite large scattering in the effective properties due to the process.

- *Truss-lattices, corrugations and honeycombs.* These organized cellular materials typically include the architectures shown on figure 1.6. Honeycomb is the most widespread core material, sometime in aluminum brazed on aluminum faces, sometime in polymer with aluminum skins again or laminated plates. The cardboard remains the cheapest sandwich structure with a corrugated core. The deterministic aspect avoids the properties scattering, but makes difficult the high rate manufacturing.

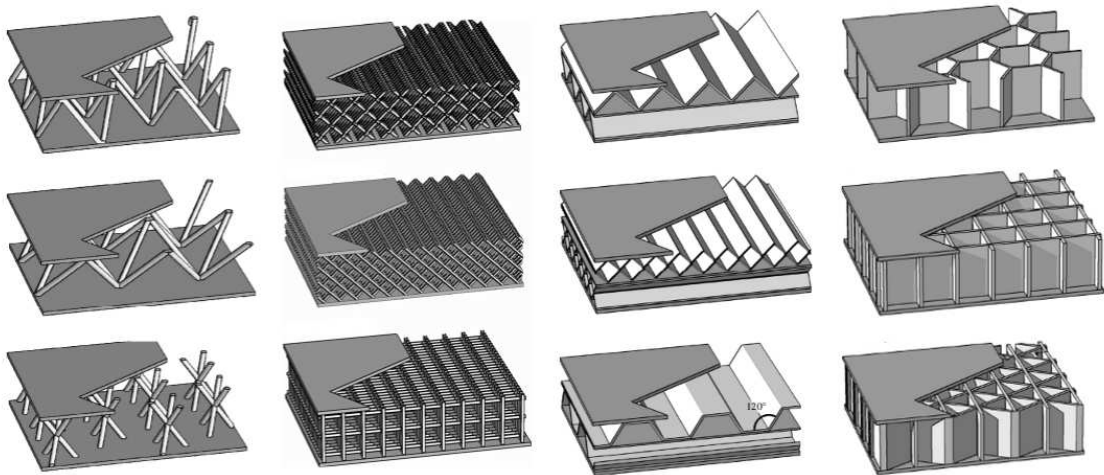


Figure 1.6: Examples of lattices, prismatic corrugations and honeycombs as core materials for sandwich structures developed for impact energy absorption. (Wadley, 2006)

Finally, porous and cellular materials provide particularly good properties to be included in a sandwich structures. The diversity of constitutive materials and process enables a large number of degrees of freedom that help to tune the effective properties. The result is a two-level architected material.

The figure 1.7 shows how optimized truss-lattices may reveal an index $E^{1/2}/\rho$ — the performance metric for designing a flexural beam at minimum mass (Ashby, 2005) — 10 times higher than the foam with a same relative density. The bending deformation of the foams truss implies a quadratic evolution with the density, whereas truss-lattices only involved uniaxial deformation of the trusses and are subjected to a linear evolution.

This observation confirms the architecture could have a large influence on the mechanical properties. It encourages to explore the possible shapes in order to get the optimal performance, such it was proposed in the literature for cellular core materials (Valdevit, 2004, Queheillalt and Wadley, 2005, Wadley, 2006).

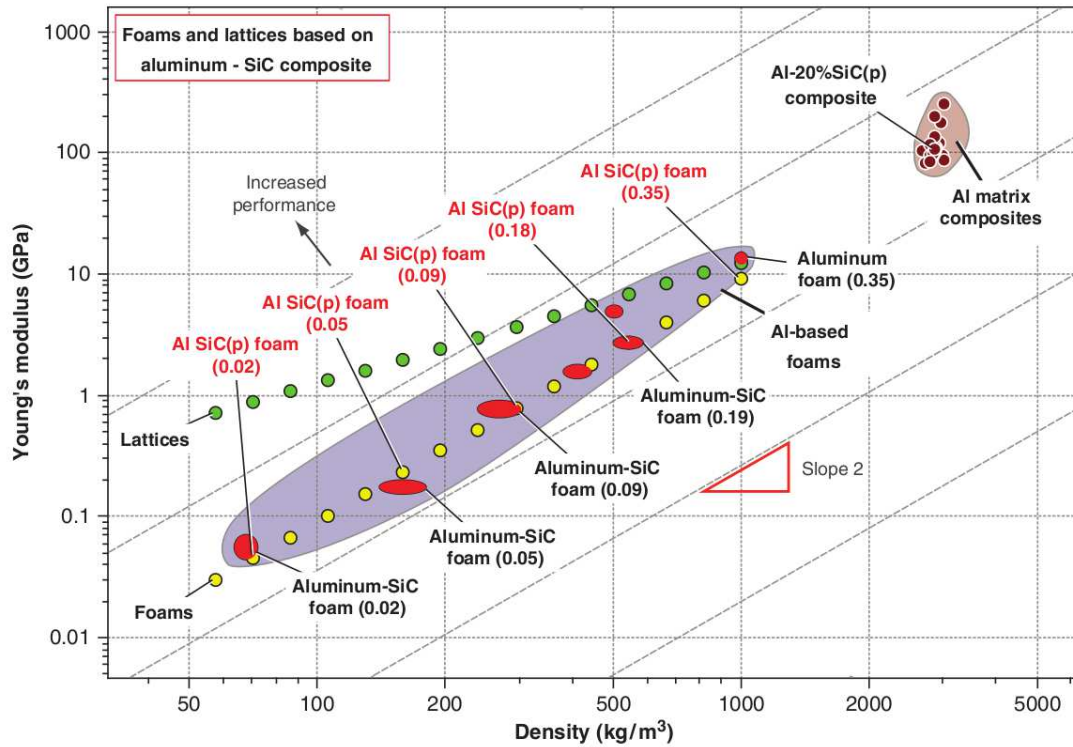


Figure 1.7: The starting material, Al-SiC (Aluminum with 20% of SiC particulates) appears at the upper right of this chart. The line of yellow ellipses with red labels show the modulus and density of open-cell foams made from Al-SiC. They should be compared with the measured values for real Al-SiC foams, shown in red with black labels. The relative densities are listed in brackets. The modulus and density of lattices made of the same material are shown in green for comparison. (Ashby, 2011)

1.3 Mechanical properties of sandwich materials

After briefly presenting the main architected materials possibly involved in a sandwich structure, this section focuses the mechanical properties of the sandwich itself. Maintaining the duality between material and structure, the mechanical properties are presented here as material properties in order to compare with others. The elastic properties of the sandwich we are interested in are reminded in the following with a special emphasize on the transverse-shear contribution. In this section, skins and core are both reduced to homogeneous material properties (possibly effective if architected materials).

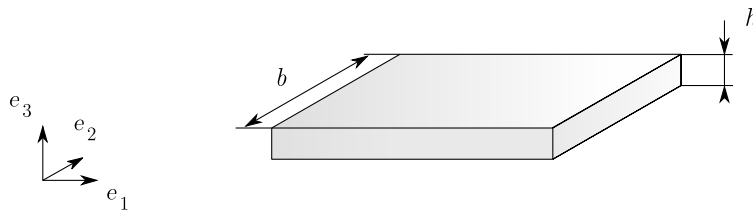


Figure 1.8: The sandwich structure. The face thickness is t , the panel thickness is h and the panel depth is b .

According to (Allen, 1970) “a sandwich panel is a *thick* sheet of *lightweight* material with a *thin* of *much stronger, stiffer* material bonded *securely* to each side” (figure 1.8). The emphasized words are essential features assumed in the following models.

The elastic properties are taken from reference books (Zenkert, 1997, Allen, 1969) that detail all the aspects of the mechanical behavior of sandwich structures. The relevant material moduli and geometrical constants used in the following expressions are : the face thickness t , the panel thickness h , the panel depth b , the volume fraction of the faces $f = 2t/h$, the Young’s modulus and the shear-modulus of the faces and of the core (assumed isotropic) respectively E_f , G_f , E_c and G_c .

The global properties of the panel are denoted with a tilde. The density $\tilde{\rho}$ and the in-plane Young’s modulus \tilde{E} are arithmetical averages of the constitutive materials properties weighted by their volume fraction. The through-thickness Young’s modulus \tilde{E}_{tt} is computed by averaging the inverse of the Young’s modulus. And the flexural Young’s modulus \tilde{E}_{flex} is obtained by normalizing the flexural stiffness component by the inertial moment $I = h^3/12$.

- Density :

$$\tilde{\rho} = \int_{-\frac{h}{2}}^{\frac{h}{2}} \rho(x_3) dx_3 = f\rho_f + (1-f)\rho_c \quad (1.1)$$

- In-plane Young's modulus :

$$\tilde{E} = \frac{1}{h} \int_{-\frac{h}{2}}^{\frac{h}{2}} E(x_3) dx_3 = E_f \left(f + (1-f) \frac{E_c}{E_f} \right) \quad (1.2)$$

- Through-thickness Young's modulus :

$$\tilde{E}_{tt} = \left(\frac{1}{h} \int_{-\frac{h}{2}}^{\frac{h}{2}} \frac{1}{E(x_3)} dx_3 \right)^{-1} = E_f \left(f + (1-f) \frac{E_f}{E_c} \right)^{-1} \quad (1.3)$$

- Flexural Young's modulus :

$$\tilde{E}_{flex} = \frac{12}{h^3} \int_{-\frac{h}{2}}^{\frac{h}{2}} E(x_3) x_3^2 dx_3 = E_f \left(1 - (1-f)^3 + \frac{E_c}{E_f} (1-f)^3 \right) \quad (1.4)$$

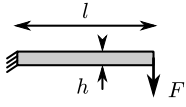
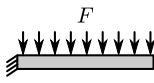
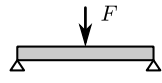
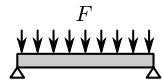
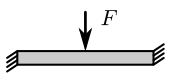
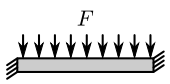
	Mode of loading	Description	B_1	B_2
1		Cantilever, end load	3	1
2		Cantilever, uniformly distributed load	8	2
3		Three-point bend, central load	48	4
4		Three-point bend, uniformly distributed load	384/5	8
5		End built-in, central load	192	4
6		End built-in, uniformly distributed load	384	4

Table 1.1: Constants to describe modes of loading. (Ashby, 2011)

Whereas the previous properties are intrinsic to the choice of the constitutive materials and the sizing, the following bending modulus \tilde{E}_{bend} also depends on the loading of the panel. This modulus consists in the normalized stiffness of the panel for the different bending tests of table 1.1.

- Bending modulus :

$$\tilde{E}_{bend} = \left(\frac{1}{\tilde{E}_{flex}} + \frac{B_1}{B_2} \left(\frac{h}{l} \right)^2 \frac{(1-f)}{G_c} \right)^{-1} \quad (1.5)$$

The ratio B_1/B_2 represents the type of loading (numerical values are given in table 1.1), while the ratio h/l is the relative thickness of the panel (l is the panel length, see illustration on table 1.1). This modulus is much more a performance metric than a material modulus but it is expressed in the unit of a modulus in order to be compared with monolithic materials. The first term in equation (1.5) is the contribution of the pure flexural deformation, the second term is the transverse-shear contribution. In this second contribution, the shear deformation is assumed to be strictly restricted to the core. This is justified by the typical contrast in shear modulus between the faces and the core.

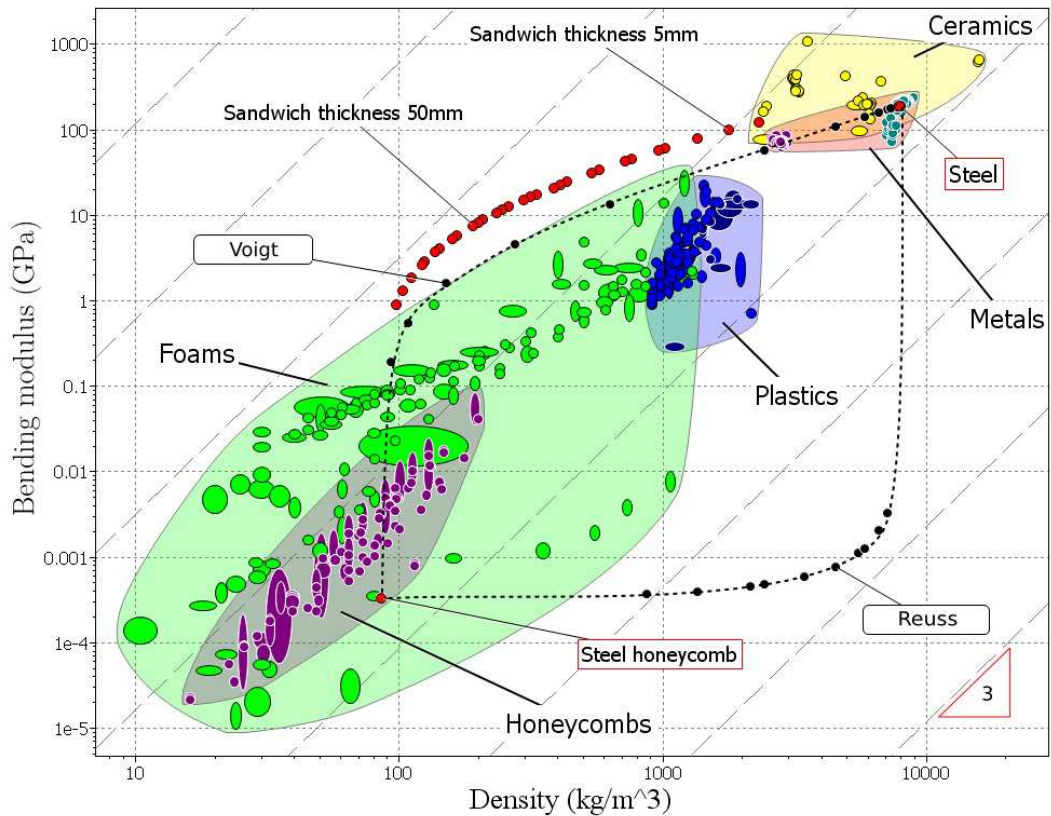


Figure 1.9: Bending modulus – density chart that compare different sizings of a sandwich structures made of steel faces with honeycomb steel core (red circles) with the extreme Voigt and Reuss bounds (black circles). The dashed grey lines corresponding to the performance index $E^{1/3}/\rho$ (high bending stiffness of a plate at minimum weight) show the sandwiches overlap all monolithic materials.

Figure 1.9 illustrates the bending modulus of a sandwich in comparison with monolithic

and composite materials. The associations of bulk steel with steel honeycombs is compared to few classes of materials. Different sizings of sandwich structures (faces thickness from 0.4 to 1 mm, and core thickness from 5 to 50 mm) are compared to an homogeneous panel that would have respectively the Voigt and the Reuss Young's modulus approximation. It shows that the spatial distribution of the two materials involved in the sandwich enables to overlap all the other solutions. In this case, the Voigt and Reuss approximations are not reachable since making a fiber or inclusion reinforced matrix with bulk steel and honeycombs have no sense. But it illustrates that the bending modulus is indeed a performance metric with the dimension of a modulus, and not a real effective modulus.

Transverse-shear contribution It is usually admitted that the core of sandwich constructions has no mechanical participation except for splitting as much as possible the two skins. But for low contrast between face and core materials and especially for thick plates, the transverse-shear contribution in equation (1.5) may drastically fall down the global bending modulus.

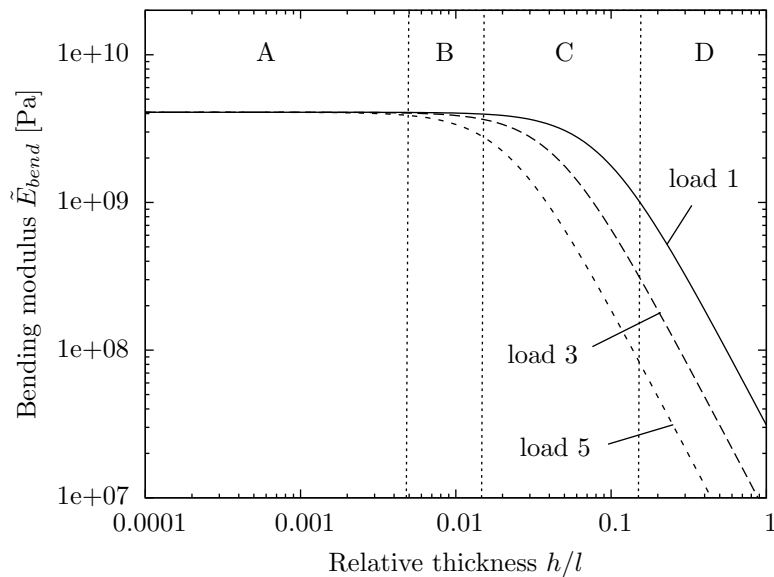


Figure 1.10: Evolution of the bending modulus versus the slenderness for three types of loading (the load numbered 1, 3 and 5 from table 1.1). Four domains, from A to D, are identifiable respectively to the intensity of the shear contribution. The boundaries of these domains (the vertical dashed lines) are given by the equation (1.6) for $\epsilon = 0.01, 0.1$ and 10 .

For a given type of loading, the shear contribution depends on the relative thickness h/l — inverse of the slenderness of the plate. A classification in four domains can be done with respect to the level of the shear contribution to the bending modulus. Figure 1.10 illustrates these categories on a plot that represents the bending stiffness versus the relative thickness. The limit between each domain is given by the ratio of the flexural contribution

over transverse-shear contribution :

$$\tilde{E}_{flex} \left(\frac{h}{l} \right)^2 \frac{(1-f)}{G_c} < \epsilon \quad (1.6)$$

for three value of the criteria $\epsilon = 0.01, 0.1$ and 10 (Allen, 1970). The category A means the transverse-shear contribution is negligible ; the classical beam theory (see section 1.4.1) is valid. The category B means the contributions of pure bending and shear are comparable; the classical beam theory is mainly valid except for concentrated loads. The category C means the transverse-shear contribution is dominant and have to be taken into account. The category D means a beam model is no longer relevant.

This remark on the shear contribution predicts that an estimation of the global bending stiffness for a sandwich with any core architecture — which will be the case while optimizing — won't be relevant without taking into account the transverse-shear mode of deformation.

1.4 Mechanical shell and plate models

In order to compute the effective compliance of any architected panel and to get local informations for future optimization, we need to detail about kinematic and stresses involved in the shell and plate models. In this section, except if specified, no assumption on the internal architecture of the panel is done. The idea is to get macroscopic models still valid for any possible architecture by integrating them into the constitutive behavior (the compliance tensor).

Shell and plate models are deduced from the three-dimensional continuous media by letting down one dimension. Vanishing it can be done when the out-of-plane dimension is small compared to the in-plane dimensions. It means that the relative thickness h/l is small. The three-dimensional displacements and the stress field are expressed from *macroscopic* quantities. Then, the balance equation and the constitutive equation are reformulated in terms of these quantities.

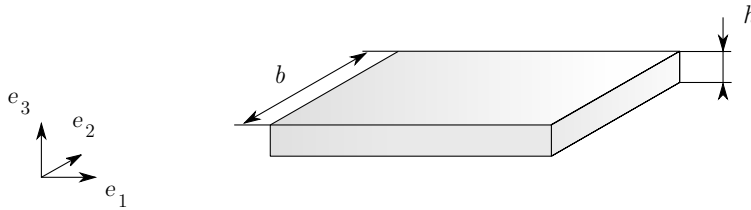


Figure 1.11: *The homogeneous plate with thickness h and depth is b .*

1.4.1 Bi-dimensional plane-strain specific case

Considering a panel structure with an invariant direction e_2 and a planar loading (e_1, e_3), the three-dimensional mechanical problem in this case is reduced to two dimensions with plane-strain assumption (see figure 1.11 for the frame definition). The slenderness of the panel geometry enables to simplify again the problem to a unidimensional domain along e_1 . Then, the shell and plate models are reduced to beam models normalized by the width b .

Macroscopic stresses and equilibrium

Isolating a part of a beam and balancing the stresses enables to identify *macroscopic stresses*, also denoted *internal stresses* or *generalized stresses*. The “macroscopic” denomination underlies an integration in the direction e_3 such that these stresses only depend on the spatial component x_1 . The macroscopic stresses are the *normal force* N , the *bending*

moment M and the transverse force Q :

$$\begin{cases} N(x_1) = \int_{-h/2}^{h/2} \sigma_{11} dx_3 \\ M(x_1) = \int_{-h/2}^{h/2} \sigma_{11} x_3 dx_3 \\ Q(x_1) = \int_{-h/2}^{h/2} \sigma_{13} dx_3 \end{cases} \quad (1.7)$$

where σ_{ij} are the three-dimensional stress components and h the thickness of the panel.

Integrating the three-dimensional equilibrium equation, one obtains the following equilibrium equations in terms of macroscopic stresses :

$$\begin{cases} N' + f_1 = 0 \\ Q' + f_3 = 0 \\ M' - Q + \mu_2 = 0 \end{cases} \quad (1.8)$$

where the apostrophe denotes the derivation with respect to the direction x_1 . The scalars f_1 and f_3 are body forces by unit of length respectively in the direction e_1 and e_3 . The quantity μ_2 is a body moment by unit of length in the direction e_2 .

Constitutive relation

Using a constitutive equation, *macroscopic strains* are introduced with different assumptions depending on the model. The Navier-Bernoulli condition imposes the section to lie perpendicular to the generating line of the beam. This condition gives the so-called ‘‘Classical beam theory’’ based on the Euler-Bernoulli equation (Salençon, 2002). The macroscopic strains are the *membrane strain* e and the *curvature* χ . The constitutive equation comes :

$$\begin{bmatrix} e \\ \chi \end{bmatrix} = \begin{bmatrix} \mathbf{a} & \mathbf{b} \\ \mathbf{b} & \mathbf{d} \end{bmatrix} \begin{bmatrix} N \\ M \end{bmatrix} \quad (1.9)$$

where \mathbf{a} , \mathbf{b} and \mathbf{d} are respectively the membrane compliance, the coupling membrane–flexural compliance and the flexural compliance. For an isotropic homogeneous plate of Young’s modulus E and Poisson’s ratio ν , the expressions of these compliances are :

$$\begin{cases} \mathbf{a} = \frac{1 - \nu^2}{E} \frac{1}{h} \\ \mathbf{d} = \frac{1 - \nu^2}{E} \frac{12}{h^3} \\ \mathbf{b} = 0 \end{cases} \quad (1.10)$$

The factor $(1 - \nu^2)$ comes from the invariance in the direction e_2 (plane-strain hypothesis).

The ‘‘Timoshenko theory’’ is an extension that takes into account the *transverse-shear strain* γ when ignoring the Navier-Bernoulli restriction. Constitutive equations become :

$$\begin{bmatrix} e \\ \chi \\ \gamma \end{bmatrix} = \begin{bmatrix} a & b & k \\ b & d & l \\ k & l & f \end{bmatrix} \begin{bmatrix} N \\ M \\ Q \end{bmatrix} \quad (1.11)$$

where k , l and f are respectively the coupling membrane-transverse-shear compliance, the coupling bending-transverse-shear compliance and the transverse-shear compliance. For an isotropic homogeneous panel, the expressions of these compliances are :

$$\begin{cases} f = \frac{1}{G} \frac{s_r}{h} \\ k = l = 0 \end{cases} \quad (1.12)$$

where G is the shear modulus and $s_r = 6/5$ the shear area ratio for a rectangular homogeneous section. This ratio would be $7/6$ for a circular homogeneous section, and 2 for a circular tube. This ratio is a correction to get the same transverse-shear energy density as in the three-dimensional model :

$$w^*(Q) = \frac{1}{2} f Q^2 = \frac{1}{2} \int_{-h/2}^{h/2} \frac{\sigma_{12}^2}{G} dS \quad (1.13)$$

This correction is often neglected *i.e.* taking $s_r = 1$. The previous classical beam theory is recovered with $s_r = 0$.

One could notice that all the coupling terms of equations (1.10) and (1.12) are zeros for the homogeneous panel. It remains true for any geometry with specific symmetries — rotational or (e_1, e_2) -reflection symmetries.

Equivalence with effective material properties

The sandwich properties are obviously connected with the components of the compliance. The relations based on the compliance of an homogeneous panel (equation (1.10)) are :

- In-plane Young’s modulus :

$$\tilde{E} = \frac{(1 - \nu^2)}{a} \frac{1}{h} \quad (1.14)$$

- Flexural Young’s modulus :

$$\tilde{E}_{flex} = \frac{1 - \nu^2}{d} \frac{12}{h^3} \quad (1.15)$$

Kinematic

Until now, only macroscopic quantities have been discussed and we have not mentioned local quantities yet. It ensures all previous equations to be valid for both homogeneous plates and any architected panels.

• **Specificities for homogeneous panels** The macroscopic strains in the case of an homogeneous panel are such that :

$$\begin{cases} \varepsilon_{11} = e + \chi x_3 \\ \varepsilon_{13} = \frac{\gamma}{2} \frac{6}{h^2} \left(\frac{h^2}{4} - x_3^2 \right) \end{cases} \quad (1.16)$$

If the shear-strain is zero, the displacement field of an homogeneous panel is obtained by integration of equation (1.16) :

$$\begin{cases} u_1 = (e + \chi x_3) x_1 \\ u_3 = -\frac{\chi}{2} x_1^2 + g(x_3) \end{cases} \quad (1.17)$$

where the function g is free to accommodate the equilibrium equation.

• **Specificities for sandwich panels** In the case of sandwich structure, the contrast in shear modulus between skins and core is so high that the shear deformation is negligible in the skins and quite homogeneous in the core. That means $\varepsilon_{13} \approx \frac{\gamma}{2}$ inside the core.

• **Specificities for architected panels** Separation of scales along axis e_1 ensures that the effective kinematic of an architected panel takes the form (1.16). Variations around this kinematic appear because of the spatial organization of the matter.

Whereas the origin of the frame is trivial in both homogeneous and sandwich cases, the question remains when modeling architected panels. For instance, translating the frame origin of a value δx_3 in the direction e_3 gives a new 3rd coordinate $\hat{x}_3 = x_3 - \delta x_3$. Thus, the macroscopic strains and stresses become :

$$\begin{cases} \hat{e} = e + \chi \delta x_3 \\ \hat{\chi} = \chi \end{cases} \quad \text{and} \quad \begin{cases} \hat{N} = N \\ \hat{M} = -\delta x_3 N + M \end{cases} \quad (1.18)$$

Then, the compliance matrix becomes :

$$\begin{bmatrix} \hat{\mathbf{a}} & \hat{\mathbf{b}} \\ \hat{\mathbf{b}} & \hat{\mathbf{d}} \end{bmatrix} = \begin{pmatrix} 1 & -\delta x_3 \\ 0 & 1 \end{pmatrix} \begin{bmatrix} \mathbf{a} & \mathbf{b} \\ \mathbf{b} & \mathbf{d} \end{bmatrix} \begin{pmatrix} 1 & 0 \\ \delta x_3 & 1 \end{pmatrix} \quad (1.19)$$

These expressions reveal the dependence of the macroscopic stresses, strains and compli-

ance components with respect to the frame origin. To be able to compare architected panel properties with relevance, the origin is chosen such that the coupling terms are zeros if possible. In the case where a material central symmetry, a rotation or a plane symmetry exists, it gives a location where this condition can be satisfied.

1.4.2 General plate models

A plate model consists in reducing the three-dimensional domain in a two dimensions domain into the plane of the plate. It is a generalization of the previous beam model with vanishing the plane-strain assumption.

Macroscopic stresses and equilibrium

The integration of the stress components in the out-of-plane direction leads to the following macroscopic stresses (second-order tensors) :

$$\left\{ \begin{array}{l} N_{\alpha\beta}(x_1, x_2) = \int_{-h/2}^{h/2} \sigma_{\alpha\beta} dx_3 \\ M_{\alpha\beta}(x_1, x_2) = \int_{-h/2}^{h/2} \sigma_{\alpha\beta} x_3 dx_3 \\ Q_{\alpha}(x_1, x_2) = \int_{-h/2}^{h/2} \sigma_{\alpha 3} dx_3 \end{array} \right. \quad (1.20)$$

where $\alpha, \beta = 1, 2$ are the subscripts corresponding to the plane of the panel. The macroscopic stresses are the *membrane forces* \mathbf{N} and the *moments* \mathbf{M} (both 2nd order tensors), and the *transverse-shear force* Q . A translation of the Navier-Bernoulli condition to the general case exists and refers to the ‘‘Kirchhoff-Love’’ model (equivalent to the classical beam theory).

Constitutive relation

The shell model provides a constitutive equation that links membrane forces and moments to *membrane strains* \mathbf{e} and *curvatures* $\boldsymbol{\chi}$. The expression is similar to eq. (1.9) with the only difference that the compliances are fourth order tensors and macroscopic stresses and

strains are second order tensors. It writes using Kelvin's notation :

$$\begin{bmatrix} e_{11} \\ e_{22} \\ \sqrt{2}e_{12} \\ \chi_{11} \\ \chi_{22} \\ \sqrt{2}\chi_{12} \end{bmatrix} = \begin{bmatrix} \mathbf{a}_{11} & \mathbf{a}_{12} & \mathbf{a}_{61} & | & \mathbf{b}_{11} & \mathbf{b}_{12} & \mathbf{b}_{61} \\ \mathbf{a}_{12} & \mathbf{a}_{11} & \mathbf{a}_{26} & | & \mathbf{b}_{12} & \mathbf{b}_{11} & \mathbf{b}_{26} \\ \mathbf{a}_{61} & \mathbf{a}_{26} & \mathbf{a}_{66} & | & \mathbf{b}_{61} & \mathbf{b}_{26} & \mathbf{b}_{66} \\ \hline \mathbf{b}_{11} & \mathbf{b}_{12} & \mathbf{b}_{61} & | & \mathbf{d}_{11} & \mathbf{d}_{12} & \mathbf{d}_{61} \\ \mathbf{b}_{12} & \mathbf{b}_{11} & \mathbf{b}_{26} & | & \mathbf{d}_{12} & \mathbf{d}_{11} & \mathbf{d}_{26} \\ \mathbf{b}_{61} & \mathbf{b}_{26} & \mathbf{b}_{66} & | & \mathbf{d}_{61} & \mathbf{d}_{26} & \mathbf{d}_{66} \end{bmatrix} \begin{bmatrix} N_{11} \\ N_{22} \\ \sqrt{2}N_{12} \\ M_{11} \\ M_{22} \\ \sqrt{2}M_{12} \end{bmatrix} \quad (1.21)$$

For an orthotropic symmetry, the membrane compliance is reduced to :

$$[\mathbf{a}] = \begin{bmatrix} \mathbf{a}_{11} & \mathbf{a}_{12} & 0 \\ \mathbf{a}_{12} & \mathbf{a}_{11} & 0 \\ 0 & 0 & \mathbf{a}_{66} \end{bmatrix} \quad (1.22)$$

The remaining terms become for an isotropic homogeneous material :

$$\mathbf{a}_{11} = \frac{1}{Eh}, \quad \mathbf{a}_{66} = \frac{1}{2Gh} \quad \text{and} \quad \mathbf{a}_{12} = \mathbf{a}_{11} - \mathbf{a}_{66} \quad (1.23)$$

Similarly, the bending compliance is reduced to :

$$[\mathbf{d}] = \begin{bmatrix} \mathbf{d}_{11} & \mathbf{d}_{12} & 0 \\ \mathbf{d}_{12} & \mathbf{d}_{11} & 0 \\ 0 & 0 & \mathbf{d}_{66} \end{bmatrix} \quad (1.24)$$

with the following expression for an isotropic homogeneous material :

$$\mathbf{d}_{11} = \frac{12}{Eh^3}, \quad \mathbf{d}_{66} = \frac{12}{2Gh^3} \quad \text{and} \quad \mathbf{d}_{12} = \mathbf{d}_{11} - \mathbf{d}_{66} \quad (1.25)$$

The coupling membrane-bending compliance is zero, $\mathbf{b} = 0$.

The plate model or "Reissner-Mindlin" model takes into account the transverse shear, such as the Timoshenko model for beams. The constitutive equation is the same as eq. (1.11) with the only difference that the compliance \mathbf{f} is a second order tensor, the coupling compliances \mathbf{k} and \mathbf{l} are third order tensors and the transverse-shear force and strain are vectors. For an homogeneous isotropic panel with thickness h , the compliance matrices are :

$$\begin{cases} \mathbf{f} = \frac{6}{5Gh} \mathbf{I}_2 \\ \mathbf{k} = \mathbf{l} = 0 \end{cases} \quad (1.26)$$

where \mathbf{I}_2 is the identity second order tensor in two dimensions.

Kinematics

Relationships equivalent to eq. (1.16) and (1.17) can be written. The strain components for an homogeneous panel become :

$$\begin{cases} \varepsilon_{\alpha\beta} = e_{\alpha\beta} + \chi_{\alpha\beta}x_3 \\ \varepsilon_{\alpha 3} = \frac{\gamma_\alpha}{2} \frac{6}{h^2} \left(x_3^2 - \frac{h^2}{4} \right) \end{cases} \quad (1.27)$$

For a shear equals to zero (the restriction to the Love-Kirchhoff model), the displacements become :

$$\begin{cases} u_\alpha = (e_{\alpha\beta} + \chi_{\alpha\beta}x_3) x_\beta \\ u_3 = -\frac{1}{2} (\chi_{1\beta} + \chi_{2\beta}) x_\beta^2 + g(x_3) \end{cases} \quad (1.28)$$

with a summation over $\beta = 1$ to 2 . The function g is free to accommodate the equilibrium equations. Figure 1.12 illustrates these six modes of deformation of the Kirchhoff-Love kinematic : the two in-plane elongations e_{11} and e_{22} , the in-plane shear e_{12} , the two curvatures χ_{11} and χ_{22} , and the twist χ_{12} . Figure 1.13 exhibits the two additional transverse-shear ratios of the Reissner-Mindlin kinematics.

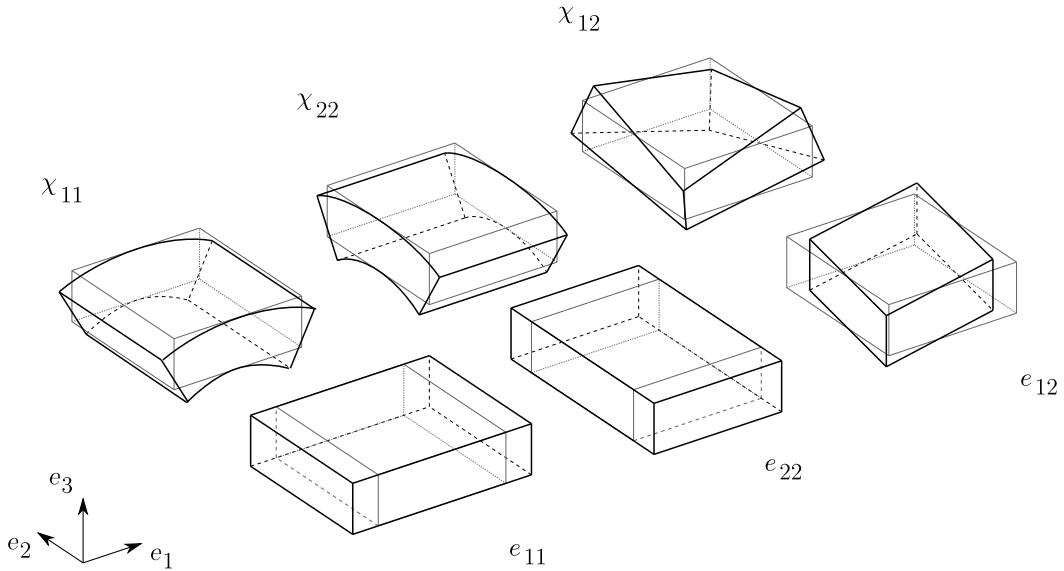


Figure 1.12: Deformed parallelepiped for the six macroscopic strains of the Kirchhoff-Love kinematic.

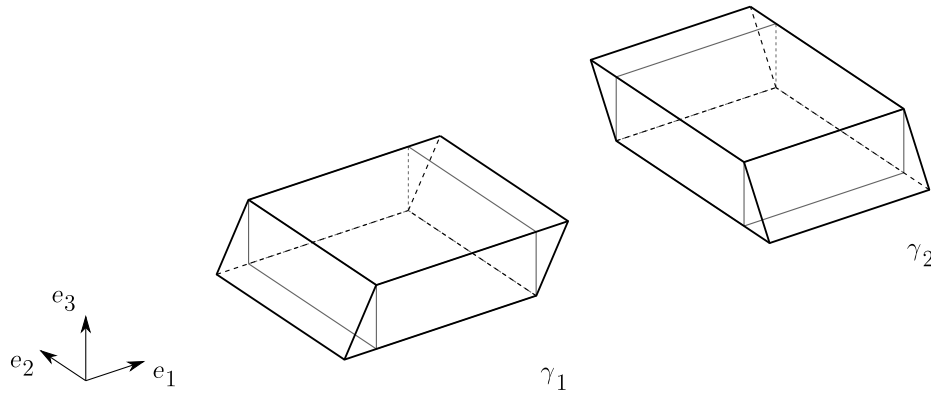


Figure 1.13: Deformed parallelepiped for the two transverse-shear ratios of the Reissner-Mindlin kinematic.

Equilibrium equation

The equilibrium equation is obtained by integration of the three-dimensional equation :

$$\begin{cases} N_{\alpha,\beta,\beta} + f_\alpha = 0 \\ Q_{\alpha,\alpha} + f_3 = 0 \\ M_{\alpha\beta,\beta} - Q_\alpha + \mu_\alpha = 0 \end{cases} \quad (1.29)$$

where f_α and f_3 are the spatial components of the body force by unit of surface and μ_α is the body moment by unit of surface in the direction e_α .

Other models

The two presented plate models, Love-Kirchhoff and Reissner-Mindlin, are the most classical models implemented in numerous finite element codes. While the first model is limited to slender configurations, the second give better estimates taking into account the transverse shear. But the constant, or even parabolic, shear distribution into the thickness is often far from the reality especially for laminated composite plates. Since the demand is strong to get a reliable model to be implemented in a low time-consuming 2D finite element code, the suggestions of enriched models are numerous.

The composite laminates concentrate most of the literature in two classes of models : the equivalent single layer models and the layerwise models. The single layer models often assume presupposed distributions of the stress or strain fields through the thickness. The zigzag models (Whitney and Leissa, 1969, Carrera, 2003) seems to reproduce quite well the three-dimensional behavior such as the continuity of the shear stress through the thickness. But they are restricted to symmetric sequences and materials. The layerwise

models are based on the refinement of the kinematic (Reddy, 1989, Carrera, 2002). Both local displacements and stresses are well predicted, but the high number of additional degrees of freedom leads to an extra computational cost.

Proceeding in an asymptotic expansion of the three-dimensional problem in the small parameter h/l (Caillerie, 1984), the Love-Kirchhoff model is refunded as a first order problem. Going further into the expansion, higher-order models can be obtained (Buannic and Cartraud, 2001, Yu et al., 2002a,b) but turn out to be complex to implement. However, the gradient-bending model (Lebée, 2010) is a higher-order single layer model that seems to give an interesting compromise between accuracy of the solution, number of additional variables and complexity of the theory. Highlighting the connection between the transverse shear and the bending gradient, it follows the Reissner approach and introduces the full bending gradient as additional macroscopic stresses. This higher-order plate model is not used in this PhD work but it highlights the connection between transverse shear and bending gradient that will enable the shear homogenization problem.

1.5 Experimental identification

Models have a limited interest without being confirmed by experimental tests. This section details the way to measure the flexural modulus, as well as the transverse-shear modulus in the case that it is non negligible (section 1.3).

Both three- and four-point bending tests are widely use to characterize panels that are essentially designed for bending. The four-point bending test has the advantage to produce a pure-bending zone in-between the internal pads (figure 1.14).

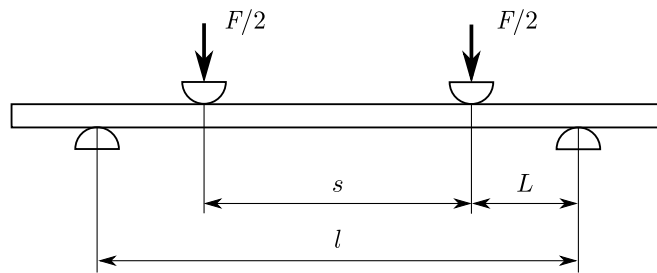


Figure 1.14: Four-point bending test setup. The load is share on the two loading points. The upper and lower span length are respectively s and l . The shear length is L .

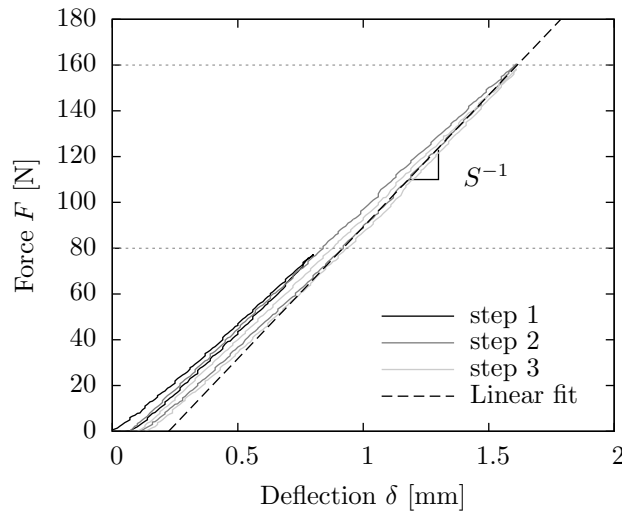


Figure 1.15: Force–deflection curve for three sequences of loading–unloading on a four-point bending test. The compliance S is fitted on the unloading slope between 80 and 160 N, for steps 2 and 3.

The bending compliance is measured from the slope of the force–deflection curve — such as the typical figure 1.15. One has :

$$S = \frac{\partial \delta}{\partial F} \quad (1.30)$$

where F is the total load force equally distributed on the two load pads, and δ is the vertical deflection of the load pads with respect to the support pads. Figure 1.15 plots the force versus the deflection for three steps of loading–unloading respectively up to 80 N for the first one and 160 N for the last two ones. The slope must be fitted on the beginning of the unloading curve.

The evolution of the macroscopic stresses along the beam are plotted on figure 1.16. By integration of the elastic energy along the beam, one deduces the following four-point bending compliance S_{4p} :

$$S_{4p} = \frac{(3l - 4L)L^2}{12} d + \frac{L}{2} f \quad (1.31)$$

where the lower span length l and the shear length L are shown on figure 1.14. The three-point bending compliance S_{3p} is obtained from the previous equation by taking $L = l/2$:

$$S_{3p} = \frac{l^3}{48} d + \frac{l}{4} f \quad (1.32)$$

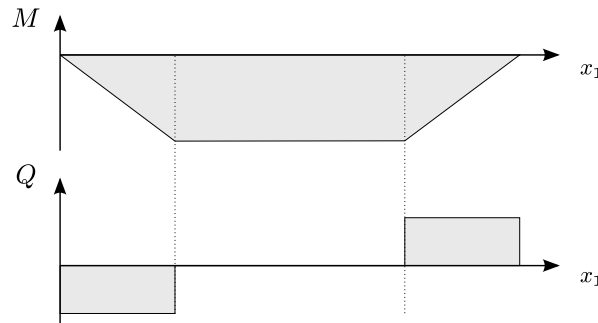


Figure 1.16: Variations of the bending moment M and the transverse force Q along the beam for a four-point bending test.

An overestimation of the flexural compliance d can be obtained by neglecting the shear contribution. More precisely, ASTM standards (C393, D7250) define an experimental procedure to determine both the flexural and shear compliances. This procedure consists in several four-point bending tests with different values of the lower span length l while keeping fixed the shear length L . The bending compliance is measured for two or three values of the lower span length and plotted versus the span length (figure 1.17). The equation (1.31) predicts a linear evolution and enables to express the compliance components with respect to the slope S' and the intercept S_0 :

$$\begin{cases} d = \frac{4}{L^2} S' \\ f = \frac{8}{3} S' + \frac{2}{L} S_0 \end{cases} \quad (1.33)$$

The values of the lower span length must be chosen in order to get a length ratio l/L

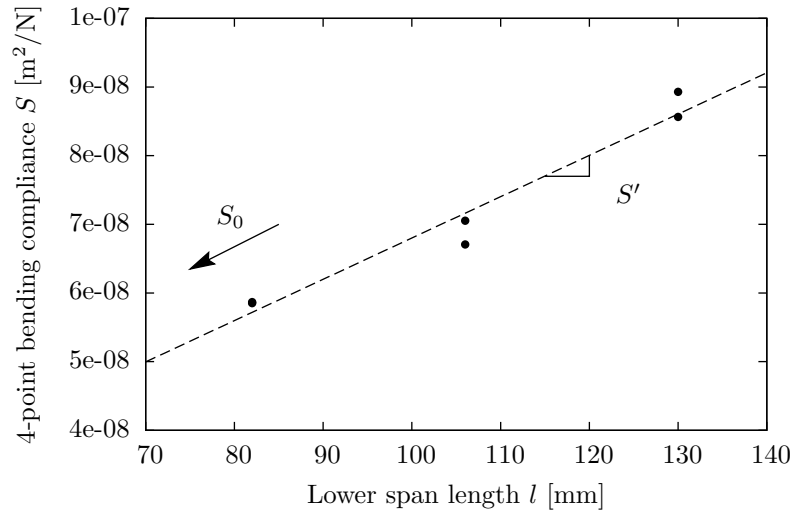


Figure 1.17: Measured 4-point bending compliance S versus the lower span length l . The flexural and shear compliance components can be deduce from the slope S' and the intercept S_0 of this linear evolution.

between 3 and 5. The choice of the shear length L depends itself on the thickness, the pad width and on the characteristic length of the internal architecture. It should satisfy a ratio L/h larger than 2. The geometry of the pads can be flat or cylindrical. It must have a contact surface large enough to avoid indentation of the faces but still relatively small compared to the shear length L . A pad width too thin will cause a non-linearity and an overestimation of the shear compliance (i.e. the panel will appear to be softer than it really is). A pad width too large will lead to an underestimate in the shear compliance (i.e. stiffer).

Even if the transverse shear is taken into account the slenderness have to be sufficient in order to guaranty the validity of the plate model, one should check the relative thickness h/l to be lower than 0.3. Such as for the shear length, the characteristic length of the architecture have to be included into the choice of the width. However, the width-thickness ratio b/h must vary from 2 to 5 depending on the thickness (respectively from thick to thin).

Conclusion

This chapter starts from the observation that the transport and building sectors impose complex multi-functional requirements for materials. Instead of an incremental improvement of the existing materials, it seems more efficient to design architected materials. Few examples have given an overview of the gains affordable by spatially organizing matter in a well controlled manner. This is particularly significant for the design of core materials that must perform a high shear stiffness at a minimum weight.

The infinite number of shape possibilities and the non-intuitive multi-functional specifications drive to the development of a numerical method to solve that optimization problem. But before any optimization, one needs to be able to compute the objective function or performance index. The selection approach applied to composites and sandwich panels shows that effective properties is the appropriate manner to evaluate and compare the performance of architected materials.

Highlights

- **Architected materials** are shown to be a way to develop new material that may provides tailored properties. The diversity of materials and processes, as well as the high refinement of predictive models enable to design customized architected material in order to fulfill complex multi-functional specifications.
- The **sandwich structure** is an emblematic case for such “material by design” approach. The association between faces and core is especially appropriate to provide several function such as bending stiffness in combination with shear stiffness, thermal insulation, electromagnetic properties, etc.
- Studying **effective properties** is a convenient approach to evaluate the performance of any architecture. Considering a heterogeneous architecture as an equivalent homogeneous material enables to compare with other architected or monolithic materials, as well as analyzing the influence of the design parameters. It is illustrated by presenting the material selection approach on sandwich structures.
- The **shell and plate models** provide an appropriate framework to identify the elastic properties of the concerned architected panels. **Four-point bending test** is an efficient experimental way to characterized both the flexural and transverse-shear (if significant) stiffness moduli.

CHAPTER 2

Homogenization of periodic architected panels

Introduction

The present chapter describes a computational approach to identify the effective elastic behavior of periodic architected panels. A validation is done by comparing homogenization results with both experimental data and finite element simulations of four-point bending test. Then as a direct application of the described homogenization procedure, a parametric study is performed in order to design embossed steel sheets.

The first section deals with the homogenization techniques. It begins with describing periodic homogenization of bulk media before focusing on the specific case of panels. Compliance components of the classical shell and plate models (Kirchhoff-Love and Reissner-Mindlin) can be identified with finite element simulations on the unit cell. Static approach is used such that the Kirchhoff-Love compliances are computed by applying membrane forces and bending moments. The homogenization problem for transverse-shear compliances is more difficult to defined, since a single shear-force is not self-balanced with stress-free boundary conditions on top-and-bottom faces.

In the second section, an illustrative architected panel is studied from the experimental, numerical and analytical view points. The contribution of the transverse-shear is more particularly pointed out.

Finally, an example of architected panel for automotive applications is studied. It consists in embossing a steel sheet in order to increase its flexural stiffness. An analysis of the effective properties of such plates is presented. A parametric study is performed and promising solutions are proposed.

2.1 Periodic homogenization of elastic properties

Homogenization consists in replacing a heterogeneous material by an effective homogeneous material that provides the same overall response. It enables to predict the response of a part or a structure without the need of modeling locally the heterogeneities. The relevance of homogenization is usually based on the separation of two scales : the scale of the stress and strain variations generated by the loading ; and the scale of the variations due to the heterogeneities.

Both random and periodic heterogeneities can be treated. Since no randomly architected material have been studied in this PhD work, only the periodic case is mentioned in the following. Notions are first introduced on bulk media, then one focuses on the particular case of panels. The specificity of panels is that the periodicity is restricted to two directions. In addition, the obtained effective model (shell or plate) is defined on a bi-dimensional geometry while the heterogeneous material is modeled with three-dimensional continuous mechanic.

2.1.1 Bulk media

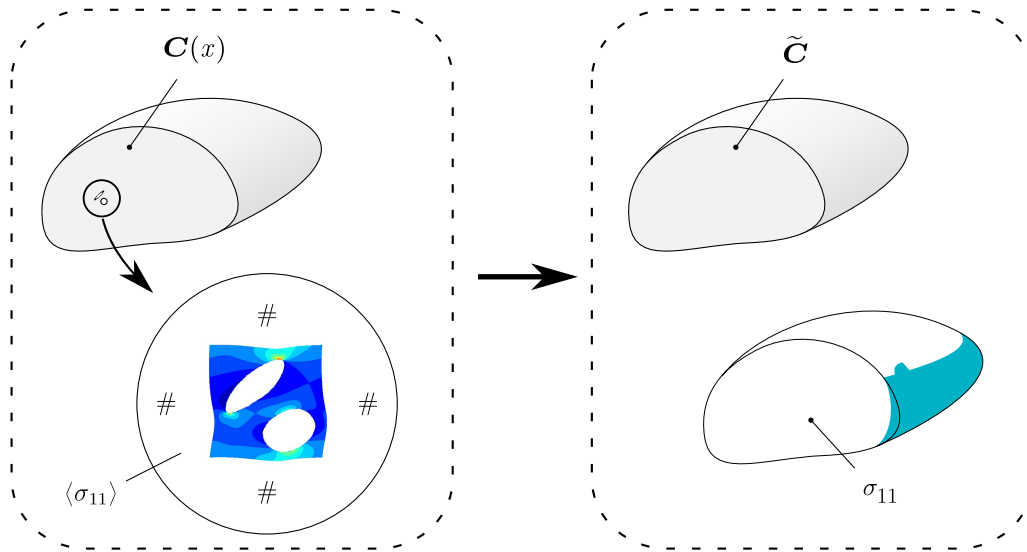


Figure 2.1: Periodic homogenization of bulk media : heterogeneities are replaced by an effective homogeneous media.

In this section, the unit cell V , periodic in the three directions, is subjected to an “averaging operation” in order to provide an effective homogeneous media (figure 2.1). Effective stiffness and compliance tensors are defined such that a linear relation can be written between mean stress and strain tensors. Mean quantities are defined by averaging

over the unit cell and denoted :

$$\langle \cdot \rangle = \frac{1}{V} \int_V \cdot dV \quad (2.1)$$

Following definitions are based on Hill's lemma which states that the average work over V equals the work of mean fields :

$$\langle \boldsymbol{\sigma} \cdot \boldsymbol{\varepsilon} \rangle = \langle \boldsymbol{\sigma} \rangle \cdot \langle \boldsymbol{\varepsilon} \rangle \quad (2.2)$$

This equation holds for any statically admissible stress field $\boldsymbol{\sigma}$ and any kinematically admissible strain field $\boldsymbol{\varepsilon}$.

The kinematic approach enables to define the effective stiffness with respect to the stress average that results for applying a mean strain $\bar{\boldsymbol{\varepsilon}}$. The tensor components are identified on :

$$\langle \boldsymbol{\sigma} \rangle = \tilde{\mathbf{C}} \bar{\boldsymbol{\varepsilon}} \quad (2.3)$$

An identification on the average strain energy-density $\langle w \rangle$ is equivalent as a consequence of Hill's lemma (2.2) :

$$\langle w \rangle = \frac{1}{2} \bar{\boldsymbol{\varepsilon}} \cdot \tilde{\mathbf{C}} \bar{\boldsymbol{\varepsilon}} \quad (2.4)$$

Kinematic uniform boundary conditions $u = \bar{\boldsymbol{\varepsilon}} \cdot x$, which satisfy $\langle \boldsymbol{\varepsilon} \rangle = \bar{\boldsymbol{\varepsilon}}$, provide a rough estimate denoted $\tilde{\mathbf{C}}_{\text{KUBC}}$. Following Michel et al. (1999), a more accurate estimate can be computed with taking into account periodicity. It deals with applying periodic conditions on stress and strain, and with searching for a solution to the displacement under the form :

$$u = \bar{\boldsymbol{\varepsilon}} x + u' \quad (2.5)$$

where u' is a periodic fluctuation field. The condition on the averaged strain $\langle \boldsymbol{\varepsilon} \rangle = \bar{\boldsymbol{\varepsilon}}$ is consequently satisfied. It can be implemented in a finite element solver either with periodic boundary conditions on $(u - \bar{\boldsymbol{\varepsilon}} \cdot x)$, or with applying an initial strain $\bar{\boldsymbol{\varepsilon}}$ and solving with respect to the unknown perturbation u' (with periodic boundary conditions).

The static approach is analog to the kinematic approach but applying stress instead of strain. It enables to define the effective compliance tensor by identification on the strain average :

$$\langle \boldsymbol{\varepsilon} \rangle = \tilde{\mathbf{S}} \bar{\boldsymbol{\sigma}} \quad (2.6)$$

Again, an identification on the average stress energy-density $\langle w^* \rangle$ is equivalent :

$$\langle w^* \rangle = \frac{1}{2} \bar{\boldsymbol{\sigma}} \cdot \tilde{\mathbf{S}}_{\text{SUBC}} \bar{\boldsymbol{\sigma}} \quad (2.7)$$

Static uniform boundary conditions $\boldsymbol{\sigma} \cdot n = \bar{\boldsymbol{\sigma}} \cdot n$, which satisfy $\langle \boldsymbol{\sigma} \rangle = \bar{\boldsymbol{\sigma}}$, provide a rough estimate denoted $\tilde{\mathbf{S}}_{\text{SUBC}}$. Inverse of this tensor $\tilde{\mathbf{S}}_{\text{SUBC}}^{-1}$ is strongly different from $\tilde{\mathbf{C}}_{\text{KUBC}}^{-1}$ since

kinematics are different, at least close to the boundaries. In the case of periodic estimates, a static approach also exists. It assumes the displacement as in equation (2.5) excepted that the mean strain $\bar{\epsilon}$ is replaced with an unknown mean strain ϵ^* . This additional unknown is calculated in order to satisfy the stress average constraint :

$$\begin{cases} u = \epsilon^* x + u' & \text{with } u' \text{ periodic on } \partial V \\ \langle \sigma(\epsilon^*) \rangle = \bar{\sigma} \end{cases} \quad (2.8)$$

The inverse of the effective compliance $\tilde{S}_{\#}^{-1}$ obtained by solving this problem is identical to $\tilde{C}_{\#}$. It leads from the identical boundary conditions in both approaches. However, it might be interesting for some reasons to prescribe mean stress instead of mean strain (for instance in non-linear case, or in the following transverse-shear homogenization).

As developed by Bornert et al. (2001), arguments on admissibility sets of these four homogenization problems enables to rank the effective tensors as :

$$\tilde{S}_{\text{SUBC}}^{-1} \leq \tilde{S}_{\#}^{-1} = \tilde{C}_{\#} \leq \tilde{C}_{\text{KUBC}} \quad (2.9)$$

These relations give a qualitative way to validate any new estimation method of effective properties.

2.1.2 Panels

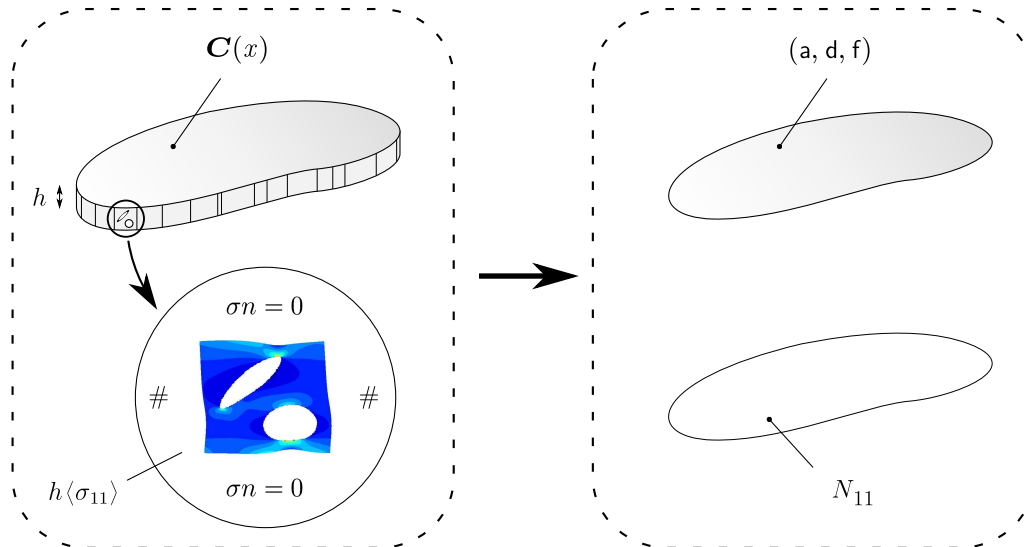


Figure 2.2: Periodic homogenization of panel : three-dimensional heterogeneous panel is replaced with an effective homogeneous bi-dimensional shell or plate.

Periodic panels, in comparison with full-periodic bulk media, introduce additional difficulties since the effective homogeneous panel is reduced to a bi-dimensional plate model. One direction is no more periodic and is subjected to an “integrating operation” rather than “averaging” (figure 2.2).

The unit cell V is subjected to mixed boundary conditions. Periodicity is still imposed for in-plane directions, but stress-free boundary conditions have to be ensured on the upper-and-lower faces ∂V^\pm (figure 2.3).

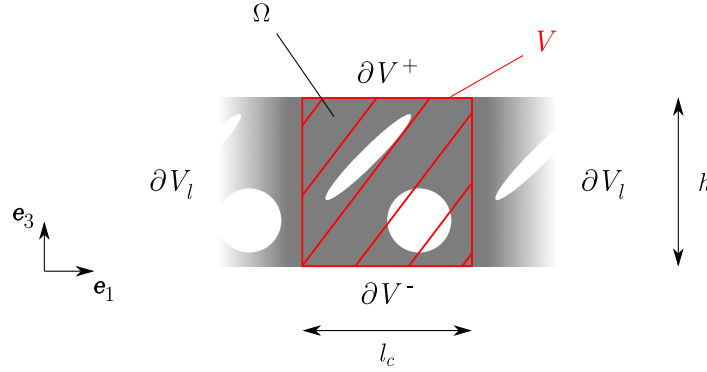


Figure 2.3: Example of unit cell of an architected plate with normal e_3 , periodic in direction e_1 and invariant in the direction e_2 . The unit cell is defined by the domain V , with length l_c and thickness h . The upper and lower boundaries are denoted respectively ∂V^+ and ∂V^- . The lateral boundaries are denoted ∂V_l without any distinction. The domain Ω is the subset of the unit cell V filled with matter.

Two homogenization problems enable to identify compliances of the plate model (Reissner-Mindlin) : one for membrane and flexural compliances, one for transverse-shear compliance.

Membrane and flexural compliance

Buannic et al. (2003) proposed an asymptotic approach for corrugated sandwich panels. The effective compliances are identified by solving elementary mechanical problems on the unit cell. Following the asymptotic approach of Caillerie (1984), a solution of the three-dimensional elasticity problem on the unit cell V is searched under the following form :

$$\begin{cases} u = \bar{e}x + \bar{\chi}x x_3 + u' \\ u_3 = -\frac{1}{2}x \cdot \bar{\chi}x + u'_3 \end{cases} \quad (2.10)$$

where the first equation is limited to the two dimensions of the plane (e_1, e_2). The bi-dimensional tensors \bar{e} and $\bar{\chi}$ are respectively the macroscopic membrane strain and the macroscopic curvature (see section 1.4.2). The fluctuation field u' is periodic along the in-plane directions and unconstrained on the top-and-bottom faces.

Prescribing the kinematic through an initial strain, the homogenization problem to be solved with respect to u' becomes :

$$\begin{cases} \operatorname{div} \boldsymbol{\sigma} = 0 & \text{on } V \\ \boldsymbol{\sigma} = \mathbf{C}(x) (\nabla^s u' + \bar{\mathbf{e}} + \bar{\boldsymbol{\chi}} x_3) & \text{on } V \\ \boldsymbol{\sigma} \cdot \mathbf{n} = 0 & \text{on } \partial V^\pm \\ u' & x_1, x_2\text{-periodic on } \partial V_l \end{cases} \quad (2.11)$$

where $\nabla^s \cdot$ denotes the symmetric gradient operator.

Similarly to bulk media, the static approach exist and consists in applying a mean stress. This is the approach we choose in the following in order to identify compliance components. One introduces unknown main strain \mathbf{e}^* and main curvature $\boldsymbol{\chi}^*$ and adds two constraints on the membrane forces \mathbf{N} and moments \mathbf{M} (Bourgeois, 1997, Bourgeois et al., 1997) :

$$\begin{cases} \operatorname{div} \boldsymbol{\sigma} = 0 & \text{on } V \\ \boldsymbol{\sigma} = \mathbf{C}(x) (\nabla^s u' + \mathbf{e}^* + \boldsymbol{\chi}^* x_3) & \text{on } V \\ \boldsymbol{\sigma} \cdot \mathbf{n} = 0 & \text{on } \partial V^\pm \\ u' & x_1, x_2\text{-periodic on } \partial V_l \\ \langle \mathbf{N}(\mathbf{e}^*, \boldsymbol{\chi}^*) \rangle = \bar{\mathbf{N}} \\ \langle \mathbf{M}(\mathbf{e}^*, \boldsymbol{\chi}^*) \rangle = \bar{\mathbf{M}} \end{cases} \quad (2.12)$$

where $\langle \cdot \rangle$ denotes in this case the average over the 2D in-plane unit cell since \mathbf{N} and \mathbf{M} are two dimensions tensors. The identification of compliance components is straightforward since the generated macroscopic strains are identical to the unknowns \mathbf{e}^* and $\boldsymbol{\chi}^*$. Solving only three unit cell problems allows to identify all the components of the membrane compliance :

$$[\mathbf{a}] = \begin{bmatrix} e_{11}^*(\bar{N}_{11}) & e_{11}^*(\bar{N}_{22}) & e_{11}^*(\bar{N}_{12})/\sqrt{2} \\ e_{22}^*(\bar{N}_{11}) & e_{22}^*(\bar{N}_{22}) & e_{22}^*(\bar{N}_{12})/\sqrt{2} \\ \sqrt{2}e_{12}^*(\bar{N}_{11}) & \sqrt{2}e_{12}^*(\bar{N}_{22}) & e_{12}^*(\bar{N}_{12}) \end{bmatrix} \quad (2.13)$$

where $\mathbf{e}^*(\bar{N}_{\alpha'\beta'})$ is solution of the problem (2.12) with $\forall(\alpha, \beta) \bar{N}_{\alpha\beta} = \delta_{\alpha'\alpha}\delta_{\beta'\beta}$ ¹ and $\bar{\mathbf{M}} = 0$. Idem for the flexural compliance :

$$[\mathbf{d}] = \begin{bmatrix} \chi_{11}^*(\bar{M}_{11}) & \chi_{11}^*(\bar{M}_{22}) & \chi_{11}^*(\bar{M}_{12})/\sqrt{2} \\ \chi_{22}^*(\bar{M}_{11}) & \chi_{22}^*(\bar{M}_{22}) & \chi_{22}^*(\bar{M}_{12})/\sqrt{2} \\ \sqrt{2}\chi_{12}^*(\bar{M}_{11}) & \sqrt{2}\chi_{12}^*(\bar{M}_{22}) & \chi_{12}^*(\bar{M}_{12}) \end{bmatrix} \quad (2.14)$$

where $\boldsymbol{\chi}^*(\bar{M}_{\alpha'\beta'})$ is solution of the problem (2.12) with $\bar{\mathbf{N}} = 0$ and $\forall(\alpha, \beta) \bar{M}_{\alpha\beta} = \delta_{\alpha'\alpha}\delta_{\beta'\beta}$.

¹where δ is the Kronecker symbol. $\delta_{ij} = 1$ if $i = j$, $\delta_{ij} = 0$ if not.

Tensors (2.13) and (2.14) are written using the Kelvin's notation. An identification on the energy is also possible for diagonal components, as it was introduced in the section 2.1.1. For instance :

$$\mathbf{a}_{11} = \frac{2h \langle w^* \rangle}{\bar{N}_{11}^2} \quad (2.15)$$

where w^* is the stress-energy of the problem (2.12) with $\forall(\alpha, \beta) \bar{N}_{\alpha\beta} = \delta_{1\alpha}\delta_{1\beta}$ and $\bar{\mathbf{M}} = 0$.

Remark As mentioned in the section 1.4.1, the location of the frame is an issue. For architected materials that mix matter and space — which is the case in the following — a generic frame origin can be chosen. It is usually defined such as the coupling membrane–flexural compliance component vanishes. This choice is such that no membrane strain is produced from a pure bending moment. It consists in choosing a new frame translated in the direction e_3 with coordinate $\hat{x}_3 = x_3 - \delta x_3$ and :

$$\delta x_3 = \frac{1}{|\Omega|} \int_{\Omega} x_3 \, dx \quad (2.16)$$

where Ω is the subset of the unit cell V filled with matter.

Transverse-shear compliance

The case of transverse-shear compliance is not obvious since no self-balanced shear force can be applied on lateral boundaries while keeping the upper-and-lower faces stress-free. Then alternative problems are presented with two types of loading : uniform boundary conditions even on upper-and-lower faces, and bending gradient body load.

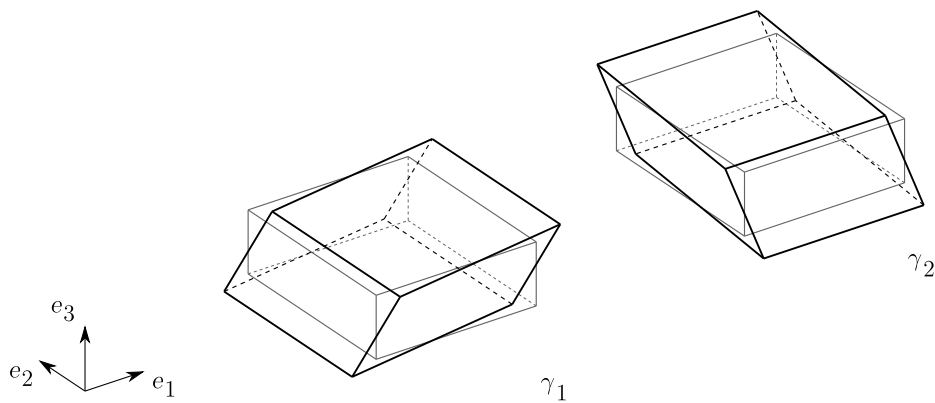


Figure 2.4: Deformed parallelepiped subjected to transverse-shear force through static uniform boundary conditions (SUBC).

Uniform boundary conditions A first way to estimate the shear compliance components is to solve a problem with uniform (kinematic or static) boundary conditions.

For instance, static uniform boundary conditions (SUBC) imply the following elasticity problem :

$$\begin{cases} \operatorname{div} \boldsymbol{\sigma} = 0 & \text{on } V \\ \boldsymbol{\sigma} = \mathbf{C}(x) \nabla^s u & \text{on } V \\ \boldsymbol{\sigma} \cdot \mathbf{n} = \bar{\mathbf{Q}} & \text{on } \partial V^\pm \\ \boldsymbol{\sigma} \cdot \mathbf{n} = (\bar{\mathbf{Q}} \cdot \mathbf{n}) \mathbf{e}_3 & \text{on } \partial V_l \end{cases} \quad (2.17)$$

where $\bar{\mathbf{Q}}$ is the applied overall shear stress. Then, the shear compliance tensor is estimated by :

$$[\mathbf{f}] = \begin{bmatrix} \bar{\gamma}_1(\bar{\mathbf{Q}}_1) & \bar{\gamma}_1(\bar{\mathbf{Q}}_2) \\ \bar{\gamma}_2(\bar{\mathbf{Q}}_1) & \bar{\gamma}_2(\bar{\mathbf{Q}}_2) \end{bmatrix} \quad (2.18)$$

where $\bar{\gamma}_\alpha$ is the overall shear strain given by :

$$\gamma_\alpha = \left\langle \int_{-\frac{h}{2}}^{\frac{h}{2}} \frac{1}{2} (u_{\alpha,3} + u_{3,\alpha}) dx_3 \right\rangle \quad \forall \alpha = 1, 2 \quad (2.19)$$

In addition to the approximation of the periodic boundary conditions with uniform Neumann conditions (like for bulk media), the stress-free conditions on top-and-bottom faces are not satisfied. Consequently, this static approach is not yet a bound and the identified compliance may be far from the real value depending on the architecture. Moreover, the stress distribution is skewed all over the unit cell and not only close to the boundaries. For instance, a non-architected panel presents a homogeneous shear stress in the SUBC loading, whereas the real stress field is parabolic when taking into account the stress-free faces. This point will be even more significant in shape optimization because matter displacement is based on the local stress and strain fields.

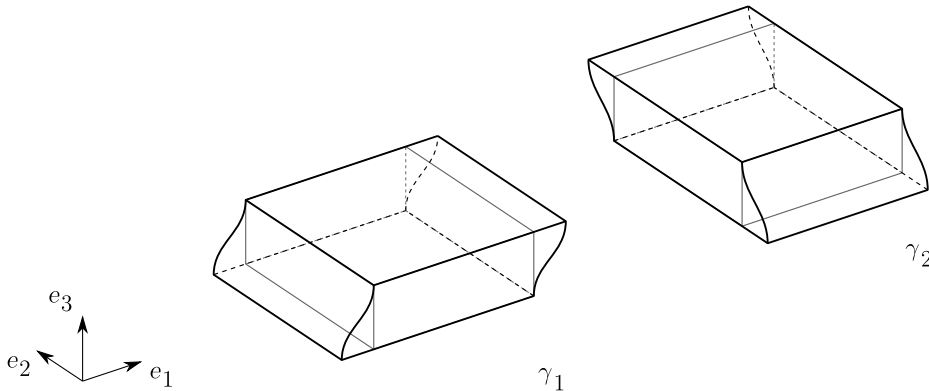


Figure 2.5: Deformed parallelepiped subjected to transverse-shear force through bending gradient body load (BG).

Stress-free and periodic boundary conditions A unit cell problem respectful of the stress-free boundary conditions was recently proposed by Cecchi and Sab (2007). This approach was studied in details by Lebée (2010, PhD thesis) up to develop a higher order plate model. These works formalize the link between transverse-shear and bending gradient and offer a homogenization problem for shear that uses results from bending. A boundary shear load with stress-free upper-and-lower faces is not self-balanced but must be combined with a bending gradient. The idea is to load the unit cell not only through the boundary conditions but also through a body force load that results from the homogenization problem (2.12). Finally, the unit cell problem is :

$$\begin{cases} \operatorname{div} \boldsymbol{\sigma} + \mathbf{f} = 0 & \text{on } V \\ \boldsymbol{\sigma} = \mathbf{C}(x) \nabla^s u & \text{on } V \\ \boldsymbol{\sigma} \cdot \mathbf{n} = 0 & \text{on } \partial V^\pm \\ u & x_1, x_2\text{-periodic on } \partial V_l \end{cases} \quad (2.20)$$

with

$$f_i = \sigma_{i\alpha}^{(\bar{M}_{\alpha\alpha})} \frac{\bar{Q}_\alpha}{\bar{M}_{\alpha\alpha}} \quad (2.21)$$

where $\sigma_{i\alpha}^{(\bar{M}_{\alpha\alpha})}$ is the stress solution to problem (2.12) with $\bar{\mathbf{N}} = 0$ and $\bar{\mathbf{M}} = \bar{M}_{\alpha\alpha} e_\alpha \otimes e_\alpha$. Finally, the effective shear compliance is identified again according to equation (2.18). Diagonal components can also be calculated from the stress-energy w^* such as :

$$\mathbf{f}_{\alpha\alpha} = \frac{2h \langle w^* \rangle}{\bar{Q}_\alpha} \quad (2.22)$$

2.1.3 Conclusion

After recalling the context of periodic homogenization, the specific case of Love-Kirchhoff and Reissner-Mindlin periodic plates have been developed.

The static approach is preferred and the compliance components are obtained consecutively by computing the macroscopic strains that result from each membrane force and bending moment. Calculation of the transverse-shear compliances faces the inability to apply a self-balanced shear force with stress-free top-and-bottom boundary conditions. The relationship between bending gradient and transverse-shear gives a method to apply a shear force through a body load.

In all cases, diagonal compliance components can be derived from the stress-energy density, which is interesting for further shape optimization.

2.2 Level-set method and ersatz phase

In this section, level-set method coupled with finite element method is used to solve the previous homogenization problems on a whole mesh of the unit cell. This approach enables an implicit definition of the geometry and will be useful in shape optimization to transform shape and topology without remeshing.

Following the approach of Sethian (1999), a level-set function is introduced in order to capture the geometry. The domain Ω filled with matter is defined implicitly through the level-set function $\phi : \mathbb{R}^3 \rightarrow \mathbb{R}$, such that :

$$\begin{cases} \phi(x) > 0 & \Leftrightarrow x \in \Omega \\ \phi(x) = 0 & \Leftrightarrow x \in \partial\Omega \cap V \\ \phi(x) < 0 & \Leftrightarrow x \in V \setminus \bar{\Omega} \end{cases} \quad (2.23)$$

Figure 2.6 illustrates this relation between the level-set function $\phi(x)$ and the domain Ω .

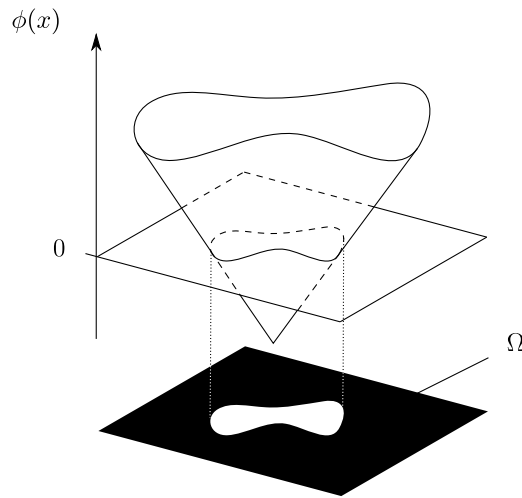


Figure 2.6: Sketch of an arbitrary level-set function $\phi(x)$ and the corresponding domain Ω .

Then, unit cell is entirely meshed and empty spaces are mimicked with an ersatz phase with a Hooke's tensor close to zero. This is done using a heterogeneous Hooke's tensor defined as :

$$\mathbf{C}(x) = \varsigma(\phi(x)) \bar{\mathbf{C}} \quad (2.24)$$

where the value of the Hooke's tensor $\bar{\mathbf{C}}$ for the constitutive material is multiplied by a smoothed characteristic function of Ω . This function is obtained from applying a smoothed heavy-side function ς to the level-set function. Among other typical expressions, the heavy-

side function $\varsigma : \mathbb{R} \rightarrow \mathbb{R}$ is written as (Yamada et al., 2010) :

$$\varsigma(\phi) = \begin{cases} 1 & \text{if } \phi > \frac{\epsilon}{2}, \\ \frac{1}{2} - \frac{\phi}{\omega} \left(\frac{15}{8} - \frac{\phi^2}{\omega^2} \left(5 - 6 \frac{\phi^2}{\omega^2} \right) \right) & \text{if } |\phi| < \frac{\epsilon}{2}, \\ \frac{1}{c} & \text{if } \phi < -\frac{\epsilon}{2}. \end{cases} \quad (2.25)$$

where ω is the *smoothing width* which is the width of the phase transition, and c the *phase contrast* (see figure 2.7). The phase contrast c must be large to mimic holes, but not too much because that would give a ill-conditioned matrix to invert.

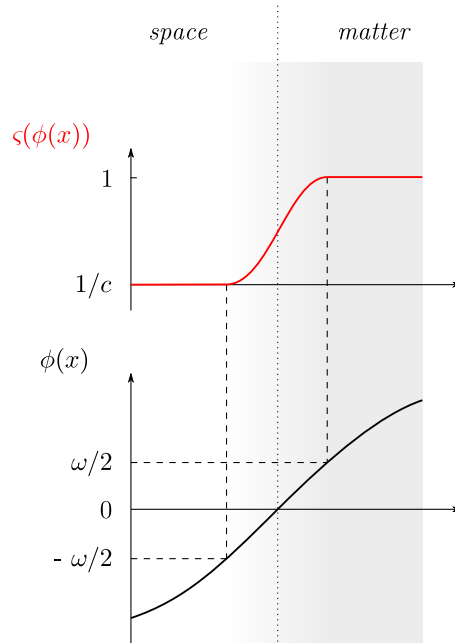


Figure 2.7: Illustration of an arbitrary level-set function $\phi(x)$ and the corresponding characteristic function $\varsigma(\phi(x))$ of equation (2.25).

As for usual FEM simulations, the sensitivity to the mesh size should be analyzed in order to check the coupling with the heterogeneous constitutive relation and choose the minimum number of elements that provides an admissible error. More specifically, the level-set method introduces two artificial parameters — phase contrast and smoothing width — which have to be fixed.

As a benchmark, homogenization problems are solved with varying the values of previous parameters c and ω , with the illustrative unit cell geometry shown on figure 2.8a. This geometry is the result of a trigonometric level-set function plotted on figure 2.8b,

which is typically used for shape optimization. Its expression is :

$$\phi(x_1, x_3) = \cos\left(p_1 \frac{2\pi x_1}{l_c}\right) \cos\left(p_3 \frac{2\pi x_3}{h}\right) + \delta \quad (2.26)$$

where p_1 , resp. p_3 , is the number of holes in the direction e_1 , resp. e_3 . The offset δ controls the size of the holes and consequently the area fraction of matter.

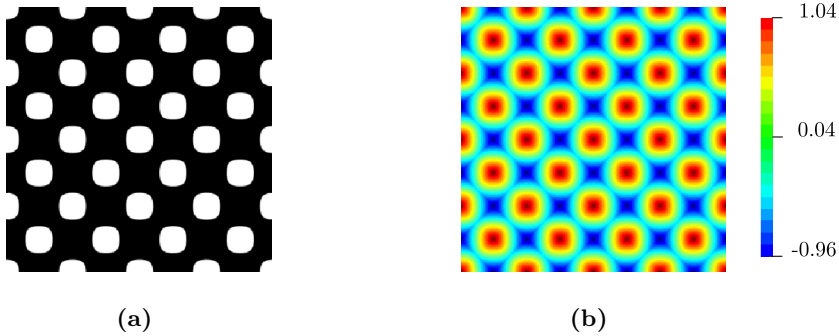


Figure 2.8: (a) Unit cell geometry chosen to study the influence of mesh size, phases contrast and smoothing width on FEM computations ; (b) Corresponding level-set function with expression (2.26). The offset is $\delta = 0.04$ and the corresponding area fraction is 0.72.

Effect of the mesh size

The whole unit cell is meshed with triangular linear elements, as shown on figure 2.9 for respectively 108, 1710 and 4281 elements.

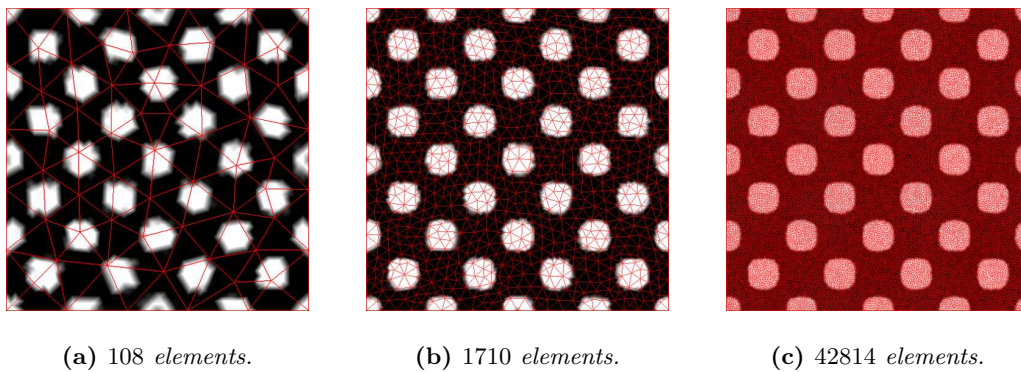


Figure 2.9: Same unit cell geometry discretized respectively with 108, 1710 and 42814 elements. Computational triangular mesh (red) and discretized geometry (black) displayed with a finer post-treatment mesh (Comsol Multiphysics).

The flexural and transverse-shear compliances are computed for the same unit cell geometry (figure 2.8a) but with different meshes. Their evolution with respect to the number of elements is presented on figures 2.10a and 2.10b.

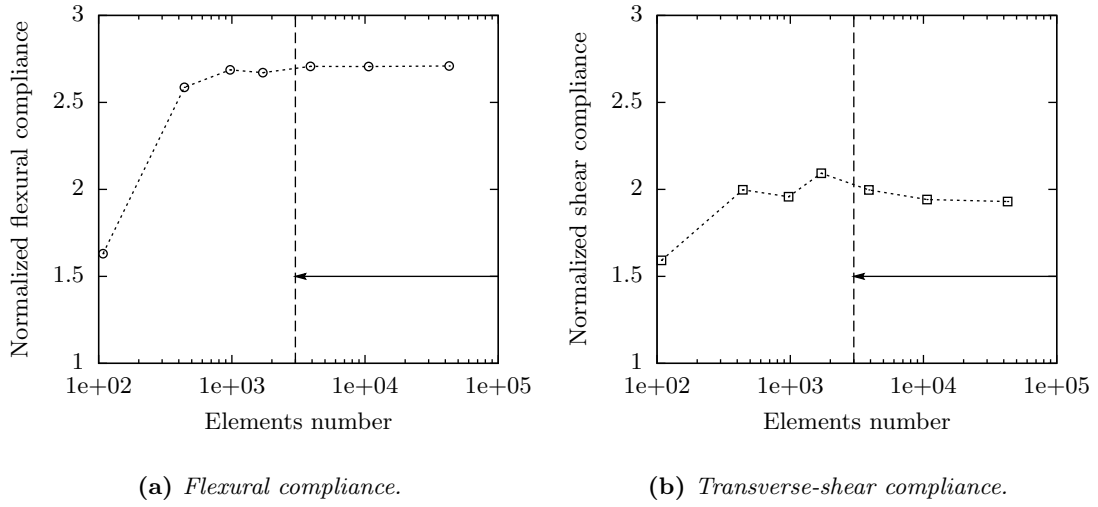


Figure 2.10: Evolution of the flexural and transverse-shear compliance components with respect to the number of triangular elements to mesh the unit cell with the same geometry (figure 2.8a). Other parameters are : $c = 10^3$, $\omega = 0.04$.

The compliance values are normalized by those of a non-architected panel (a unit cell without any holes). A good estimation is obtained from a relatively low number of elements (~ 500). The complete convergence of both flexural and shear components is observed for finer mesh with more than 3000 elements. In the following, one will care to solve any mechanical problem with a sufficiently fine mesh.

Effect of the phases contrast

Figures 2.11a and 2.11b plot the normalized flexural and shear compliances with respect to phase contrast c . The convergence of the flexural component is observed from a phase contrast of $c = 10^3$. Concerning the shear component, a similar behavior is observed below $c = 10^4$ but a divergence occurs for larger values. This divergence may be due to local stress peaks within elements on the interface. Since the stress field from flexural homogenization is applied as a body load for shear homogenization, the prescribed shear force may be larger than expected.

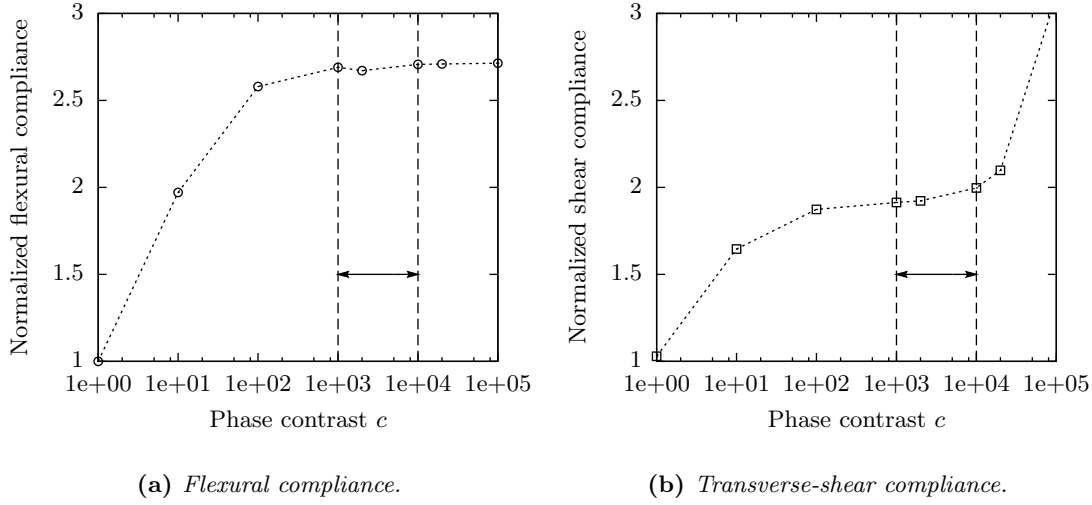


Figure 2.11: Evolution of the flexural and shear compliance components with the phases contrast in Young's modulus. Other parameters are : 3890 elements, $\omega = 0.04$.

In the following, phase contrast c is chosen in-between 10^3 and 10^4 in order to provide moderate errors on both flexural and shear compliances.

Effect of the smoothing width

The geometry is captured thanks to the level-set function, such that the mesh is the same whatever the geometry is. Then, the interface between matter and space is not explicitly meshed and it crosses elements. Within these elements, the variation in Young's modulus may produce stress peaks. In order to limit this, the heavy-side function ζ is smoothed such that it introduces a fictitious thick interface. The thickness of this transition is the smoothing width ω defined in equation (2.25). Solving the homogenization problems with several values of the smoothing width — for instance $\omega = 0.04$, 0.4 and 1 as shown on figure 2.12 — enables to plot flexural and shear compliances versus ω , respectively on figures 2.13a and 2.13b.

Finally, the value of the smoothing width is fixed in the following lower than 0.2 in order to limit the influence of this artificial parameter while providing a smooth transition between matter and space. This value makes sense for a level-set function with a gradient along the zero contour as close as possible to unity. And one has to keep in mind the real interface thickness may be larger if the level-set gradient is locally weaker than one.

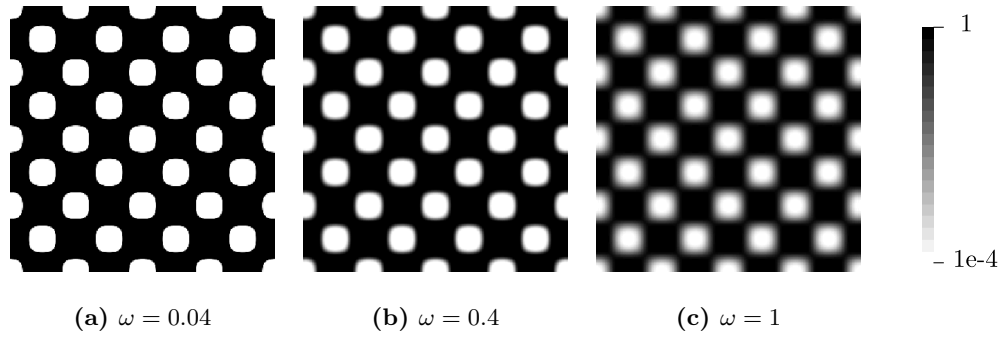


Figure 2.12: Same unit cell geometry obtained from the level-set function plotted on figure 2.8 with a smoothing width ω — see equation (2.25) — equal respectively to 0.2, 2 and 5.

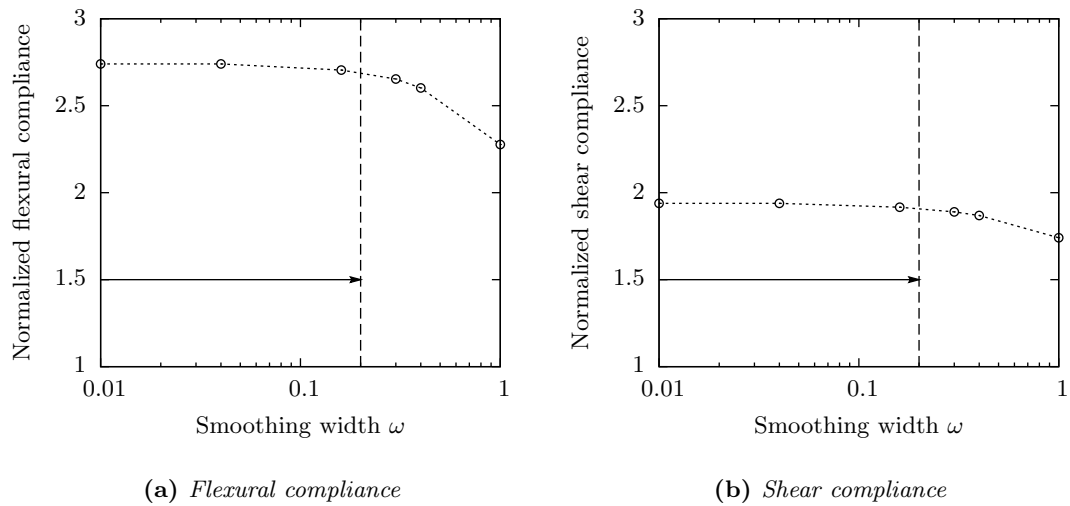


Figure 2.13: Evolution of the flexural and shear compliance components with the smoothing width. Other parameters are : 3890 elements, $c = 10^3$.

2.3 Validation of the homogenization approach

An illustration of the homogenization procedure is given in this section on a bi-dimensional plane strain periodic panel. The aim is to highlight with a given architected panel how the four-point bending behavior can be predicted from the homogenization approach previously described. The bending compliance S_{4p} will be deduced from the numerical effective compliance \mathbf{d} and \mathbf{f} . Results will be compared to bending tests and full-field FEM simulations. The idea is to validate the choice of taking into account the transverse-shear contribution as well as the type of loading into the shear homogenization problem.

Unit cell of the architecture chosen for this study is shown on figure 2.14. The panel is oriented with out-of-plane direction along e_3 . The unit cell is repeated periodically in direction e_1 and architecture is invariant in direction e_2 . Sizes of the unit cell are $l_c = 24$ mm and $h = 12$ mm. This geometry of architected panel presents a non-negligible transverse-shear contribution. Thus it is a good candidate to verify if the bending-gradient homogenization problem is needed to provide a good prediction.

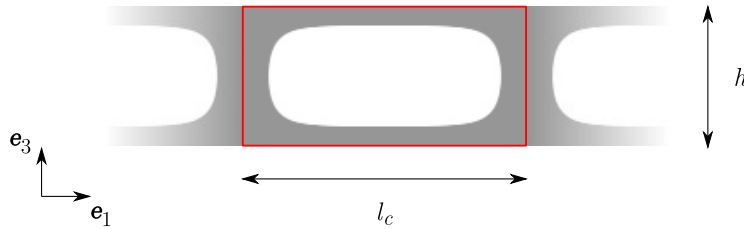


Figure 2.14: Unit cell of the considered architected plate, with length $l_c = 24$ mm and thickness $h = 12$ mm.

2.3.1 Four-point bending tests

A panel sample based on the unit cell geometry of figure 2.14 was produced in polyamide by selective laser sintering (SLS). This additive manufacturing technique consists in building a three-dimensional part by alternative steps of powder bed deposition and selective laser fusion (Gibson et al., 2009). The company *Polyshape* was in charge of the process, as part of a collaboration with the CdM Paris (*Centre des Matériaux*). The commercial powder *DuraForm PA* was used with an average particle size of $60 \mu\text{m}$. The Young's modulus E is given in the literature between 1.5 to 3.0 GPa, depending on the composition, porosity and crystallinity (3DSystems, 2011, Salmoria et al., 2009). Humidity also strongly impact the elastic behavior (Guérin), thus tests have been performed after a drying operation (1 hour to 40°C , then stored into a desiccator) in order to get a humidity as low as possible.

Figure 2.15 shows the prototype sample within the bending test device. The size of the sample is $210 \times 40 \times 12$ mm, that is 17.5 unit cells. In order to measure the flexural and

transverse-shear compliance components, the procedure detailed in section 1.5 is followed. It consists in four-point bending tests with different shear lengths, in the present : $L = 29$, 41 and 53 mm. Additional data have been measured for lower span length $l = 82$, 106 and 130 mm.

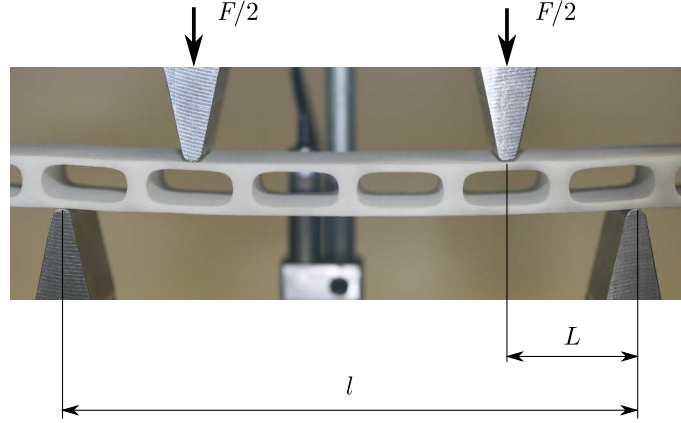


Figure 2.15: Prototype sample made from selective laser sintering (SLS) of polyamide 6 powder. The unit cell geometry is plotted on figure 2.14. Lower span length is denoted l and shear length L .

The four-point bending compliance is measured from the unloading slope of the force–deflection curve :

$$S_{4p} = \frac{\partial \delta}{\partial F} \quad (2.27)$$

where F [N/m] is the total applied force per unit width and δ [m] is the deflection (i.e. the vertical displacement of the upper loading points).

Figure 2.16 summarizes compliance data measured thanks to two loading–unloading sequences and five sets of test lengths (lower span length l and shear length L). Each point is measured on unloading slopes. The maximum applied force was chosen sufficiently low such that no damage is produced. It enables to perform several test on the same sample.

2.3.2 Full-field FEM simulations of tests

A simulation by finite element method (FEM) of the test is performed to complete the experimental data. The symmetry of the test enables to reduce the simulation domain to half. Stress-free conditions are imposed on all the edges, excepted one subjected to symmetry. The loading and support points are modeled respectively by traction force and displacement point constraints. The constitutive material (polyamide) is assumed to provide an isotropic elasticity with Young’s modulus $E = 2.0$ GPa and Poisson’s ratio $\nu = 0.33$. Figure 2.17 shows the resulting stress components σ_{13} (left) and σ_{11} (right) of this full field simulation.

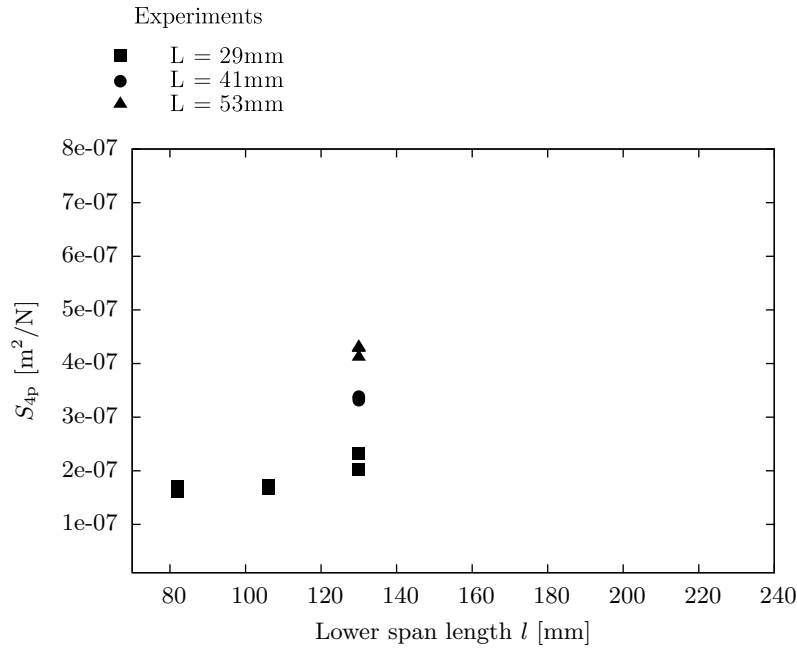


Figure 2.16: Four-point bending compliance S_{4p} of the sample from figure 2.15. Data were measured for three values of the span length l and three values of the shear length L .

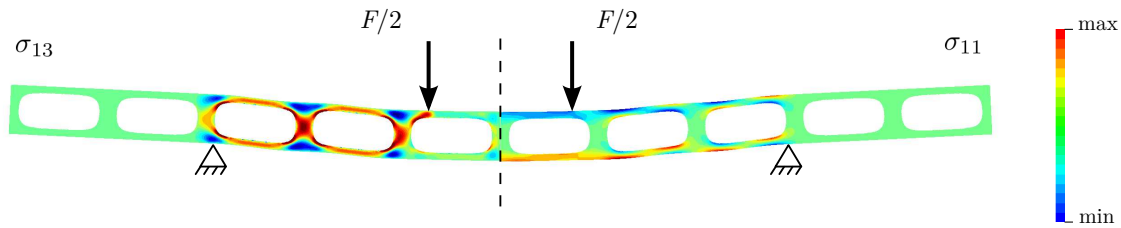


Figure 2.17: Full-field FEM simulation of a four-point bending test. The dash line show the symmetry axis. The plotted fields are the stress components σ_{13} (left) and σ_{11} (right). Test lengths are : $l = 140$ mm and $L = 53$ mm.

This linear elastic simulation is not a very time-consuming so that it can be repeated consecutively for several values of the span and shear lengths. The computed values of the four-point bending compliance are added to the experimental data on figure 2.18 and present a good agreement. Oscillations around a linear evolution is noted. They result from the local behavior around the loading and support points. And they depend on the exact position of these points with respect to the unit cell. The largest oscillations are obtained for a shear length that is multiple of the unit cell length.

This agreement confirms both the experimental measurement of the compliance on the unloading slopes, and the assumption of punctual loading and support pads.

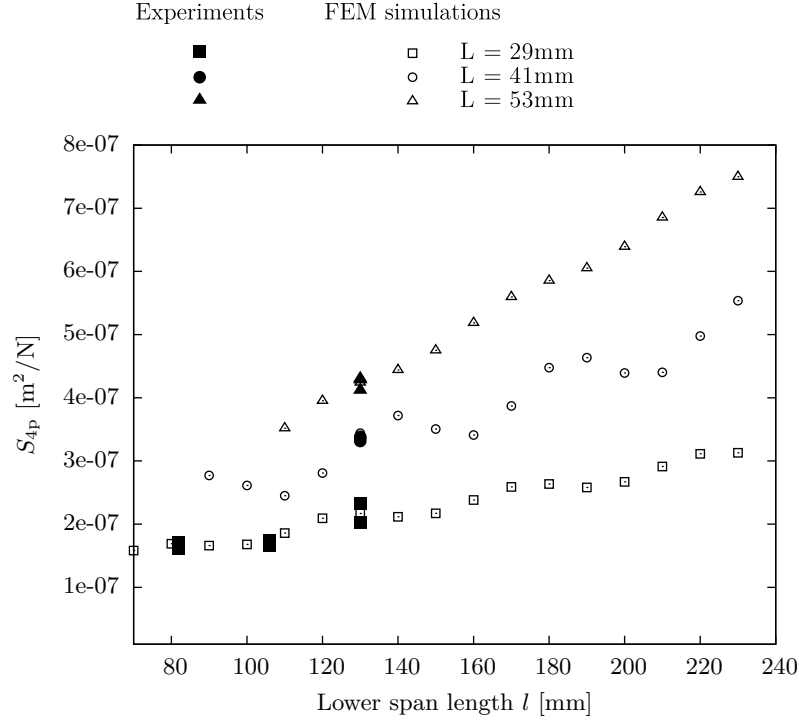


Figure 2.18: Comparison of the computed compliances (white) with the experimental data from figure 2.16 (black). A good agreement is observed between full-field simulations and experiments.

2.3.3 Effective approach

The present section describes the way to predict the measured and computed four-point bending behavior (figure 2.18), from an analytic expression based on beam analysis using macroscopic compliances computed on the unit cell. The predictive model is progressively enriched in order to evaluate the contribution of each aspect : with and without shear contribution ; with uniform or bending gradient boundary conditions.

Without transverse-shear contribution

Beam analysis provide analytical expression for the four-point bending compliance S_{4p} of an homogeneous beam (or plane-strain panel). They were recalled in section 1.5. Neglecting the transverse-shear contribution, one obtains the following estimation :

$$S_{4p} \approx \frac{1}{4}L^2d l - \frac{1}{3}L^3d \quad (2.28)$$

where d is the flexural compliance. The value of this compliance is computed by solving the homogenization problem (2.12) with $\bar{N} = 0$, $\bar{M}_{11} = 1$ and $\bar{M}_{12} = \bar{M}_{22} = 0$. The solution stress component σ_{11} of this problem is plotted on figure 2.19.

Comparison of effective analytical expression (2.28) with experimental data and full-

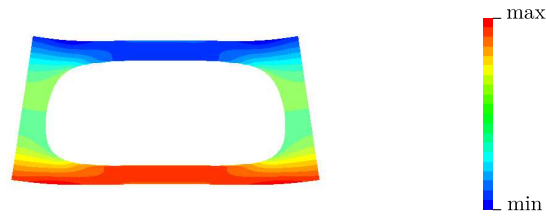


Figure 2.19: Stress component σ_{11} on the unit cell subjected to a pure bending moment \bar{M} .

field simulations is shown on figure 2.20. The slope seems well reproduced, but the absolute values of compliance are underestimated. Indeed, neglecting the shear contribution means assuming the shear stiffness to be infinite.

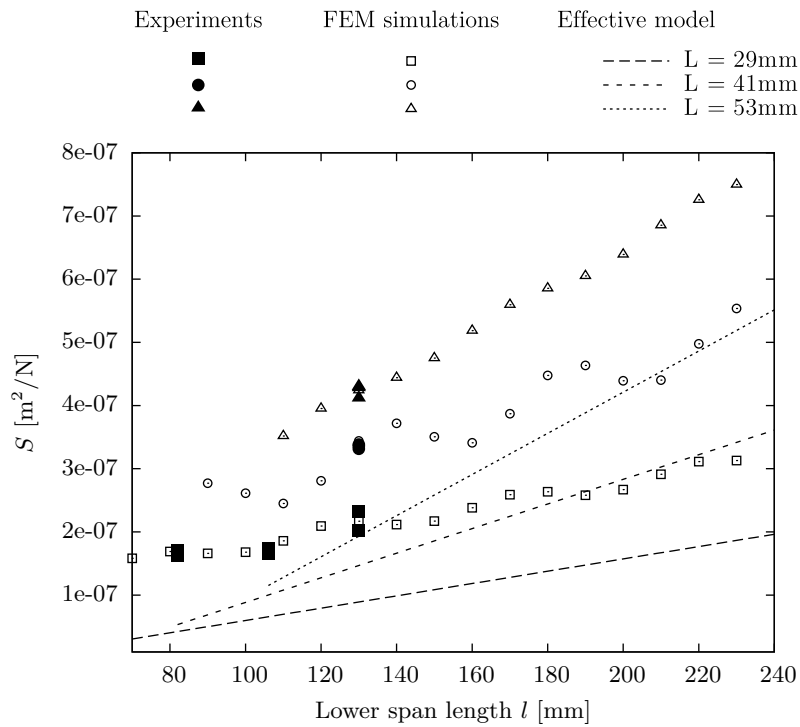


Figure 2.20: Comparison of the analytical estimation (2.28) with the simulation and experimental data of figure 2.18. The flexural compliance d is computed by solving the homogenization problem with pure bending.

With transverse-shear contribution

Previous results encourage to take into account the transverse-shear contribution within the analytical expression. Equation (1.31) could be rewritten as following in order to

exhibit the linear dependence on l :

$$S_{4p} = \frac{1}{4}L^2d \, l + \left(\frac{6}{10}Lf - \frac{1}{3}L^3d \right) \quad (2.29)$$

where f is the transverse-shear compliance. The slope of this expression only depends on the flexural compliance and is not going to change from previous section (Without transverse-shear contribution). However, the intercept is sensitive to both flexural and shear compliances.

The transverse-shear compliance can be computed using one of the two homogenization problems detailed in section 2.1.2 : with static uniform boundary conditions (SUBC) or with bending gradient body load (BG). The shear stress component σ_{13} is plotted in both cases on figure 2.21. Most of differences lies close to edges because of the different boundary conditions. Values are specified into table 2.1.

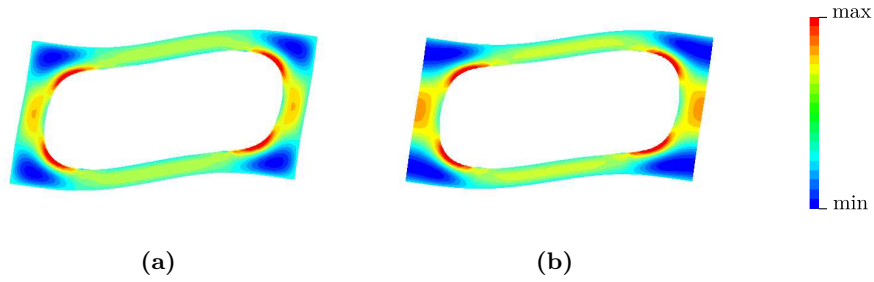


Figure 2.21: Stress component σ_{13} on the unit cell subjected to a shear force \bar{Q} applied through with : (a) uniform boundary conditions ; (b) an heterogeneous body load proportional to the pure bending stress field (figure 2.19).

One compares again on figure 2.22 experimental data and full-field FEM simulations with effective analytical expression (2.29) with the two shear compliance values of table 2.1. In both cases (SUBC and BG), taking into account the shear contribution makes the model to get closer to experiments and simulations. However, only the shear compliance computed with bending gradient body load is able to fit with. The compliances computed with uniform boundary condition remain too low.

Flexural [$10^{-5}/(\text{N}\cdot\text{m})$]	Transverse-shear [$10^{-8}\text{m}/\text{N}$]	
d	f (SUBC)	f (BG)
4.64	1.74	8.64

Table 2.1: Compliance components computed on the unit cell for bending and transverse-shear. The shear component is given for the two loadings : static uniform boundary conditions (SUBC) and bending gradient (BG).

The impact of the shear contribution and the loading of the homogenization problem

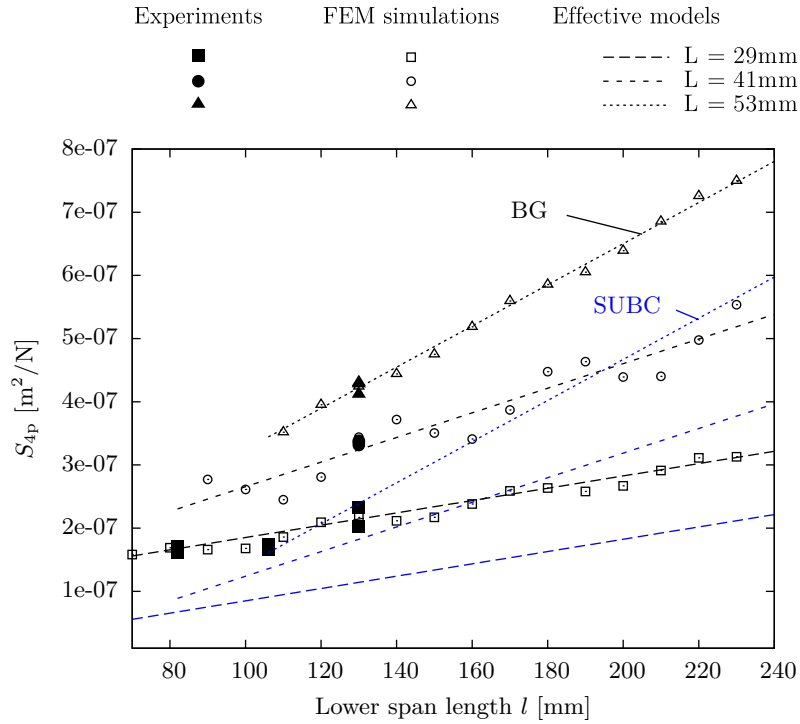


Figure 2.22: Comparison of the analytical estimation (2.29) with the simulation and experimental data of figure 2.18. The shear compliance f computed with : (blue lines) static uniform boundary conditions ; (black lines) gradient bending body load.

reveals to be relatively important in the case treated here. For instance, at $l = 130$ mm on figure 2.22, a ratio 2 is observed between the expression with bending gradient method and the others.

Recalling the discussion of Allen on the shear contribution (see section 1.3), it seems interesting to check the relevance of the flexural–shear ratio :

$$\frac{f}{l^2 d} = \frac{8.64 \cdot 10^{-8}}{0.15^2 \times 4.64 \cdot 10^{-5}} = 0.083 \quad (2.30)$$

This ratio, which is equivalent to expression (1.6), is between 0.01 and 0.1. This ensures the flexural and shear contributions are comparable which is indeed what the present calculation confirms.

2.3.4 Conclusion

The bending stiffness analysis of a strongly heterogeneous panel has been performed through experiments, test simulations, homogenization calculations and effective models. It leads to two main conclusions.

It was shown how to predict an effective behavior of such periodic architected plate

from analytical expression and homogenization simulation on unit cell. However, full-field simulations show oscillations of the four-point bending compliance depending on the exact location of the load and support points. The obtained effective behavior provides only a mean value and gives no information about the possible deviation from it.

One also concludes that the transverse-shear contribution has to be taken into account depending on the value of the ratio $f/(l^2d)$. Boundary conditions of the shear homogenization problem may have a significant impact on the results and have to be carefully chosen. This is still more relevant when the local stress distribution is an issue such as in shape optimization methods.

2.4 Homogenization of embossed steel sheets

As an other illustrative example of plate homogenization, the practical case of embossed steel is treated in the present section.

Ten years ago, 75% of the steel alloys involved in car did not exist. It shows how innovation is central in the development of new steel solutions to fulfill the challenges of the car makers and to face the competition of concurrent materials. One of the main objectives for material research consists in lightening structural parts in order to lower gas consumption and carbon dioxide emissions.

The sheet parts are mainly subjected to bending loading. Then lighten these parts consists in increasing the flexural stiffness at a minimum weight. Embossing steel sheets — such that exhibited on figure 2.23 — seems to be a way to increase the moment of inertia while keeping the mass unchanged. One could imagine replacing a flat sheet with a thinner embossed sheet that would have identical flexural stiffness.



Figure 2.23: Example of embossed steel sheet made by ArcelorMittal.

In the following, three types of embossed pattern are studied. Plate compliances are computed using the homogenization procedure presented in section 2.1. A parametric study is performed in order to select the most promising design.

2.4.1 Embossed patterns

The three periodic patterns proposed are denoted *am*, *hexa* and *vault* patterns. They consist in an embossed steel sheet defined by a mean surface $z = f(x_1, x_2)$. The pattern *am* models the experimental pattern obtained by ArcelorMittal (figure 2.23). The mean surface equation of this pattern is assumed to be :

$$f_H^{am}(x_1, x_2) = \frac{H}{4} \left(\cos \frac{2\pi x_1}{l_c} + \cos \frac{2\pi x_2}{l_c} \right) \quad (2.31)$$

where l_c is the edge size of the square unit cell, and H the amplitude of the embossing.

Because the square symmetry of this pattern leads to an anisotropic behavior, two alternative patterns are proposed exhibiting hexagonal symmetry. Pattern *hexa* is obtained from the surface expression :

$$f_H^{\text{hexa}}(x_1, x_2) = H \left(\frac{8}{9} \cos \frac{2\pi x_1}{\sqrt{3}l_c} \cos \frac{2\pi x_2'}{\sqrt{3}l_c} \cos \frac{2\pi x_2''}{\sqrt{3}l_c} - \frac{7}{18} \right) \quad (2.32)$$

where :

$$\begin{cases} x_2' = \frac{1}{2} (x_1 + \sqrt{3}x_2) \\ x_2'' = \frac{1}{2} (-x_1 + \sqrt{3}x_2) \end{cases} \quad (2.33)$$

And pattern *vault* — similar to that mentioned in the literature (Mirtsch et al., 2006, Bouaziz et al., 2008) — results from :

$$f_H^{\text{vault}}(x_1, x_2) = H \left(\frac{1}{2} \left(\left| \cos \frac{2\pi x_1}{\sqrt{3}l_c} \right| + \left| \cos \frac{2\pi x_2'}{\sqrt{3}l_c} \right| + \left| \cos \frac{2\pi x_2''}{\sqrt{3}l_c} \right| \right) - 1 \right) \quad (2.34)$$

For these hexagonal patterns, the projection of the unit cell on the plane (e_1, e_2) is rectangular with size $\sqrt{3}l_c \times l_c$. The thickness of the steel sheet is $t = 0.5$ mm for all patterns.

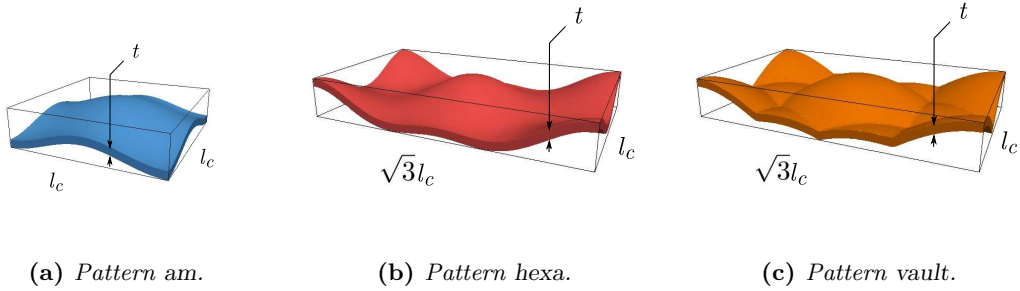
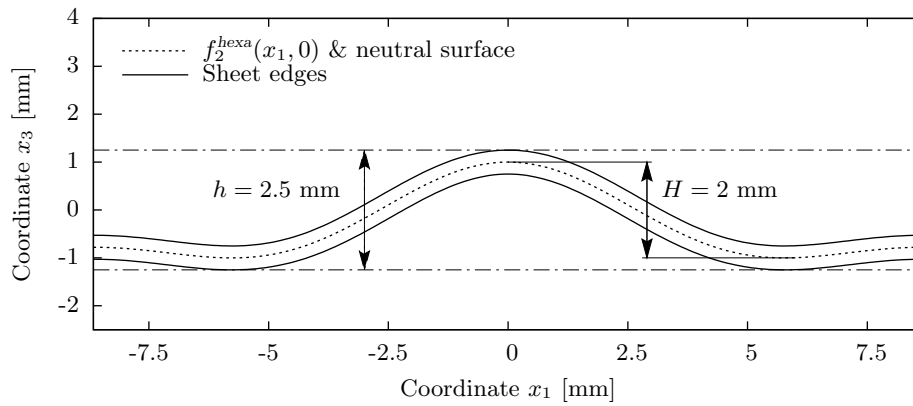


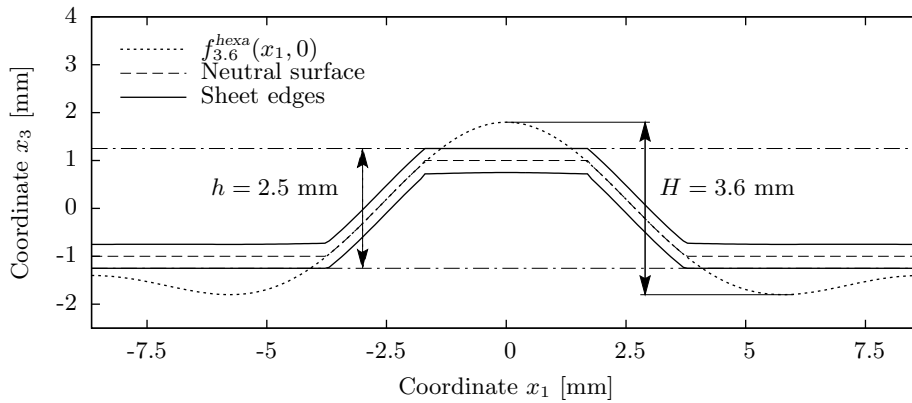
Figure 2.24: Unit cell of the three patterns of embossed sheet with : (a) square symmetry and square cell size ; (b,c) hexagonal symmetry and rectangular cell size. The amplitude is $H = 2$ mm.

As illustrated on figure 2.25, it is proposed to introduce “cropped patterns” defined by a maximal embossing thickness h . They have the advantage to flatten the top-and-bottom extremities², and one could also expect a larger flexural stiffness with an unchanged occupied volume. Then each pattern provides a non-cropped version when $H \leq h + t$, and a cropped version when $H > h + t$. Figure 2.25 shows non-cropped and cropped pattern *hexa* for sheet thickness $t = 0.5$ mm, embossing thickness $h = 2.5$ mm, and embossing amplitudes respectively $H = 2$ mm and $H = 3.6$ mm.

²Flattening extremities could enable joining with external plates for instance.



(a) *Cropped pattern ($H = 2$ mm).*



(b) *Non-cropped pattern ($H = 3.6$ mm).*

Figure 2.25: Section in plane $x_2 = 0$ of the embossed pattern hexa for : (a) $H = 2$ mm ; (b) $H = 3.6$ mm.

2.4.2 Adaptive mesh

Similarly to the bi-dimensional case, the whole unit cell V is meshed and the geometry is defined implicitly through a level-set function. But in three-dimensions, the issue of computing time is a limit and an adaptive mesh is required in order to catch properly the geometry with an affordable computational cost. Adaptive mesh consists in an iterative operation that starts from a rough tetrahedral mesh and progressively refines it by dividing elements close to the interface.

Figure 2.26 exhibits an adaptive mesh used for the simulations on pattern *hexa* with $H = 3.6$ mm. All the following simulations have been performed with meshes that provide at least two elements in the sheet thickness.

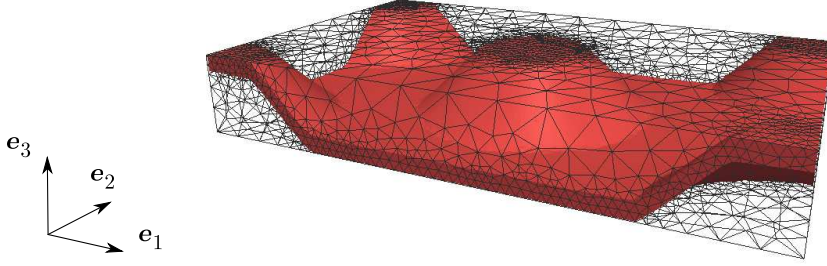


Figure 2.26: Adaptive mesh with 140408 elements of the unit cell with pattern hexa ($H = 3.6$ mm).

2.4.3 Membrane and flexural compliances

Since the slenderness of the embossed plates seems sufficiently large, performances of each pattern are discussed only considering the Love-Kirchhoff compliances. It will be confirmed afterward by computation of the transverse-shear compliances, that the shear contribution is indeed negligible.

A reference sizing is first chosen for identifying compliance components and comparing patterns. Then, a parametric study enables to select and size the most promising design. The values of compliance are systematically compared to the non-embossed or *flat* steel sheet with same thickness t .

Simulations have been performed with the FEM software *Comsol Multiphysics 4.0a*. Adaptive mesh is used as mentioned above. The constitutive material is assumed to be a representative steel with isotropic elastic properties : Young's modulus $E = 200$ GPa and Poisson's ratio $\nu = 0.33$. Since we are concerned only with elastic stiffness, it is not necessary to define more precisely the specific steel considered.

Reference sizing : $h = 2.5$ mm, $H = 2$ mm and $t = 0.5$ mm

The homogenization problem (2.12) is solved applying consecutively each Love-Kirchhoff membrane force and bending moment. The deformed unit cells with displacement magnitude contours are presented for pattern *am* subjected to membrane forces on figure 2.27, and to bending moments on figure 2.28.

The compliance values of the flat sheet and the embossed sheets are gathered in table 2.2 (note that the Kelvin notations are used, see appendix A). All patterns provide no coupling terms $\mathbf{a}_{61} = \mathbf{a}_{26} = 0$ and the same behavior in directions e_1 and e_2 . This is the case for both membrane and bending components. This is due to the isotropy of the flat sheet, the rotational invariance of 90° around e_3 for pattern *am*, and the hexagonal symmetry of patterns *hexa* and *vault*.

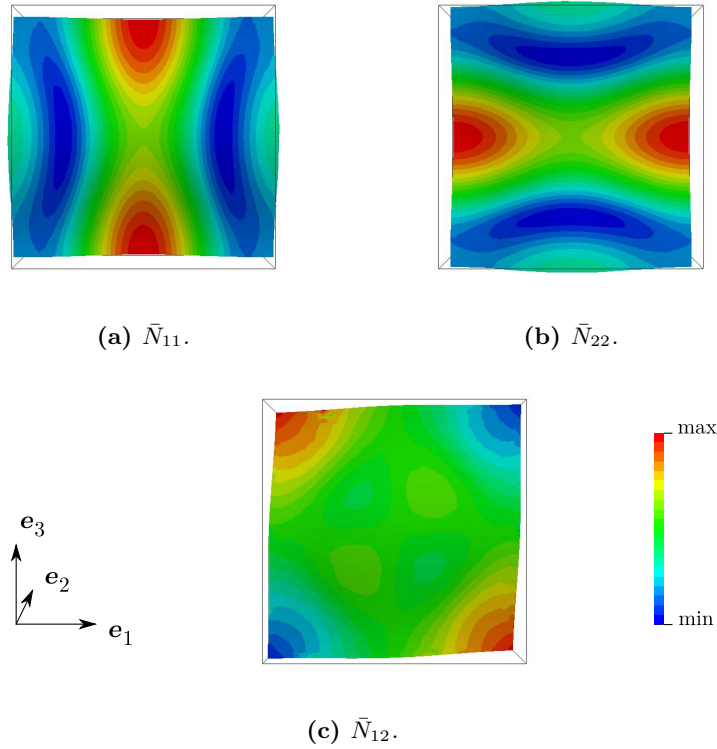


Figure 2.27: Displacement magnitude plotted on the wrapped unit cell for pattern *am* subjected to each membrane force : \bar{N}_{11} , \bar{N}_{22} and \bar{N}_{12} .

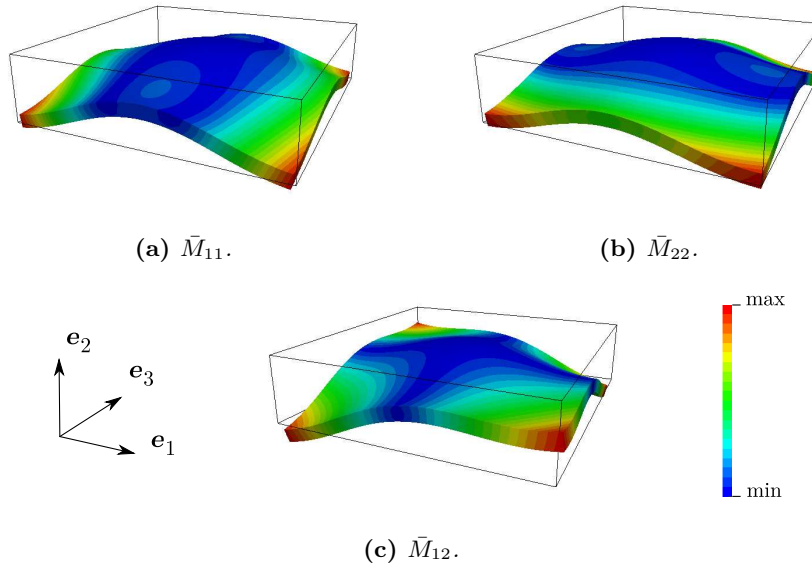


Figure 2.28: Displacement magnitude plotted on the wrapped unit cell for pattern *am* subjected to each bending moment : \bar{M}_{11} , \bar{M}_{22} and \bar{M}_{12} .

Pattern	Membrane [10^{-8}m/N]			Flexural [$10^{-1}/(\text{N}\cdot\text{m})$]			Averaged thickness [mm]
	$a_{11} = a_{22}$	a_{66}	a_{12}	$d_{11} = d_{22}$	d_{66}	d_{12}	
<i>flat</i>	1.00	1.33	-0.33	4.80	6.38	-1.58	0.500
<i>am</i>	4.38	1.46	-2.16	1.19	6.41	0.413	0.503
<i>hexa</i>	3.68	3.76	-0.08	1.76	1.95	-0.190	0.538
<i>vault</i>	3.95	3.50	0.45	1.89	1.96	-0.073	0.513

Table 2.2: Love-Kirchhoff compliance components computed on the unit cell for each pattern (Kelvin notations).

Presenting stiffness components are usually easier to assess and compare than compliance components. Written in engineering notations, the membrane compliance becomes :

$$[\mathbf{a}] = \frac{1}{t} \begin{bmatrix} 1/E_1^a & -\nu_{21}^a/E_2^a & 0 \\ -\nu_{12}^a/E_1^a & 1/E_2^a & 0 \\ 0 & 0 & 1/(2G_{12}^a) \end{bmatrix} \quad (2.35)$$

with the in-plane Young's moduli E_1^a and E_2^a , the membrane shear modulus G_{12}^a and the membrane Poisson's ratios ν_{12}^a and ν_{21}^a . And the flexural compliance becomes :

$$[\mathbf{d}] = \frac{12}{t^3} \begin{bmatrix} 1/E_1^d & -\nu_{21}^d/E_2^d & 0 \\ -\nu_{12}^d/E_1^d & 1/E_2^d & 0 \\ 0 & 0 & 1/(2G_{12}^d) \end{bmatrix} \quad (2.36)$$

with the flexural Young's moduli E_1^d and E_2^d , the flexural shear modulus G_{12}^d and the flexural Poisson's ratios ν_{12}^d and ν_{21}^d .

Table 2.3 summarized the effective plate stiffness of each pattern, according to the previous engineer notations.

Pattern	Membrane behavior			Flexural behavior			Mass per unit area [kg/m ²]
	Moduli [GPa]		Poisson's ratio, $\nu_{12}^a = \nu_{21}^a$	Moduli [GPa]		Poisson's ratio, $\nu_{12}^d = \nu_{21}^d$	
	$E_1^a = E_2^a$	G_{12}^a		$E_1^d = E_2^d$	G_{12}^d		
<i>flat</i>	200	75.2	0.330	200	75.2	0.330	3.93
<i>am</i>	45.7	68.5	0.493	806	74.9	-0.347	3.95
<i>hexa</i>	54.3	26.6	0.022	545	246	0.108	4.22
<i>vault</i>	50.6	28.6	-0.114	508	245	0.039	4.02

Table 2.3: Effective plate stiffness computed on the unit cell for each pattern (engineer notations).

For the three patterns and in comparison with the flat sheet, embossing leads to an increase of the flexural moduli but a decrease of the membrane moduli (up to -75% for the Young's modulus of am). For instance on the pattern am , the flexural Young's modulus is multiplied by 4, but the in-plane Young's modulus is divided by 4.4. For patterns $hexa$ and $vault$, the deviations from the flat sheet are weaker but show a similar tendency.

Even if such tables of compliance or stiffness values contain the whole elastic behavior, the intensity of anisotropy is not directly obvious. It becomes clear when plotting the moduli E_1^a , G_{12}^a , E_1^d and G_{12}^d with respect to angle θ around the normal axis e_3 (figure 2.29). Relations about rotation of tensors are recalled in appendix A.

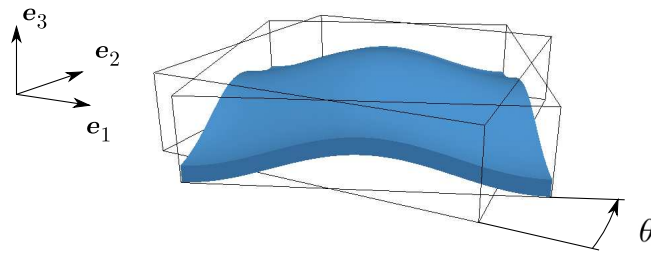
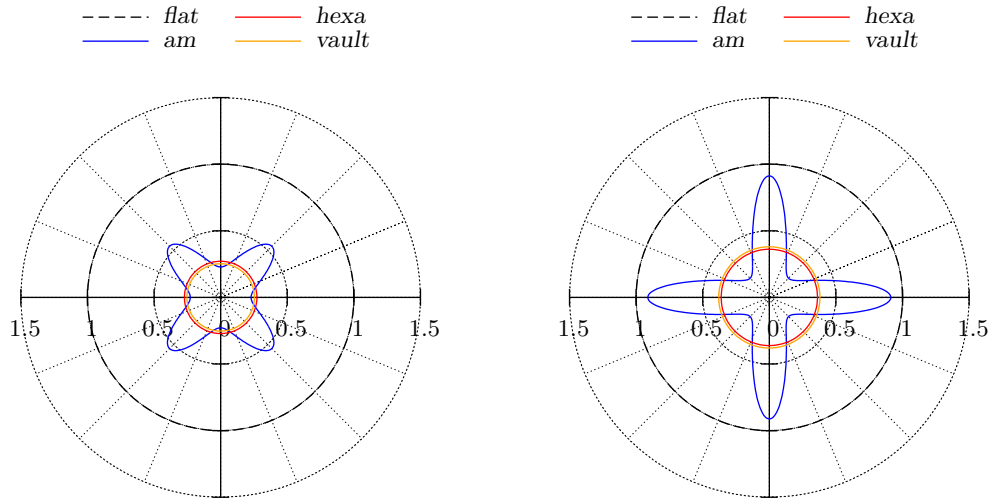


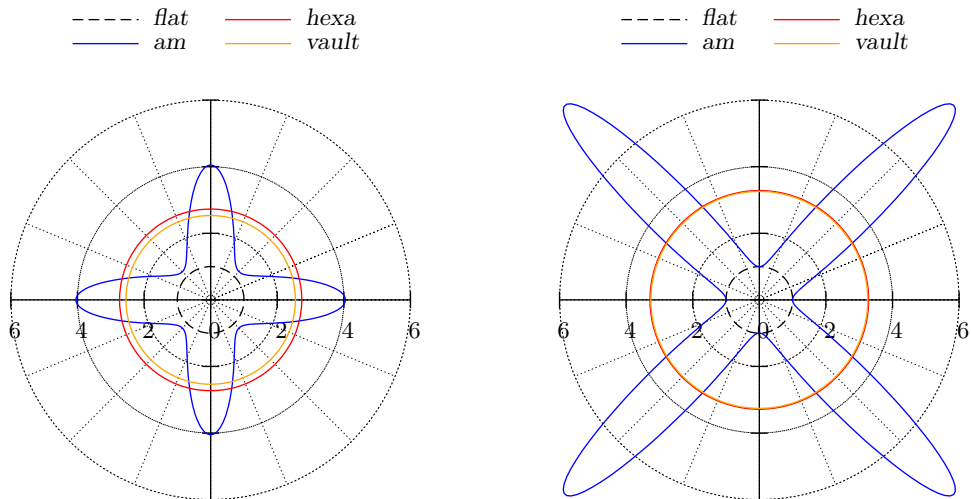
Figure 2.29: Sketch of the rotation of the unit cell around axis e_3 .

Figures 2.30 and 2.31 plot the variations of the moduli with respect to the angle θ . They are respectively normalized by the Young's modulus E and the shear modulus G of the constitutive steel. The high anisotropy of pattern am , especially on flexural moduli, is directly quantified. For instance, this pattern reveals to be two times stiffer when subjected to a in-plane force at 45° than along the axis e_1 or e_2 . And the flexural Young's modulus is about four times weaker at 45° than along the frame axis.



(a) Normalized in-plane Young's modulus E_1^a/E (b) Normalized in-plane shear modulus G_{12}^a/G

Figure 2.30: Variations of the in-plane moduli with respect to the angle θ for all patterns.



(a) Normalized flexural Young's modulus E_1^d/E (b) Normalized flexural shear modulus G_{12}^d/G

Figure 2.31: Variations of the flexural moduli with respect to the angle θ for all patterns.

Parametric study on the amplitude H

Coming back to the initial objective, the embossed steel solution would be promising if it could provide the same flexural stiffness to a thinner sheet than that of the currently used flat sheets. For instance, reducing the thickness of the steel sheet from 0.7 to 0.5 mm would save around 1.5 kg/m^2 . Could embossing stiffen a 0.5-thick steel sheet sufficiently to reach the flexural stiffness of a 0.7-thick sheet? This question is illustrated on the compliances chart on figure 2.32.

it seems interesting to explore the embossed designs by varying one of the characteristic design variable. The amplitude H typically enables to explore continuously the design from the flat sheet to the cropped embossed sheet.

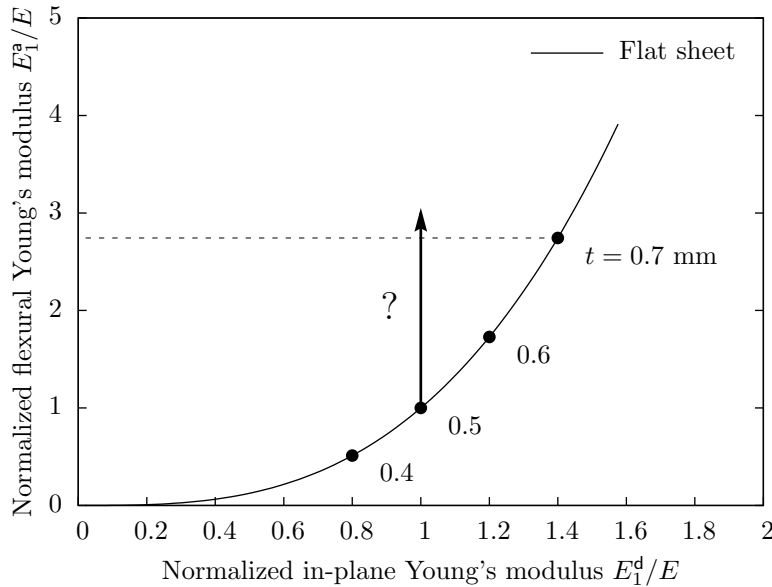


Figure 2.32: Flexural versus in-plane Young's modulus. Could embossing drag a 0.5mm-thick steel sheet up to the flexural stiffness of a 0.7mm-thick steel sheet? And then save about 1.5 kg/m^2 when shifting the thickness from 0.7 to 0.5 mm.

In order to explore some of the embossed solutions, a parametric study is proposed on the embossing amplitude H . Figure 2.33 exhibits the unit cell for each pattern *am*, *hexa* and *vault*, when scanning the design variable H from 0 to 3.6 mm. The maximal embossing thickness is chosen to $h = 2.5 \text{ mm}$, such that the embossing amplitude $H = 2 \text{ mm}$ is the limit between non-cropped and cropped versions.

Figure 2.34 shows the variations in flexural and in-plane Young's moduli when changing the embossing amplitude H . For $H = 0 \text{ mm}$, one (fortunately) finds the modulus of the flat sheet with $t = 0.5 \text{ mm}$. Concerning the flexural modulus, raising H increases the stiffness up to a maximum for $H = 2.4 \text{ mm}$ and slightly decreases it afterward. These two ranges almost coincide with the two types of geometries, non-cropped and cropped, which

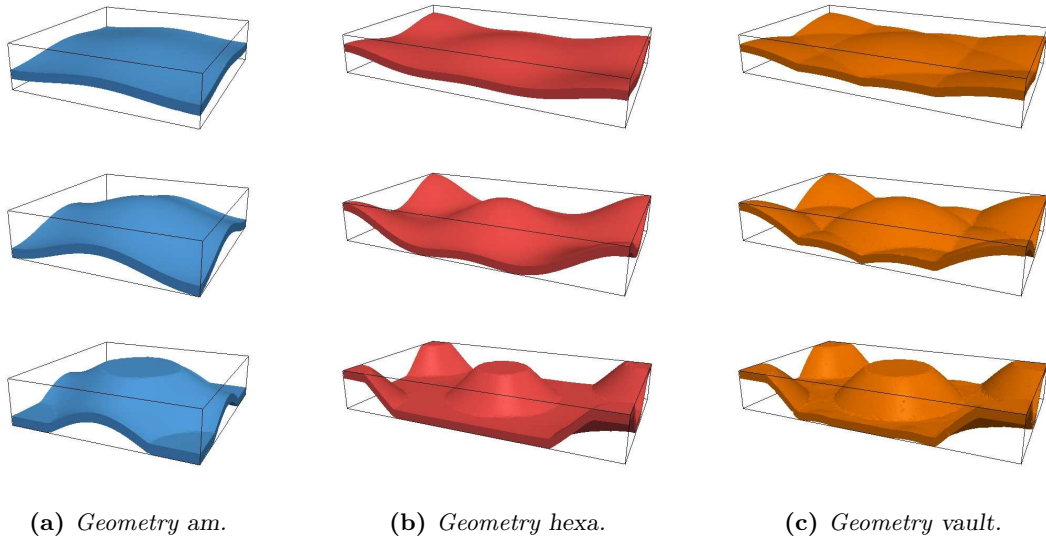


Figure 2.33: Periodic unit cell of each pattern with scanning the embossing amplitude H . From top to bottom : non-cropped patterns ($H = 0.8$ and 2 mm) and a cropped pattern ($H = 3.6$ mm).

limit is $H = 2$ mm. Concerning the in-plane modulus, one observes a monotonic decrease which also stabilizes for cropped patterns.

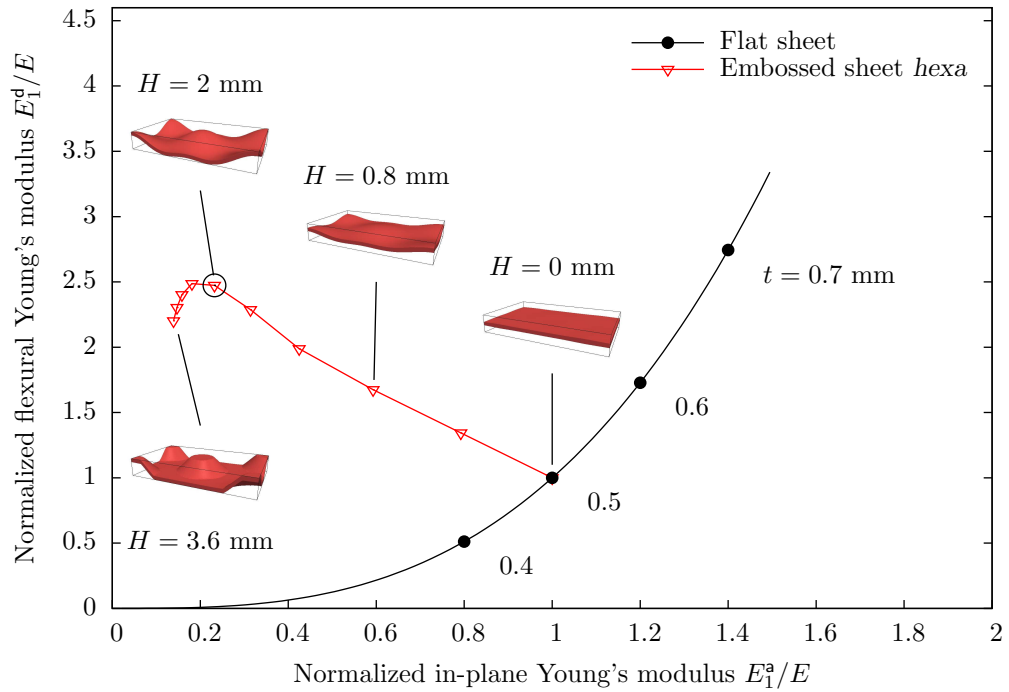


Figure 2.34: Variations of the flexural and in-plane moduli when changing the embossing amplitude H . Two ranges of values appear : from the flat sheet ($H = 0$ mm) to the thicker non-cropped pattern ($H = 2$ mm), followed by the cropped patterns ($H > 2$ mm).

The same stiffness chart is completed on figure 2.35 with the additional patterns *am* and *vault*. Variations of the moduli of each pattern are compared together when changing the embossing amplitude H . For pattern *am*, two sets of values are presented : for $\theta = 0^\circ$ and for $\theta = 45^\circ$. Even if a good compromise between bending and shear is obtained at 0° , it has to be contrasted with the poor results at 45° . One could notice the maximum in flexural stiffness do not coincide necessarily with the thickest non-cropped pattern ($H = 2$ mm), especially for pattern *am*.

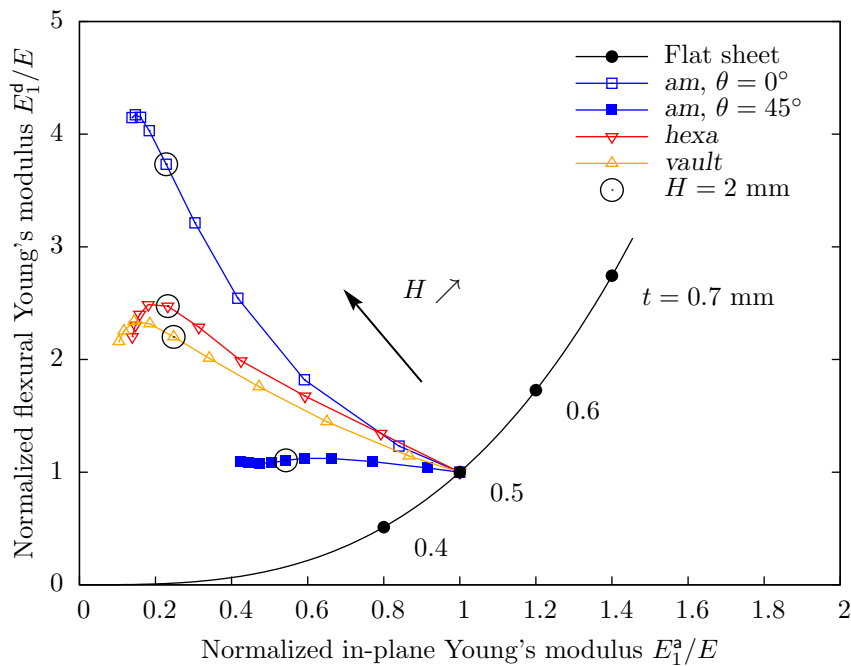


Figure 2.35: Reporting patterns *am*, *hexa* and *vault* on the flexural versus in-plane stiffness chart. Scanning the design variable H (from 0 to 3.6 mm) enables to shift the flat 0.5mm-thick sheet to the upper-left direction.

The salient result from this study is that pattern *hexa* provides the highest flexural stiffness (if we forget pattern *am* because of its high anisotropy). However, the challenge that was to reach a flexural modulus equivalent to that of the 0.7mm-thick flat sheet is not completed. The constitutive sheet thickness must be taken thicker than 0.5 mm.

In order to avoid additional time-consuming computations, one can scale the pattern size in the direction e_3 . Figure 2.36 proposes several scaling to shift the constitutive sheet thickness from 0.5 mm to respectively 0.55, 0.6 and 0.65 mm.

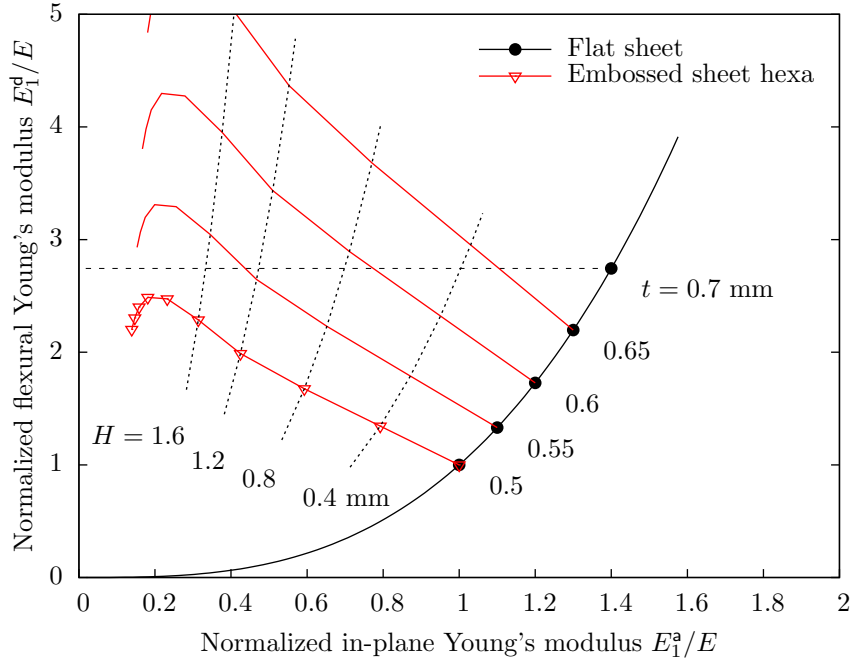


Figure 2.36: Abacus that enables to read the appropriate sizing (sheet thickness t and embossing amplitude H) with respect to the required flexural and in-plane Young's moduli. The resulting weight saving is given by the sheet thickness.

The objective flexural stiffness is obtained for any design having a sheet thickness $t > 0.52$ mm. The most interesting sizing is not necessary that with the smaller thickness since weight saving have to be contrasted with a substantial decrease of the in-plane Young's modulus. Even if the parts that would include such embossed sheets are mainly subjected to bending, a too weak in-plane modulus could have non-negligible adverse impacts. Figure 2.36 can be read as an abacus in order to choose a sizing (sheet thickness and embossing amplitude) from prescribed flexural and in-plane Young's modulus. The saved weight is deduced from the thickness reduction of the constitutive sheet.

2.4.4 Transverse-shear compliance

The shear compliance components of Reissner-Mindlin model are obtained from homogenization (2.20) with bending gradient body load. Results are gathered into table 2.4. One could notice that the scalar dimension of transverse-shear leads to an isotropic behavior for all patterns, even for the square-symmetric pattern am .

Even if the deviation in shear compliance of the embossed sheets from the flat sheet is large, one should first calculate the following ratio to estimate the impact of the shear contribution to further global stiffness :

$$\frac{f}{l^2 d} < 10^{-6} \quad (2.37)$$

Pattern	Transverse-shear [10^{-9}m/N]	
	$f_{11} = f_{22}$	f_{12}
<i>flat</i>	31.9	0
<i>am</i>	1.04	0
<i>hexa</i>	0.455	0
<i>vault</i>	0.456	0

Table 2.4: Transverse-shear compliances computed on the unit cell by solving the homogenization problem with bending gradient body load (see section 2.1.2).

for all patterns and whatever is the in-plane direction. Since this ratio is much lower than 0.01, the transverse-shear contribution is negligible and embossing does not imply significant change in global stiffness due to the shear contribution.

2.4.5 Global stiffness

One of the key issues for the implementation of architected solutions into a component is to avoid a refined meshing of the architecture and to consider an effective material. We will illustrate here this strategy.

An illustrative integration of an embossed plate into a fictitious component is proposed. Abaqus FEM simulations of a rectangular plate (80×40 mm) have been performed using the compliance components of the previous patterns into an effective homogeneous plate. Figure 2.37a exhibits the geometry and the applied homogeneous vertical force per unit area. Clamped boundary conditions are imposed on all the surrounded edges. Elements S4 are used and general shell stiffness matrix is specified with the values of table 2.3.

The resulting fields of bending moments M_{12} , M_{11} and M_{22} are shown respectively on figure 2.37b, 2.38a and 2.38b, for a flat steel sheet of thickness 0.5 mm.

The global stiffness of the plate is computed as the ratio of the applied force per unit area over the deflection at the center point. The values are plotted on figure 2.39 for all patterns and two orientations of the pattern *am* (0° and 45°).

Assuming that this rectangular plate was only subjected to bending, the expected global stiffness with pattern *hexa* should be equal to the global stiffness of the flat sheet times the normalized flexural modulus E_1^d/E , i.e. 1387 N/m. The FEM simulation gives 1254 N/m and it can be explained by the contribution of the membrane stiffness which is particularly low for the embossed sheet³. A similar shift is observed on pattern *vault*. As a conclusion, in the case of isotropic behavior, ranking and selecting with respect to the flexural modulus is probably still valid with respect to the global stiffness.

³Simulations confirmed the transverse-shear contribution is negligible for any design, as predicted in section 2.4.4.

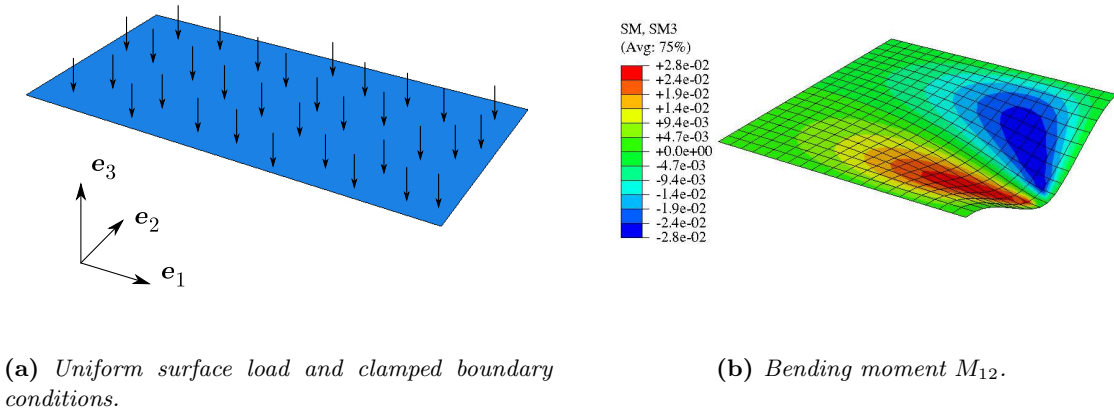


Figure 2.37: Abaqus FEM simulation on a rectangular plate. (a) Geometry and loading. (b) Resulting field of bending moment M_{12} for a flat steel sheet of thickness 0.5 mm.

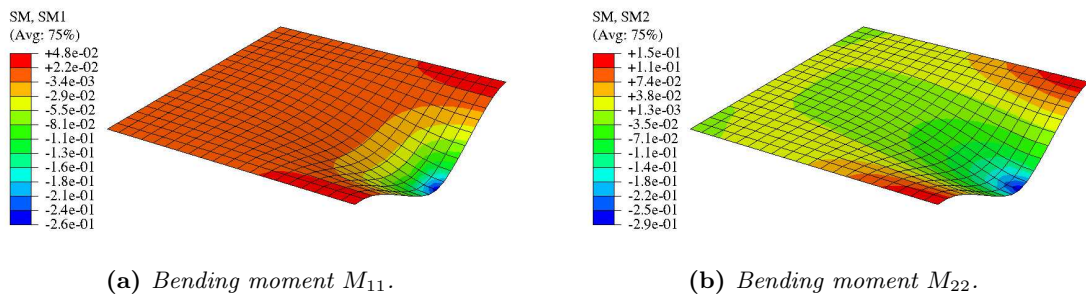


Figure 2.38: Abaqus FEM simulation on a rectangular plate. Resulting fields of bending moments M_{11} and M_{22} for a flat steel sheet of thickness 0.5 mm.

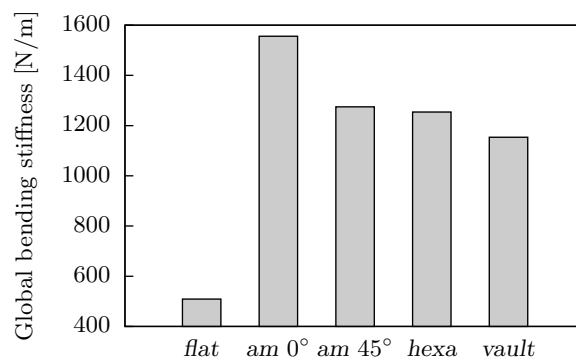


Figure 2.39: Global bending stiffness of the rectangular plate, figure 2.37a, subjected to a uniform force per unit area for each pattern. Two orientations are presented for pattern am (0° and 45°).

The case of anisotropic pattern seems more difficult. The decision to dismiss the pattern am because of the large anisotropy of its behavior might not be justified. Figure 2.39

reveals that this pattern, in both 0° and 45° directions, provides a larger global stiffness than the others. Not any feature on the comparison of moduli on figure 2.35 could help to predict such results. However, anisotropy might be a problem to avoid for other reasons than elasticity.

Thinking about more complex parts, the contributions of the other moduli (in-plane tension, in-plane shear or twisting) could be less negligible, even for isotropic behavior. In this case, that would be interesting to write a performance index that takes into account the contribution of each of these moduli. It sounds like a way to design architected materials, such as embossed plates, with respect to this performance index and to compare with other monolithic materials.

Conclusion

Methods of periodic homogenization of panels have been presented in this chapter from the effective properties definition toward an application of architected panel design.

In comparison with bulk periodic media, the case of panels adds to homogenization the concept of “integration” in the out-of-plane direction with identifying effective properties of a bi-dimensional model from a three-dimensional unit cell. In the case of transverse-shear behavior, the non-periodicity in the out-of-plane direction excludes homogenization problem with classical boundary conditions. It requires results on bending gradient theory in order to have a homogenization problem that keeps satisfied the stress-free boundary conditions.

The implementation of the homogenization problems have been described in the case of an implicit definition of the geometry using the level-set method. The influence of the artificial parameters introduced by the method is studied. Values have been chosen for the homogenization computations of this chapter and the next optimization chapters.

A validation of the homogenization procedure have been proposed in section 2.3. An illustrative architected panel has been produced by additive manufacturing and tested. Experimental data in addition with FEM simulations of the test enable to validate the homogenization problems and their implementation. The importance of the shear contribution, as well as the type of loading into the shear homogenization problem, have been also evaluated thanks to this comparison.

Finally, the implemented homogenization procedure has been used to evaluate the stiffness performance of embossed steel in an automotive applicative context. Analysis of few proposed embossing patterns enables to select the most promising and to determine the appropriated design variables thanks to a parametric study.

The latter example shows that such parametric study is necessarily reduced to few parametric geometries usually built from intuition. It highlights the interest of adding a preliminary shape optimization stage which could provide optimized geometries before a more complete parametric study.

Highlights

- An efficient **homogenization procedure** exists in order to identify the Love-Kirchhoff compliance components, by computing the unit cell response to each macroscopic loading.
- The **transverse-shear contribution** in the global bending compliance of a panel is well predicted by the Allen ratio $f/(l^2d)$. The shear compliance can be roughly estimated on a homogenization problem with uniform boundary conditions, but a more precise estimation is given with a bending gradient body load. The latter provides an aesthetic way to apply a balanced mean shear force while keeping satisfied the stress-free boundary conditions on the top-and-bottom boundary conditions. It will be useful for optimization.
- The **level-set method** enables to defined implicitly any distribution of matter into the unit cell on a given mesh. It is done by meshing the whole unit cell and by mimicking holes with an ersatz material.
- **Embossed steel** is a solution to improve the moment of inertia following the “material by design” approach in an automotive applicative context. Periodic homogenization methods are used to identify Love-Kirchhoff moduli, to compare three different patterns and to propose rules for choosing the design parameters.

CHAPTER 3

Shape optimization

Introduction

In the previous chapters, it has been argued with examples that architecturing materials is a way to improve the performance of multi-functional materials. Engineering approaches by trial and error, or by parametric study, enable to compute the properties of such material and their dependence to the design. However, all architectures cannot be explored and high-performance designs, especially for multi-functional specifications, may not be intuitive. Thus the use of optimization methods seems relevant in order to highlight promising architectures.

Optimization consists in searching for the minimum (or maximum) of an objective function (or a combination of objective functions in the case of multi-functional optimization) with respect to variables. In design optimization, objective function often depends on these variables through partial differential equations which may imply an extensive numerical resolution (for instance a finite element simulation of mechanical equations). Usually, constraints on the optimization variables are added such that they reduce the admissible space in which the variables are searched for. They can be either explicit such as bounds on the variables (or a limited domain of design), or implicit such as volume (or area) constraint.

Literature is extensive on optimization techniques applied to the design of structures, products or materials. One could classify these methods into three families illustrated on figure 3.1 : parametric optimization, functional optimization and shape optimization (with and without ability to change topology). This classification is based on the nature of the optimization variables, respectively scalars, functions or domains.

Parametric optimization Also named engineering design optimization (EDO), parametric optimization consists in describing the design with parameters (continuous or discrete) and finding the set of these parameters that provide the highest performance while satisfying constraints. Depending on the problem, a suitable algorithm can be found among a large diversity of optimization methods (Kicinger et al., 2005, Roy et al., 2008, Awad et al., 2011). Two main groups exist depending on the choice of either a deterministic approach (gradient method, interpolation method, etc.) or a heuristic approach (evolutionary, genetic, particle swarm, simulated annealing, etc.). On one hand, deterministic algorithms are more suitable for expensive objective function evaluation (finite element computation, for instance) and enhanced methods of sensitivity analysis (Barthold and Stein, 1996, Vankeulen et al., 2005) enable to efficiently evaluate the derivative with respect to the design variables. Main disadvantages are the sensitivity to the initial value since only local optima are found, and difficulties to manage discrete variables. On the other hand, heuristic methods enable to find global optimum for both continuous and

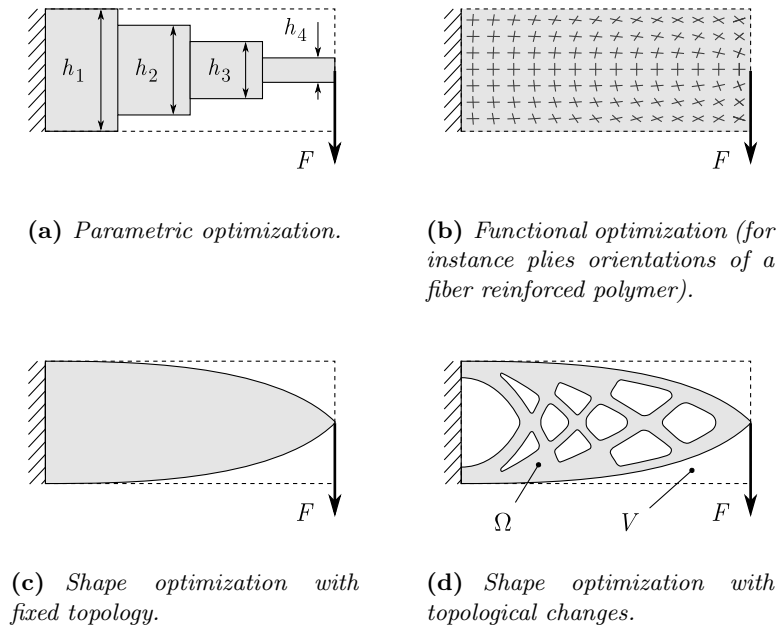


Figure 3.1: Illustration of the different families of design optimization : parametric, functional and shape optimization with and without topological change. Figure (d) specifies the optimization domain Ω and the design domain V .

discrete variables, but usually need a large number of function evaluation.

Functional optimization It consists in optimizing an objective function with respect to a design functional. In few cases (linear elasticity, eigenvalue problem, etc.), analytical expressions exist for the objective function derivative and iterative optimization can be done using local information. For instance, it was applied to optimize orthotropic material orientation (Bendsøe et al., 1996), plies orientation in laminated composites (Jibawy et al., 2011), or microstructure orientation in lamellar metal–ceramic composites (Piat et al., 2011). But in most of the cases, the design functional is discretized and then parametric optimization is performed using for instance sensitivity analysis (Lund, 2009).

Shape optimization In this case, the objective function is optimized with respect to a domain Ω (filled with matter) included into an admissible domain of design V (see figure 3.1d). The iterative evolution of the domain is based on analytical shape derivative of the objective function, which is the sensitivity to boundary variations. First results on shape derivative were obtained for the compliance, so that literature on shape optimization initially proposed methods to maximize structures stiffness.

Whereas the term “shape optimization” is sometimes restricted to methods with fixed

topology, we use here the global term that also includes methods that enable partial or full topological changes. We synthesize below the main techniques, but an extended bibliography can be found in Hassani (1998a,b,c), Eschenauer and Olhoff (2001), Mackerle (2003).

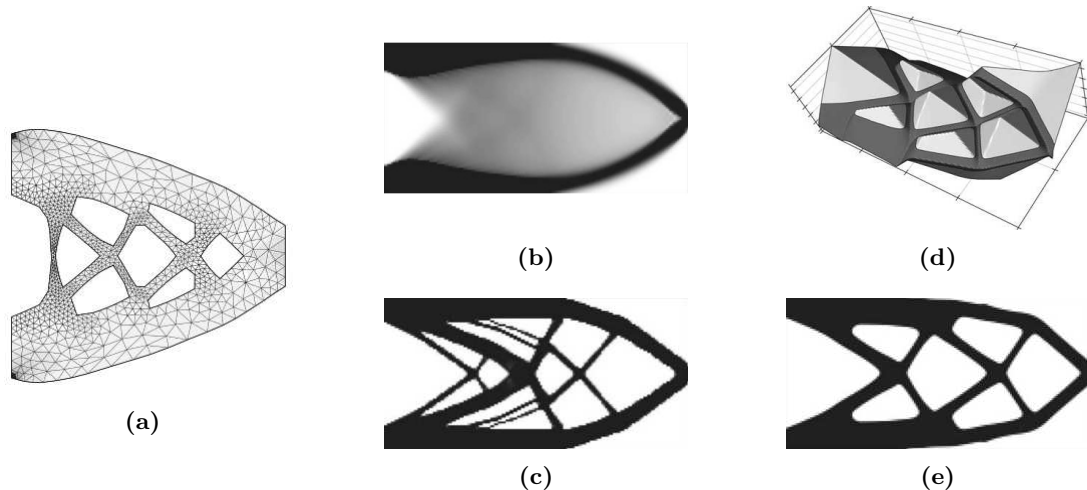


Figure 3.2: *Illustration of some shape optimization method applied on the minimum compliance cantilever : (a) geometrical optimization with moving mesh ; (b-c) homogenization method respectively before and after penalization ; (d-e) level-set function and corresponding optimized shape. (www.cmap.polytechnique.fr/~optopo/ and Allaire et al. 2004)*

Geometrical optimization consists in meshing the domain Ω and deforming it at each optimization step (Sokolowski and Zolésio, 1992, Allaire and Pantz, 2006, Liu and Korvink, 2007). It regularly requires time-expensive remeshing when the mesh distortions become too large. Moreover, no topological change is available (figure 3.2a).

Material approaches are based on a full mesh of the design domain V , on which is defined a fictitious density field. The objective function is evaluated by solving the physical equations with material properties that depend on the fictitious density according to an interpolation scheme — which specifies how stiffness varies from that of the constitutive material when the density value is 1, to zero when the density is 0. This material interpolation scheme may be a power law such as in the widely used SIMP¹ method (Bendsøe, 1995, Tcherniak and Sigmund, 2001, Bendsøe and Sigmund, 2003, Andreassen et al., 2010), or based on physical schemes such as in the homogenization method (Bendsøe and Kikuchi, 1988, Fuchs, 1999, Allaire, 2002) and others (Bendsøe and Sigmund, 1999). The optimization is then reduced to a functional optimization with respect to the fictitious density function, based on analytical derivative. At the end of the optimization procedure, a “composite” solution is obtained with a density in-between 0 and 1 (figure 3.2b). Thus

¹Solid Isotropic Material with Penalization.

a penalization stage is added in order to progressively prohibit the intermediate values of density (figure 3.2c). The main disadvantage of these material approaches is that the obtained optimized shape is strongly sensitive to the material interpolation scheme as well as penalization method.

Inspired from free-interfaces and front-tracking methods, the level-set method (figure 3.2d,e) is a way to define implicitly the domain Ω on a fixed mesh of the design domain V (see section 2.2). The iterative optimization of the shape is done by applying on the level-set function a velocity field that depends on the shape derivative (Sethian, 2000, Osher, 2001, Allaire et al., 2004). The transport equation is usually Hamilton-Jacobi equation (Sethian, 1999). Physical equations are solved on the full design domain and empty spaces are mimicked with extremely weak material properties. A smoothed fictitious interface is introduced to avoid instabilities such as it is done in phase field simulations. When using Hamilton-Jacobi equation, only partial topological changes are allowed. Indeed, the maximum principle satisfied by this transport equation makes the nucleation of new holes impossible. But coarsening of existing holes can occur, which still enables partial topological changes. Thus initial geometry are usually chosen with a large number of holes, for instance with trigonometric level-set functions. In the following, level-set method using Hamilton-Jacobi equation is chosen for the optimization simulations (following Allaire et al., 2004).

Applications In the context of multi-functional optimization of architected materials, it seems interesting to mention some examples of the literature. Apart the development of new methods illustrated on classical compliance problems, shape optimization was applied to many other problems with various objective functions such as Von Mises stress (Allaire and Jouve, 2008, Amstutz and Novotny, 2009), actuator compliance (Sigmund and Torquato, 1999), thermal conductivity (Gersborg-Hansen et al., 2006, Munoz et al., 2007), shell compliance (Ansola et al., 2002, Novotny et al., 2005, Park and Youn, 2008), vibration modes (Ma et al., 1995). The particular case of periodic microstructures was first studied by Sigmund (1995) to tailor materials with prescribed elastic properties. Then, optimization of various properties have been proposed : thermal expansion (Sigmund and Torquato, 1997), bulk and shear modulus (Neves et al., 2000, Huang et al., 2011), porosity and permeability for tissue engineering (Hollister et al., 2002, Hollister, 2005), elastic properties to get auxetic materials (Schwerdtfeger et al., 2011), piezoelectricity (Nelli Silva et al., 1998), thermal conductivity (Zhuang et al., 2007), stiffness and conductivity (Chen et al., 2010).

This chapter is dedicated to applying shape optimization to plate unit cell with respect to membrane, bending and transverse-shear compliances.

3.1 Shape derivative and optimization algorithm

The present section shortly presents the concept of shape derivative and its use into a compliance minimization algorithm based on (Allaire et al., 2004). Implementation in two dimensions was validated on classical problems and then applied to architected panels.

3.1.1 Shape Derivative

The description of shape derivative and compliance minimization problem will be done in two dimensions, but generalization to three dimensions is trivial.

Considering a function J of domain $\Omega \in \mathbb{R}^2$, shape derivative quantifies its sensitivity to any infinitesimal variation of the boundary of Ω . One denotes Ω_θ the resulting domain to a small transformation of domain Ω with respect to vector field θ (figure 3.3), i.e. :

$$\Omega_\theta := \{x_\theta \in \mathbb{R}^2 : x_\theta = x + \theta(x), x \in \Omega\} \quad (3.1)$$

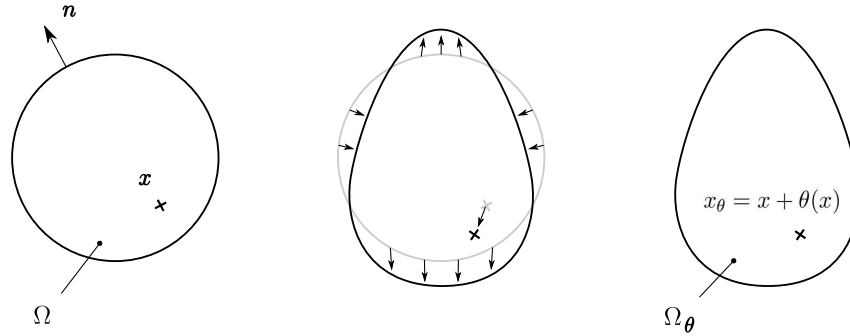


Figure 3.3: Small transformation of the domain Ω to the domain Ω_θ through the vector field θ . The transformation is sufficiently small and regular to be a diffeomorphism (smoothed and invertible function).

Then shape derivative of function $J(\Omega)$ is defined as the Fréchet derivative at 0 of the application $\theta \rightarrow J(\Omega_\theta)$, i.e. :

$$J'(\Omega)(\theta) = \lim_{\|\theta\| \rightarrow 0} \frac{J(\Omega_\theta) - J(\Omega)}{\|\theta\|} \quad (3.2)$$

In the case of area $\mathcal{A}(\Omega)$, which only depends on Ω through integration support, one has :

$$\mathcal{A}(\Omega) = \int_{\Omega} dx \quad \text{and} \quad \mathcal{A}'(\Omega)(\theta) = \int_{\partial\Omega} \theta(x) \cdot n(x) dx \quad (3.3)$$

where n is the normal to the boundary of Ω . When the function J is the integral of a field

$j(\Omega)$ that also depends on the domain, one can formally denotes :

$$J(\Omega) = \int_{\Omega} j(\Omega) dx \quad \text{and} \quad J'(\Omega)(\theta) = \int_{\partial\Omega} j'(\Omega) \theta \cdot n dx \quad (3.4)$$

If $j(\Omega)$ is the result of the solution of a partial differential equation, the derivative field $j'(\Omega)$ do not have an analytical expression in the general case. Only specific cases lead to analytical expressions that depend on an adjoint problem (Allaire, 2002). The simplest result concerns shape derivative of elastic energy, which leads to a self-adjoint problem and the following expression :

$$J(\Omega) = \int_{\Omega} \varepsilon(u) \cdot \mathbf{C}\varepsilon(u) dx \quad \text{and} \quad J'(\Omega)(\theta) = \int_{\partial\Omega} (-\varepsilon(u) \cdot \mathbf{C}\varepsilon(u)) \theta \cdot n dx \quad (3.5)$$

where u is the solution of a linear elastic problem with no body load and stress-free condition on the boundaries to optimize. This important result enables, with choosing the elastic energy as objective function, to compute from a single FEM simulation both values of objective function and derivative field $j'(\Omega)$.

3.1.2 Optimization algorithm

The optimization problem is usually written as minimizing an objective function J with a given amount of matter :

$$\min_{\{\Omega \subset V \text{ s.t. } F(\Omega)=0\}} J(\Omega) \quad (3.6)$$

where V is the design domain and $F(\Omega)$ the area fraction constraint :

$$F(\Omega) = \frac{\mathcal{A}(\Omega)}{\mathcal{A}(V)} - \bar{A}_f = 0 \quad (3.7)$$

and \bar{A}_f is the prescribed area fraction.

The constraint problem (3.6) is reduced to an unconstrained minimization problem by the Lagrangian method. The objective function $J(\Omega)$ is replaced by the Lagrangian $\hat{J}(\Omega, \lambda)$ such that :

$$\hat{J}(\Omega, \lambda) = J(\Omega) + \lambda F(\Omega) \quad (3.8)$$

where λ is the Lagrange coefficient which becomes an optimization variable in addition to Ω . Using equations (3.3) and (3.4), the shape derivative of the Lagrangian becomes :

$$\hat{J}'(\Omega)(\theta) = \int_{\partial\Omega} \left(j'(\Omega) + \frac{\lambda}{\mathcal{A}(V)} \right) \theta \cdot n dx \quad (3.9)$$

Since $j'(\Omega) < 0$ and $\lambda \geq 0$, this expression must be interpreted as the local competition between the mechanical derivative that tends to extend Ω (more or less depending on the

energy density) and the Lagrange coefficient that tends to withdraw uniformly Ω .

The optimization algorithm is synthesized in frame 3.1. The evaluation of the objective function and the shape derivative is done by finite element method on a fixed mesh of design domain V . Matter organization is defined by the level-set function (see section 2.2). The deformation of the shape results from transporting the level-set function ϕ with the Hamilton-Jacobi equation :

$$\frac{\partial \phi}{\partial t} + v|\nabla \phi| = 0 \quad (3.10)$$

where v is the velocity field. This partial differential equation is solved by a finite difference method on a regular grid using an explicit first order upwind mesh (Sethian, 1999). Evolving the level-set function on a time range δt is equivalent to a transforming field $\theta = v \delta t n$. Thus choosing the velocity field as $v = -j'(\Omega)$, the shape is deformed in a descent direction since equation (3.4) ensures $\hat{J}'(\Omega)(\theta) < 0$.

Because the velocity v is not strongly regular through the interface, the level-set function loses progressively its regularity. Then it has to be reinitialized, for instance to the signed distance function (for all x it is the distance to the closest boundary $\partial\Omega$, positive if $x \in \Omega$ and negative if not). This operation is done by solving the following equation until steady-state :

$$\frac{\partial \phi}{\partial t} + \text{sign}(\phi_0) (|\nabla \phi| - 1) = 0 \quad (3.11)$$

where the initial value ϕ_0 is the level-set function to reinitialize.

The maximum principle satisfied by Hamilton-Jacobi equation disables the creation of new holes, but partial topological changes are still available by coarsening. Thus the number of holes in the starting geometry is a key parameter.

The algorithm have been implemented in *Matlab* coupled with *Comsol Multiphysics 3.5* for the finite elements simulations. The level-set management and the resolution of the Hamilton-Jacobi equation by finite difference method are done using *Matlab*.

Frame 3.1 Algorithm which optimizes bi-dimensional shape under area constraint. Shape transformation results from the transport of the level-set function with Hamilton-Jacobi equation. (Allaire et al., 2004)

1. Initialize the level-set function to obtain the expected starting geometry and area fraction.
 2. While the maximum number of iterations is not reached :
 - (a) Evaluate the objective function and shape derivative with FEM simulations.
 - (b) While the area constraint is not satisfied :
 - Update the Lagrange coefficient from its previous value and the previous constraint errors.
 - Deform the shape by transporting the level-set function with Hamilton-Jacobi equation. The equation is solved on a time range δt and for a velocity $v = -j'(\Omega)$.
 - (c) Reinitialize the level-set function to the signed distance function. It improves the conditioning for Hamilton-Jacobi equation while keeping the same zero contour line.
-

3.1.3 Numerical results

As a validation of the implementation of this method, numerical results are presented for two classical problems : a cantilever clamped on one side and subjected to a vertical force on the other, and a “bridge” with two support points on each side and a vertical force applied on the middle of the bottom edge. Figure 3.5a shows boundary conditions and loading for a bending cantilever, and figures 3.5b and 3.5c show the corresponding shape evolution to minimum compliance at given weight for two different initial geometries. Features of the final geometry are similar to those obtained from analytical (Dewhurst, 2001), parametric (Martínez et al., 2006), as well as topological optimization (Allaire and Jouve, 2008), exhibited on figure 3.4.

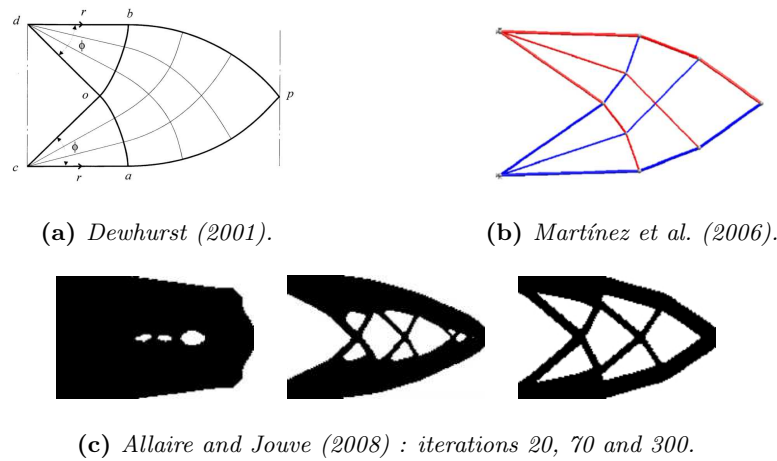


Figure 3.4: Some results of analytical, parametric and shape optimization from literature on the cantilever problem. Shape ratio and volume constraint are different.

A sensitivity of the final shape to the number of holes in the initial geometry is observed. However the difference in stiffness between the two optimized structures is less than 1%. Comparison with topological optimization shows that starting from a sufficient number of holes enables to compensate for the inability to create holes.

Figure 3.6b presents an other result when minimizing compliance at given weight with respect to the “bridge” loading specified on figure 3.6a. Topological changes are observed by coarsening holes.

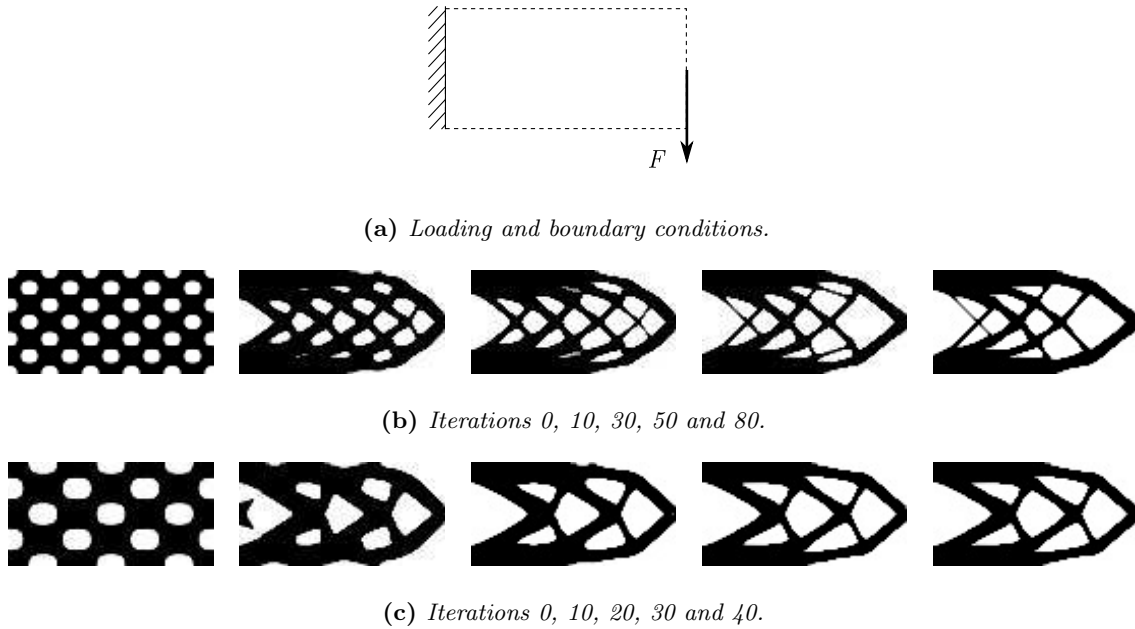


Figure 3.5: Compliance minimization of the cantilever boundary condition problem. Level-set discretized on 100×50 pixels and FEM simulations with 50000 elements. The area fraction is imposed to 0.5 in the two cases.

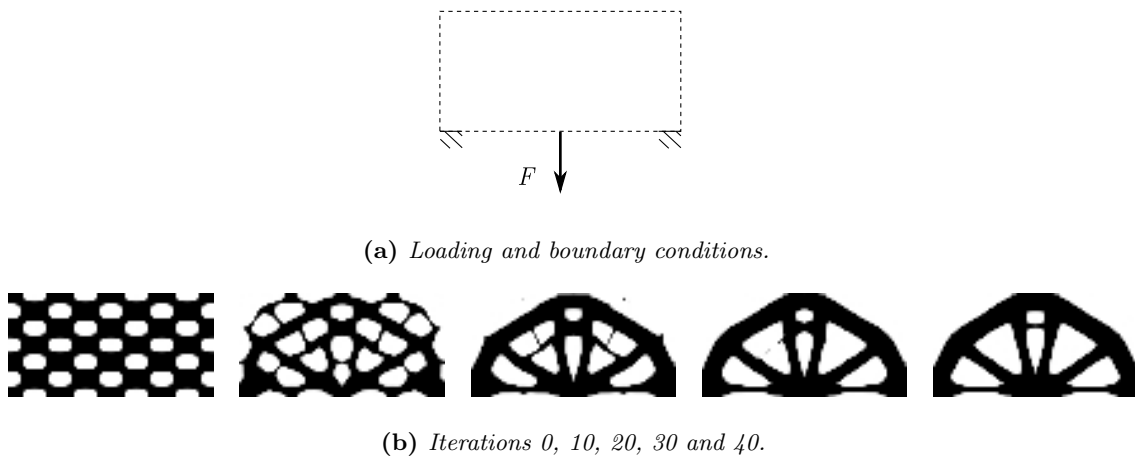
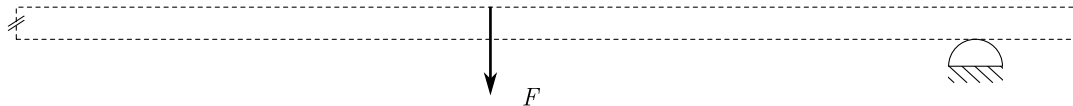


Figure 3.6: Compliance minimization of the bridge boundary condition problem. Level-set discretized on 80×40 pixels and FEM simulations with 3200 elements. The area fraction is imposed to 0.5.

More refined but similar features are observed when optimizing with respect to a panel subjected to a four-point bending loading (figure 3.7). Only the right half of the panel is simulated since geometry and loads are symmetric. The part subjected to pure bending is filled with two disconnected and invariant faces. The shear area (between load point and support point) shows a graded decrease of the faces thickness and an increase of diagonal shear bars that connect the two faces.



(a) Four-point bending load with symmetric boundary condition on left edge.



(b) Optimized structure after 100 iterations.

Figure 3.7: Shape optimization of a panel subjected to a four-point bending test. The resulting stiffness strongly depends on the location of load point and support point. The area fraction is imposed to 0.5.

Even if this optimization provides interesting shapes, it results in an optimized structure which is not robust if the load and support points are changed. Focusing on a periodic architecture should help to find a compromise between flexural stiffness, transverse-shear stiffness and weight, which does not depend on the loading location.

3.2 Optimization of 2D architected panel

The current section deals with shape optimization of periodic unit cell of architected panel. As already mentioned in chapter 1 and 2, the contribution of transverse-shear to the global bending stiffness is usually negligible excepted for very thick panels or particularly low shear stiffness. Thus, optimizing with respect to the flexural compliance is justified in the case presented on figures 3.8 and 3.9. The obtained geometry provides indeed the maximal flexural stiffness (as far as possible from the neutral axis) but shear stiffness is zero and any three or four-point bending stiffness of such panel will be also zero.

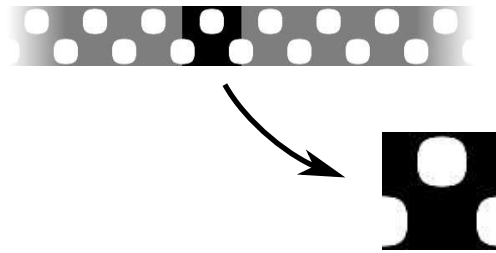


Figure 3.8: *The problem is to find the optimal geometry for the unit cell of an architected flexural panel.*



Figure 3.9: *Optimization of the flexural stiffness with respect to the matter distribution in a square unit cell (iterations 1, 10, 20, 30, 40 and 50). The resulting shape is not interesting because global bending stiffness is zero. The shear stiffness must be also included into a multi-functional objective function.*

Even if the shear contribution can be neglected in the performance of the initial geometry, shape optimization with respect to flexural compliance only will inevitably transform into a geometry for which the shear compliance is critical. Then, shear compliance has to be included into the objective function in order to converge toward non trivial shapes. The weight (proportional to the area fraction) take also part of the problem. If not, a unit cell entirely filled with matter will do it.

Finally, it results in a multi-functional optimization problem with an area fraction constraint. It will be written as minimization of compliances in order to fit with the shape optimization problems presented in section 3.1. As a consequence, the following properties will be discussed in terms of compliances.

3.2.1 A multi-functional optimization

As described in section 2.1.2, applying a bending moment M on the unit cell enables to compute the flexural stiffness from the elastic energy :

$$\mathbf{d} = \frac{2h \langle w^{(M)} \rangle}{M} = \frac{2h}{M} \frac{1}{|V|} \int_{\Omega} \varepsilon \cdot \mathbf{C} \varepsilon \, dx \quad (3.12)$$

where $w^{(M)}$ is the energy density that results from applying the bending moment M . The unit cell is denoted V and Ω is the domain filled with matter. Result (3.5) gives an analytical expression for the shape derivative of the flexural compliance :

$$\mathbf{d}'(\Omega)(\theta) = \frac{2h}{M} \frac{1}{|V|} \int_{\partial\Omega} (-\varepsilon \cdot \mathbf{C} \varepsilon) \theta \cdot \mathbf{n} \, dx := \int_{\partial\Omega} d' \theta \cdot \mathbf{n} \, dx \quad (3.13)$$

where d' denotes the derivative field of the flexural compliance \mathbf{d} .

Similarly, the expression of the transverse-shear compliance is :

$$\mathbf{f} = \frac{2h \langle w^{(Q)} \rangle}{Q} = \frac{2h}{Q} \frac{1}{|V|} \int_{\Omega} \varepsilon \cdot \mathbf{C} \varepsilon \, dx \quad (3.14)$$

where $w^{(Q)}$ is the energy density that results from applying the shear force Q . The shape derivative expression is :

$$\mathbf{f}'(\Omega)(\theta) = \frac{2h}{Q} \frac{1}{|V|} \int_{\partial\Omega} (-\varepsilon \cdot \mathbf{C} \varepsilon) \theta \cdot \mathbf{n} \, dx := \int_{\partial\Omega} f' \theta \cdot \mathbf{n} \, dx \quad (3.15)$$

where f' denotes the derivative field of the transverse-shear compliance \mathbf{f} .

In order to find an architecture that provides a compromise between flexural and transverse-shear stiffness, at a given weight, the following optimization problem is written :

$$\min_{\{\Omega \subset V \text{ s.t. } F(\Omega)=0\}} J_{\alpha}(\Omega) = \mathbf{d}^{\alpha} \mathbf{f}^{(1-\alpha)} \quad (3.16)$$

The constraint $F(\Omega) = 0$ enforces the area fraction to be \bar{A}_f , with :

$$F(\Omega) = \frac{\mathcal{A}(\Omega)}{\mathcal{A}(V)} - \bar{A}_f \quad (3.17)$$

The objective function $J_{\alpha}(\Omega)$ introduces a weighting factor α that quantifies the relative importance between bending and shear. Choosing $\alpha = 1$ means optimizing only the flexural compliance, and $\alpha = 0$ means optimizing only the shear compliance.

The combination of the previous shape derivatives for flexural compliance (3.13) and for shear compliance (3.15), gives the following expression for the derivative of the objective

function :

$$\begin{aligned} J'_\alpha(\Omega)(\theta) &= J_\alpha(\Omega) \left(\alpha \frac{d'(\Omega)(\theta)}{d} + (1 - \alpha) \frac{f'(\Omega)(\theta)}{f} \right) \\ &= \int_{\partial\Omega} J_\alpha(\Omega) \left(\alpha \frac{d'}{d} + (1 - \alpha) \frac{f'}{f} \right) \theta \cdot n \, dx \end{aligned} \quad (3.18)$$

Using the optimization algorithm described in section 3.1.2, any initial geometry can be iteratively transformed such that the objective function J_α is decreased, by solving the Hamilton-Jacobi equation with a velocity based on the integrand of equation (3.18).

Area fraction constraint

The area fraction constraint is treated by replacing the objective function by a Lagrangian that introduces a Lagrange coefficient as an additional optimization variable (see section 3.1.2). It simply results in decreasing the velocity field of the Hamilton-Jacobi equation by a constant proportional to the Lagrange coefficient. This constant competes against the mechanical derivative field in order to get an unchanged area fraction. And the constraint is being satisfied just by finding the appropriate value of Lagrange coefficient.

However for prescribing low area fraction (typically under 0.6), if the constraint is being satisfied from the first iteration, either vanishing of small connections of matter or holes coarsening may occur. For instance, on first picture of figure 3.10, the vanishing of the upper and lower connections is observed with respect to figure 3.9. It drastically reduces the connectivity of the geometry and since new holes cannot nucleate it makes the results uninteresting.



Figure 3.10: Optimization with area fraction $\bar{A}_f = 0.5$ and satisfying the constraint from the first iteration. Weighting factor is $\alpha = 0.6$ and pictures correspond to iterations 1, 10, 20, 30, 40 and 50.

A way to avoid this problem is to delay the satisfaction of the constraint such that optimization occurs and enables area fraction reduction without coarsening. This delay was done with a progressive decrease of the prescribed area fraction. For instance, figure 3.11 shows linear decrease of the prescribed area fraction from $\bar{A}_f = 0.7$ to 0.5. Four slopes have been used such that the real constraint is respectively satisfied at step 5, 10, 20 and 30.

The corresponding evolution of the objective function is plotted on figure 3.12. Plot 3.12a compares optimization with a fixed constraint $\bar{A}_f = 0.5$ for the initial step, and optimizations with a progressive constraint from $\bar{A}_f = 0.7$ to 0.5. The curve with fixed constraint

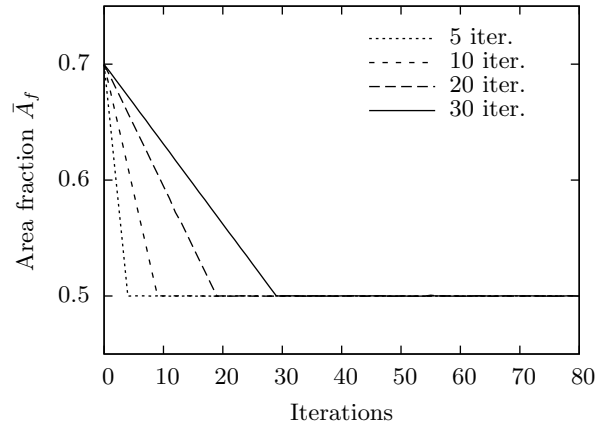


Figure 3.11: Evolution of the prescribed area fraction when linearly decreased from $\bar{A}_f = 0.7$ to 0.5 within respectively 5, 10, 20 and 30 iterations.

starts upper than that with progressive constraint since the area fraction is lower. Then it decreases while optimizing. But a gap remains with the others because of the much simpler topology that cannot be refined.

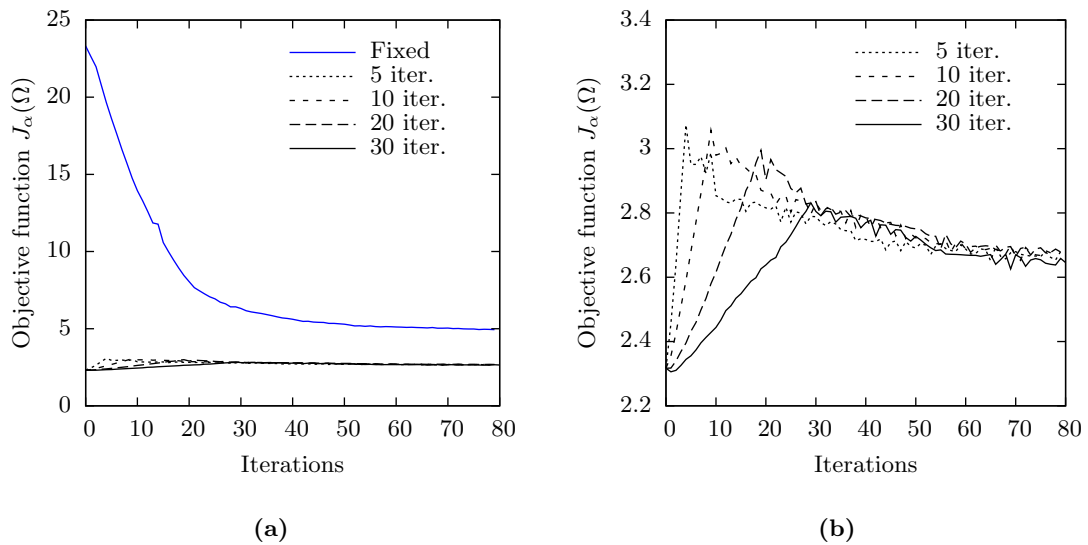


Figure 3.12: Evolution of the objective function with and without progressive constraint. Plot (b) focuses on progressive constraints with lowering of the area fraction within respectively 5, 10, 20 and 30 iterations.

The results with a progressive constraint cannot be distinguished, thus a focus on these curves is reproduced on figure 3.12b. They reveal two stages : a quasi-linear increase of the objective function that results from the decrease of the area fraction in addition with optimization, followed by a decrease as a consequence of the optimization only. For these

four simulations the connectivity is maintained thanks to a progressive satisfaction of the constraint that let time to the matter rearrangement. No influence of the number of iterations is observed on the objective function convergence and the optimized geometry. Then the most progressive constraint (30 iterations) is chosen in the following.

Figure 3.13 compares the shape evolution when optimizing with a progressive constraint spent on 5 and 30 iterations.

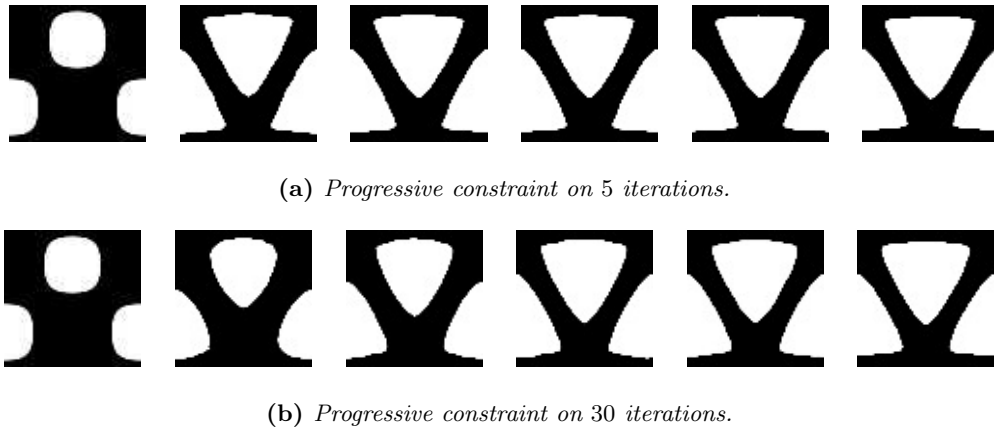


Figure 3.13: Optimization with satisfying the constraint progressively from $\bar{A}_f = 0.7$ to $\bar{A}_f = 0.5$. Weighting factor is $\alpha = 0.6$ and iterations 1, 10, 20, 30, 40 and 50.

Flexural and shear contributions

In this section, one focuses on the simulation of figure 3.13. It results from the minimization of the weighted product J_α with $\alpha = 0.6$ and a prescribed final area fraction $\bar{A}_f = 0.5$. The evolution of the objective function was presented on figure 3.12b (plain line). It deals with the mean response of the architected unit cell. By contrast, figure 3.14 concerns the local response and the evolution of the geometry. For each iteration (1, 10, 20, 30, 40 and 50), the energy density is plotted on the deformed geometry when subjected respectively to a bending moment $M = 1 \text{ N}\cdot\text{m}/\text{m}$ (figure 3.14b) and a shear force $Q = 1 \text{ N}/\text{m}$ (figure 3.14c). Magnification is identical in both case.

Concerning the velocity of the Hamilton-Jacobi equation, one has the competition of three contributions : the shape derivative of the flexural compliance which depends on the energy density $w^{(M)}$, the shape derivative of the shear compliance which depends on $w^{(Q)}$ and the Lagrange coefficient. The contributions of the compliances tend to extend the domain proportionally to the respective energy density, whereas the Lagrange coefficient tends to withdraw uniformly the domain in order to get the prescribed area fraction. The transformation from an iteration to the next iteration is given by the result of this competition, and optimization has converged when these driving forces balance.

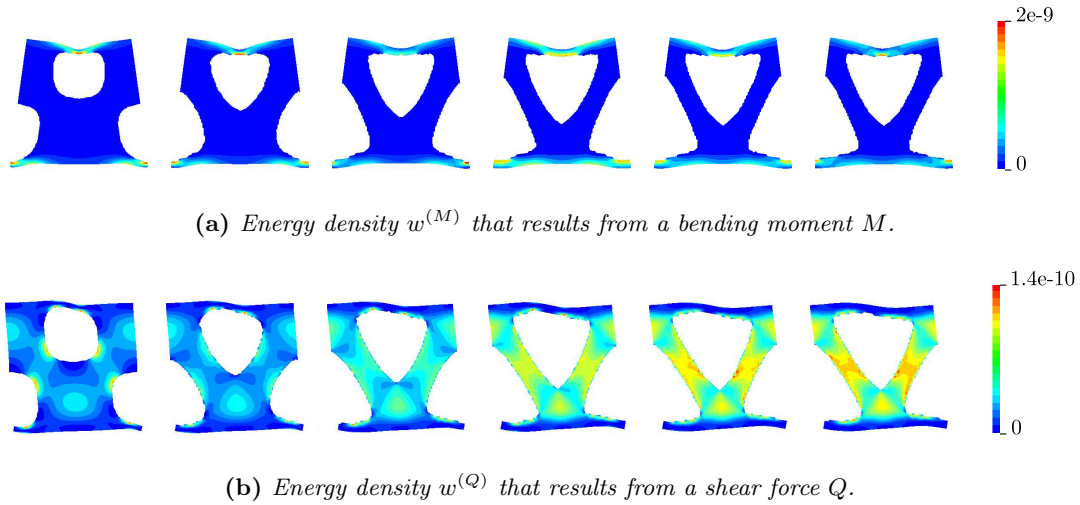


Figure 3.14: Evolution of the deformed unit cell and the energy density fields corresponding to the homogenization problems for flexural and transverse-shear compliance (iterations 1, 10, 20, 30, 40 and 50). The surface fraction of matter decreases progressively from $\bar{A}_f = 0.7$ to $\bar{A}_f = 0.5$. The weighting factor is equal to $\alpha = 0.6$.

The transformation of the geometry on figure 3.14 must be interpreted as follows. The shape derivative, which is the driving force of the motion of matter, is a combination of the two energy density plotted respectively on figure 3.14a and 3.14b. On the three first pictures, the area fraction is decreased by locally removing matter where the shape derivative is the lowest. That is why matter is mainly removed within the core but not in the faces. Then for the three last pictures, the area fraction is unchanged and matter added in some place is removed for others, until a balance is found. The weighting factor α controls the relative importance between flexural and shear contributions.

Influence of the transverse-shear homogenization problem

As described above, the optimization process results from the local value of the energy density. Consequently, the type of boundary conditions used in the homogenization problem will impact the distribution of energy density and the results of shape optimization.

In the case of the shear compliance, two types of loading have been mentioned in section 2.1.2. The problem with bending gradient body load was chosen in all the optimization simulations since it preserves the appropriate boundary conditions. But in this section, the influence of the loading is studied.

Figure 3.15 compares similar optimizations — with same initial geometry, same weighting factor $\alpha = 0.6$ and same prescribed area fraction $\bar{A}_f = 0.5$ — but with different shear homogenization problems : kinematic uniform boundary conditions (KUBC), static uniform boundary conditions (SUBC) and bending gradient body load (BG).

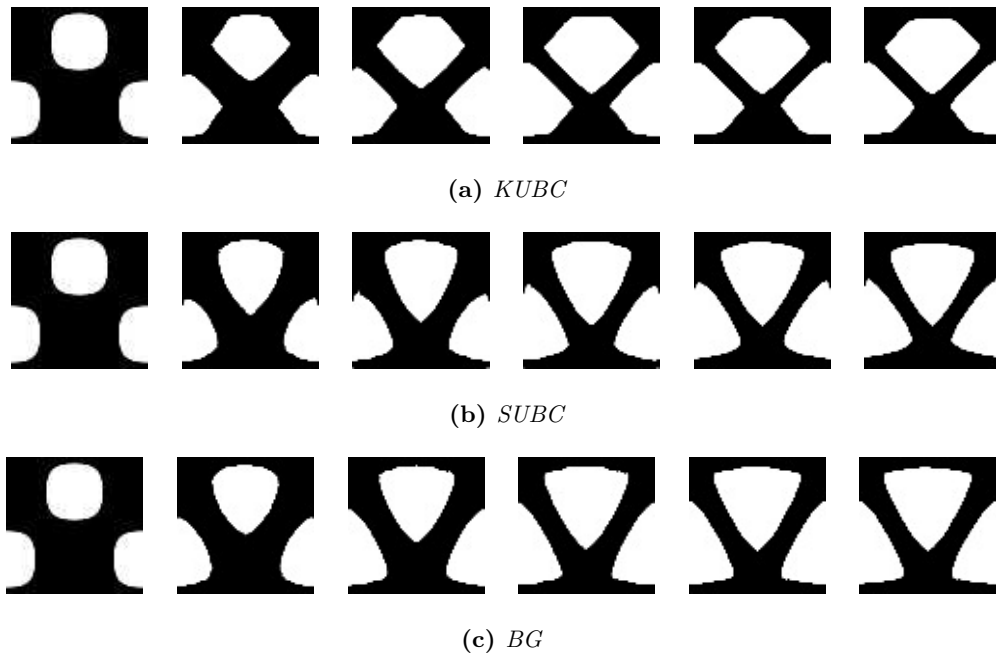


Figure 3.15: Comparison of similar optimizations (same initial geometry, $\bar{A}_f = 0.5$, $\alpha = 0.6$) but with different types of shear homogenization problem : kinematic uniform boundary conditions (KUBC), static uniform boundary conditions (SUBC) and bending gradient body load (BG). Iterations 1, 10, 20, 30, 40 and 50 are presented.

Optimization 3.15a is probably the most intuitive since it lets appear bars along the 45° directions which are the direction of the principal stresses for a pure shear stress field. Optimized geometries with SUBC and BC are closer but it still remains differences. The case of SUBC consists in applying forces on the parts of the lateral edges that present matter. This boundary condition affects the shape derivative which explains the remaining trace of matter on the lateral boundaries that seems delayed with respect to the interface motion.

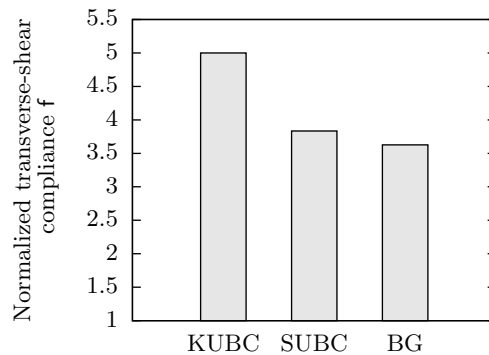


Figure 3.16: Transverse-shear compliance f of the optimized geometries of figure 3.15, identified on a unit cell subjected to a bending gradient body load.

Histograms on figure 3.16 quantifies the deviations in shear compliance that result from the geometrical differences between the optimized unit cells of figure 3.15. Optimization with BG homogenization provides the lowest shear compliance, slightly below that with the SUBC loading but far from that with the KUBC loading. As expected, the BG homogenization problem is the most appropriate for the present study.

Pareto front

A Pareto front denotes the subset of solutions (geometries in the present case) providing all the best compromises between several performance indexes. For each solution of the front, no other solution can be found such that it provides better values for all the performance indexes. More details in a context of material design and selection can be found in the literature (Ashby, 2000).

The weighting factor α , introduced in the multi-objective function J_α (equation (3.16)), quantifies the relative importance given to the flexural compliance with respect to the shear compliance. Varying α from 1 (only bending) to 0 (only shear) scans all the possible compromises between the two compliances and optimization with respect to these compromises should give indications on a Pareto front. Figure 3.17 exhibits the optimized unit cell for several values of α . The corresponding values of compliances are reported on a shear–flexural compliance chart. The compliances are normalized by those of a unit cell entirely filled with matter, in order to give comprehensive figures. The area fraction is fixed to 0.5.

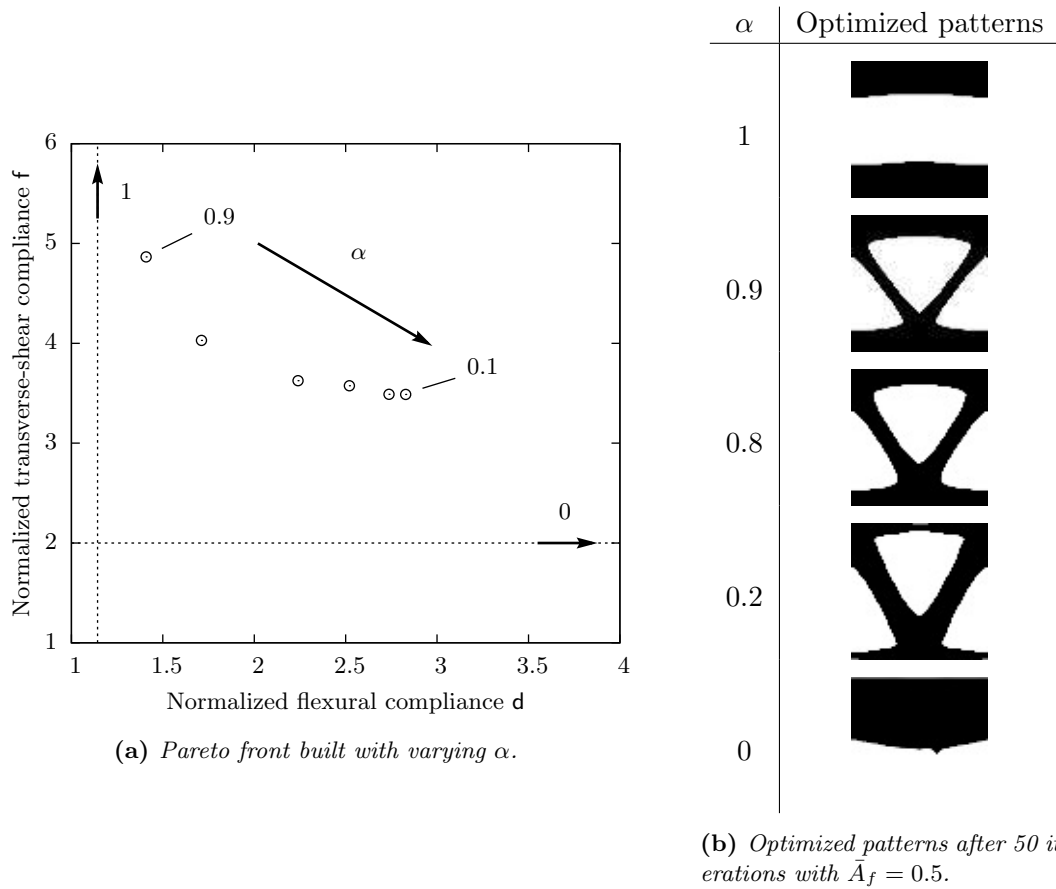


Figure 3.17: Influence of the weighting factor α on the compliances, while minimizing the weighted product (3.16). Results are obtained from the starting geometry of figure 3.9 with square size ($l_c = h$) and an area fraction $\bar{A}_f = 0.5$.

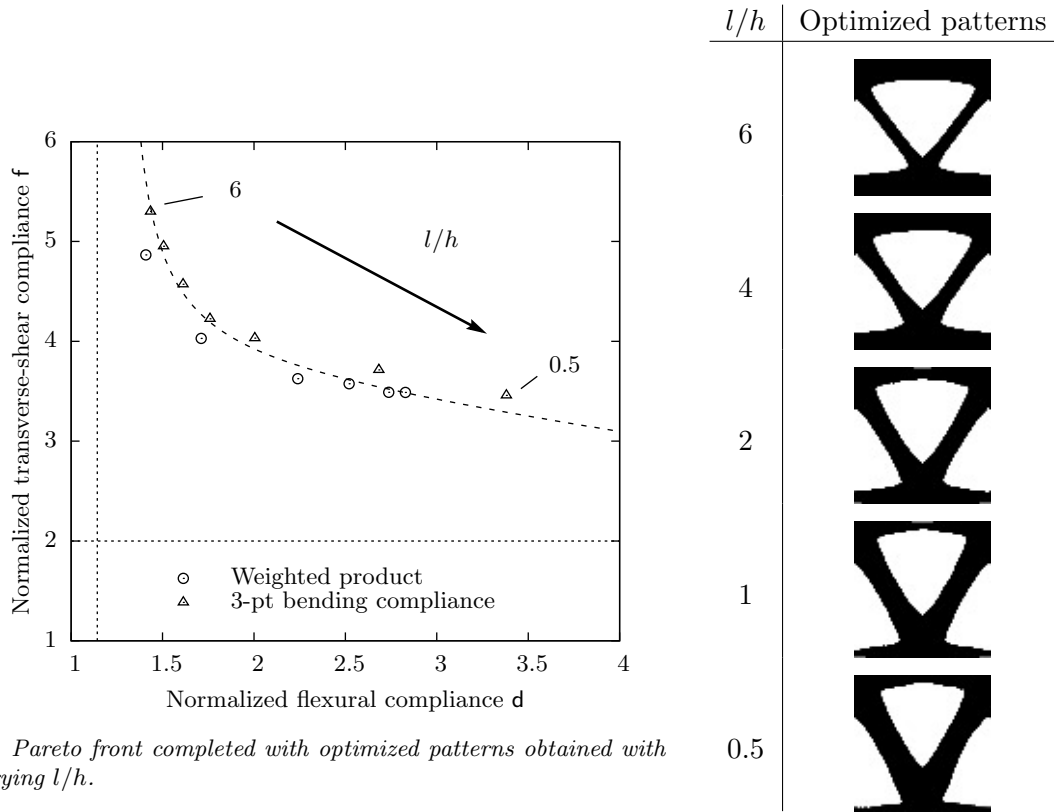
For $\alpha = 1$, the normalized flexural compliance is 1.14 (which is equal to the analytical value for two faces of thickness $0.25h$) whereas the shear compliance is infinite. Optimization with $\alpha = 0$ slowly converges to a homogeneous panel with thickness $0.5h$, whose normalized flexural compliance is 8 and whose normalized shear compliance is 2.

In order to give to the weighting factor a physical meaning, the three-point bending compliance can be used as objective function :

$$S_{3p} = \frac{l^3}{48}d + \frac{l}{4}f \quad (3.19)$$

In this case, the span length l becomes the weighting factor. Figure 3.18 completes the Pareto front on the shear–flexural compliance chart. The span length l is normalized by the panel thickness h .

As a conclusion, a Pareto front is well identified and results obtained by minimizing



(a) Pareto front completed with optimized patterns obtained with varying l/h .

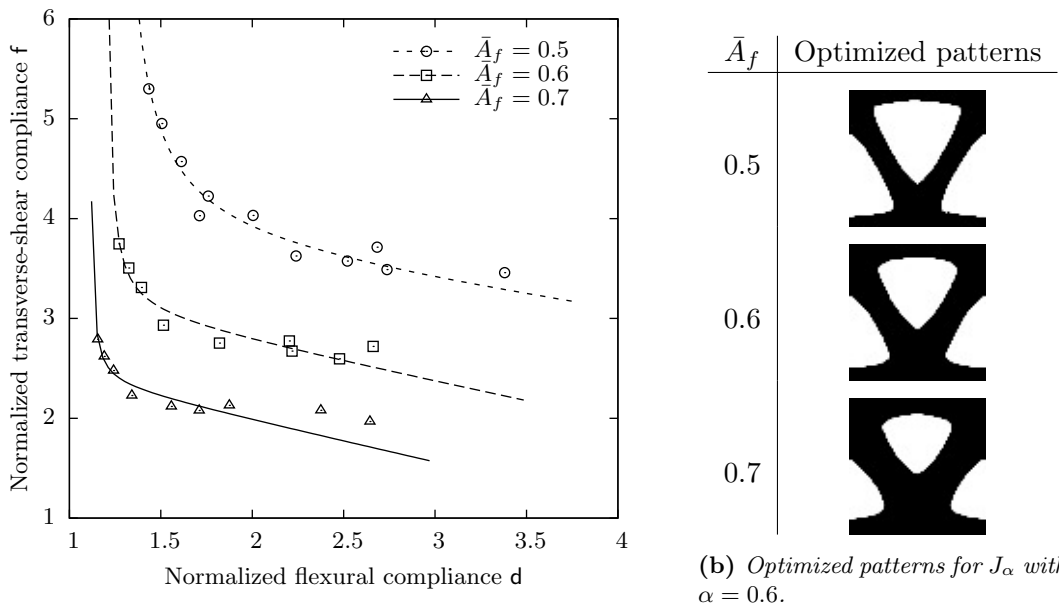
(b) Optimized patterns after 50 iterations with $\bar{A}_f = 0.5$.

Figure 3.18: Influence of the span length l (normalized by the thickness h) on the compliances, while minimizing the three-point bending compliance (3.19). Results are obtained from the starting geometry of figure 3.9 and an area fraction $\bar{A}_f = 0.5$.

either the weighted product or the three-point bending compliance are consistent. The weighted product seems to provide a more efficient optimization than the bending compliance. The difference is so small that it is not relevant, but still can be explained by the fact that the path optimization is changed when the objective function is changed.

3.2.2 Influence of the prescribed area fraction

This section presents the impact of the area fraction value on the previous Pareto front. Figure 3.2.1 gathers optimization results with both weighted product and bending compliance objective function for three values of prescribed area fraction : $\bar{A}_f = 0.5, 0.6$ and 0.7 . It results in a shift of the Pareto front toward the lower values of flexural and shear compliances.



(a) Pareto fronts for $\bar{A}_f = 0.5, 0.6$ and 0.7 .

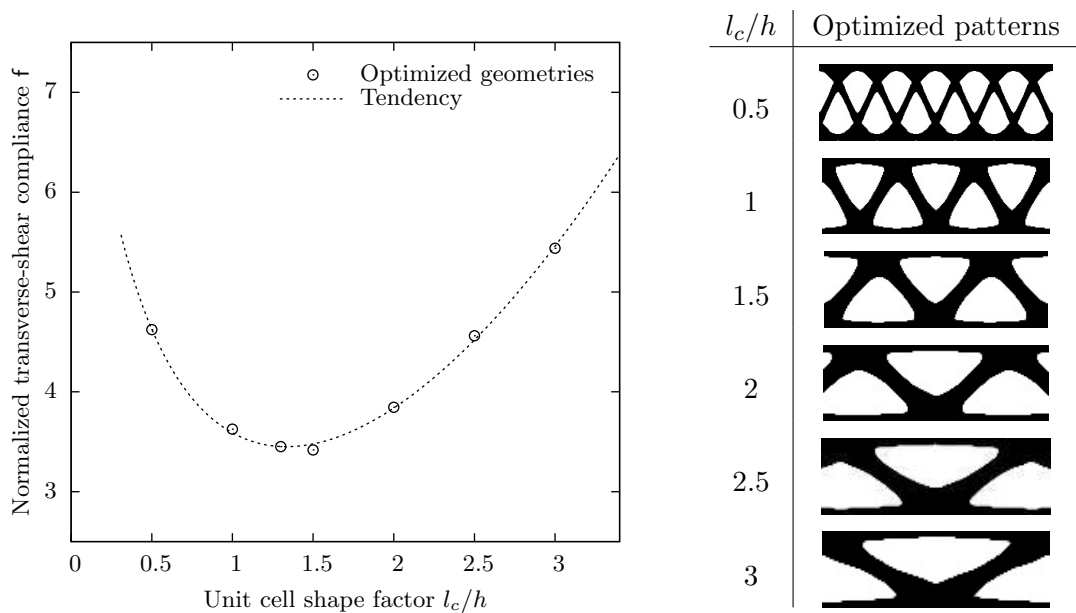
(b) Optimized patterns for J_α with $\alpha = 0.6$.

Figure 3.19: Shift of the Pareto front when varying the prescribed area fraction \bar{A}_f from 0.5 to 0.6 and 0.7. Results with both weighted sum and three-point bending compliance as objective function are plotted.

High area fraction implies lower compliances values. At the same time, it reduces the number of degrees of freedom and in particular the influence of the matter distribution on the transverse-shear compliance. A prescribed area fraction of 0.5 encourages the diversity in geometries as well as in compromises between flexural and shear compliances.

3.2.3 Influence of unit cell shape factor

Even if shape optimization enables a large number of transformations and topological changes, the choice of the unit cell length strongly reduces the space of shapes effectively explored. Then a parametric study has been performed on the unit cell length l_c for a given panel thickness h . Results of optimization conclude that the shape factor l_c/h impacts mostly the shear compliance. The flexural compliances of the optimized geometries are slightly affected since the normalized values are included between 1.90 and 2.23. Figure 3.20 shows the optimized patterns when varying l_c/h from 0.5 to 3, and the corresponding values of the shear compliance.



(a) Evolution of the shear stiffness with varying the unit cell shape ratio l_c/h .

(b) Optimized designs after 50 iterations with $\bar{A}_f = 0.5$.

Figure 3.20: Influence of the unit cell shape ratio l_c/h on the transverse-shear compliance f , while minimizing the weighted product (3.16). Results obtained for a prescribed area fraction $\bar{A}_f = 0.5$.

Figure 3.20a reveals an optimal shape factor with respect to the transverse-shear compliance. The optimum seems to be reached for a shape factor around 1.3. It corresponds to a tilt angle of the core bars with respect to the horizontal of 50° , which is slightly different from 45° as it could have been intuited.

3.2.4 Influence of the initial geometry

First numerical results on the cantilever example (section 3.1.3) introduces the sensitivity to the initial geometry. Optimizations with several initial geometries and shape factor have been performed in order to study this point. The three-point bending compliance is chosen as objective function with $l/h = 4$ and $\bar{A}_f = 0.5$. Results are gathered in figure 3.21 for both regular geometries (from trigonometric level-set functions) and random geometries (randomly distributed circular holes). The compliances of each optimized pattern are plotted in the flexural–shear compliance chart, in comparison with the Pareto front fitted on figure 3.18a.

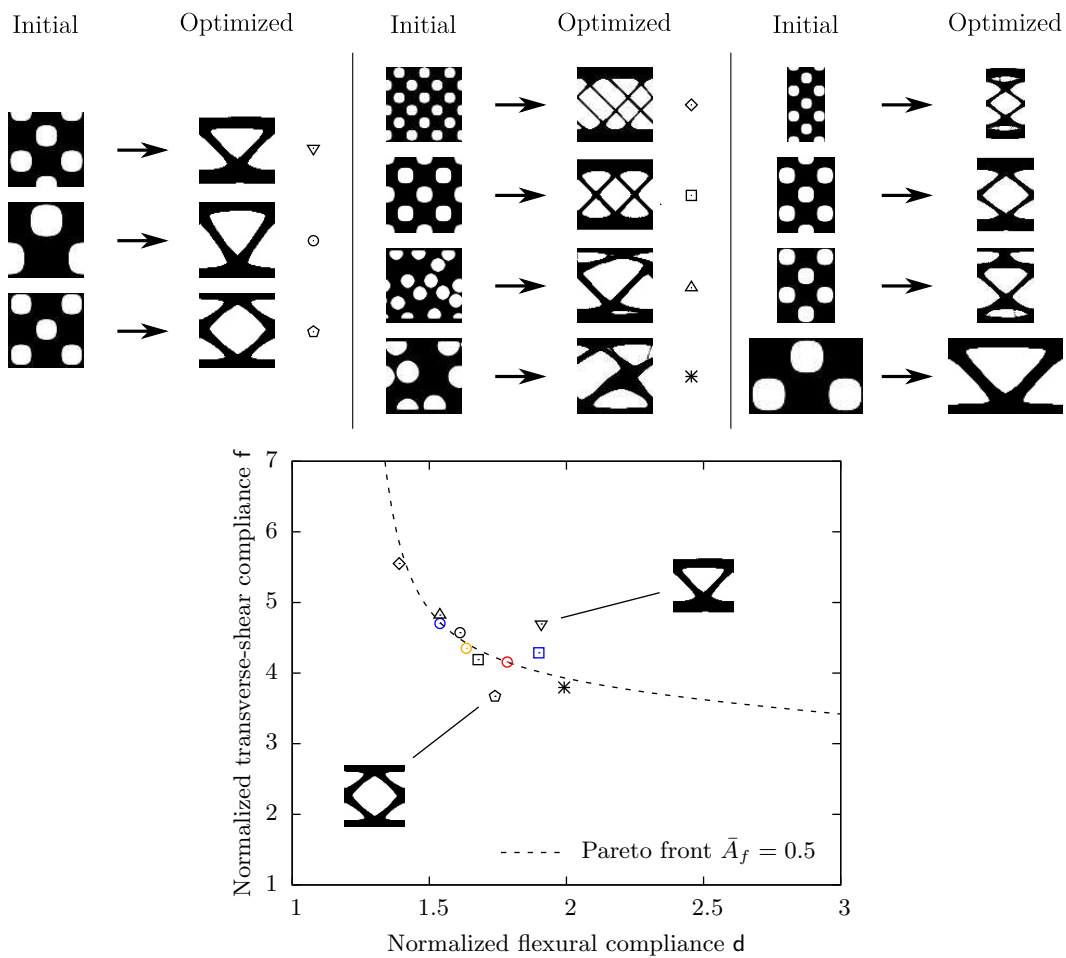
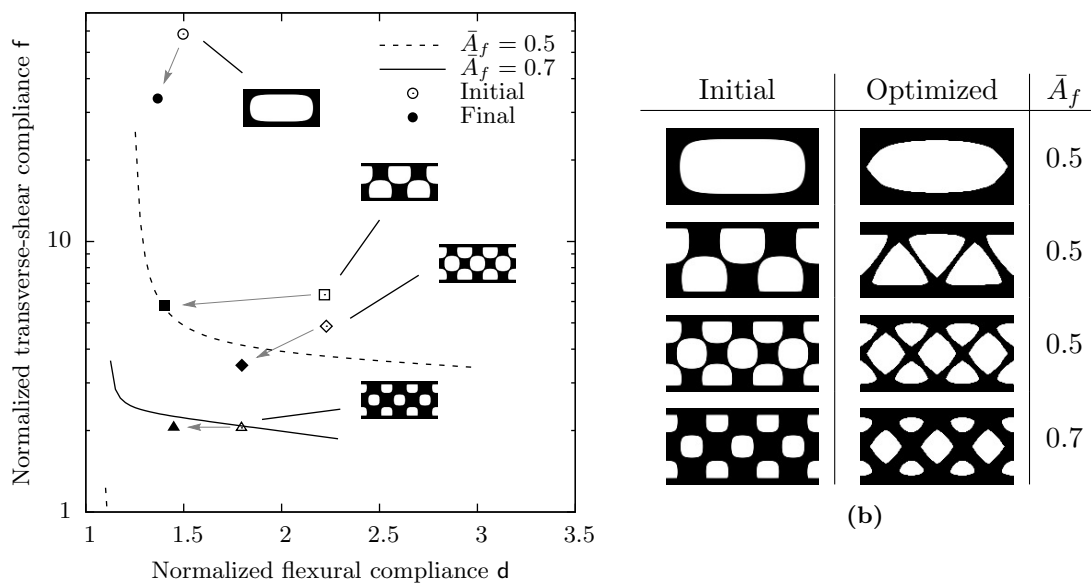


Figure 3.21: Comparison of the compliances of optimized patterns obtained from several initial geometries.

This graph shows that even if a large variety of optimized geometries is found, the previously built Pareto front is still valid. Only one geometry really overcomes this front, the square unit cell with lozenge bars.

3.3 Prototype samples produced by selective laser sintering

In order to validate the previous numerical approach, it makes sense to compare — numerically and experimentally — initial and optimized unit cell geometries. To do so, we consider three initial geometries with an area fraction of $\bar{A}_f = 0.5$ and one with $\bar{A}_f = 0.7$. Optimization is performed for each initial geometry with respect to the weighted product with $\alpha = 0.5$ (same weight for flexural and shear compliances). The computed compliances for initial and final geometries are plotted on chart 3.22a and compared to the previously fitted Pareto fronts.



(a) Flexural-shear compliance chart with four initial geometry and the corresponding optimized shapes.

Figure 3.22: Comparison between compliances of initial and optimized unit cells with three different initial topologies and two prescribed area fraction $\bar{A}_f = 0.5$ and 0.7 . The weighted product is used as objective function with $\alpha = 0.5$.

Prototype panels with all these unit cell geometries have been produced by additive manufacturing. Images of the unit cell geometries can be translated in STL files², which enable to produce polyamide samples by selective laser sintering. It was done in a collaboration with the company *Polyshape* and the *Centre des Matériaux des Mines de Paris*.

Figures 3.23 exhibits the prototype samples : initial geometries (a-d) and corresponding optimized geometries (e-h). The size of the samples is $210 \times 40 \times 12$ mm, that is 17.5 unit cells. Four-point bending tests have been performed on each sample with changing the

²File format to describe three-dimensional objects, widely used by computer-aided design software and manufacturing. From 2011, ASTM Standard F2915 replaced the STL format with the Additive Manufacturing File (AMF) format .

lower span lengths to $l = 82, 106$ and 130 mm, while keeping unchanged the shear length $L = 29$ mm.

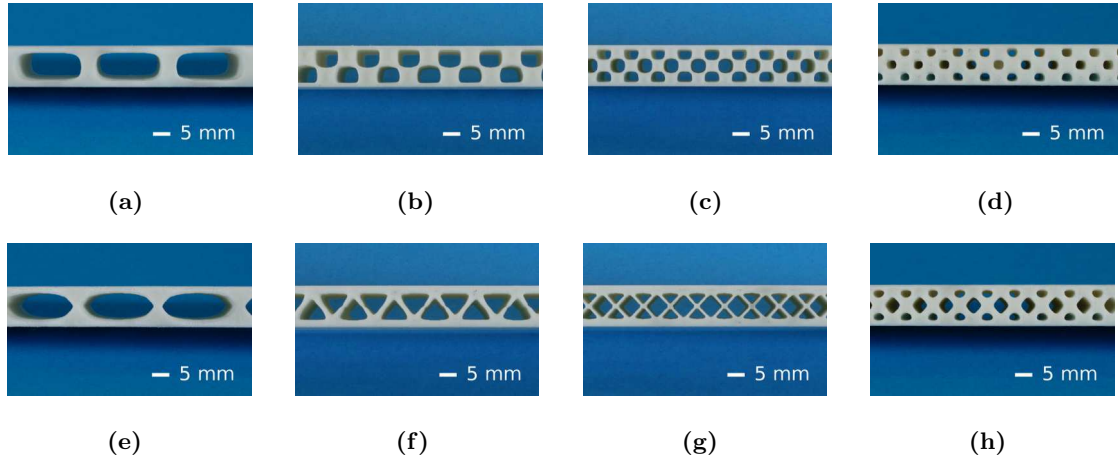


Figure 3.23: Prototype samples produced in polyamide by selective laser sintering : initial geometries (a-d), and the corresponding optimized shapes (e-h). Results of four-point bending test on these samples are presented on figure 3.24 and 3.25.

Four-point bending compliances for each geometry and each span length value are presented on figure 3.24 and 3.25. These data are compared to the following analytical expression :

$$S_{4p} = \frac{(3l - 4L)L^2}{12} d + \frac{L}{2} f \quad (3.20)$$

where d and f are identified thanks to the homogenization problem solved on the unit cell.

A relatively good agreement is obtained between experiments and the effective model. An improvement of the compliance is clearly observed for $\bar{A}_f = 0.5$. Even on figure 3.25, which is the less convincing, it is noticed a 20% decrease of the compliance for $l = 130$ mm.

As mentioned in section 3.2.2, increasing the area fraction limits the impact of the geometry on the properties. Figure 3.25b confirms this feature since no significant decrease of the compliance is experimentally observed between initial and optimal geometries for $\bar{A}_f = 0.7$.

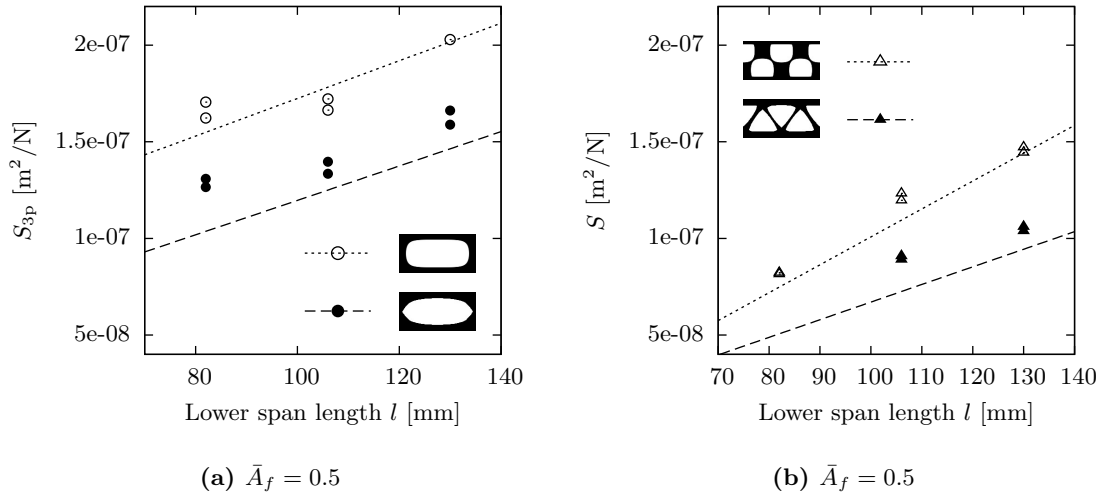


Figure 3.24: Comparison of the four-point bending compliance S_{4p} measured experimentally (points) and that calculated from the analytical expression with effective compliances (lines).

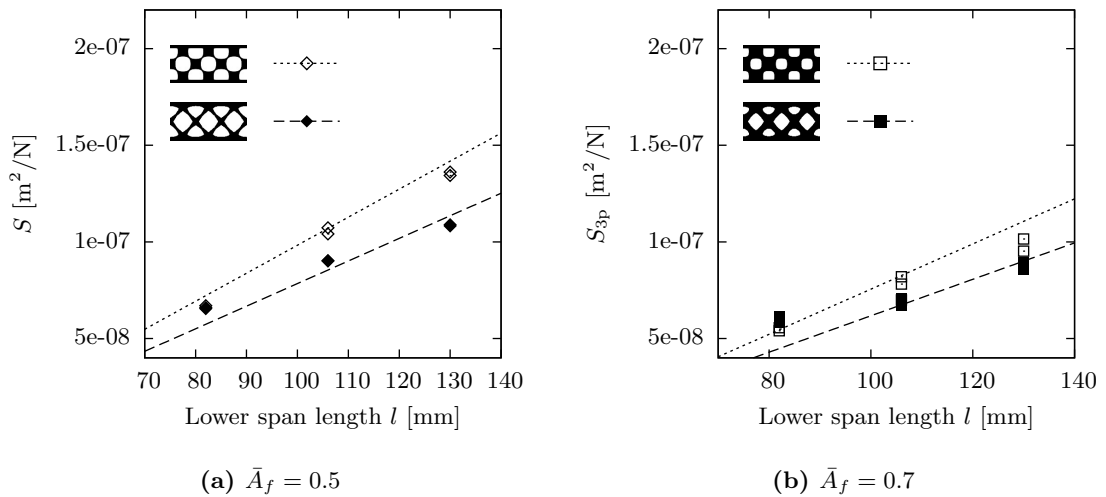


Figure 3.25: Comparison of the four-point bending compliance S_{4p} measured experimentally (points) and that calculated from the analytical expression with effective compliances (lines).

Conclusion

This chapter begins with a general overview of the literature in the field of shape optimization. The wide interest about this approach is confirmed by the large number of new methods and applicative problems.

Basis on shape derivation and details on the implemented algorithm are presented. The geometry is defined by the level-set method introduced in section 2.2. Few numerical results for typical structural optimization problems are discussed and compared to the literature. It validates the implementation of a topological optimization algorithm by the level-set method.

The area fraction constraint is satisfied progressively, starting from a higher value of the area fraction $A_f = 0.7$ and slowly decreasing down to the prescribed value (for instance $A_f = 0.5$). Then, optimization of periodic architected panels is treated by searching a compromise between flexural and shear compliances.

A weighting factor controls the relative importance given to the flexural compliance with respect to the shear compliance. Optimization simulations are performed with respect to the shear compliance. Objective function written as either weighted product or three-point bending compliance reveals to be equivalent in terms of both optimized geometries and properties. Optimization simulations performed with several values enable to estimate a Pareto front. The evolution of this front when changing the prescribed value of area fraction was studied. It was shown that high values tend to limit the impact of the matter organization on the compliances.

Unfortunately, even if the optimization method enables topological changes, it is shown to be widely sensitive to the initial geometry — as every gradient-based method. Optimization results on several starting geometries present only few deviations from the Pareto front. The influence of the unit cell shape ratio is also studied and reveals an optimal value. Integrating the unit cell size as an additional optimization variable seems relevant.

Finally, an experimental validation of the predicted improvements in properties is performed. Prototype samples of four initial geometries and the corresponding optimized geometries are produced by additive manufacturing. The expected compliance values are confirmed by experimental identification on four-point bending tests.

Highlights

- **Topological optimization** by the level-set method is coupled with homogenization problems in order to find a compromise between flexural and shear compliance at a given weight (i.e. area fraction). A **Pareto front** is built in the flexural–shear compliance chart and studied with changing the prescribed value of area fraction.
- The **initial geometry** reveals to strongly impact the optimization results as it is always the case with gradient-based optimization method. However, main of the optimized architectures are located on the Pareto front, and there is only few differences in the optimality of the properties.
- **Prototypes** produced by selective laser sintering confirm the expected improvement of architected material by topological optimization.

CHAPTER 4

Optimal design of an insulation sandwich panel

Introduction

This chapter addresses an industrial application of the previously developed optimization approach for architected materials. It consists in improving the design of an insulation sandwich panel produced by the company *Sainte-Marie Constructions Isothermes*. This panel provides mechanical, thermal and acoustic performances as well as modularity — it is easy to include doors and windows —, lightness, reasonable thickness and competitive cost. It is currently sold singly for buildings (for instance safety rooms on offshore platforms, figure 4.1).



(a)



(b)

Figure 4.1: (a) Integration of the sandwich panels into a safety room to be part of offshore platforms (b).

An optimal design procedure is developed and applied to the design of a component of the panel. This procedure comprises four steps :

- Defining an optimization problem by translating the specifications of the component into objectives and constraints ;
- Optimizing topology and shape with varying parameters such as initial geometry, relative density and relative importance of each objective ;
- Selecting few promising designs with respect to the estimated performances and adjusting the selected designs to comply with the process requirements ;
- Manufacturing and testing prototype panels that integrate the optimized designs, in order to evaluate the impact of the new designs on the panels performance.

The outline of the current chapter follows these steps. The first section 4.1 starts with details on the sandwich panel components : faces, stiffeners and mineral wool (section 4.1.1). The stiffener is the component on which is applied the optimal design procedure. Then, the panel specifications provided by *Sainte-Marie Constructions Isothermes* are

described (section 4.1.2) and translated into an optimization problem written in terms of physical properties of the stiffener (section 4.1.3). Section 4.2 presents optimization results and discussions on the influence of each parameters. Section 4.3 details the way to select and adjust optimized design in order to convert optimization results into real prototype panels. Finally, performance evaluation of the prototype panels is done in the last section 4.4. Thermal properties of the whole panels are estimated with 3D transient finite elements simulations, whereas mechanical properties are measured using four-point bending tests on samples provided by the company *Sainte-Marie Constructions Isothermes*.

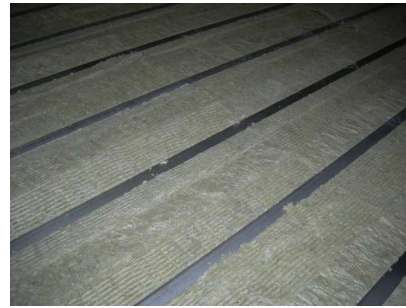
4.1 From specifications to optimization problem

4.1.1 Panel description

The panel, produced by *Sainte-Marie Constructions Isothermes*, is made of two steel faces spaced by stainless steel stiffeners (figure 4.2a and 4.3). The stiffeners are parallel and regularly distributed. They are welded to one face from the inside, and to the other from the outside through holes drilled in the face. High-density mineral wool (200kg/m^3) fills the empty space between the stiffeners (figure 4.2b). Its high thermal inertia provides to the panel a high insulating property. The stiffeners are usually set horizontally into the structure to avoid the wool densification with time — which results into a degradation of thermal insulation.



(a) Lower face with stiffeners.



(b) Mineral wool fills the inter-space between stiffeners.

Figure 4.2: Details on the structural sandwich panel produced by *Sainte-Marie Constructions Isothermes*. While stiffeners ensure the stiffness, the mineral wool ensures the thermal insulation.

The contrast in thermal conduction between steel and mineral wool creates short-circuits through the stiffeners. To reduce this shortcutting, the stiffeners are “aerated” according to a periodic design. The choice of this design is not trivial and involves the multi-physic functions of the panel. The optimization method presented in chapter 3 is applied in the current chapter to the optimization of the stiffener design.

Each stiffener is tailored by laser cutting from a flat sheet, then folded to get the final U-shape. Close to the fold, a zone must remain free of holes otherwise the fold will be affected. This zone is characterized by a *folding distance* shown on figure 4.3.

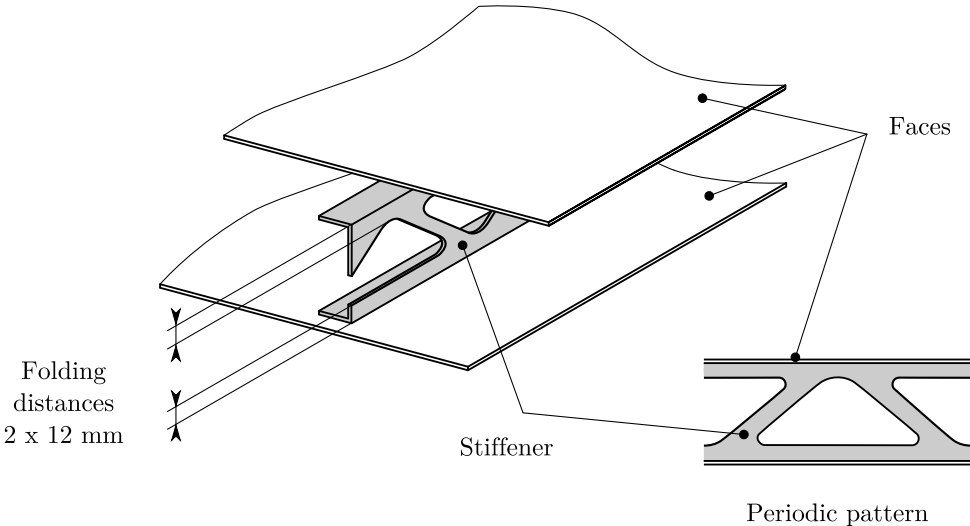


Figure 4.3: Sketch of one stiffener welded in-between the two faces. The folding distance defines two areas free of hole in order to control the folding process.

4.1.2 Specifications

As described in chapter 1, sandwich constructions for buildings and transports are usually developed for bending stiffness and additional functions. The present sandwich panel is a relatively thin¹ structural structure that provides mechanical stiffness and strength, thermal insulation and acoustic absorption at a minimum mass. Table 4.1 summarizes each function the panel must fulfill.

Functions	Technical descriptions
Mechanical <i>Protect working persons and devices that are inside the safety room.</i>	Low-energy impacts must imply only non-visible plastic deflection (lower than a limit value.)
	High-energy impacts must not punch through the panel neither imply large plastic deformation that may damage the devices or persons.
	The mass should be minimum.
	The maximum deflection of a panel subjected to a distributed load must be lower than a prescribed value.
Thermal <i>Maintain the temperature inside the safety room under a critical threshold.</i>	Thermal resistance and heat capacity must be higher than that of the current design.
	The criteria A-60 from the modified standard A754(18) prescribed by the International Maritime Organization (IMO) must be satisfied.
Acoustic <i>Maintain the sound level inside the safety room under a critical threshold</i>	The acoustic insulating properties must be higher than prescribed values.
Cost	The cost must be lower than a competitive cost
Recycling	The panel must be recyclable
Environmental impact	The carbon footprint must be lower than that of the current design

Table 4.1: Specifications for a new version of the insulation sandwich panel to be integrated in a safety room on offshore platform (provided by Sainte-Marie Constructions Isothermes).

¹in comparison with similar products

In the following, we will focus on the two main functions of the stiffeners :

- **Mechanical** As the name states, stiffeners are mainly concerned with the global bending stiffness of the panel. They are involved more precisely into the transverse-shear contribution, whereas the flexural one is ensured by the faces. Dynamic specification such as low-energy or even high-energy impacts are ensured by the faces, the panel thickness and the wool density.
- **Thermal** Thermal resistance and heat capacity are difficult to measure and the test from standard A754(18), described in frame 4.1, is preferred. Strictly speaking, the physical property quantified by this test is the diffusivity D :

$$D = \frac{k}{C_v} \quad (4.1)$$

where k is the thermal conductivity in $\text{W}/(\text{m}\cdot\text{K})$ and C_v the volumetric heat capacity in $\text{J}/(\text{m}^3\cdot\text{K})$. During the transient heating test, the temperature inside the heated face increases while the non-exposed face keeps a low temperature. Stiffeners are thermally insulated (by the wool) excepted through the contact with the heated face and with the non-exposed face. The transient time of stiffeners is negligible such that the temperature evolution within the stiffeners is quasi-static. It results from a small Biot number for stiffeners (Incropera et al., 2007). Then, stiffener are mainly subjected to a conductive behavior characterized by the effective thermal conductivity.

Mass contribution of the stiffeners is negligible with respect to the total mass of the panel. Indeed, the stiffeners mass is 12 % of the total steel mass of the panel, and 9 % of the total mass of the panel (faces, stiffeners and mineral wool).

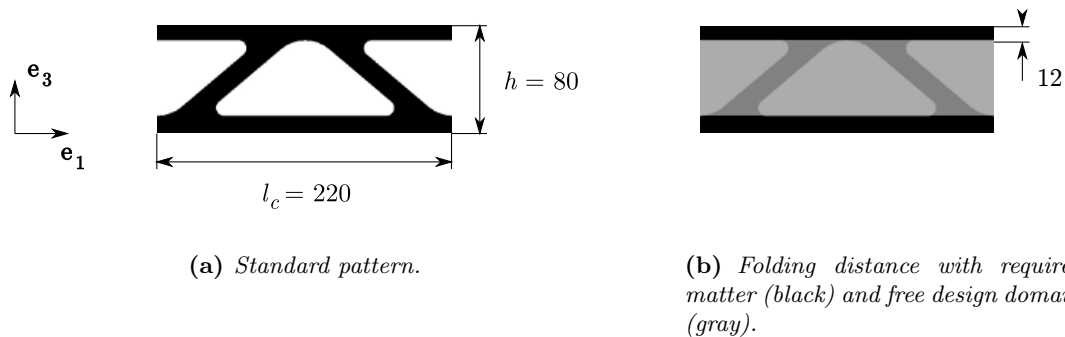
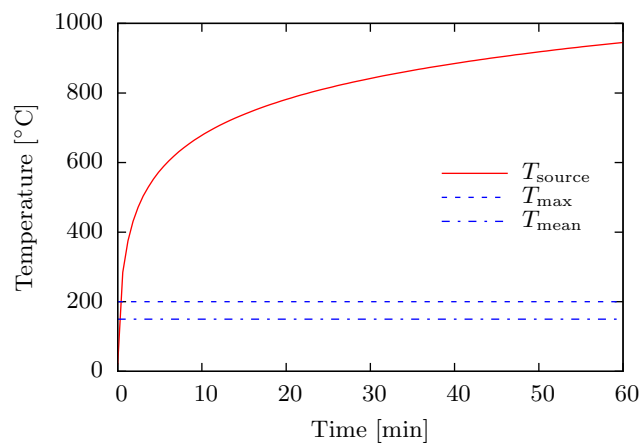


Figure 4.4: Shape and dimensions (in millimeters) of the unit cell of the standard geometry (a) and the representation of the constraint of imposed matter areas.

Frame 4.1 Modified standard IMO A754(18)

It is a slight modification of the standard ISO 834. It consists in exposing one side of the panel to a heating source and in measuring the temperature on the opposite face. The temperature of the source T_{source} must raise according to the curve below. The maximum temperature T_{max} and the mean temperature T_{mean} over the non-exposed face must remain, as long as possible, lower than respectively $+180^{\circ}\text{C}$ and $+140^{\circ}\text{C}$ above the room temperature. The criteria A-60 is fulfilled if these thresholds are maintained for 60 min.



Evolution of the temperature T_{source} of the convective source in contact with the exposed face, and limits on the maximal and mean temperatures on the non-exposed face (respectively 165°C and 205°C , for a room temperature of 25°C).

Moreover, some geometrical constraints have to be taken into account. The thickness of the panel is assumed to be fixed to $h = 80$ mm. The unit cell with length l_c is replicated in direction e_1 to obtain the whole stiffener design. Figure 4.4a shows the unit cell of the current geometry (as produced by *Sainte-Marie Constructions Isothermes*), which is denoted as *standard* design in the following. In addition, a process requirement has been mentioned about a minimal distance from the top-and-bottom borders to the closest holes. This *folding distance* of 12 mm will be excluded from the design domain — in which the matter is free to be organized — highlighted in gray on figure 4.4b. By doing this, we enforce this zone to remain fully dense.

4.1.3 Optimization problem

Objectives

The aim of this section is to translate the previous specifications on the stiffeners to an optimization written as the minimization of a global objective function $J(\Omega)$:

$$\min_{\Omega} J(\Omega) \quad (4.2)$$

The choice is done to include the mechanical and thermal objectives into the global objective function using a weighted product, such as :

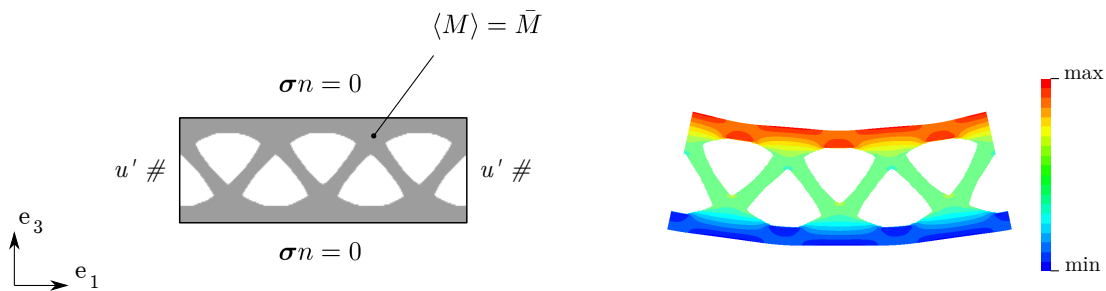
$$J(\Omega) = J_m^{(1-\alpha)} J_{th}^\alpha \quad (4.3)$$

where the mechanical and thermal objective functions, respectively J_m and J_{th} , are weighted with a factor α to take between 0 and 1 — unchanged during optimization. To build a Pareto front, several optimizations will be performed with varying α from 0 to 1, that is to say increasing the importance of thermal objective relative to stiffness objective.

Mechanical objective function As discussed in the previous section, the stiffeners must be designed in order to maximize the transverse-shear stiffness. The mechanical objective function is then the normalized shear compliance introduced in chapter 1 :

$$J_m(\Omega) = f \frac{Gh}{s_r} \quad (4.4)$$

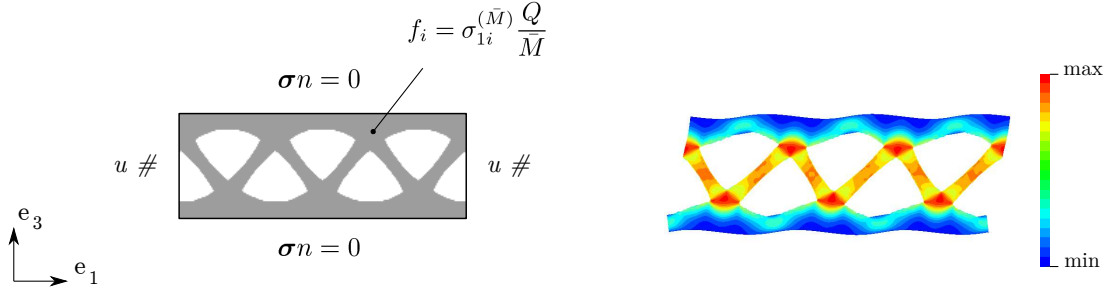
where G is the shear modulus of the constitutive material and $s_r = \frac{6}{5}$ the shear area ratio (section 1.4).



(a) The fluctuation u' is periodic on the sides. The stress is free on the top and bottom. An overall bending moment \bar{M} is applied.

(b) Component σ_{11} of the resulting stress field.

Figure 4.5: Computation of the stress field that results from applying a bending moment \bar{M} : (a) loading and boundary conditions ; (b) component σ_{11} of the resulting stress field.



(a) The displacement u is periodic on the sides. The stress is free on the top and bottom. A body force with components f_i is applied to get an overall shear force \bar{Q} .

(b) Component σ_{13} of the resulting stress field.

Figure 4.6: Homogenization problem to compute the transverse-shear compliance : (a) loading and boundary conditions ; (b) component σ_{13} of the resulting stress field.

Based on the homogenization method introduced in chapter 2 and in light of the results of chapter 3, the shear compliance is computed with a two-steps method. First, one solves the problem of the unit cell subjected to an overall bending moment \bar{M} with periodic condition for the fluctuation² on the right-and-left boundaries and stress-free condition on the top-and-bottom boundaries (figure 4.5a). Then, one solves the shear problem itself with applying the previous solution stress field as a body load (figure 4.6a). This method enables to apply an overall shear force \bar{Q} while keeping the correct boundary conditions : periodicity of the displacement on the right-and-left boundaries and stress-free condition on the top-and-bottom boundaries. The expression of the shear compliance is :

$$f = \frac{1}{l_c \bar{Q}^2} \int_{\Omega} \mathbf{C} \boldsymbol{\varepsilon} \cdot \boldsymbol{\varepsilon} dx \quad (4.5)$$

where \mathbf{C} is the isotropic Hooke's tensor of the constitutive material and $\boldsymbol{\varepsilon}$ the strain field solution of the shear problem illustrated on figure 4.6.

Since the mechanical objective function is directly proportional to the stress energy (eq. (4.4) and (4.5)), an analytical expression for the shape derivative exists and will be included into the transport equation of the level-set function (see section 3.2.1).

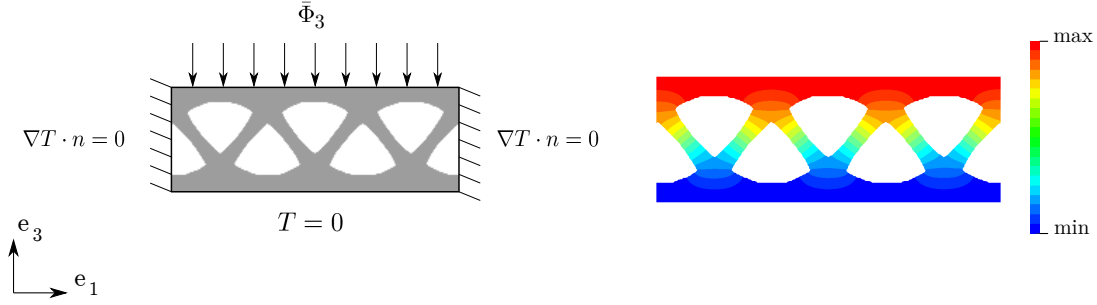
Thermal objective function Considering the conductive behavior of the stiffener during the test prescribed by the modified standard A754(18), the thermal objective function to minimize should be the effective thermal conductivity \tilde{k}_3 through the thickness of the

²The curvature is defined as an additional global degree of freedom, and takes place in the initial strain. Thus, the unknown variables are no more the displacements u but the fluctuations u' around the parabolic displacements generated by the curvature. See section 2.1 for further details.

panel. It can be estimated using the expression :

$$\tilde{k}_3 \approx \left(\frac{1}{l_c h \bar{\Phi}_3^2} \int_{\Omega} k \nabla T \cdot \nabla T \, dx \right)^{-1} \quad (4.6)$$

where k is the thermal conductivity of the constitutive material. The temperature T is solution of the steady state problem illustrated on figure 4.7, and $\bar{\Phi}_3$ is the heat flux applied on the top boundary.



(a) The sides are insulated. A through-thickness heat flux $\bar{\Phi}_3$ is applied on the top boundary. And the temperature of the bottom boundary is imposed.

(b) Resulting temperature field.

Figure 4.7: Through-thickness conductivity problem in order to identify \tilde{k}_3 : (a) boundary conditions ; (b) resulting temperature field.

However, by choosing the through-thickness conductivity as thermal objective function, instabilities appear in solving the Hamilton-Jacobi equation. Indeed, minimizing \tilde{k}_3 at a given step means removing matter where the thermal energy density is the largest. Consequently, the new geometry will present even larger energy density around these points since the amount of matter has locally decreased. By this way, the energy density becomes progressively singular. Its introduction into the evolution scheme as a transport velocity obviously generates numerical instabilities (e.g. figure 4.8).

To prevent this problem, one chooses the objective function to be the normalized in-plane thermal resistivity :

$$J_{\text{th}}(\Omega) = \tilde{\rho}_1 k \quad (4.7)$$

where k is the thermal conductivity of the constitutive material. The effective thermal resistivity $\tilde{\rho}_1$ is obtained by the following expression :

$$\tilde{\rho}_1 = \frac{1}{l_c h \bar{\Phi}_1^2} \int_{\Omega} k \nabla T \cdot \nabla T \, dx \quad (4.8)$$

where the temperature field T is solution of the steady state problem illustrated on figure 4.9a, and $\bar{\Phi}_1$ is the applied in-plane heat flux. In so doing, we assume that, as far as

geometrical distribution of matter is concerned, minimizing the through-thickness conductivity is equivalent to maximizing the in-plane conductivity. This is at least suggested by the restricted case of lamellar geometries shown on figure 4.10. The decrease of the through-thickness conductivity will be checked a posteriori.

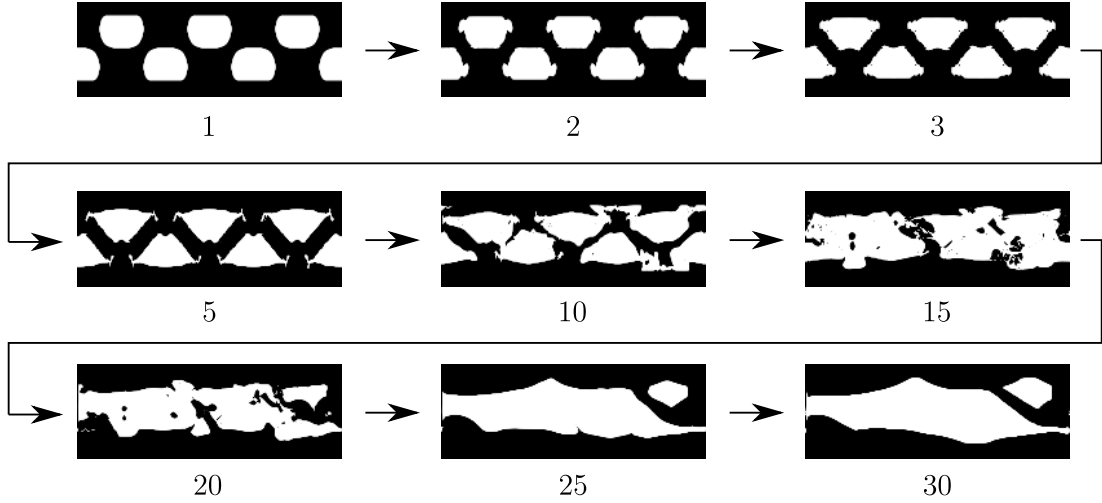
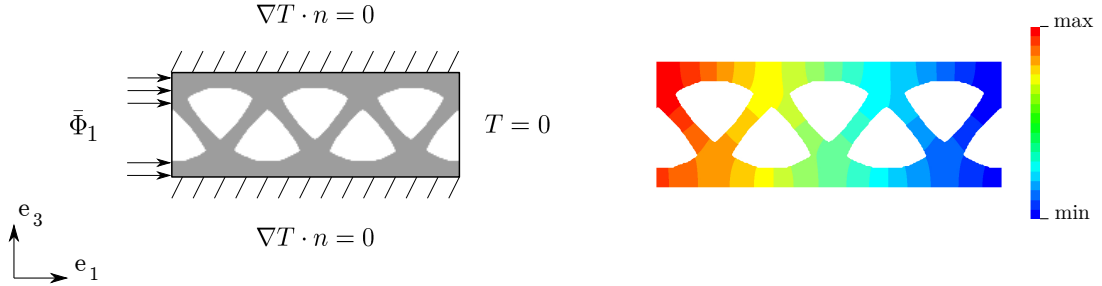


Figure 4.8: *Instabilities in the level-set evolution for a thermal objective function $J_{th}(\Omega) = k_3$. Other parameters are : $l = 0.1$, $\alpha = 0.4$, $\bar{\rho} = 0.6$.*



(a) *The top-and-bottom boundaries are insulated. An in-plane heat flux $\bar{\Phi}_1$ is applied on the left side. And the temperature of the right side is imposed.*

(b) *Resulting temperature field.*

Figure 4.9: *In-plane conductivity problem in order to identify \tilde{k}_1 : (a) boundary conditions ; (b) resulting temperature field.*

From the minimization of the objective function (4.7), it results an analytical expression for the shape derivative (Allaire, 2002) :

$$\frac{\partial J_{th}}{\partial \omega}(\Omega)(\theta) = \frac{1}{l_c h \bar{\Phi}_1^2} \int_{\partial \Omega} -(\mathbf{k} |\nabla T|^2) \theta \cdot \mathbf{n} \, ds \quad (4.9)$$

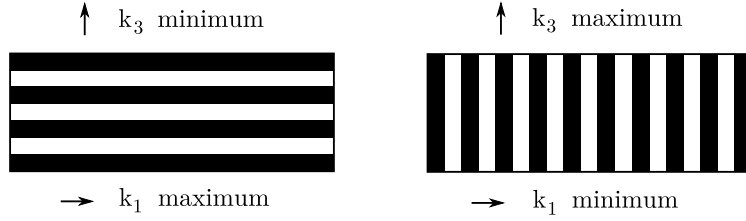


Figure 4.10: Illustration of the “orthogonality” of the through-thickness conductivity k_3 and the in-plane conductivity k_1 .

In addition with the mechanical shape derivative, the expression (4.9) will be included into the transport equation of the level-set function.

Constraints

The geometrical constraints mentioned in section 4.1.2 are implicitly integrated in the optimization problem through the choice of the design domain. The mechanical and thermal simulations — in order to evaluate the objective function as well as the velocity field for the transport equation — are performed on the whole unit cell. Whereas the design domain — on which is solved the transport equation — is reduced by the folding distance on both top and bottom borders (figure 4.4b).

The contribution of the stiffeners to the global mass of the panel is negligible. However, a constraint on the volume of matter is added to the optimization problem in order to ensure the stability of the optimization algorithm. It consists in imposing a value for the area fraction of matter $A_f(\Omega) = \bar{A}_f$, with :

$$A_f(\Omega) = \frac{\mathcal{A}(\Omega)}{hl_c} \quad (4.10)$$

where $\mathcal{A}(\Omega)$ is the area of the domain Ω . This constraint has to be taken into account explicitly by introducing a Lagrangian. One notices that the area fraction of the *standard* design is $A_f = 0.5$.

Summary

Finally, our translation of the specifications into an optimization problem is summarized in table 4.2 and can be written as :

$$\min_{\left\{ \Omega \text{ such as } \frac{\mathcal{A}(\Omega)}{hl_c} = \bar{A}_f \right\}} \left(\mathbf{f} \frac{Gh}{s_r} \right)^{(1-\alpha)} \left(\tilde{\rho}_1 k \right)^\alpha \quad (4.11)$$

with the computation of the displacements and temperature fields on the whole unit cell, including a design domain reduced by the folding distance on top and bottom borders.

	Specifications	Optimization problem
Objectives	Maximize the shear stiffness $(fGh/s_r)^{-1}$	Minimize the shear compliance $J_m = fGh/s_r$
	Minimize the thermal through-thickness conductivity \tilde{k}_3/k	Minimize the effective in-plane thermal resistivity $J_{th} = \tilde{\rho}_1 k$
Constraints		Area fraction constraint $A_f(\Omega) = \bar{A}_f$
	Thickness h and folding distance constraints	Definition of the simulation and design domains

Table 4.2: Summary of the stiffeners specifications and optimization problem.

In the following, results are presented in terms of performances of the design with respect to the two specifications, that is to say with respect to the normalized shear stiffness $(fGh/s_r)^{-1}$ and the normalized effective through-thickness conductivity \tilde{k}_3/k .

4.2 Shape optimization

The optimization algorithm described in section 3.1.2 is used to solve the problem (4.11). As an example, figure 4.11 shows the evolution of the stiffener's shape from an initial geometry defined by a sinusoidal level-set.

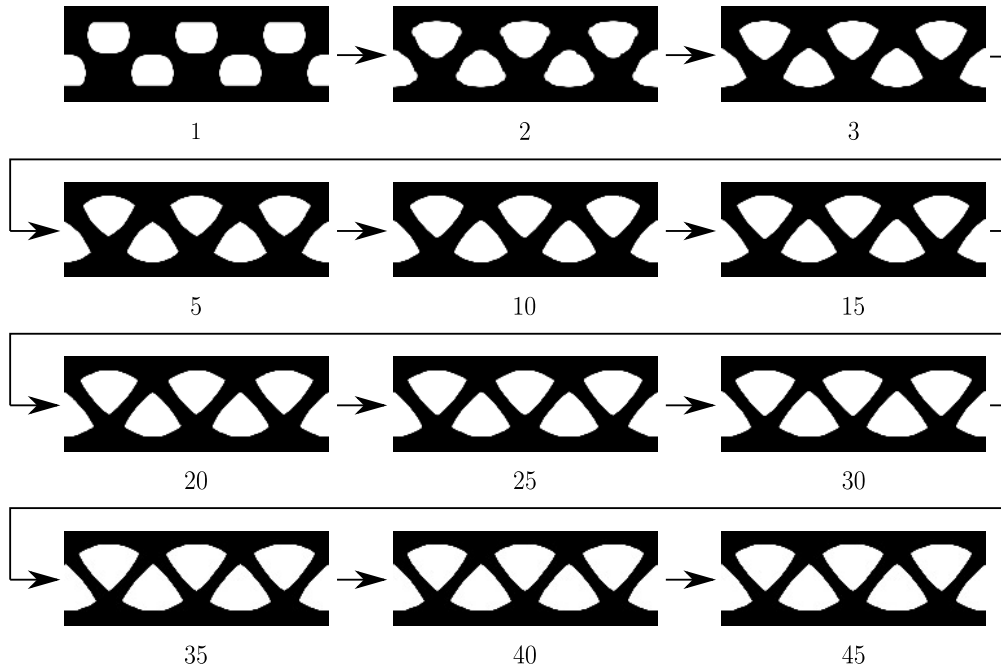


Figure 4.11: Evolution of the design from the starting geometry (iteration 1) to the optimized geometry (iteration 45) for parameters : $\alpha = 0.2$, $\bar{A}_f = 0.6$.

Figures 4.12a and 4.12b plot respectively the evolution of the area fraction and that of the normalized properties during the simulation of figure 4.11. As mentioned in section 3.2.1, the area fraction is monitored at each iteration with introducing a Lagrange coefficient. The initial value is purposely imposed higher than the final target value, in order to improve the optimization efficiency. In the present case, the area fraction at step 1 is 0.7 and decrease progressively down to 0.6 at step 30.

Conductivities in both directions and shear stiffness decrease with the area fraction, as shown on figure 4.12b. One can notice the impact of optimization with comparing the slope of decrease of each conductivity, which is steeper for the through-thickness conductivity k_3 . This is not obvious for the mechanical objective. A decrease of the stiffness is observed whereas optimization should increase it. This is due to its large sensitivity with respect to the area fraction. Thus, optimization does not increase the stiffness but limits its decrease caused by the lowering of the area fraction.

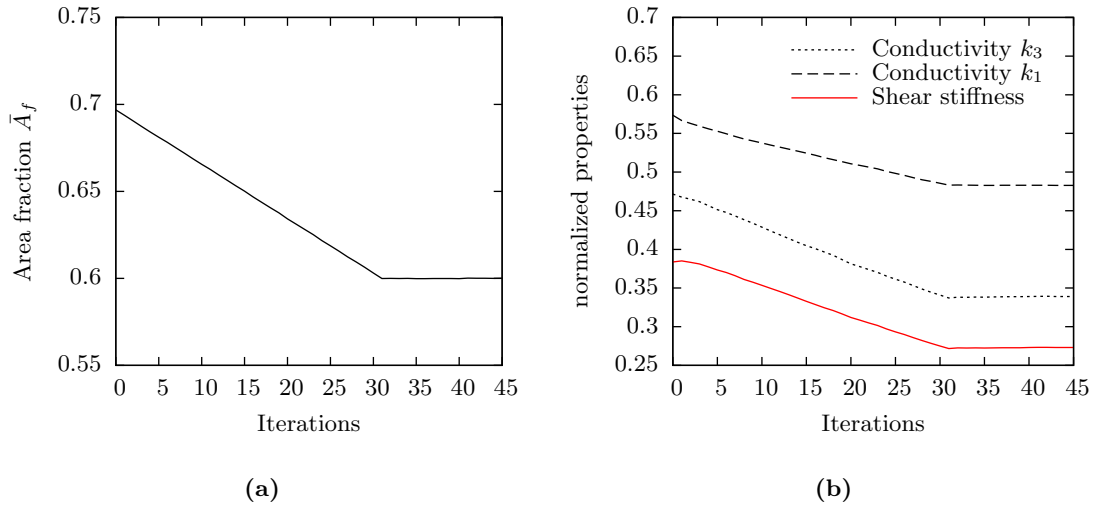


Figure 4.12: Evolution during optimization of : (a) the area fraction ; (b) the normalized effective properties. Data correspond to design evolution displayed on figure 4.11.

Figures 4.13 and 4.14 show respectively the mechanical and the thermal energy density for the simulation presented on figure 4.11. Both mechanical and thermal energy densities tend to increase with iterations since the amount of matter decreases. The mechanical objective function encourages the adding of matter, even more where the energy density is large. The thermal objective function encourages the removing of matter, even more where the energy density is large. From iteration 20, the two energy density fields look similar and a stability occurs between the driving forces for both objective functions. This balance is related to the weighting factor α .

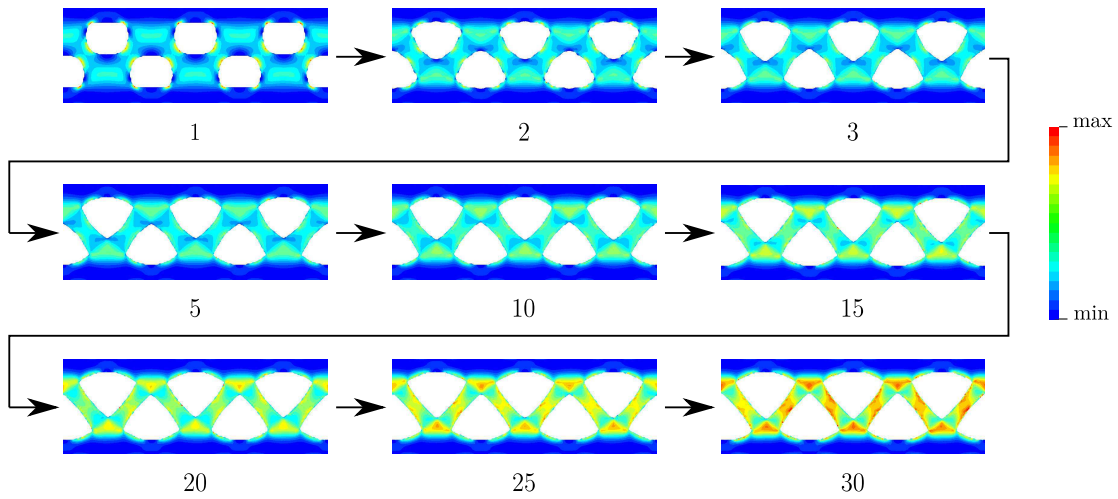


Figure 4.13: Transverse-shear energy density versus the iterations of simulation figure 4.11. All iterations are plotted with the same color scale.

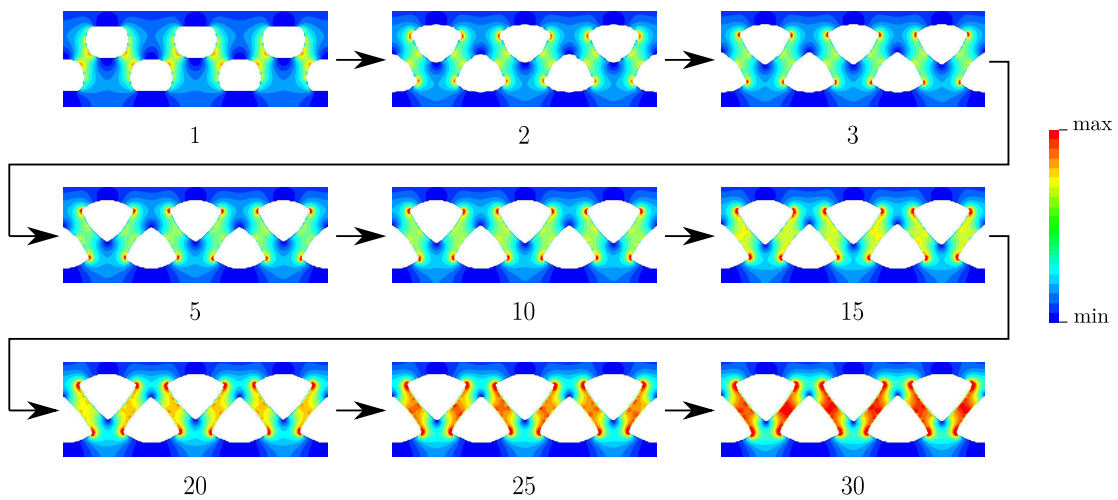


Figure 4.14: Thermal energy density (applying an in-plane flux) versus the iterations of simulation figure 4.11. All iterations are plotted with the same color scale.

4.2.1 Influence of the relative importance between thermal and mechanical objectives

The weighting factor α , from eq. (4.3), is a parameter that controls the relative importance given to the thermal objective function with respect to the mechanical one. It varies from 0 (mechanical-only) to 1 (thermal-only). Figure 4.15 shows five geometries optimized with various values of α , and their location on the stiffness–conductivity chart. An arrow specifies the values of α , while another shows the direction of improvement : increasing shear stiffness and decreasing through-thickness conductivity. The set of optimized geometries materializes an extreme limit in this direction that can be reached with any geometry of area fraction $\bar{A}_f = 0.6$. It can be considered as an estimated Pareto front for stiffness–conductivity with this given area fraction.

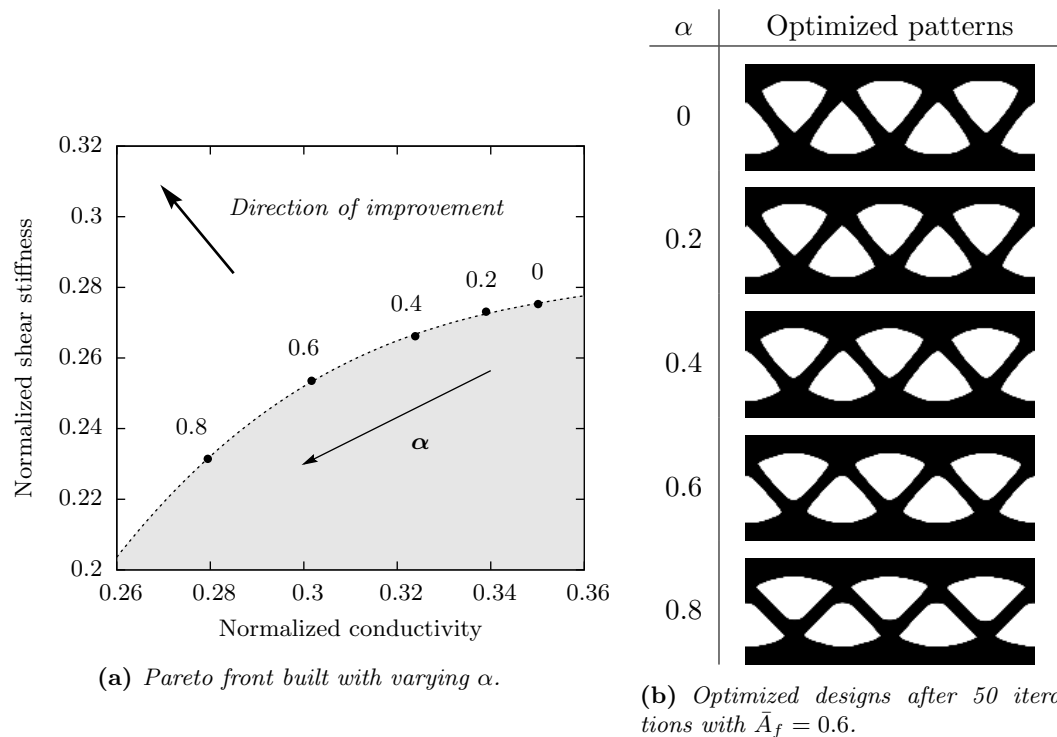


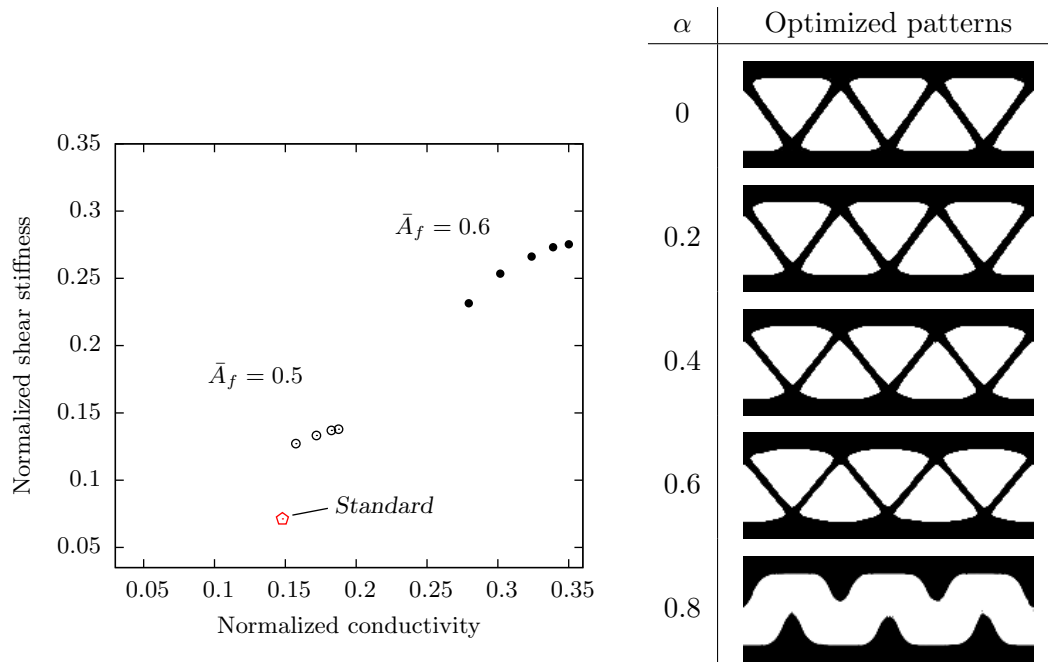
Figure 4.15: Influence of the weighting factor α on the optimized designs and their properties. Results obtained from the starting geometry of figure 4.11 and area fraction $\bar{A}_f = 0.6$.

The variations of geometry might appear visually negligible but the resulting variation in performance are not. Between the design optimized with $\alpha = 0$ and that with $\alpha = 0.8$, one can observe a decrease of about 20% of the conductivity and 10% of the shear stiffness. The value $\alpha = 0.2$ is widely used in the following, with keeping in mind that the conductivity could be reduced by increasing the weighting factor, i.e. by giving more importance to thermal design criteria.

The case $\alpha = 1$ is not represented here, being a singular situation. In this case, optimization leads to divide the geometry into two parts disconnected (up and bottom). Thus, both the through-thickness conductivity and the shear stiffness become zero. It is the result of totally neglecting the stiffness design criteria, and is clearly an unrealistic geometry.

4.2.2 Influence of the prescribed area fraction

The control of the area fraction is implemented using a Lagrangian method as detailed in section 3.2.1. Two values have been compared $\bar{A}_f = 0.5$, which is the area fraction of the *standard* design, and $\bar{A}_f = 0.6$. Figure 4.16a is the same stiffness–conductivity chart than figure 4.15 with reporting the additional designs with an area fraction $A_f = 0.5$ (4.16b).



(a) Pareto front built with varying α with $\bar{A}_f = 0.5$ and 0.6.

(b) Optimized designs after 50 iterations with $\bar{A}_f = 0.5$.

Figure 4.16: Influence of the weighting factor α on the optimized designs and their properties. Results obtained from the starting geometry of figure 4.11 and area fraction $\bar{A}_f = 0.5$ or 0.6.

Note that for the case $\alpha = 0.8$, the geometry is divided into two parts. Indeed, the weighting factor dedicated to the mechanical objective ($\alpha - 1 = 0.2$) is too small to enforce some matter to sit in the middle of the sandwich. From the iteration when the geometry splits, stiffness and conductivity becomes zero and optimization is no more possible.

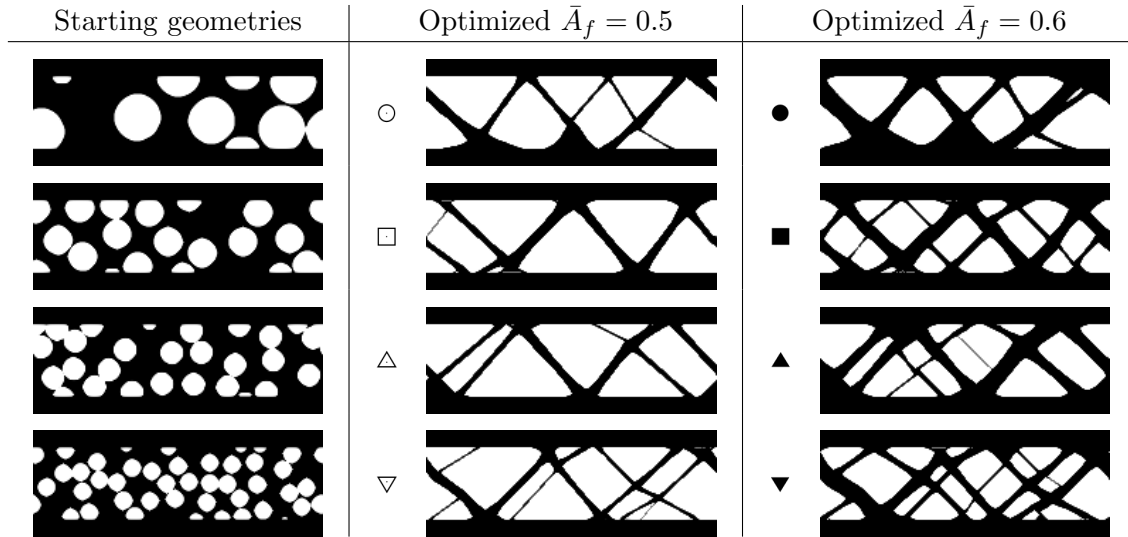
As already observed on figure 4.12a, reducing the area fraction decreases both the shear stiffness and the conductivity. The present results have the same area fraction

than the design *standard* but provide a larger shear stiffness and only a slightly larger through-thickness conductivity.

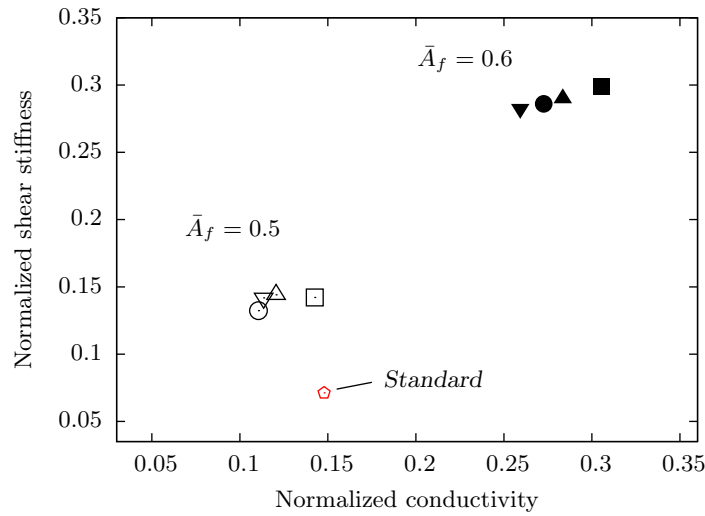
4.2.3 Influence of the initial geometry

In the previous examples, shapes evolve but topology (number of holes) remains constant excepted for extreme value of α . Figures 4.17 and 4.18 show different initial geometries and the corresponding optimized geometries for $\bar{A}_f = 0.5$ and 0.6. Each optimized design matches to a point on the stiffness–conductivity chart.

The Hamilton-Jacobi equation used to transform the level-set function cannot create new holes. This disability becomes here an advantage since it enables to control the maximum number of holes, and so to optimize inside a subset of feasible geometries. The initial geometry implicitly defines a region into the set of admissible geometries, in which a local optimum is found by the gradient descent algorithm. We can consider initially random and regular topologies as starting conditions. Figure 4.17 shows optimized designs with a similar stiffness–conductivity optimality, such that they form a Pareto front. These optimized designs are local optima around random initial geometries. The regular initial geometries (figure 4.18) reveal special symmetries that make a difference with the previous random initializations. The topological refinement (increasing the holes number of the initial geometry) globally tends to improve the optimality of the multi-functional objective (toward the upper left corner of the chart).

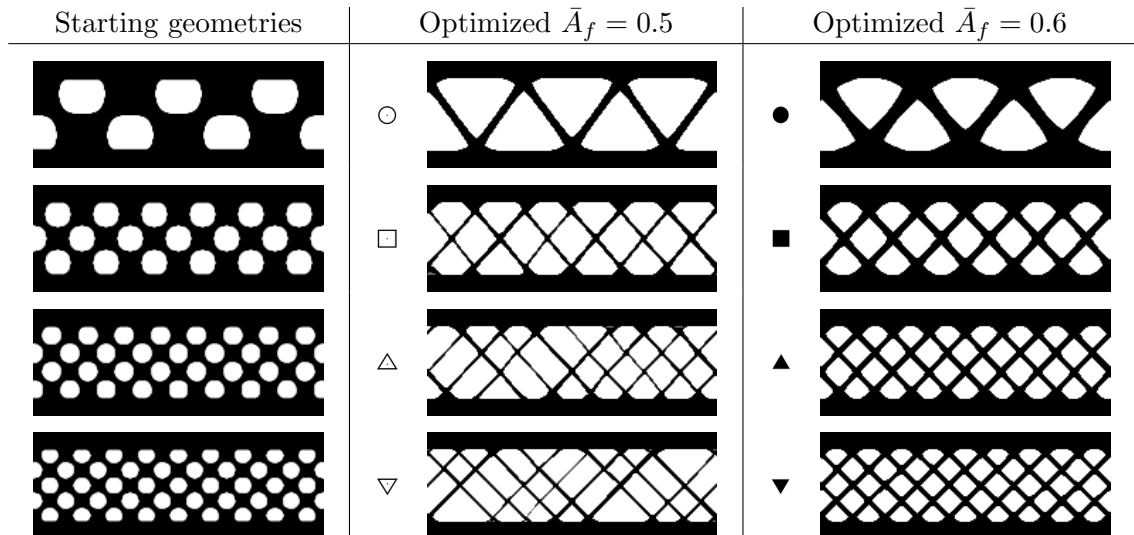


(a) Optimized designs after 50 iterations, with different initial disordered geometries and area fractions.

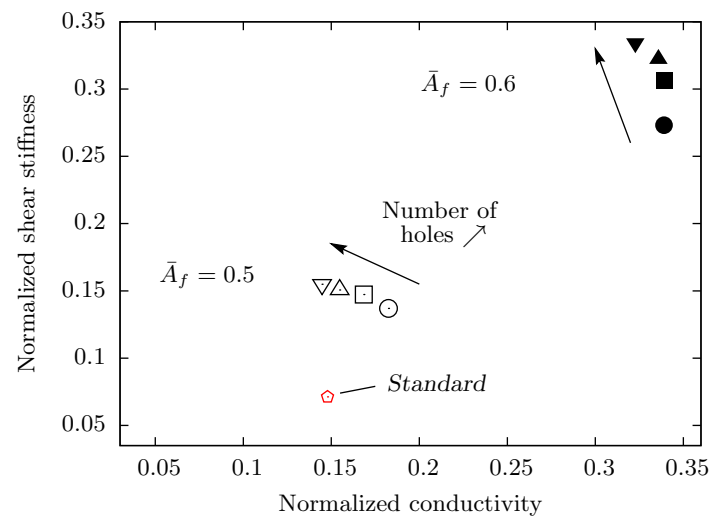


(b) Location of the above geometries on the stiffness-conductivity chart. Symbols are defined in (a).

Figure 4.17: Influence of the starting disordered geometries on shear stiffness and through-thickness thermal conductivity, with parameters : $\alpha = 0.2$ and $\bar{A}_f = 0.5$ or 0.6 .



(a) Optimized designs after 50 iterations, with different initial regular geometries and area fractions.

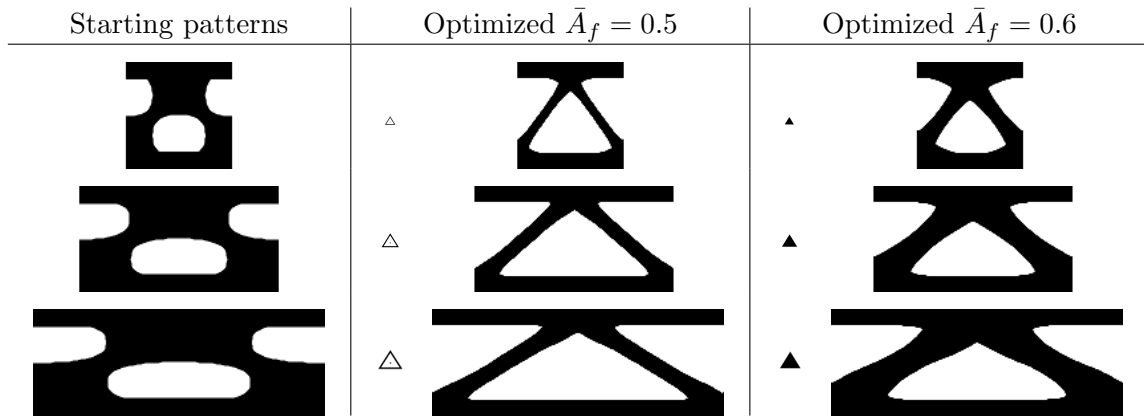


(b) Location of the above geometries on the stiffness–conductivity chart. Symbols are defined in (a).

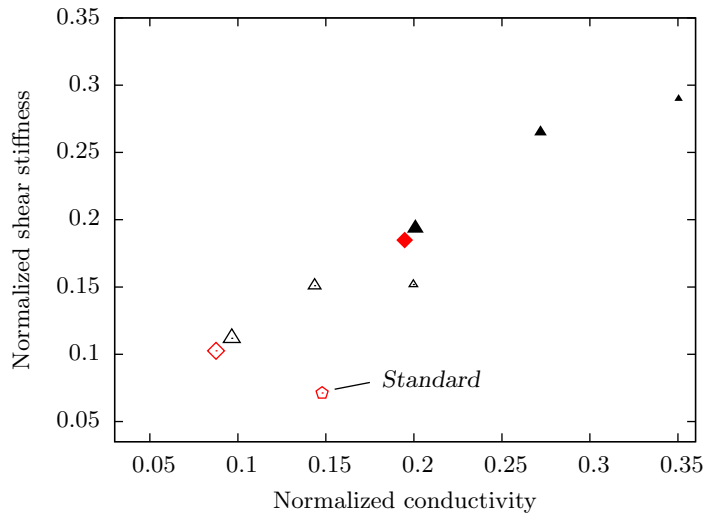
Figure 4.18: Influence of the starting regular geometries on shear stiffness and through-thickness thermal conductivity, with parameters : $\alpha = 0.2$ and $\bar{A}_f = 0.5$ or 0.6 .

4.2.4 Influence of the unit cell shape factor

The height of the periodic cell is imposed by the sandwich panel thickness. Then, the shape factor is controlled by the cell length l_c . Figures 4.19a and 4.21a presents optimized designs obtained from different initial geometries : *standard*, triangle (denoted with the sign \triangle) and lozenge (denoted with the sign \diamond).



(a) Optimized geometries obtained from the initial geometry \triangle (cell length $l_c = 80, 150$ and 220 mm) with area fraction constraint $\bar{A}_f = 0.5$ or 0.6 .



(b) Location of the above geometries in the stiffness-conductivity chart. Symbols are defined in(a).

Figure 4.19: Influence of the shape factor on shear stiffness and through-thickness thermal conductivity, with initial geometry \triangle or standard, and parameters : $\alpha = 0.2$ and $\bar{A}_f = 0.5$ or 0.6 .

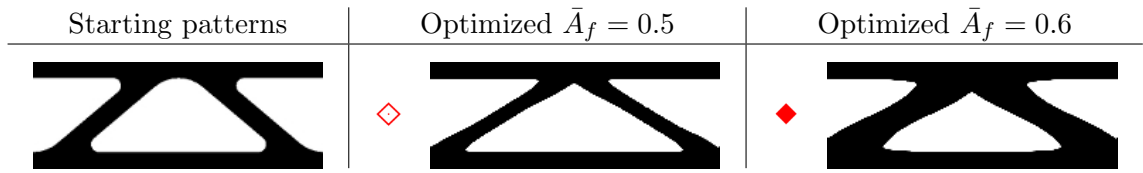
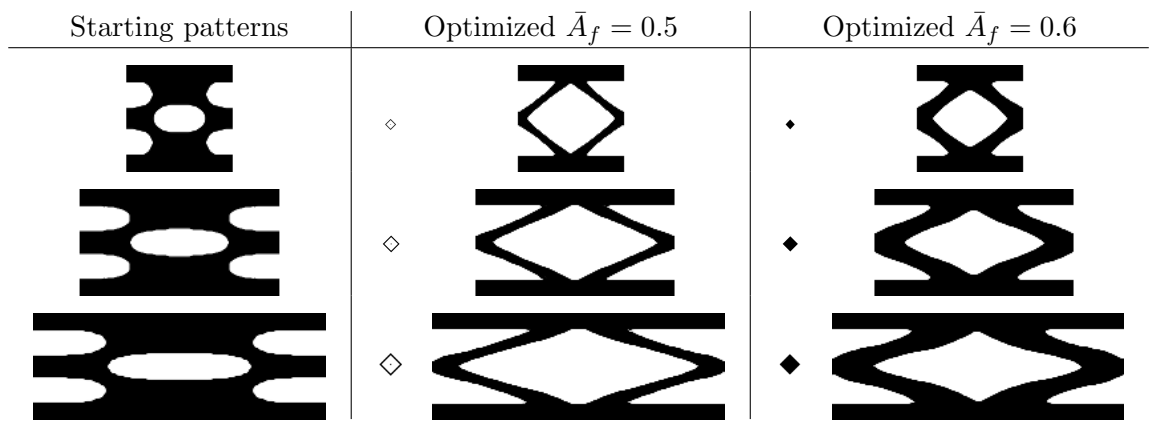
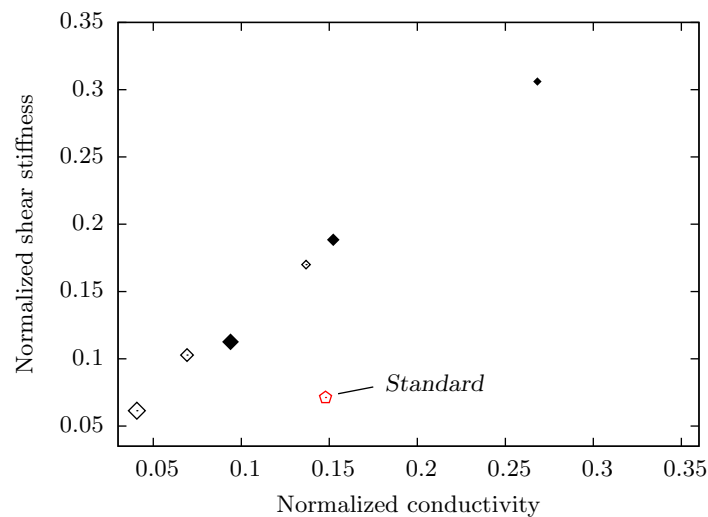


Figure 4.20: Optimized shapes obtained from the initial geometry standard, with an area fraction constraint $\bar{A}_f = 0.5$ or 0.6 .

Three shape ratios are simulated with scaling the initial geometry in the horizontal direction e_3 such that $l_c = 80, 150$ and 220 mm. Though the topology has a limited effect on the properties, the shape ratio enables large shifts on the charts 4.19b and 4.21b.



(a) Optimized geometries obtained from the initial geometry \diamond (cell length $l_c = 80, 150$ and 220 mm) with area fraction constraint $\bar{A}_f = 0.5$ or 0.6 .



(b) Location of the above geometries in the stiffness–conductivity chart. Symbols are defined in(a).

Figure 4.21: Influence of the shape factor on shear stiffness and through-thickness thermal conductivity, with initial geometry lozenge, and parameters : $\alpha = 0.2$ and $\bar{A}_f = 0.5$ or 0.6 .

The tendency observed on both figure 4.19 and 4.21 is that large unit cells have smaller conductivity but smaller stiffness. Moreover, it seems to provide more degrees of freedom — the design domain is larger — which results in an increase in optimality, especially for initial geometry Δ . For instance on figure 4.19b, the optimized design with $l_c = 220$ mm and $\bar{A}_f = 0.6$ provides a similar effective conductivity and a larger shear stiffness than the one with $l_c = 80$ mm and $\bar{A}_f = 0.5$.

Comparison of initial geometry Δ and *standard* (figure 4.19) shows that distinct initial geometries with same topology and shape ratio will give the same optimized design. This result is comforting.

4.2.5 Summary

The influence on optimization of the weight factor, the area fraction, the initial geometry and the shape factor of the periodic cell have been systematically investigated. The table 4.3 summarizes the influence of each parameter on the shear stiffness, the through-thickness thermal insulation and the optimality. The optimality qualify the distance to the theoretical Pareto front, in other words, the quality of the stiffness–insulation compromise.

	Shear stiffness	Through-thickness thermal insulation	Optimality
Increasing the weighting factor α	--	++	0
Increasing the area fraction $\bar{\rho}$	+++	---	0
Increasing the number of holes in the initial geometry	+	+	+ for regular initial geometries
Increasing the cell length l_c	--	+++	+

Table 4.3: Summary of the effect of different control parameters on the efficiency of the optimization strategy.

4.3 From optimization results to prototype panels

Numerous designs have been obtained in the previous section and it is now necessary to select among these geometries the ones that are the most promising. Then, the selected designs have to be adjusted in order to be integrated into prototype panels and produced.

4.3.1 Selection of promising designs



Figure 4.22: Promising geometries selected on figure 4.23 for a further analysis.

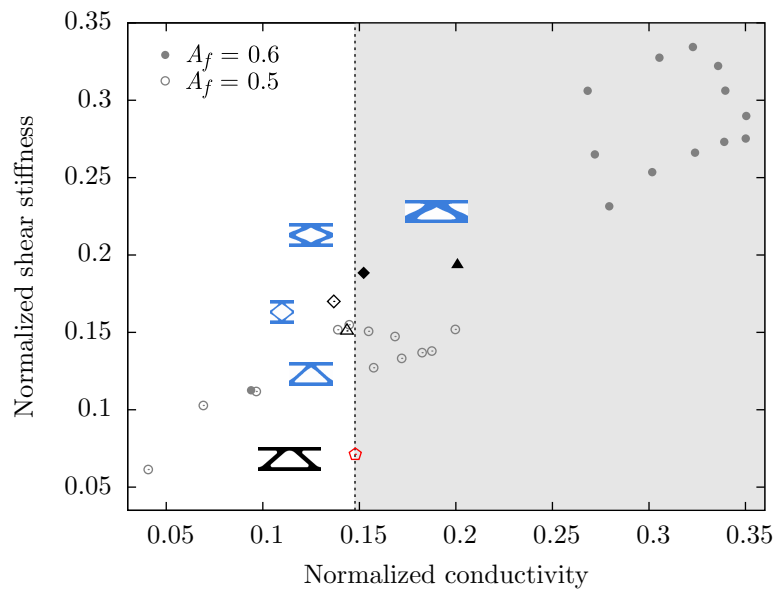


Figure 4.23: Selection of four interesting optimized geometries that provide a similar conductivity than the standard pattern and a larger stiffness.

The goal of *Sainte-Marie Constructions Isothermes* is to find a design which, compared to the standard one, would improve the mechanical properties while keeping a similar insulating performance. Figure 4.23 gathers all the previously optimized designs as well as the standard design on the stiffness–conductivity chart. A vertical line divides the chart into two parts : the part where conductivity is smaller than that of the standard design (white), and the part where conductivity is larger (gray). The selection rule is to get a design with a conductivity around this border and a shear stiffness as high as possible. The four enhanced dots represents the optimized designs selected to be integrated into

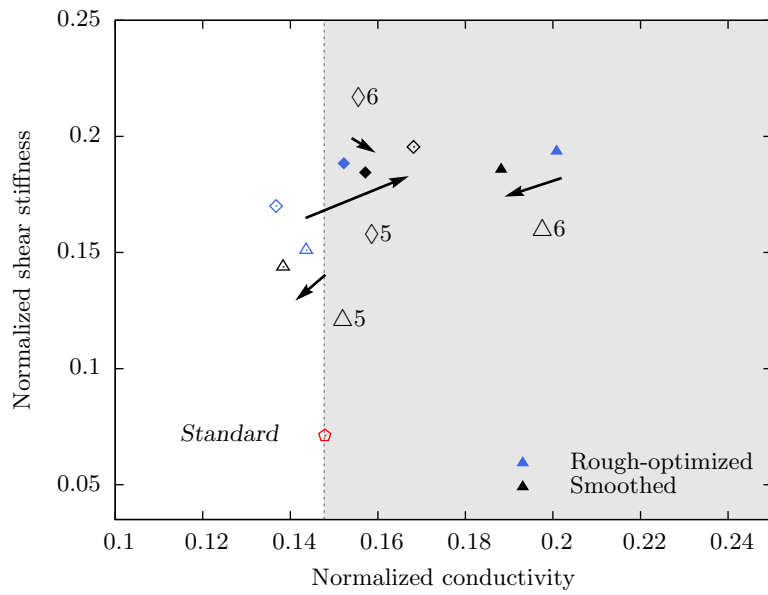
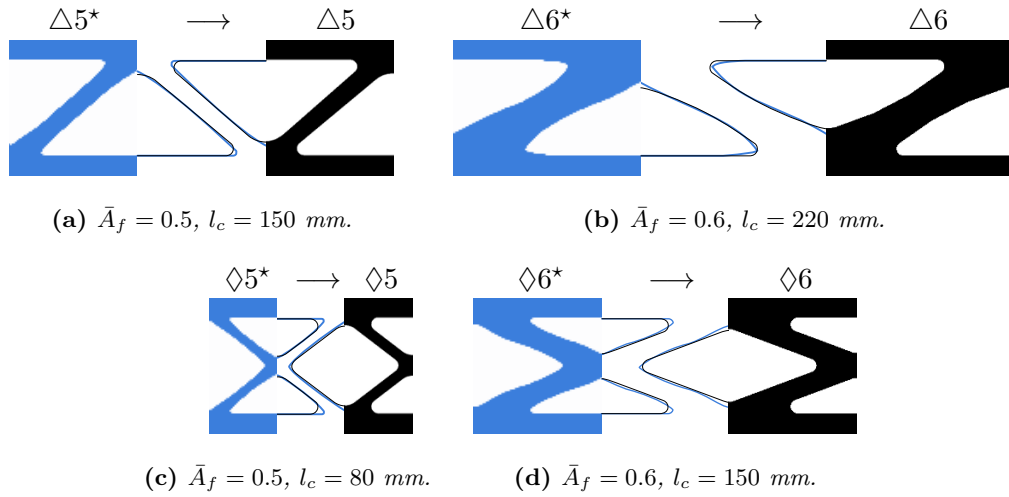
prototypes and produced. Figure 4.22 shows the selected geometries and their reference name. They are topologically gathered in two groups : the “ \triangle -shape” (*Standard*, $\triangle 5$ and $\triangle 6$) and the “ \diamond -shape” ($\diamond 5$ and $\diamond 6$).

4.3.2 Adjusting to process requirements

To produce prototypes from the selected optimized designs, the optimal geometries computed have to be “adjusted”. That means that the geometrical features have to be simplified such that they meet the requirements of the laser cutting. In order to do so, the design edges have to be based on straight lines, circles and simple splines. In addition, sharp angles are smoothed in order to limit weaknesses in damaging and fatigue phenomenon, which have not been taken into account in the optimization problem. Figures 4.24a-d shows the four selected designs rough-optimized (blue) and smoothed (black).

Changes due to smoothing obviously affect the mechanical and thermal properties. Figure 4.24e locates on the properties chart the selected design before and after this adjusting operation. It reveals no tendency in the properties shifts, which remain relatively small except for the design $\diamond 5$. In the case of this design with a small cell length, the smoothing of sharp angles implies relatively large modifications that are amplified by periodicity.

The previous performances are estimated by computing the shear compliance and the effective through-thickness conductivity with 2D finite element simulations. The next step consists in validating the simplifying hypothesis that have been done to write the optimization problem. Three-dimensional transient thermal analysis and bending test have to be performed on the prototypes panel in order to confirm the improvement of the performances.



(e) Shift on the properties chart of the four geometries, due to the above smoothing operation.

Figure 4.24: Adjusted designs to be conformed with the laser cutting process. Rough-optimized designs (blue) and adjusted designs (black).

4.4 Prototype panels performances

In the previous section, optimization results and discussions on the influence of each control parameters of the optimization procedure were presented. Some promising geometries have been selected and “adapted” in order to cope with process requirements of laser cutting. In this section, thermal and mechanical properties of prototype panels integrating new designs of stiffener are studied. First, a numerical analysis of the transient thermal behavior of the panels is discussed. Then, scale-one samples (3 m × 34 cm) have been produced and tested under a four-point bending loading.

4.4.1 Thermal transient analysis

In section 4.1.2, the specification on the insulating performance of the panel has been translated into a specification on the thermal conductivity of the stiffener. It was assumed the response of the stiffener to be mainly quasi-static. To check the relevance of the steady state assumption, three-dimensional transient analysis of the whole sandwich panel (skins, stiffeners and mineral wool) have been performed by *Sainte-Marie Constructions Isothermes*. The insulation test prescribed by the modified standard 754(18) of the IMO (detailed in section 4.1.2) is simulated on the 3D periodic cell of the panel as shown on figure 4.25. One face is exposed to a convective source with a progressively increasing temperature. The non-exposed face is in contact with the ambient air.

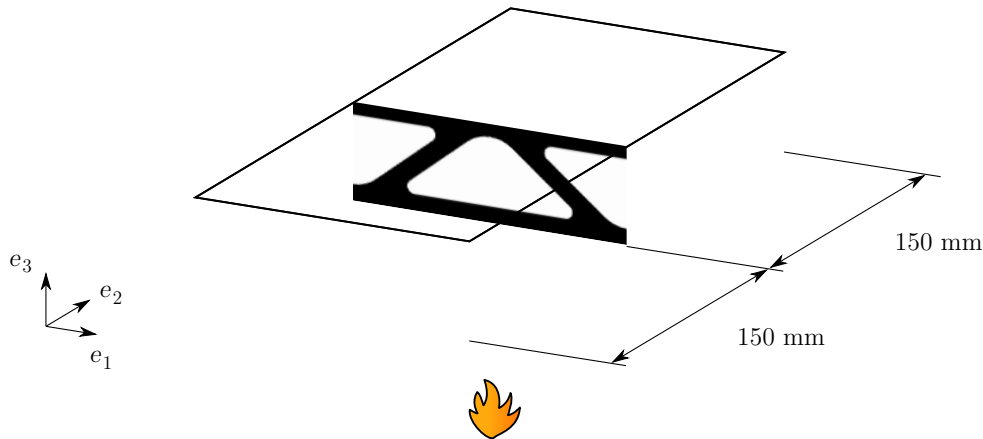


Figure 4.25: Sketch of the three-dimensional unit cell for the transient thermal simulations.

Figure 4.26 compares the temperature fields on the non-exposed face after 60 min for all stiffener designs. The maximal temperature is obtained right above the stiffener, at the center of the unit cell. And the minimum is observed on a line at equidistance of the stiffeners (top and bottom edge of the faces presented on figure 4.26).

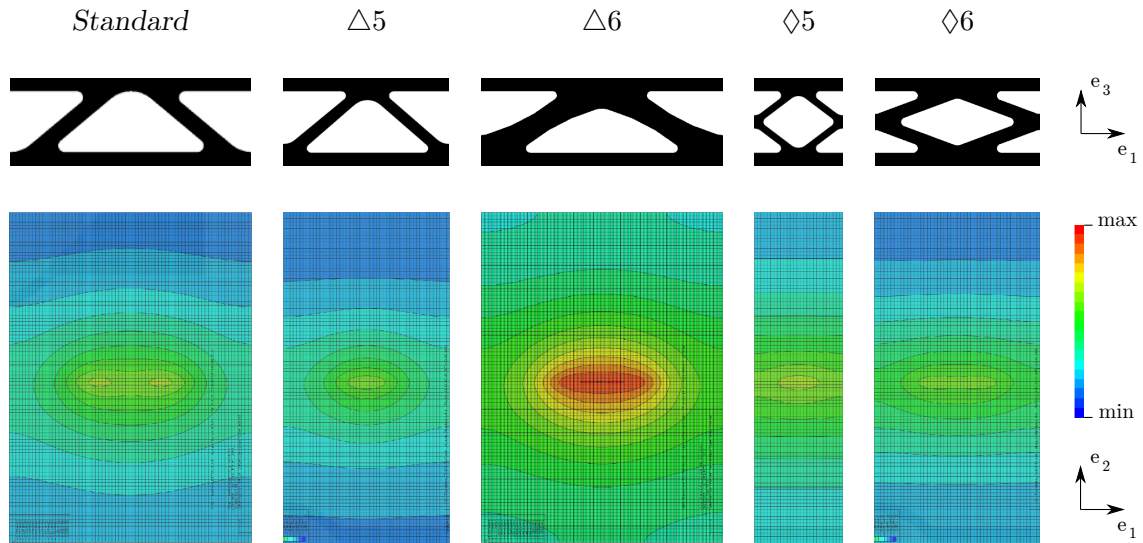


Figure 4.26: Three-dimensional transient thermal analysis of the standard design and the prototype designs : temperature field on the non-exposed face corresponding to each design after 60 min.

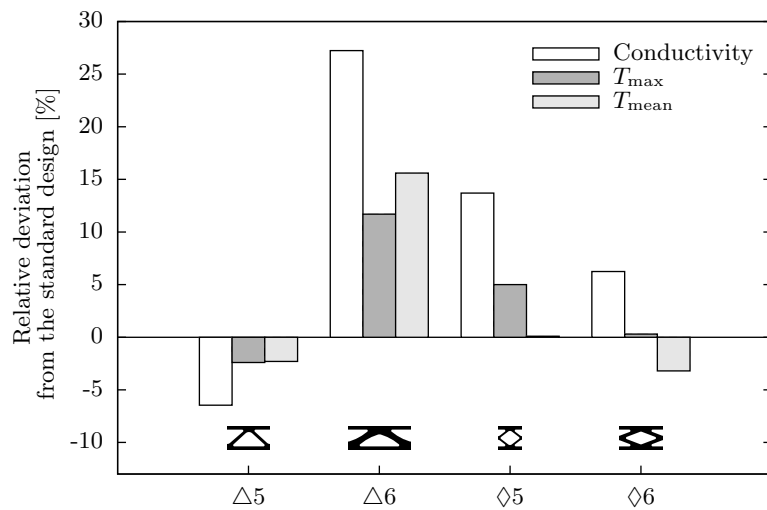


Figure 4.27: Relative difference in conductivity, maximum temperature and mean temperature, with taking the standard design as reference.

On figure 4.27, the relative deviation from the standard design for conductivity (2D linear simulations) is compared to the relative difference on both the maximum and the average temperatures over the non-exposed face (3D transient simulations). There is no precise correlation between results in conductivity and temperatures, because transient analysis is done with taking into account faces and mineral wool that should hide partially the influence of the stiffener. But the same tendency is globally observed and more precisely, conductivity and maximal temperature rank the prototype designs in the same

order.

Finally, the estimations done for optimizing seem relevant. And the selection strategy, that is to get a new design with an equivalent insulation performance, is satisfied by all except one. Only the design $\Delta 6$ could be filtered out because of the high maximum and mean temperatures computed.

4.4.2 Prototypes testing

This section presents an experimental study of the four-point bending behavior of the prototype panels. Following the method detailed in section 1.5, the flexural and shear compliance components are deduced from the four-point bending compliances for three different shear lengths. Few tests have been performed up to damage of the panel, in such a way that a discussion is proposed on the influence of the stiffener design on the damage mode and the ultimate force.

Samples

The four stiffener designs from section 4.3 have been produced by *Sainte-Marie Constructions Isothermes* and integrated into sandwich samples (figure 4.28).



Figure 4.28: Sandwich samples with optimized and standard stiffeners.

The samples are made with two steel faces (with thickness $t = 3$ mm) and two stiffeners cut out in stainless steel plates (thickness 2 mm). Geometry and size are drawn on figure 4.29. Two specimens have been produced for each design (standard, $\Delta 5$, $\Delta 6$, $\diamond 5$ and $\diamond 6$; see figure 4.26).

Experimental setup

In order to identify independently the flexural and shear compliance components, three four-point bending tests are performed for each sample with varying the shear length L (see section 1.5). The lengths (recalled on figure 4.30) for the three setups (A , B and C) are given into table 4.4. The upper and lower pads are flat and their width is $w_p = 100$ mm.

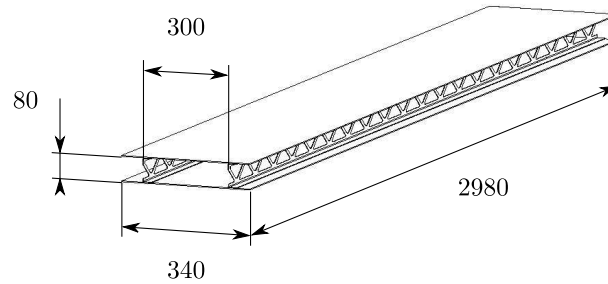


Figure 4.29: Geometry and size in millimeters of the sandwich samples produced and tested.

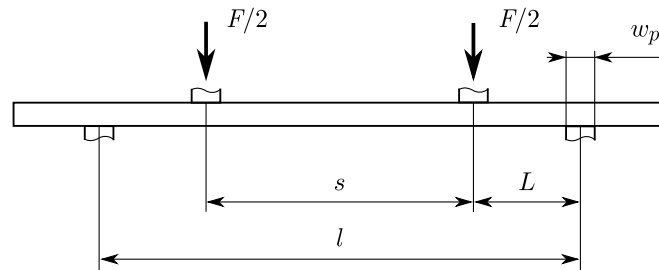


Figure 4.30: Four-point bending test setup and lengths : upper span s , lower span l and shear length L .

	s	l	L
Setup A	1400	2600	600
Setup B	1000	2200	600
Setup C	600	1800	600

Table 4.4: Lengths in millimeters of the four-point bending tests for the three setups.

The test is performed by applying a vertical displacement with the central cylinder. The resulting force is transferred through a ball-and-socket joint to a transmitter, that lies itself on the upper load points (figure 4.31). The transmitter is an I-shape beam sufficiently stiff to provide a negligible deflection during the test in comparison with that of the panel.

During the test, displacement and force of the cylinder are continuously measured with sensors. In addition, small stickers (a white cross on a black background ; see figure 4.28) are regularly spaced on the visible side of the upper and lower faces. Photos of this visible side are shot every 10 seconds. Digital image correlation techniques enable to post-treat the images in order to extract the displacement of each sticker during the bending test. Image analysis tools were adapted from ImageJ³ plugins (Lhuissier, 2009, PhD thesis).

³Image processing and analysis software in Java, under GNU license.

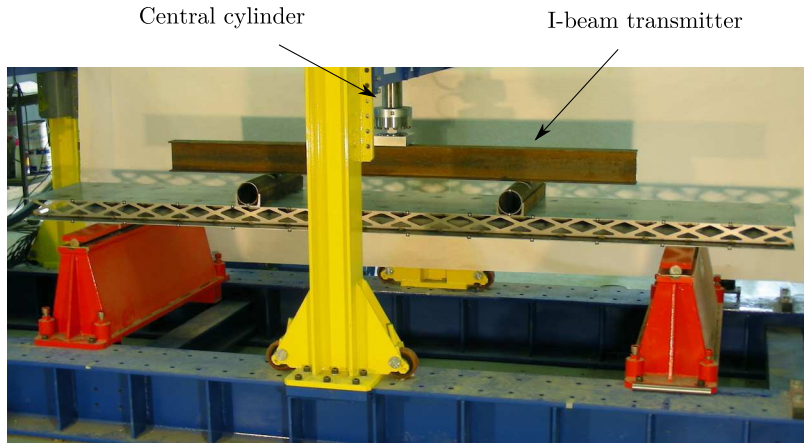


Figure 4.31: Four-point bending test setup. A central cylinder applies a displacement on the two upper load points through the transmitter.

Elastic properties

For each of the ten samples, two loading–unloading sequences were applied. The maximal displacement is chosen in order to stay in the elastic domain and not to damage the samples. The four-point bending compliances S_{4p} are measured on the unloading slope of the force–deflection curve. Figure 4.32 plots the measured compliances for all the samples and for each setup. As detailed in section 1.5, the variation of the four-point bending compliance versus the lower span length l should be linear. The slope only depends on the flexural compliance, whereas the intercept depends on both flexural and shear compliances. Since the contribution of the core to the flexural modulus is negligible with respect to that of the faces, it is assumed to be unchanged for all stiffener designs. It is estimated by :

$$d = \frac{1 - \nu^2}{E} \frac{12}{h^3(1 - (1 - f)^3)} \quad (4.12)$$

where $E = 210$ GPa is the Young’s modulus of the steel faces, $\nu = 0.33$ the Poisson ratio, and $f = 2t/h$ the volume fraction of the faces.

Then, the shear compliance is obtained from the fitted intercept S_0 :

$$f = \frac{2}{3}L^2d + \frac{2}{L}S_0 \quad (4.13)$$

where L is the shear length (figure 4.30).

Dots on figure 4.32 result from the average of few unloading force–deflection slopes, measured on two samples for each design and each setup. Lines are fitted on the data with keeping the analytical slope that just depends on the flexural compliance, eq. (4.12). The samples with design $\Delta 5$ have been unfortunately slightly damaged during the loading–

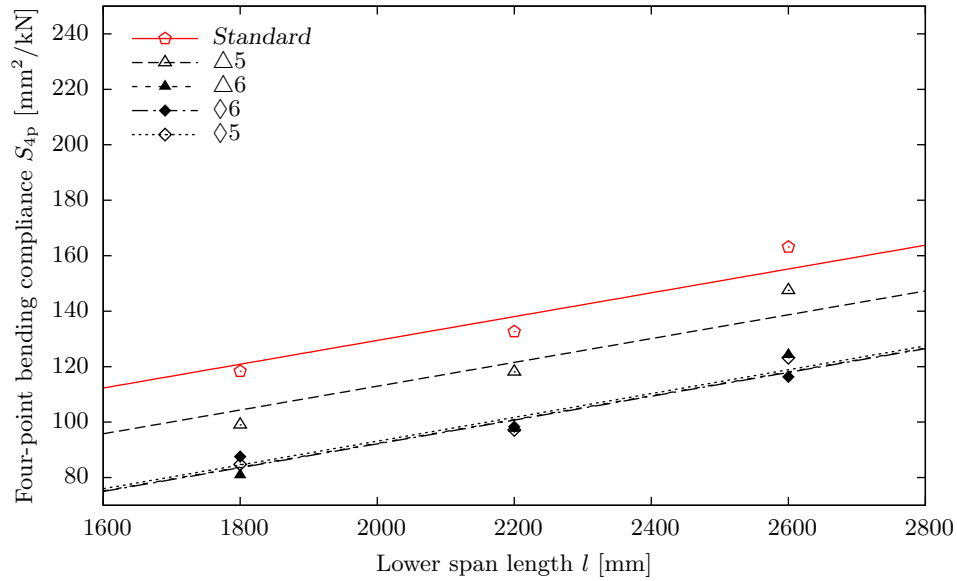


Figure 4.32: Variation of the four-point bending compliance versus the lower span length for the five designs. The compliances are measured on the unloading slopes of the force–deflection curve. A linear fit is done for each design with the same slope that just depends on the flexural compliance, eq. (4.12).

unloading sequences since the buckling limit is particularly low. That could explain the abnormal compliance for setup A with the largest lower span value $l = 2600$ mm.

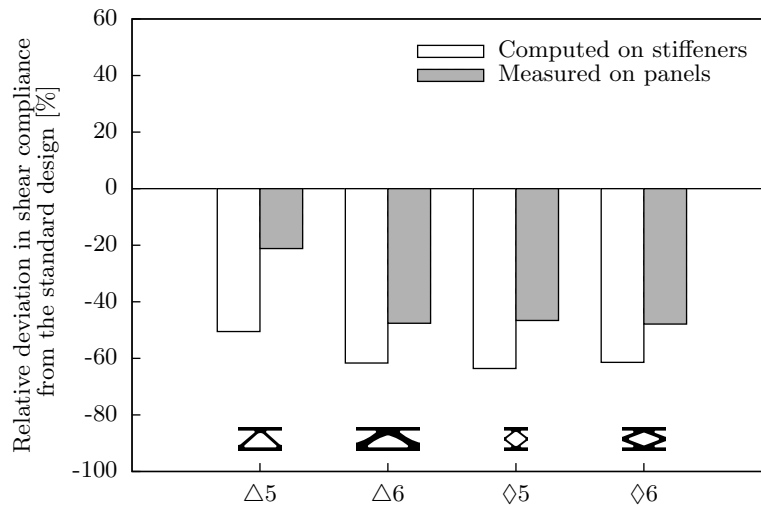


Figure 4.33: Comparison between the shear compliance of the stiffeners computed by homogenization (section 4.3.2) and that of the panel measured on figure 4.32. The shift may be due to the faces contribution included into the panel compliance.

Figure 4.33 shows the deviation from the *standard* design of the shear compliance of the stiffener computed by homogenization simulations, and of the shear compliance the

panel measured on figure 4.32. The trend is respected, the observed shift might be caused by the faces that are included into the measured shear compliance of the panel, but not for the computed stiffeners compliance.

To conclude, design $\triangle 5$ could be filtered out because it has the lowest stiffness. The three others provide an improvement in elastic properties with respect to the current design — a negative deviation on figure 4.33.

Non-linear properties

For each design, the two samples have been tested further, leaving the elastic regime and up to failure : one on the setup *A* with a deflection up to 50 mm (if possible), and the other on the setup *C* with a deflection up to 20 mm. The force–deflection curves are plotted on figure 4.34a for setup *A* and on figure 4.34b for setup *C*.

All the force–deflection curves are divided into three parts. The first part is the elastic region characterized by a linear increase of the force and a way back along the same straight line if the panel is unloaded. The second part is an irreversible region presenting either buckling or plasticity, or more probably both. According to the design, it could occur at a force intensity unchanged or slightly decreasing. The third part is the final unloading. The remaining deflection at zero force is directly correlated with the amount of energy stored into the plastic deformation.

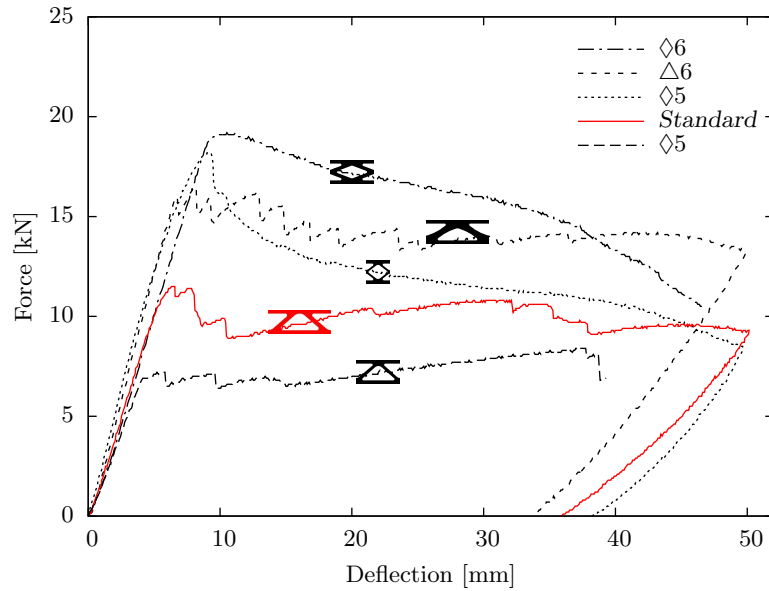
Visually, the first buckling event on the stiffeners was observed at the end of the elastic region. The buckling phenomenon is a bifurcation at a critical force between an unstable loading state to another more stable. Here, the bars of the stiffeners that are loaded in compression buckle into an out-of-plane bending mode. This sudden phenomenon leads to the plastification of the bars. The maximal force reached at the end of the elastic region is related to the critical compressive load on the beam that provokes buckling, given by :

$$F_c = \frac{\pi^2 E b' t'^3}{12(Kl')^2} \quad (4.14)$$

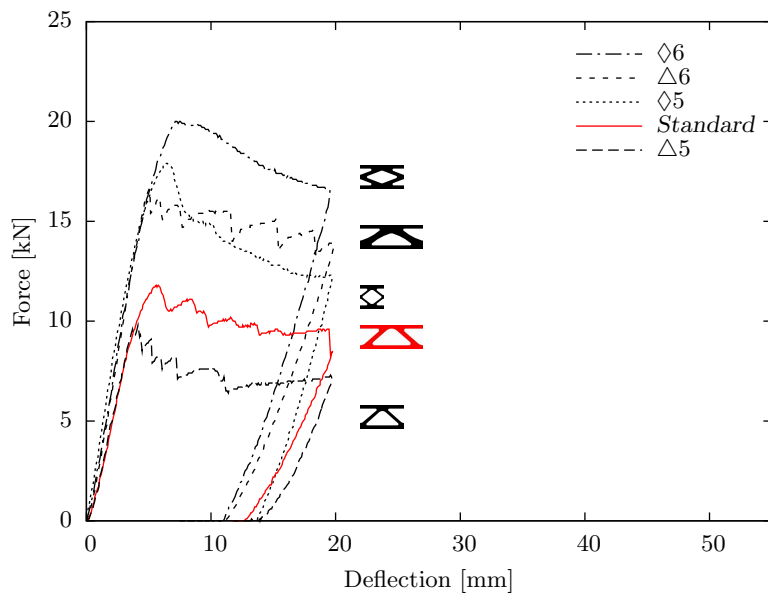
where E is the Young's modulus, b' , t' and l' respectively the width, the thickness and the length of the constitutive bars, and K the effective length factor that takes into account the boundary conditions.

Figure 4.35a compares the theoretical critical force F_c to the maximal forces measured on the force–deflection curves (figure 4.34) for each geometry. The critical forces are computed from lengths estimated as shown in figure 4.36 with a factor $K = 0.5$, which corresponds to two clamped boundaries (figure 4.35b). In the case of \diamond -shape geometries, the critical force is also computed with $K = 0.7$, which corresponds to one clamped

boundary and one rotation-free boundary condition. Actually, the torsion stiffness of the other connected bars leads to a boundary condition in-between rotation-free and clamped.



(a) Setup A, $l = 2600$ mm.

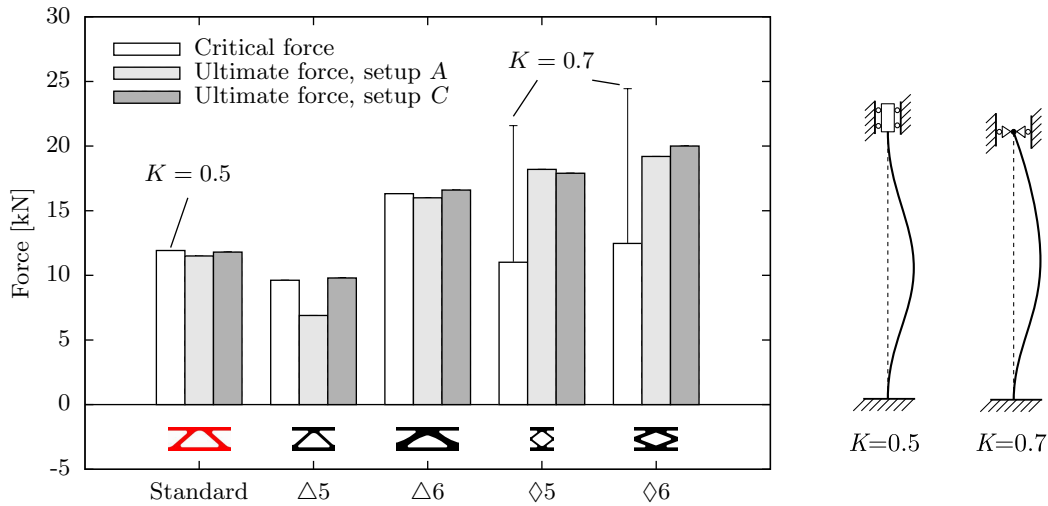


(b) Setup C, $l = 1800$ mm.

Figure 4.34: Force–displacement curve resulting from four–point bending tests on the five prototype panels. The setup C implies larger forces at a given deflection than the setup A, because the span lengths are smaller. The ultimate force for each design is almost unchanged between the two setups.

The correlation between the estimated force and the experimental data is good, but

one should be careful about the strong sensitivity of the estimated buckling lengths on the results. \diamond -shape designs implies a higher critical force than the others because of modified buckling mode. Moreover, the designs with a high area fraction $A_f = 0.6$ provide the largest critical force among each topology (\triangle or \diamond shapes) thanks to their low slenderness.



(a) Analytical critical forces for $K = .5$ (white) and 0.7 (bars) ; Experimental (b) Buckling beams and effective length ratio.

Figure 4.35: (a) Comparison of the critical force F_c from equation (4.14) to the ultimate forces measured on the force–deflection curves (figure 4.34) for each design. (b) Buckling beams with respectively clamped and rotation-free top-boundary conditions.

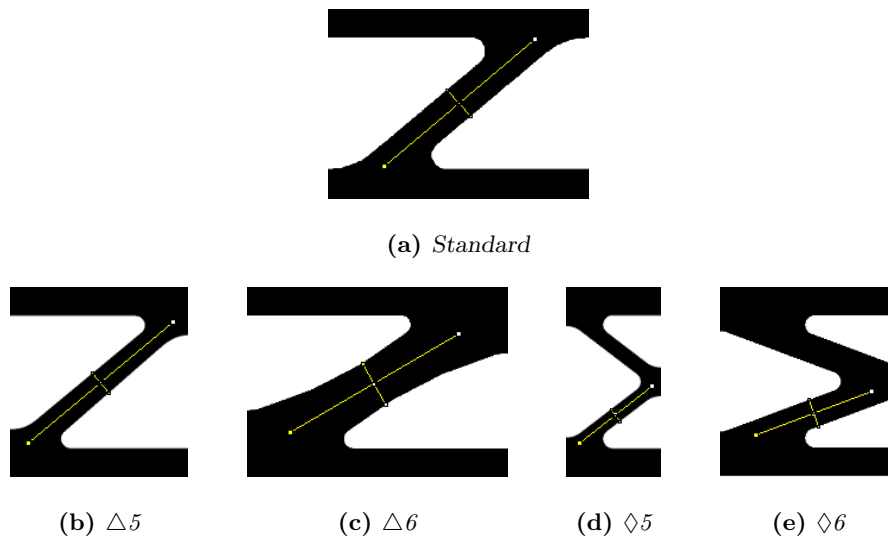


Figure 4.36: Measurements of the width and the length of the constitutive bars involved in buckling.

Examining carefully the damaging region on figure 4.34 reveals an effect of the topology on the shape of force–deflection curve. The designs with \triangle shape exhibits a damage process at a constant force with a sawtooth curve. It results from discrete steps of deformation caused by the buckling of each bar of the stiffener. The designs with \diamond shape provide a higher ultimate force, as well as a smooth damage curve regularly decreasing (sample $\diamond 5$ still shows one or two steps just following the ultimate force). Even if a similar buckling phenomenon appears, it seems to be more continuous because of the different boundary conditions on the bars involved in buckling.

White cross stickers have been put on the visible side of the two faces, and photos have been taken every 10 seconds during the test of all the samples. Digital image correlation have been performed on the image sequences in order to extract the displacements of all the white crosses. The set of the correlation points enables to create a rough mesh (figure 4.37) on which displacements are linearly interpolated. In order to better understand the damage process, one computes the evolution of two significant quantities along the abscissa of the panel : the mean line deflection (average over the upper and lower face deflections) and the thickness reduction (relative difference between the upper and lower face deflections).

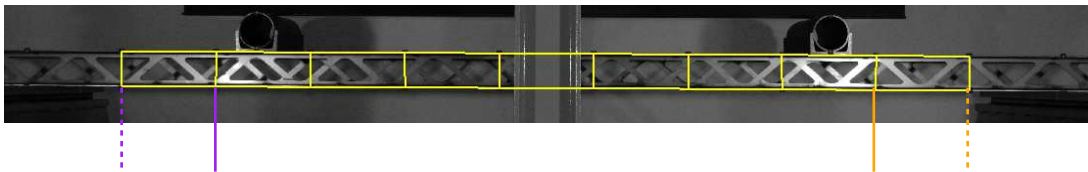


Figure 4.37: *Rough mesh built on the correlation points. Colored vertical lines are abscissa where the thickness reduction of the section is taken and plotted on figures 4.39, 4.40 and 4.41.*

Figure 4.38 shows the thickness reduction on each geometry at a deflection of 40 mm on setup *A*. It provides information on absolute intensity, symmetry and spatial localization of the thickness reduction. It reveals an asymmetrical behavior for designs with low area fraction $A_f = 0.5$, whereas symmetrical response of designs $\triangle 6$ and $\diamond 6$. However, this correlation have to be put in perspective with the fact that no precaution have been taken when assembling to set up the stiffeners symmetrically.

To enhance the analysis, figures 4.39, 4.40 and 4.41 present the force-deflection curve of each design aligned on the evolution of the thickness reduction in four points inside the right and left shear areas. Plain lines corresponds to the inner sections, whereas dashed lines correspond to the outer sections (figure 4.37).

Especially on figures 4.39 and 4.40b, the comparison of both force and thickness reduction versus deflection highlights the origin of the sawtooth. Each step on the force

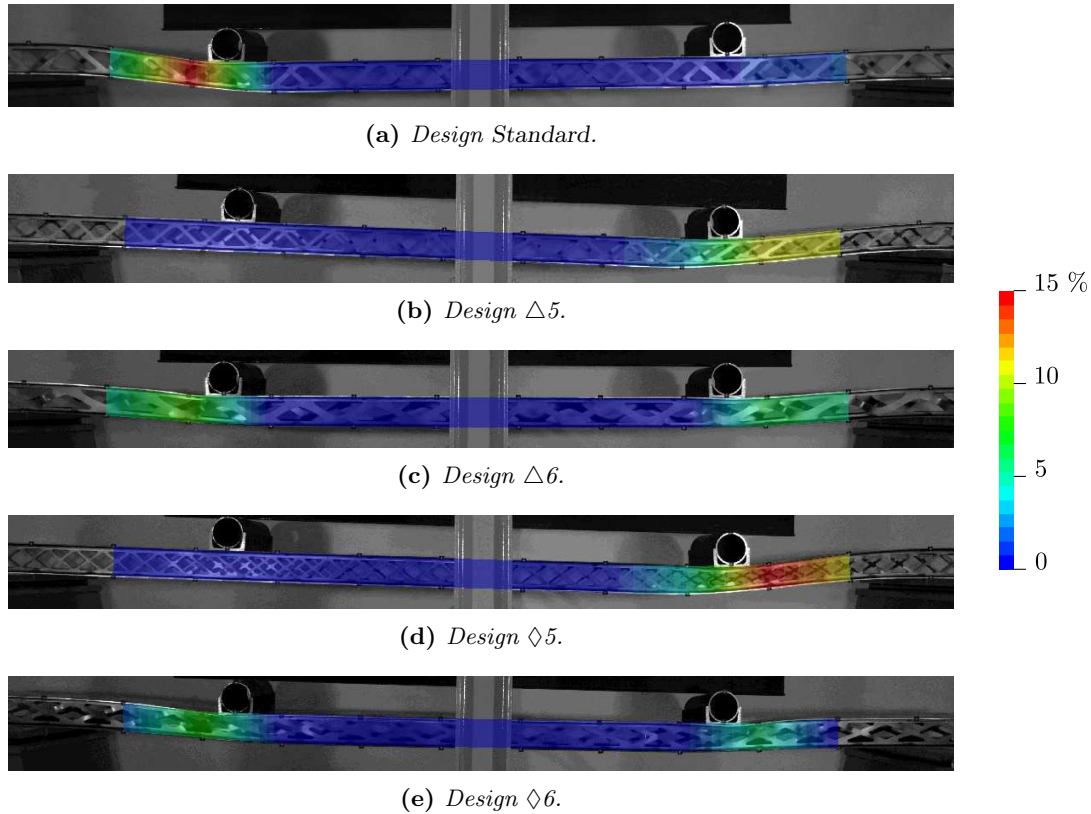


Figure 4.38: Superposition of the thickness reduction field on the image, at a deflection of 40 mm, for the five designs. The color scale of the thickness reduction (in %) is the same for all the designs.

coincides with a drop of the thickness reduction on one of the sections. Thus, it confirms the buckling and plastification of the constitutive bars is the origin of the sawtooth on the force–deflection curve.

The comparison between the thickness reduction in the right and left shear ranges enables to check the symmetry of the panel response. This is the case for designs $\Delta 6$ and $\diamond 6$, which present similar evolution between purple curves (right shear range) and orange curves (left range). One can also observe the propagation of the buckling through the shear range by comparing couples of plain and dashed lines with the same color. For instance, design $\Delta 6$ reveals a very similar evolution of the thickness reduction for the inner (plain-lines) and the outer (dashed-lines) sections. Whereas, the design $\diamond 6$ tends to localize the plastic deformation into the stiffeners below the point loads.

Figures 4.42 and 4.43 detail the kinematic of the mean line deflection and the thickness reduction along the whole panel. They provide an efficient way to interpret each feature of the force–deflection curve and highlight the differences in behavior of the two topologies (V and \diamond shapes). For instance, figure 4.42 enables to visualize the deformation sequences of each side of the panel and explain each sawtooth on the force–deflection curve. One

confirms also, on figure 4.43, that the smoothness of the force–deflection curve is the result of a relative regularity of the buckling process and a localization on the plastic deformations under the load points.

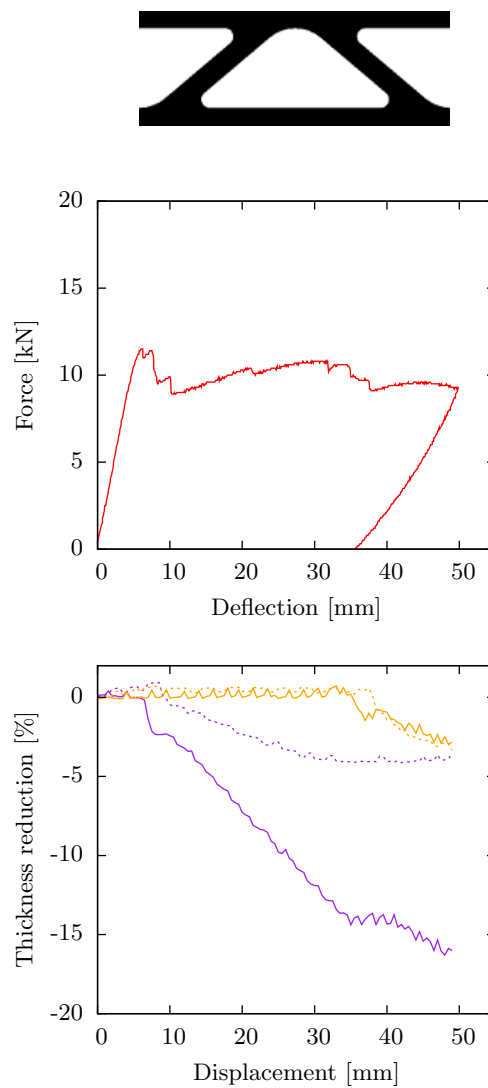


Figure 4.39: Behavior of the standard design for setup A : (top) Force–deflection curve ; (bottom) Thickness reduction into the shear area (each curve corresponds to an abscissa defined on figure 4.37).

To conclude, a low slenderness of the constitutive bars — obtained by a high area density — provides a high critical force and, as a result, a high global strength of the panel. It also seems to encourage a symmetrical behavior, which contribution to the force–deflection curve is not significant. Moreover, the topology modifies the buckling boundary conditions and increases the critical force for designs $\diamond 5$ and $\diamond 6$. It also implies a smooth force–deflection curve. For all these reasons added to its high shear stiffness, the design $\diamond 6$ seems the more mechanically efficient.

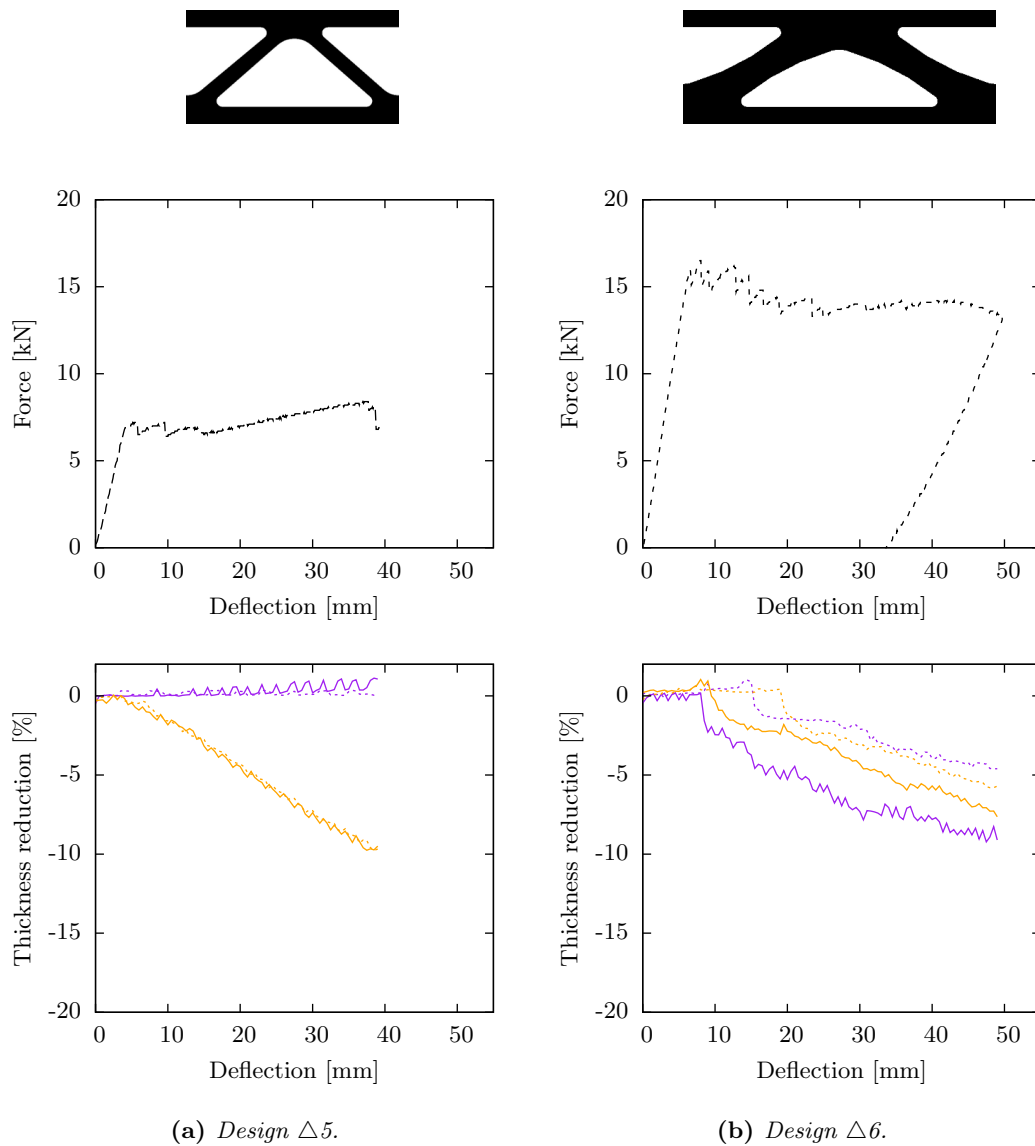


Figure 4.40: Behavior of the designs $\Delta 5$ and $\Delta 6$ for setup A : (top) Force–deflection curve ; (bottom) Thickness reduction into the shear area (each curve corresponds to an abscissa defined on figure 4.37).

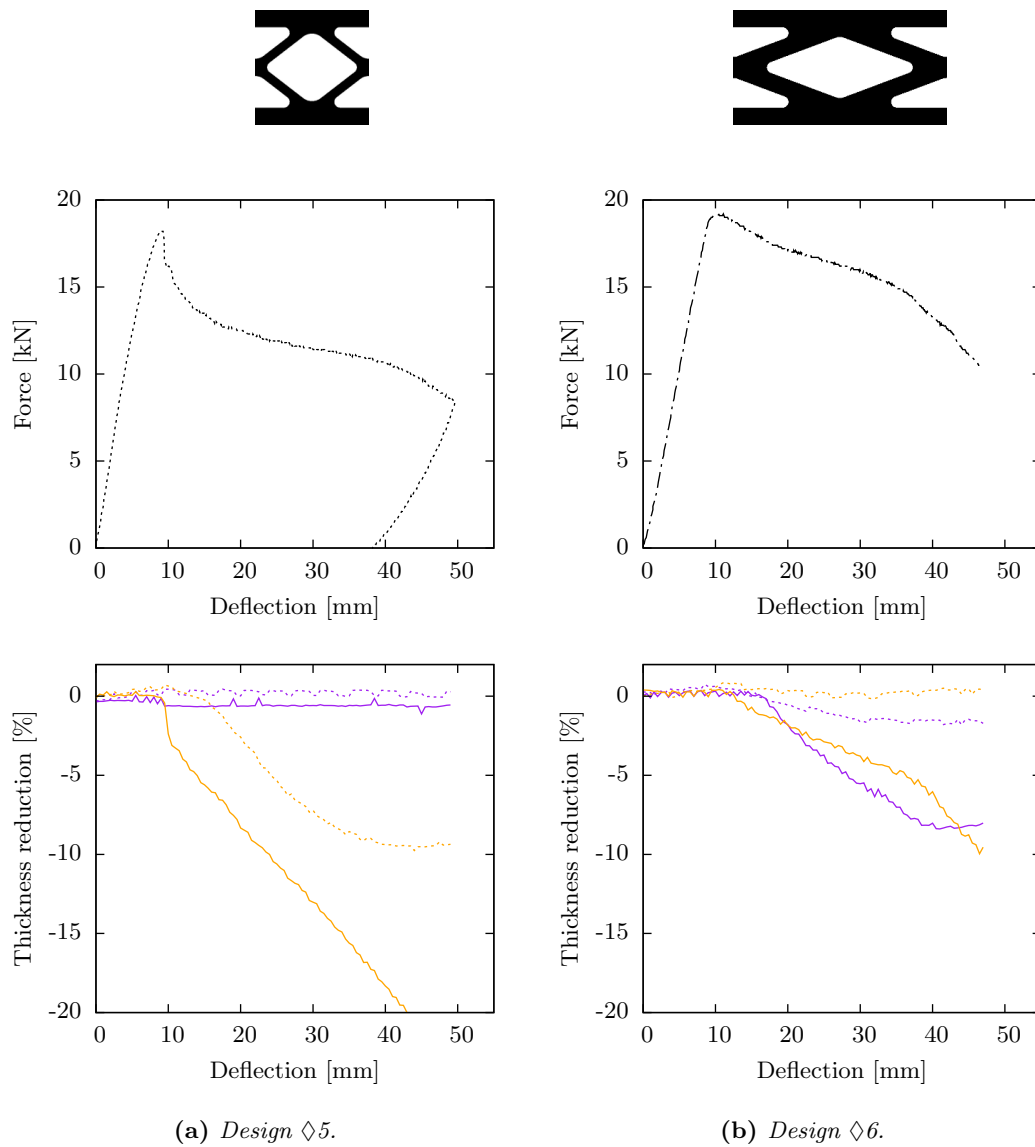
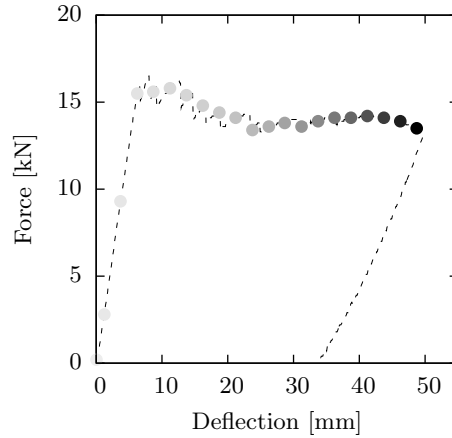
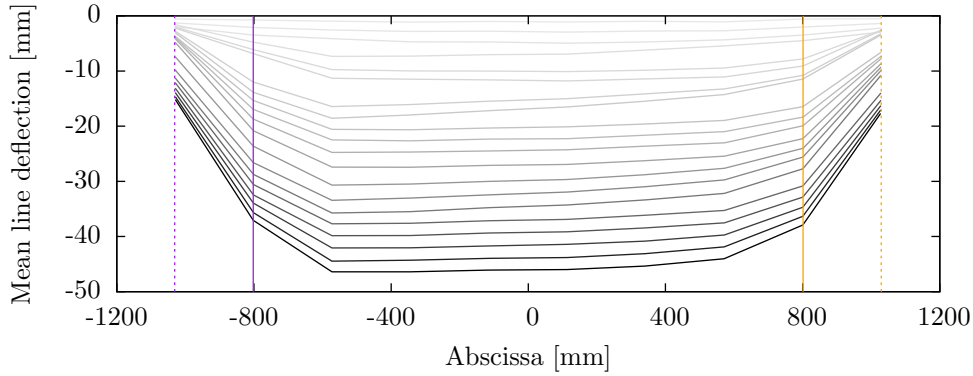


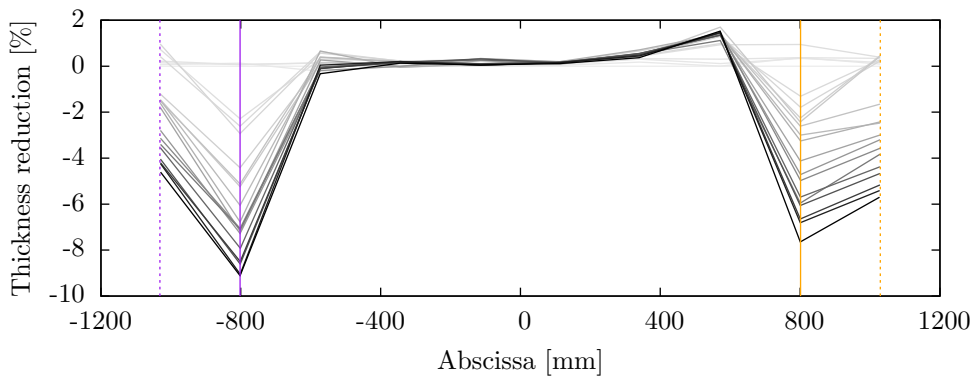
Figure 4.41: Behavior of the designs $\diamond 5$ and $\diamond 6$ for setup A : (top) Force–deflection curve ; (bottom) Thickness reduction into the shear area (each curve corresponds to an abscissa defined on figure 4.37).



(a) Location on the force–deflection curve of each time step analyzed below.

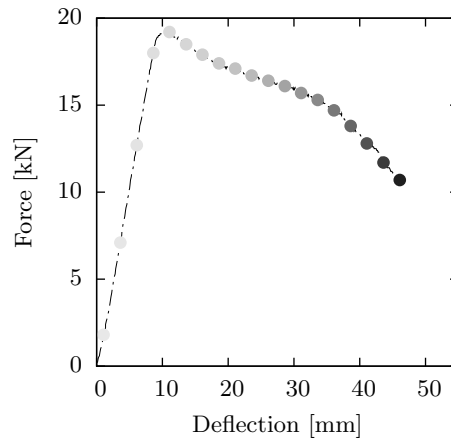


(b) Mean line deflection (average over the upper and lower face deflections) for each time step defined in (a).

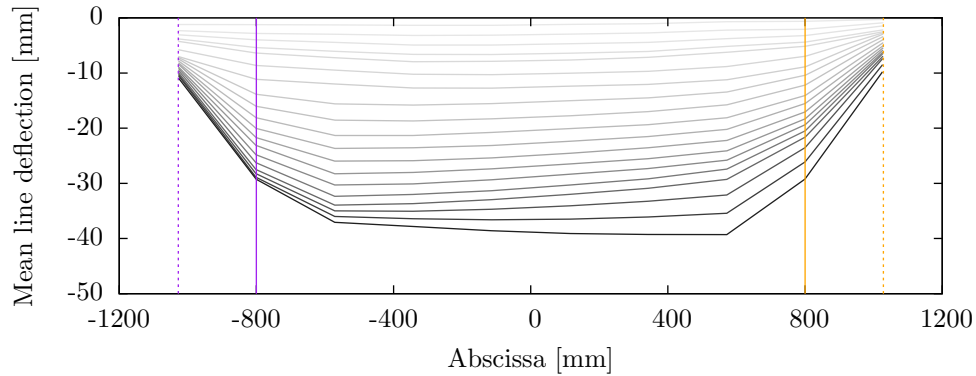


(c) Thickness deflection (relative difference between the upper and lower face deflections) for each time step defined in (a).

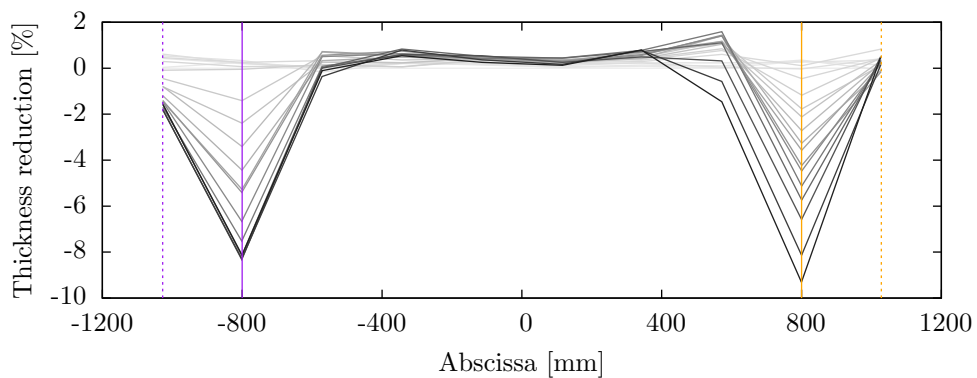
Figure 4.42: Bending test of the design $\Delta 6$ on setup A : (a) force–deflection curve, (b) mean line deflection and (c) thickness reduction. (b) and (c) are measured by image analysis. Each gray level corresponds to an image with a time step of 50 seconds. The purple and orange lines specify the abscissa where the thickness reduction is taken and plotted on figures 4.39, 4.40 and 4.41.



(a) Location on the force–deflection curve of each time step analyzed below.



(b) Mean line deflection (average over the upper and lower face deflections) for each time step defined in (a).



(c) Thickness deflection (relative difference between the upper and lower face deflections) for each time step defined in (a).

Figure 4.43: Bending test of the design $\diamond 6$ on setup A : (a) force–deflection curve, (b) mean line deflection and (c) thickness reduction. (b) and (c) are measured by image analysis. Each gray level corresponds to an image with a time step of 50 seconds. The purple and orange lines specify the abscissa where the thickness reduction is taken and plotted on figures 4.39, 4.40 and 4.41.

Conclusion

A complete optimal design of architected material has been achieved in this chapter. It was applied to the industrial case of an insulating panel produced by *Sainte-Marie Constructions Isothermes*. The aim was to develop a procedure to propose a new geometry for the stiffener design, in order to maintain equivalent thermal properties and improve the stiffness and strength of the panel.

First, specifications on the panel have been listed and some have been translated into functions that stiffeners have to fulfill. Then, the main functions have been translated into an optimization problem that can be solved by shape optimization. The problem is to minimize both the shear compliance and the in-plane thermal resistivity. The resulting geometries were compared together on a performance chart, shear stiffness versus through-thickness conductivity.

The two-dimensional shape optimization algorithm presented in chapter 3 were used to solve this multi-functional optimization problem. Each control parameters were studied : the relative importance of the thermal and mechanical objectives, the area fraction, the initial geometry and the shape factor. It results on a summary on the impact of each of these parameters on the two objectives and on the optimality. Moreover, it fulfills a Pareto front on the shear–conductivity chart and enables — by comparing with the performance of the standard design — to select four promising geometries.

The four promising geometries have been “adjusted” to cope with industrial constraints and produced to be integrated into sandwich samples. Awaiting the insulation test of the modified standard IMO 754(18), a numerical analysis has been performed by *Sainte-Marie Constructions Isothermes*. Three-dimensional transient simulations of the test have concluded in similar performances of the new geometries versus the standard design. Only the geometry V6 have been filtered out due its insufficient insulating ability.

Four-point bending tests have been performed on ten scale-one samples produced by *Sainte-Marie Constructions Isothermes*. From the compliances measured on three test setups (varying the span length), the shear compliance component have been obtained for each design. Then, the ultimate force and the damage process have been carefully studied. The force and displacement sensors in addition with digital image correlation enables to understand the origins of the damage process : buckling, plasticity, spreading out or localization of the deformation in the shear zone, symmetry. From this mechanical analysis, the geometry $\diamond 6$ reveals to be the stiffest and strongest among the four.

Finally, the design $\diamond 6$ provides equivalent thermal insulation than the standard design but increase the stiffness and strength of the panel. As a accomplishment of this work in collaboration with *Sainte-Marie Constructions Isothermes*, the next release of the insulating sandwich product will integrate this design.

Highlights

- A **study** was performed on the **optimal design** of a part of an insulation sandwich panel produced by the company *Sainte-Marie Constructions Isothermes*. The panel specification was translated into a multi-functional optimization problem treated by topological optimization : shear stiffness and thermal resistivity.
- **Influence of the parameters** is discussed. A Pareto front is built with varying the weighting factor and area fraction. The choice of the initial geometry and the cell length may have an impact of the optimality.
- A **selection stage** that consists in plotting the optimized solutions into a performance chart enables to highlight few promising unit cell geometries. These selected patterns are slightly adjusted according to the process requirements.
- Three-dimensional **thermal transient analysis** gave results consistent with optimization simulation and confirmed the quasi-static assumption.
- Four-point **bending tests** are performed on scale-one prototype samples. The ranking of the geometries with respect to the shear stiffness is similar to that estimated. One of the designs appears to be very promising and is retained by *Sainte-Marie Constructions Isothermes* for further development.

CONCLUSIONS & PERSPECTIVES

Main results obtained during this PhD

Following an approach of “material by design” the generic trend is nowadays to develop tailored materials in order to tune their properties to the application requirements. The sandwich structure is an emblematic example of a multi-functional architected material obtained by spatially organizing one or few phases at the scale of the panel (faces and core) or within the core itself.

In this context, this PhD work focuses on the development of numerical tools for optimizing matter distribution within the unit cell of architected panel. This optimization tools have been developed following three main directions :

- the **homogenization** of the membrane, flexural and transverse-shear modulus of any architected unit cell ;
- the **selection, sizing and optimization** of architected patterns with respect to multi-functional objectives at a given weight. The multi-functional objectives considered here are either bending versus shear compliance or thermal conductivity versus shear compliance ;
- the **experimental validation** of the numerical predictions by testing prototype model architected panel or industrial sandwich structures.

Homogenization of architected panels is described in order to identify the Reissner-Mindlin stiffness coefficients. Using the spatial periodicity of the heterogeneous distribution of matter, this is performed by resolving by FEM some homogenization problems on the unit cell. While the membrane and flexural components result from a classical boundary conditions problem, the transverse-shear components do not. An overall shear loading that satisfies stress-free conditions on the top-and-bottom faces can only be imposed through a body load. The bending gradient theory says that the appropriate body load is derived from the pure bending homogenization problem. This type of loading is a substitution to uniform boundary conditions that do not satisfy the stress-free conditions. The transverse-shear contribution as well as the influence of the type of loading are quantified on a particular model architected panel.

The implementation of these homogenization calculations is performed on the entirely meshed unit cell defining the subdomain filled with matter using the level-set function. It enables to systematically compute the effective properties for any architected panels, even in a parametric study or an optimization approach.

As an example, the design of embossed steel is carried out as an application of the proposed architected material approach. The previous homogenization procedure is used

to estimate the performance of such patterned sheets. It leads to the comparison of different patterns and to derivation of operational rules for a proper dimensioning of the structure.

To proceed further in the search of high performance geometries according to multi-functional objective, a topological optimization tool is developed and coupled with homogenization. The case of bi-dimensional architected panels that aim at providing a compromise between flexural and shear stiffnesses is treated. A constraint on the area fraction is added to the optimization problem by introducing a Lagrangian function. A progressive satisfaction of the prescribed area fraction while optimizing is proposed and studied. This simple numerical trick avoids topological simplifications and consequently getting trivial solutions.

The definition of the appropriate objective function has been discussed. Weighted product and three-point bending compliance are proposed as objective function and provide equivalent results. The weighting factor and the span length control the relative importance given to bending versus shear in the optimization process. In both cases, changing their value enables to build a Pareto front that gathers the best compromises reachable within a constraint of a given area fraction. A shift of the Pareto front is observed when the area fraction is increased and less deviations in terms of compliances is noted for the high values of area fraction.

Even if topological changes are in principle possible, a strong sensitivity to the initial geometry is observed. Final optimized geometries usually differ in topology, keeping that of the initial geometry. But they often provide similar features in shape (bars, faces, curvatures, etc.). It has to be noticed also that the optimized solutions obtained from several initial geometries all lie onto the estimated Pareto front, excepted few special symmetric cases. The sensitivity to the initial geometry is explained by two facts. The implemented optimization belongs to the class of gradient-based methods, which are known to find local optimum and not global ones. In addition, the homogeneity of the considered unit cell loadings encourage the multiplicity of the local optima. Concerning the design domain, the choice of the unit cell length (i.e. the shape ratio) affects the optimality of the properties, and more especially the shear component.

Finally, this numerical tool for topological optimization of panels unit cell is applied on a multi-functional industrial case. The company *Sainte-Marie Construction Isothermes* produces an insulation sandwich panel that fulfills mechanical and thermal specifications. The translation into an optimization problem has been proposed. And the optimization algorithm has been used to build stiffeners geometries with a high-performance compromise between shear stiffness and thermal insulation. The influence of each parameters is presented and selection rules are utilized to propose four promising stiffeners shapes. These panels have been realized and are currently tested for an industrial implementation.

These experiments refer to the optimized sandwich stiffeners. The company Sainte-Marie Construction Isothermes produced scale-one steel structures of sandwich panel, with respectively the current stiffeners design and four optimized designs. Four-point bending tests with several span lengths were completed and enable to characterize the elastic moduli as well as the damaging features.

Finally, model architected panels in polyamide, produced by additive manufacturing (selective laser sintering), have been realized. The first experimental results (see chapter 2) confirm FEM simulations of the four-point bending tests. They are taken as reference when compared with the analytical expression that assumes a homogeneous panel with effective properties. Then, four initial geometries and the corresponding optimized ones were produced and tested. Thanks to bending tests with several span lengths, both flexural and transverse-shear moduli can be identified. Data demonstrate experimentally the expected improvement of the elastic properties and quantifies the interest of the approach.

This work is a contribution to the development of systematic methods for optimal design in the context of architected materials, applied to sandwich structures. As an illustrative demonstration, the optimization study on the sandwich stiffeners ends up with proposing a new design that will be integrated into the next generation of panels produced by the company. Concerning embossed steel, it is part of the innovative steel solutions under development by ArcelorMittal in order to fulfill the future challenges in car lightening. Topological optimization is added to the available tools for architected material development.

Perspectives

The results obtained in this PhD work as well as the limitations and the difficulties suggest some perspectives and axes for further works. They are proposed into the following items :

- A first limitation to the implemented optimization method lies in the impossibility to nucleate holes at the transformation stage using the Hamilton-Jacobi equation. It results from the transport specificity of this equation. In order to overcome this limitation, it was proposed to locally modify the level-set function to enforce the creation of holes. Allaire and Jouve (2008) present such an extension of the level-set algorithm with choosing the location of holes nucleation with respect to the topological derivative. This expression differs from the shape derivative since it is defined at any point of the domain and quantifies the sensitivity to nucleating a infinitesimal hole (Céa, 2000, Novotny et al., 2007). Another recent and promising method was proposed by Yamada et al. (2010) and

consists in replacing the transport Hamilton-Jacobi equation by a diffusion-convection equation. Inspired by the phase field approach, the level-set function is enforced to be -1 or 1 almost everywhere excepted close to the interface. Then the time derivative of the level-set function ϕ is written to be proportional to the shape derivative j' in addition with the term $\tau \nabla^2 \phi$ that derives from a fictitious interface energy :

$$\frac{\partial \phi}{\partial t} + j' - \tau \nabla^2 \phi = 0 \quad (4.15)$$

where $\tau > 0$ is a regularization parameter that controls the relative importance between the fictitious interface energy and the shape derivative. It has been shown by Yamada et al. (2010) that the use of such an transformation equation allows the nucleation of holes and the control of the topology complexity by the parameter τ .

In addition to this topological limitation, optimization simulations were performed here only in a bi-dimensional framework and suggest a higher interest in three dimensions. Indeed, the three-dimensional case provides more complex morphologies and a larger set of possibilities that makes much weaker any intuition. An extension of the bi-dimensional optimization tool have been implemented in three dimensions using the diffusion-convection equation (4.15). Figure 4.44 shows a preliminary result of optimization from the embossed pattern *am* (from section 2.4) with respect to the flexural and transverse-shear compliance in direction e_1 .

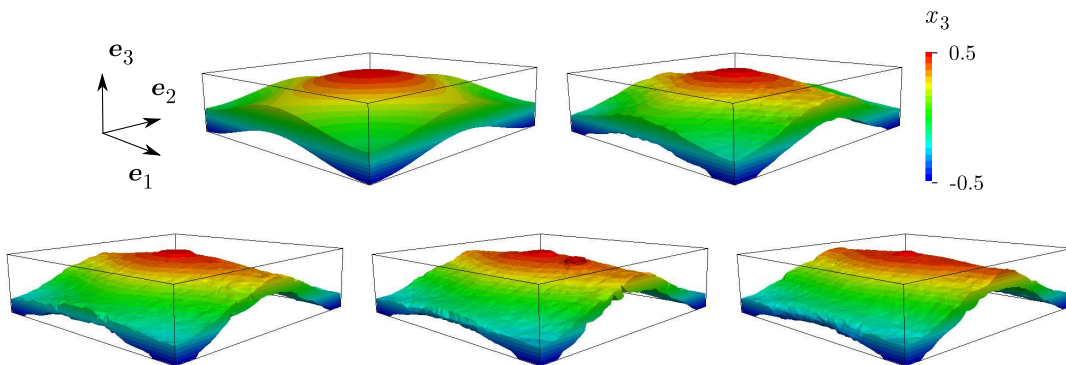


Figure 4.44: *Three-dimension optimization from pattern am with respect to the flexural and transverse-shear compliance in direction e_1 . Volume fraction progressively decreases from 0.4 to 0.2. The unit cell is plotted at iterations 0, 10, 20, 30, 40. Contours represent the coordinate x_3 .*

This result is clearly promising since the well-known corrugated sheet is obtained. However some difficulties remain. This problems is very computer-time and memory-consuming. That limits the numbers of elements available to precisely describe the geometry and avoid artificial stress peaks on the interface. It explains the quite irregular geometry observed on figure 4.44. Moreover, it would be interesting to optimize with respect to the flexural and shear compliance in both directions e_1 and e_2 . This would

add to more FEM calculations to identify these compliance components. In addition, it could be worthwhile to introduce the anisotropy factor into the objective function.

- The choice of the multi-objective function have been discussed in chapter 3 when comparing the weighted product and the three-point bending compliance. A physically-based combination of objectives enables to justify the choice of the weighting factor and to efficiently balance the contributions of each objective. But in the case of multi-physics objective functions (e.g. thermal and mechanical), such physically-based combination does not exist (except when a proper value analysis can be performed) and the choice of the multi-objective function and the weighting factor depend on a preliminary discussion on the specifications of the architected material to design. We retrieve here the classical difficulty to translate a set of requirements into an optimization problem.

Concerning objective function, the present work only focuses on minimizing the elastic compliance based on the analytical expression of the shape derivative. The extension to non-linear objective functions is still an open question. Literature provides some examples of non-linear optimization to think about, such as large displacements (Cho and Jung, 2003), elasto-plastic structures (Schwarz et al., 2001) and transient thermal properties (Li et al., 2004). It seems also interesting to include other constraints that aim at taking into account process requirements or local criteria (e.g. yield limit, fracture, etc.). For instance, integrating a curvature constraint seems feasible with regard to Yang et al. (2010).

- The analysis of how the initial geometry affects the optimization results reveals a significant influence. The approach followed in chapter 4 amounts to populating the Pareto front with optimized solutions obtained from several initial geometries, then selecting some of the more promising solutions. Another approach could be to couple the present gradient-based optimization method with a stochastic approach. For instance, such a “mixed strategy” could be to generate random initial geometries, to nucleate random holes or to exchange pixel values as it has been proposed by Garcia-Lopez et al. (2011) with coupling simulated annealing and SIMP methods.
- In the present context of architected materials, we focused on applying topological optimization — that is initially developed for structural design — to a periodic unit cell. The obtained optimized unit cell provide the best compromise between stiffness components in order to be periodically repeated everywhere into a structure panel. A multi-level approach could be proposed by optimizing the distribution of pseudo-periodic patterns to design complex part made of functionally graded material (Jackson et al., 1999). This approach is especially interesting since additive manufacturing techniques provide more and more possibilities in terms of geometry complexity, materials and

quality. Biological applications already take advantage of this strategy (Parthasarathy et al., 2011, Genet et al.), but others may come such as a planned PhD work (in continuation of the present one) on both optimization simulations and additive manufacturing by electron beam melting. Again the integration of process requirements into the optimization problem will be a key issue.

Finally, we have focussed our attention on geometrical optimisation. In parallel , the classical “materials selection methods” developed by Ashby aims at selecting the best materials and the best combination of materials. The obvious – and difficult- next step is to aim at a co-selection of materials and geometries. This would be an additional step on the road to systematic design of hybrid materials, which is the general background of the work performed in this PhD.

APPENDIX A

Tensors notations

A.1 General notations

In all the documents, scalars and vector are denoted with italic characters like the scalars l , ν , α , and the vectors x , n , etc. The context only specifies if it is a scalar or a vector. The components of the vectors are denoted with indexes like the three spatial variables x_1 , x_2 and x_3 . One exception is done for the particular vectors of the spatial reference frame which are denoted e_1 , e_2 , and e_3 .

Tensors of order 2 or larger are denoted with bold characters like \mathbf{N} , \mathbf{e} , $\boldsymbol{\sigma}$ (whatever is the dimension 2 or 3). Tensors of dimension 2 expanded to the 3rd dimension with zeros are underlined with a tilde like $\tilde{\mathbf{e}}$. The components of the tensors are denoted like scalars with indexes, for example the 1st stress component σ_{11} or the first Hook's tensor component C_{1111} .

A.2 Kelvin's notation

For an easier manipulation of the tensors of order 2 and 4, engineer's notations have been proposed. The Kelvin's notation is one of them and consists in writing the stress and strain tensors as the following vectors :

$$\{\boldsymbol{\sigma}\} = \begin{Bmatrix} \sigma_1 \\ \sigma_2 \\ \sigma_3 \\ \sigma_4 \\ \sigma_5 \\ \sigma_6 \end{Bmatrix} = \begin{Bmatrix} \sigma_{11} \\ \sigma_{22} \\ \sigma_{33} \\ \sqrt{2} \sigma_{23} \\ \sqrt{2} \sigma_{31} \\ \sqrt{2} \sigma_{12} \end{Bmatrix} \quad \text{and} \quad \{\boldsymbol{\varepsilon}\} = \begin{Bmatrix} \varepsilon_1 \\ \varepsilon_2 \\ \varepsilon_3 \\ \varepsilon_4 \\ \varepsilon_5 \\ \varepsilon_6 \end{Bmatrix} = \begin{Bmatrix} \varepsilon_{11} \\ \varepsilon_{22} \\ \varepsilon_{33} \\ \sqrt{2} \varepsilon_{23} \\ \sqrt{2} \varepsilon_{31} \\ \sqrt{2} \varepsilon_{12} \end{Bmatrix} \quad (\text{A.16})$$

The order of the components are chosen such that :

$$[\boldsymbol{\sigma}] = \begin{bmatrix} \sigma_{11} & \sigma_{12} & \sigma_{31} \\ \sigma_{12} & \sigma_{22} & \sigma_{23} \\ \sigma_{31} & \sigma_{23} & \sigma_{33} \end{bmatrix} \quad (\text{A.17})$$

Thus, the stiffness tensor becomes the following matrix :

$$[\mathbf{C}] = \begin{bmatrix} C_{1111} & C_{1122} & C_{1133} & \sqrt{2} C_{1123} & \sqrt{2} C_{1131} & \sqrt{2} C_{1112} \\ C_{2211} & C_{2222} & C_{2233} & \sqrt{2} C_{2223} & \sqrt{2} C_{2231} & \sqrt{2} C_{2212} \\ C_{3311} & C_{3322} & C_{3333} & \sqrt{2} C_{3323} & \sqrt{2} C_{3331} & \sqrt{2} C_{3312} \\ \sqrt{2} C_{2311} & \sqrt{2} C_{2322} & \sqrt{2} C_{2333} & 2 C_{2323} & 2 C_{2331} & 2 C_{2312} \\ \sqrt{2} C_{3111} & \sqrt{2} C_{3122} & \sqrt{2} C_{3133} & 2 C_{3123} & 2 C_{3131} & 2 C_{3112} \\ \sqrt{2} C_{1211} & \sqrt{2} C_{1222} & \sqrt{2} C_{1233} & 2 C_{1223} & 2 C_{1231} & 2 C_{1212} \end{bmatrix} \quad (\text{A.18})$$

This stiffness matrix in the Kelvin's notation is converted from the traditional Voigt's notation by pre and post multiply by the matrix :

$$\begin{bmatrix} 1 & 0 & 0 & 0 & 0 & 0 \\ 0 & 1 & 0 & 0 & 0 & 0 \\ 0 & 0 & 1 & 0 & 0 & 0 \\ 0 & 0 & 0 & \sqrt{2} & 0 & 0 \\ 0 & 0 & 0 & 0 & \sqrt{2} & 0 \\ 0 & 0 & 0 & 0 & 0 & \sqrt{2} \end{bmatrix} \quad (\text{A.19})$$

This Kelvin's notation have the advantage to be symmetric for strain and stress and enable to stabilize the elastic-constant inversion of the stiffness tensor. The compliance matrix becomes the inverse of the stiffness matrix.

The two-dimensional macroscopic stress and strain are treated similarly with keeping the indexes 1, 2 and 6 to be consistent with the previous three-dimensional notations :

$$\{\mathbf{N}\} = \begin{Bmatrix} N_1 \\ N_2 \\ N_6 \end{Bmatrix} = \begin{Bmatrix} N_{11} \\ N_{22} \\ \sqrt{2} N_{12} \end{Bmatrix} \quad \text{and} \quad \{\mathbf{e}\} = \begin{Bmatrix} e_1 \\ e_2 \\ e_6 \end{Bmatrix} = \begin{Bmatrix} e_{11} \\ e_{22} \\ \sqrt{2} e_{12} \end{Bmatrix} \quad (\text{A.20})$$

The compliance matrix becomes :

$$[\mathbf{a}] = \begin{bmatrix} \mathbf{a}_{11} & \mathbf{a}_{12} & \mathbf{a}_{61} \\ \mathbf{a}_{12} & \mathbf{a}_{22} & \mathbf{a}_{26} \\ \mathbf{a}_{61} & \mathbf{a}_{26} & \mathbf{a}_{66} \end{bmatrix} = \begin{bmatrix} \mathbf{a}_{1111} & \mathbf{a}_{1122} & \sqrt{2} \mathbf{a}_{1211} \\ \mathbf{a}_{1122} & \mathbf{a}_{2222} & \sqrt{2} \mathbf{a}_{2212} \\ \sqrt{2} \mathbf{a}_{1211} & \sqrt{2} \mathbf{a}_{2212} & 2 \mathbf{a}_{1212} \end{bmatrix} \quad (\text{A.21})$$

A.3 Rotations and anisotropy

The anisotropy of a constitutive law quantify how large are the variations of the material response when it is rotated. In our case, an anisotropy factor will be defined from the variations of the effective softness — the inverse of the Young's modulus — scanning the direction of the panel's plane. The representative matrix in the Kelvin's notation of an in-plane rotation is :

$$\begin{bmatrix} c^2 & 2 & -\sqrt{2}cs \\ s^2 & c^2 & \sqrt{2}cs \\ \sqrt{2}cs & -\sqrt{2}cs & c^2 - s^2 \end{bmatrix} \quad (\text{A.22})$$

where $c = \cos \theta$ and $s = \sin \theta$. The evolution of the compliance components with respect to the rotation angle θ can be computed using the following rotation matrix :

$$\begin{bmatrix} c^4 & s^4 & 2c^2s^2 & 2cs^3 & 2c^3s & \sqrt{2}c^2s^2 \\ s^4 & c^4 & 2c^2s^2 & -2c^3s & -2cs^3 & \sqrt{2}c^2s^2 \\ 2c^2s^2 & 2c^2s^2 & (c^2 - s^2)^2 & 2cs(c^2 - s^2) & -2cs(c^2 - s^2) & -2\sqrt{2}c^2s^2 \\ -2cs^3 & 2c^3s & -2cs(c^2 - s^2) & c^2(c^2 - 3s^2) & -s^2(s^2 - 3c^2) & -\sqrt{2}cs(c^2 - s^2) \\ -2c^3s & 2cs^3 & 2cs(c^2 - s^2) & s^2(s^2 - 3c^2) & c^2(c^2 - 3s^2) & \sqrt{2}cs(c^2 - s^2) \\ \sqrt{2}c^2s^2 & \sqrt{2}c^2s^2 & -2\sqrt{2}c^2s^2 & \sqrt{2}cs(c^2 - s^2) & -\sqrt{2}cs(c^2 - s^2) & (c^4 + s^4) \end{bmatrix} \quad (\text{A.23})$$

to be applied to the representative vector of the compliance tensor :

$$\{\mathbf{a}\} = \begin{Bmatrix} a_{11} \\ a_{22} \\ a_{66} \\ \sqrt{2}a_{26} \\ \sqrt{2}a_{61} \\ \sqrt{2}a_{12} \end{Bmatrix} = \begin{Bmatrix} a_{1111} \\ a_{2222} \\ 2a_{1212} \\ 2a_{2212} \\ 2a_{1211} \\ \sqrt{2}a_{1122} \end{Bmatrix} \quad (\text{A.24})$$

For example, the evolution of the first component with respect to the rotation angle is :

$$a_{11}(\theta) = c^4 a_{11} + s^4 a_{22} + 2c^2 s^2 a_{66} + 2\sqrt{2} c s^3 a_{26} + 2\sqrt{2} c^3 s a_{61} + 2c^2 s^2 a_{12} \quad (\text{A.25})$$

This evolution can be characterized by its average over θ :

$$\bar{a}_{11} = \frac{1}{2\pi} \int_0^{2\pi} a_{11} d\theta = \frac{1}{8} (3a_{11} + 3a_{22} + 2a_{66} + 2a_{12}) \quad (\text{A.26})$$

and its standard deviation, which is a measure of the anisotropy :

$$\begin{aligned} \text{std}(a_{11})^2 &= \frac{1}{128} (17(a_{11}^2 + a_{22}^2) - 30a_{11}a_{22} - 4(a_{11} + a_{22})(a_{66} + a_{12}) \\ &\quad + 4(a_{66} + a_{12})^2 + 40(a_{26}^2 + a_{61}^2) + 48a_{26}a_{61}) \end{aligned} \quad (\text{A.27})$$

In the specific case of a cubic symmetry, one has $a_{11} = a_{22}$ and $a_{61} = a_{26} = 0$, such that the previous factor becomes :

$$\text{std}(a_{11})^2 = \frac{a_{66}^2}{128} \left(1 - \frac{a_{11} - a_{12}}{a_{66}} \right)^2 \quad (\text{A.28})$$

where the ratio $(a_{11} - a_{12})/a_{66}$ is the classical anisotropy factor for materials with or-

thotropic symmetry ⁴.

⁴the tensor have to be expressed in the frame aligned on the symmetry planes

REFERENCES

- 3DSystems. Duraform ® data sheet, 2011. URL <http://production3dprinters.com/materials>. 90
- G. Allaire. *Shape optimization by the homogenization method*. Applied mathematical sciences. Springer, 2002. ISBN 9780387952987. 119, 122, 159
- G. Allaire and F. Jouve. Minimum stress optimal design with the level set method. *Engineering Analysis with Boundary Elements*, 32(11):909–918, 2008. 120, 125, 199
- G. Allaire and O. Pantz. Structural optimization with FreeFem++. *Structural and Multidisciplinary Optimization*, 32(3):173–181, July 2006. 119
- G. Allaire, F. Jouve, and A.-M. Toader. Structural optimization using sensitivity analysis and a level-set method. *Journal of Computational Physics*, 194(1):363–393, 2004. 119, 120, 121, 124
- H. G. Allen. *Analysis and Design of Structural Sandwich Panels*. Pergamon Press, oxford edition, 1969. 53
- H. G. Allen. Analysis of sandwich panels: the significance of shear deformation. *Composites*, pages 215–220, 1970. 53, 57
- S. Amstutz and A. a. Novotny. Topological optimization of structures subject to Von Mises stress constraints. *Structural and Multidisciplinary Optimization*, 41(3):407–420, 2009. 120
- E. Andreassen, A. Clausen, M. Schevenels, B. Lazarov, and O. Sigmund. Efficient topology optimization in MATLAB using 88 lines of code. *Structural and Multidisciplinary Optimization*, 43(1):1–16, 2010. 119
- R. Ansola, J. Canales, J. Tarrago, and J. Rasmussen. An integrated approach for shape and topology optimization of shell structures. *Computers & Structures*, 80(5-6):449–458, 2002. 120
- M. F. Ashby. Multi-objective optimization in material design and selection. *Acta Materialia*, 48(1):359–369, 2000. 135
- M. F. Ashby. *Materials selection in mechanical design*. Elsevier Butterworth-Heinemann, 2005. ISBN 9780750661683. 12, 37, 47, 48, 51
- M. F. Ashby. Hybrid Materials to Expand the Boundaries of Material-Property Space. *Journal of the American Ceramic Society*, 94(29018):s3–s14, June 2011. 52, 54
- M. F. Ashby and Y. Bréchet. Designing hybrid materials. *Acta Materialia*, 51(19):5801–5821, 2003. 40
- ASTM Standard C393. Standard Test Method for Core Shear Properties of Sandwich Constructions by Beam Flexure. *ASTM International*, 2006. 18, 68
- ASTM Standard D7250. Standard Practice for Determining Sandwich Beam Flexural and Shear Stiffness. *ASTM International*, 2006. 18, 68
- ASTM Standard F2915. Standard Specification for Additive Manufacturing File Format (AMF). *ASTM International*, 2011. 141

REFERENCES

- Z. K. Awad, T. Aravinthan, Y. Zhuge, and F. Gonzalez. A review of optimization techniques used in the design of fibre composite structures for civil engineering applications. *Materials & Design*, May 2011. 117
- F. J. Barthold and E. Stein. A continuum mechanical-based formulation of the variational sensitivity analysis in structural optimization. Part I: analysis. *Structural Optimization*, 11(1-2):29–42, Feb. 1996. 117
- M. P. Bendsøe. *Optimization of structural topology, shape, and material*. Springer, 1995. ISBN 9783540590576. 119
- M. P. Bendsøe and N. Kikuchi. Generating optimal topologies in structural design using a homogenization method. *Computer Methods in Applied Mechanics and Engineering*, 71:197–224, 1988. 119
- M. P. Bendsøe and O. Sigmund. Material interpolation schemes in topology optimization. *Archive of Applied Mechanics*, 69(9-10):635–654, 1999. 119
- M. P. Bendsøe and O. Sigmund. *Topology optimization: theory, methods, and applications*. Engineering online library. Springer, Berlin Heidelberg New-York, 2003. ISBN 9783540429920. 119
- M. P. Bendsøe, J. M. Guedes, S. Plaxton, and J. E. Taylor. Optimization of structure and material properties for solids composed of softening material. *International Journal of Solids and Structures*, 33(12):1799–1813, 1996. 118
- M. Bornert, T. Bretheau, and P. Gilormini. *Homogénéisation en mécanique des matériaux 1 - Matériaux aléatoires élastiques et milieux périodiques*. Hermès Science Publications, Paris, 2001. ISBN 2-7462-0199-2. 78
- O. Bouaziz, Y. Bréchet, and J. D. Embury. Heterogeneous and Architected Materials: A Possible Strategy for Design of Structural Materials. *Advanced Engineering Materials*, 10(1-2):24–36, 2008. 99
- S. Bourgeois. *Modélisation numérique des panneaux structuraux légers*. PhD thesis, Université d’Aix-Marseille 2, 1997. 80
- S. Bourgeois, P. Cartraud, and O. Débordes. Homogenization of periodic sandwiches: numerical and analytical approaches. In A. Vaurtin, editor, *EUROMECH 360*, Dordrecht (Netherlands), 1997. Kluwer Academic Publishers. 80
- N. Buannic and P. Cartraud. Higher-order effective modeling of periodic heterogeneous beams. I. Asymptotic expansion method. *International Journal of Solids and Structures*, 38(40-41):7139–7161, Oct. 2001. 66
- N. Buannic, P. Cartraud, and T. Quesnel. Homogenization of corrugated core sandwich panels. *Composite Structures*, 59(3):299–312, Mar. 2003. 79
- D. Caillerie. Thin elastic and periodic plates. *Mathematical Methods in the Applied Sciences*, 6(2):159–191, 1984. 66, 79
- L. Carlsson, P.-E. Bourban, and J.-P. Mercier. *Volume 15 de Traité des Matériaux Matériaux composites à matrice organique: constituants, procédés, propriétés*. PPUR presses polytechniques, 2004. ISBN 2880745284. 50

- E. Carrera. Theories and finite elements for multilayered, anisotropic, composite plates and shells. *Archives of Computational Methods in Engineering*, 9(2):87–140, 2002. 66
- E. Carrera. Historical review of Zig-Zag theories for multilayered plates and shells. *Applied Mechanics Reviews*, 56(3):287–308, 2003. 65
- J. C ea. The shape and topological optimizations connection. *Computer Methods in Applied Mechanics and Engineering*, 188(4):713–726, 2000. 199
- A. Cecchi and K. Sab. A homogenized Reissner–Mindlin model for orthotropic periodic plates: Application to brickwork panels. *International Journal of Solids and Structures*, 44(18-19):6055–6079, Sept. 2007. 83
- Y. Chen, S. Zhou, and Q. Li. Multiobjective topology optimization for finite periodic structures. *Computers & Structures*, 88(11-12):806–811, 2010. 120
- S. Cho and H.-S. Jung. Design sensitivity analysis and topology optimization of displacement–loaded non-linear structures. *Computer Methods in Applied Mechanics and Engineering*, 192(22-24):2539–2553, 2003. 201
- S. C. Davis, S. W. Diegel, and R. G. Boundy. *Transportation Energy Data Book: Edition 29*. U.S. Department of Energy, 2010. 11, 36
- E. De Luycker, F. Morestin, P. Boisse, and D. Marsal. Simulation of 3D interlock composite preforming. *Composite Structures*, 88(4):615–623, May 2009. 50
- J. Despois, A. Marmottant, L. Salvo, and A. Mortensen. Influence of the infiltration pressure on the structure and properties of replicated aluminium foams. *Materials Science and Engineering: A*, 462(1-2):68–75, 2007. 51
- P. Dewhurst. Analytical solutions and numerical procedures for minimum-weight Michell structures. *Journal of the Mechanics and Physics of Solids*, 49(3):445–467, Mar. 2001. 125
- J. W. Dunlop, R. Weinkamer, and P. Fratzl. Artful interfaces within biological materials. *Materials Today*, 14(3):70–78, Mar. 2011. 39
- H. a. Eschenauer and N. Olhoff. Topology optimization of continuum structures: A review. *Appl. Mech. Rev.*, 54(4):331, 2001. 119
- N. A. Fleck, V. S. Deshpande, and M. F. Ashby. Micro-architected materials: past, present and future. *Proceedings of the Royal Society A: Mathematical, Physical and Engineering Sciences*, 466(2121):2495–2516, 2010. 37
- M. Fuchs. The Aboudi micromechanical model for topology design of structures. *Computers & Structures*, 73(1-5):355–362, 1999. 119
- N. P. Garcia-Lopez, M. Sanchez-Silva, A. L. Medaglia, and A. Chateaufneuf. A hybrid topology optimization methodology combining simulated annealing and SIMP. *Computers & Structures*, 89(15-16):1512–1522, 2011. 201
- S. Gasser, Y. Brechet, and F. Paun. Materials Design for Acoustic Liners: an Example of Tailored Multifunctional Materials. *Advanced Engineering Materials*, 6(12):97–102, Feb. 2004. 47

REFERENCES

- M. Genet, M. Houmard, S. Eslava, E. Saiz, and A. P. Tomsia. A two-scale model of the mechanical behavior of bioceramic scaffolds made by robocasting: possibilities and limits. *Acta Biomaterialia*. 202
- A. Gersborg-Hansen, M. P. Bendsøe, and O. Sigmund. Topology optimization of heat conduction problems using the finite volume method. *Structural and Multidisciplinary Optimization*, 31(4):251–259, Mar. 2006. 120
- I. Gibson, D. W. Rosen, and B. Stucker. *Additive Manufacturing Technologies: Rapid Prototyping to Direct Digital Manufacturing*. Springer, 2009. ISBN 9781441911193. 90
- C. Gonzalez and J. Llorca. Mechanical behavior of unidirectional fiber-reinforced polymers under transverse compression: Microscopic mechanisms and modeling. *Composites Science and Technology*, 67(13):2795–2806, Oct. 2007. 50
- P. Grootenhuis. The control of vibrations with viscoelastic materials†. *Journal of Sound and Vibration*, 11(4):421–433, Apr. 1970. 47
- B. Guérin. Polyamides. *Techniques de l'Ingénieur*, A 3 360:1–22. 90
- A. Hanssen, Y. Girard, L. Olovsson, T. Berstad, and M. Langseth. A numerical model for bird strike of aluminium foam-based sandwich panels. *International Journal of Impact Engineering*, 32(7):1127–1144, July 2006. 47
- B. Hassani. A review of homogenization and topology optimization I—homogenization theory for media with periodic structure. *Computers & Structures*, 69(6):707–717, 1998a. 119
- B. Hassani. A review of homogenization and topology optimization III—topology optimization using optimality criteria. *Computers & Structures*, 69(6):739–756, 1998b. 119
- B. Hassani. A review of homogenization and topology optimization II—analytical and numerical solution of homogenization equations. *Computers & Structures*, 69(6):719–738, 1998c. 119
- C. Hasse, M. Grenet, A. Bontemps, R. Dendievel, and H. Sallée. Realization, test and modelling of honeycomb wallboards containing a Phase Change Material. *Energy and Buildings*, 43(1):232–238, Sept. 2010. 47
- S. J. Hollister. Porous scaffold design for tissue engineering. *Nature materials*, 4(7):518–24, 2005. 120
- S. J. Hollister, R. D. Maddox, and J. M. Taboas. Optimal design and fabrication of scaffolds to mimic tissue properties and satisfy biological constraints. *Biomaterials*, 23(20):4095–103, 2002. 120
- X. Huang, A. Radman, and Y. Xie. Topological design of microstructures of cellular materials for maximum bulk or shear modulus. *Computational Materials Science*, 50(6):1861–1870, 2011. 120
- I. Huynen, N. Quiévy, C. Bailly, P. Bollen, C. Detrembleur, S. Eggermont, I. Molenberg, J. Thomassin, L. Urbanczyk, and T. Pardoen. Multifunctional hybrids for electromagnetic absorption. *Acta Materialia*, 59(8):3255–3266, May 2011. 48
- F. Incropera, DeWitt, Bergman, and Lavine. Transient conduction. In *Fundamentals of Heat and Mass Transfer*, chapter 5, pages 255–346. John Wiley Sons, Ltd, 6 edition, 2007. ISBN 978-0-471-45728-2. 154

- T. R. Jackson, H. Liu, N. M. Patrikalakis, E. M. Sachs, and M. J. Cima. Modeling and designing functionally graded material components for fabrication with local composition control. *Materials & Design*, 20(2-3):63–75, 1999. 201
- D. Jauffrès, C. Yacou, M. Verdier, R. Dendievel, and A. Ayrat. Mechanical properties of hierarchical porous silica thin films: Experimental characterization by nanoindentation and Finite Element modeling. *Microporous and Mesoporous Materials*, 140(1-3):120–129, Apr. 2011. 50
- A. Jibawy, B. Desmorat, and A. Vincenti. Optimisation structurale de coques minces composites stratifiées. In *10ème Colloque National en Calcul des Structures*, volume 2, 2011. 118
- R. Kicinger, T. Arciszewski, and K. Jong. Evolutionary computation and structural design: A survey of the state-of-the-art. *Computers & Structures*, 83(23-24):1943–1978, Sept. 2005. 117
- A. Lebé. *Thick periodic plates homogenization, application to sandwich panels including chevron folded core*. PhD thesis, Université Paris-Est, 2010. 66, 83
- P. Lhuissier. *Random hollow spheres stackings: structure, behavior and integration into sandwich structures*. PhD thesis, Institut Polytechnique de Grenoble, 2009. 179
- Y. Li, K. Saitou, and N. Kikuchi. Topology optimization of thermally actuated compliant mechanisms considering time-transient effect. *Finite Elements in Analysis and Design*, 40:1317 – 1331, 2004. 201
- Z. Liu and J. G. Korkin. Structural Shape Optimization Using Moving Mesh Method. In *Comsol Users Conference*, 2007. 119
- E. Lund. Buckling topology optimization of laminated multi-material composite shell structures. *Composite Structures*, 91(2):158–167, Nov. 2009. 118
- Z.-D. Ma, N. Kikuchi, and H.-C. Cheng. Topological design for vibrating structures. *Comput. Methods Appl. Mech. Engrg.*, 121:259–280, 1995. 120
- J. Mackerle. Topology and shape optimization of structures using FEM and BEM A bibliography (1999–2001). *Finite Elements in Analysis and Design*, 39(3):243–253, 2003. 119
- P. Martínez, P. Martí, and O. M. Querin. Growth method for size, topology, and geometry optimization of truss structures. *Structural and Multidisciplinary Optimization*, 33(1):13–26, 2006. 125
- J. Michel, H. Moulinec, and P. Suquet. Effective properties of composite materials with periodic microstructure: a computational approach. *Comput. Methods Appl. Mech. Engrg.*, 172(1-4):109–143, Apr. 1999. 77
- F. Mirsch, N. Weinert, M. Pech, and G. Seliger. Vault Structures Enabling Sustainable Products. In *13th International Conference on Life Cycle Engineering*, volume 3, pages 629–634, 2006. 99
- E. Munoz, G. Allaire, and M. P. Bendsøe. On two formulations of an optimal insulation problem. *Structural and Multidisciplinary Optimization*, 33(4-5):363–373, 2007. 120
- E. Nelli Silva, J. Ono Fonseca, and N. Kikuchi. Optimal design of periodic piezocomposites. *Computer Methods in Applied Mechanics and Engineering*, 159:49–77, 1998. 120

REFERENCES

- M. M. Neves, H. Rodrigues, and J. M. Guedes. Optimal design of periodic linear elastic microstructures. *Computers & Structures*, 76(1-3):421–429, 2000. ISSN 00457949. doi: 10.1016/S0045-7949(99)00172-8. 120
- A. A. Novotny, R. A. Feijoo, C. Padra, and E. Taroco. Topological Derivative for Linear Elastic Plate Bending Problems. *Control and Cybernetics*, 34(1):339–361, 2005. 120
- A. A. Novotny, R. Feijoo, E. Taroco, and C. Padra. Topological sensitivity analysis for three-dimensional linear elasticity problem. *Computer Methods in Applied Mechanics and Engineering*, 196(41-44):4354–4364, Sept. 2007. 199
- S. Osher. Level Set Methods for Optimization Problems Involving Geometry and Constraints I. Frequencies of a Two-Density Inhomogeneous Drum. *Journal of Computational Physics*, 171(1):272–288, July 2001. 120
- K.-S. Park and S.-K. Youn. Topology optimization of shell structures using adaptive inner-front (AIF) level set method. *Structural and Multidisciplinary Optimization*, 36:43–58, 2008. 120
- J. Parthasarathy, B. Starly, and S. Raman. A design for the additive manufacture of functionally graded porous structures with tailored mechanical properties for biomedical applications. *Journal of Manufacturing Processes*, 13(2):160–170, 2011. 202
- R. Piat, Y. Sinchuk, M. Vasoya, and O. Sigmund. Minimal compliance design for metal–ceramic composites with lamellar microstructures. *Acta Materialia*, 59(12):4835–4846, 2011. 118
- J. Portier, J.-h. Choy, and M. A. Subramanian. Inorganic–organic-hybrids as precursors to functional materials. *International Journal of Inorganic Materials*, 3:581–592, 2001. 38
- D. Queheillalt and H. N. G. Wadley. Cellular metal lattices with hollow trusses. *Acta Materialia*, 53(2):303–313, 2005. 52
- J. N. Reddy. On refined computational models of composite laminates. *International Journal for Numerical Methods in Engineering*, 27(2):361–382, 1989. 66
- R. Roy, S. Hinduja, and R. Teti. Recent advances in engineering design optimisation: Challenges and future trends. *CIRP Annals - Manufacturing Technology*, 57(2):697–715, 2008. 117
- J. Salençon. *Mécanique des milieux continus: Milieux curvilignes*, volume 3 of *Mécanique des milieux continus*. Ecole polytechnique, 2002. ISBN 9782730209625. 59
- G. V. Salmoria, J. L. Leite, and R. A. Paggi. The microstructural characterization of PA6/PA12 blend specimens fabricated by selective laser sintering. *Polymer Testing*, 28(7):746–751, 2009. 90
- S. Schwarz, K. Maute, and E. Ramm. Topology and shape optimization for elastoplastic structural response. *Computer Methods in Applied Mechanics and Engineering*, 190(15-17):2135–2155, 2001. 201
- J. Schwerdtfeger, F. Wein, G. Leugering, R. F. Singer, C. Körner, M. Stingl, and F. Schury. Design of auxetic structures via mathematical optimization. *Advanced materials*, 23(22-23):2650–4, 2011. 120
- J. A. Sethian. *Level set methods and fast marching methods: evolving interfaces in computational geometry, fluid mechanics, computer vision, and materials science*. Cambridge monographs on applied and computational mathematics. Cambridge University Press, 1999. ISBN 9780521642040. 84, 120, 123

- J. A. Sethian. Structural Boundary Design via Level Set and Immersed Interface Methods. *Journal of Computational Physics*, 163(2):489–528, Sept. 2000. 120
- O. Sigmund. Tailoring materials with prescribed elastic properties. *Mechanics of Materials*, 20(4):351–368, 1995. 120
- O. Sigmund and S. Torquato. Design of materials with extreme thermal expansion using a three-phase topology optimization method. *Journal of the Mechanics and Physics of Solids*, 45(6):1037–1067, 1997. 120
- O. Sigmund and S. Torquato. Design of smart composite materials using topology optimization. 8:365–379, 1999. 120
- J. Sokółowski and J. P. Zolésio. *Introduction to shape optimization: shape sensitivity analysis*. Springer series in computational mathematics. Springer-Verlag, 1992. ISBN 9783540541776. 119
- D. Tcherniak and O. Sigmund. A web-based topology optimization program. *Structural and Multidisciplinary Optimization*, 22(3):179–187, 2001. 119
- L. Valdevit. Structurally optimized sandwich panels with prismatic cores. *International Journal of Solids and Structures*, 41(18-19):5105–5124, Sept. 2004. 52
- F. Vankeulen, R. Haftka, and N. Kim. Review of options for structural design sensitivity analysis. Part 1: Linear systems. *Computer Methods in Applied Mechanics and Engineering*, 194(30-33):3213–3243, Aug. 2005. 117
- H. N. G. Wadley. Multifunctional periodic cellular metals. *Philosophical transactions. Series A, Mathematical, physical, and engineering sciences*, 364(1838):31–68, Jan. 2006. 14, 51, 52
- A. Walcarius. Electrochemical Applications of Silica-Based OrganicInorganic Hybrid Materials. *Chemistry of Materials*, 13(10):3351–3372, Oct. 2001. 38
- J. M. Whitney and A. W. Leissa. Analysis of heterogeneous anisotropic plates. *Journal of applied mechanics*. *Journal of Applied Mechanics*, 36:261–266, 1969. 65
- B. Wielage and G. Thielemann. Dedicated Applications of Carbon Fiber Reinforced Plastics in Machine Engineering. *Advanced Engineering Materials*, 6(3):151–153, Mar. 2004. 49
- T. Yamada, K. Izui, S. Nishiwaki, and A. Takezawa. A topology optimization method based on the level set method incorporating a fictitious interface energy. *Computer Methods in Applied Mechanics and Engineering*, 2010. 85, 199, 200
- S.-D. Yang, H. G. Lee, and J. Kim. A phase-field approach for minimizing the area of triply periodic surfaces with volume constraint. *Computer Physics Communications*, 181(6):1037–1046, 2010. 201
- W. Yu, D. H. Hodges, and V. V. Volovoi. Asymptotic construction of Reissner-like composite plate theory with accurate strain recovery. *International Journal of Solids and Structures*, 39:5185–5203, 2002a. 66
- W. Yu, D. H. Hodges, and V. V. Volovoi. Asymptotic generalization of Reissner–Mindlin theory: accurate three-dimensional recovery for composite shells. *Computer Methods in Applied Mechanics and Engineering*, 191:5087–5109, 2002b. 66

REFERENCES

- H. Zeng, S. Pattofatto, H. Zhao, Y. Girard, and V. Fascio. Perforation of sandwich plates with graded hollow sphere cores under impact loading. *International Journal of Impact Engineering*, 37(11):1083–1091, Nov. 2010. 47
- D. Zenkert. *The Handbook of Sandwich Construction*. Engineering Materials Advisory Services, 1997. 45, 53
- C. Zhuang, Z. Xiong, and H. Ding. A level set method for topology optimization of heat conduction problem under multiple load cases. *Computer Methods in Applied Mechanics and Engineering*, 196(4-6):1074–1084, Jan. 2007. 120

Homogénéisation et optimisation topologique de panneaux architecturés

Résumé

La conception sur-mesure de matériaux architecturés à l'échelle du milli/centimètre est une stratégie pour développer des matériaux de structure plus performants vis-à-vis de cahiers des charges multifonctionnels. Ce travail de thèse s'intéresse en particulier à la conception optimale de panneaux architecturés périodiques, dans le but de combiner des exigences mécaniques de flexion et de cisaillement, ainsi que de conductivité thermique.

Le comportement élastique peut être prédit grâce à l'identification sur la cellule périodique des coefficients de la matrice des souplesses équivalente. Ces calculs d'homogénéisation ont été mis en œuvre par éléments finis pour estimer en particulier les souplesses en flexion et en cisaillement transverse. Après validation expérimentale, cette méthode de calcul constitue un outil d'évaluation des performances mécaniques pour chaque géométrie de cellule périodique (2D ou 3D). À titre d'exemple, et dans un contexte de développement de solutions matériaux architecturés pour l'automobile, la conception de tôles "texturées" est proposée en menant une étude paramétrique à l'aide de cet outil.

L'implémentation d'un algorithme d'optimisation topologique couplé à la procédure d'homogénéisation permet d'enrichir les méthodes de conception sur-mesure en élargissant l'espace de recherche des "architectures". Après l'étude modèle du compromis entre flexion et cisaillement, le cas industriel d'un panneau sandwich isolant est traité. Dans ce cas, l'optimisation fournit plusieurs compromis prometteurs entre rigidité en cisaillement et isolation thermique. Ces géométries ont été réalisées et testées, et une nouvelle version améliorée du panneau sandwich a été sélectionnée.

Mots-clés

Matériaux architecturés, structures sandwich, homogénéisation périodique, optimisation topologique, prototypage rapide, essais de flexion quatre-points.

Homogenization and topological optimization of architected panels

Abstract

The "material by design" strategy consists in tailoring architected materials in order to fulfill multi-functional specifications. This PhD study focuses more specifically on designing architected panels in regards with mechanical compliances (bending and transverse shear), as well as thermal conductivity.

Recent advances on periodic homogenization of plates are integrated into a finite elements tool that enables to identify the Reissner-Mindlin effective compliance from the unit cell geometry. The comparison with four-point bending tests illustrates a discussion on the shear loading for homogenization, and its contribution to the global bending stiffness. In a context of architected steel solutions for automotive, a parametric study is treated on "embossed" steel sheets using this homogenization tool.

As a try to enlarge the space of available "architectures", a topological optimization algorithm (using the level-set method) is coupled to the homogenization procedure. The influence of each parameters of the method are studied on the optimization problem of compromising flexural and shear compliances. Finally, the industrial case of an insulation sandwich panel is treated. Few optimized geometries, with a high combination of shear stiffness and thermal insulation, are built, produced and tested. An improved design is highlighted and proposed as next version of this product.

Keywords

Architected materials, sandwich structures, periodic homogenization, topological optimization, selective laser sintering, four-point bending test.